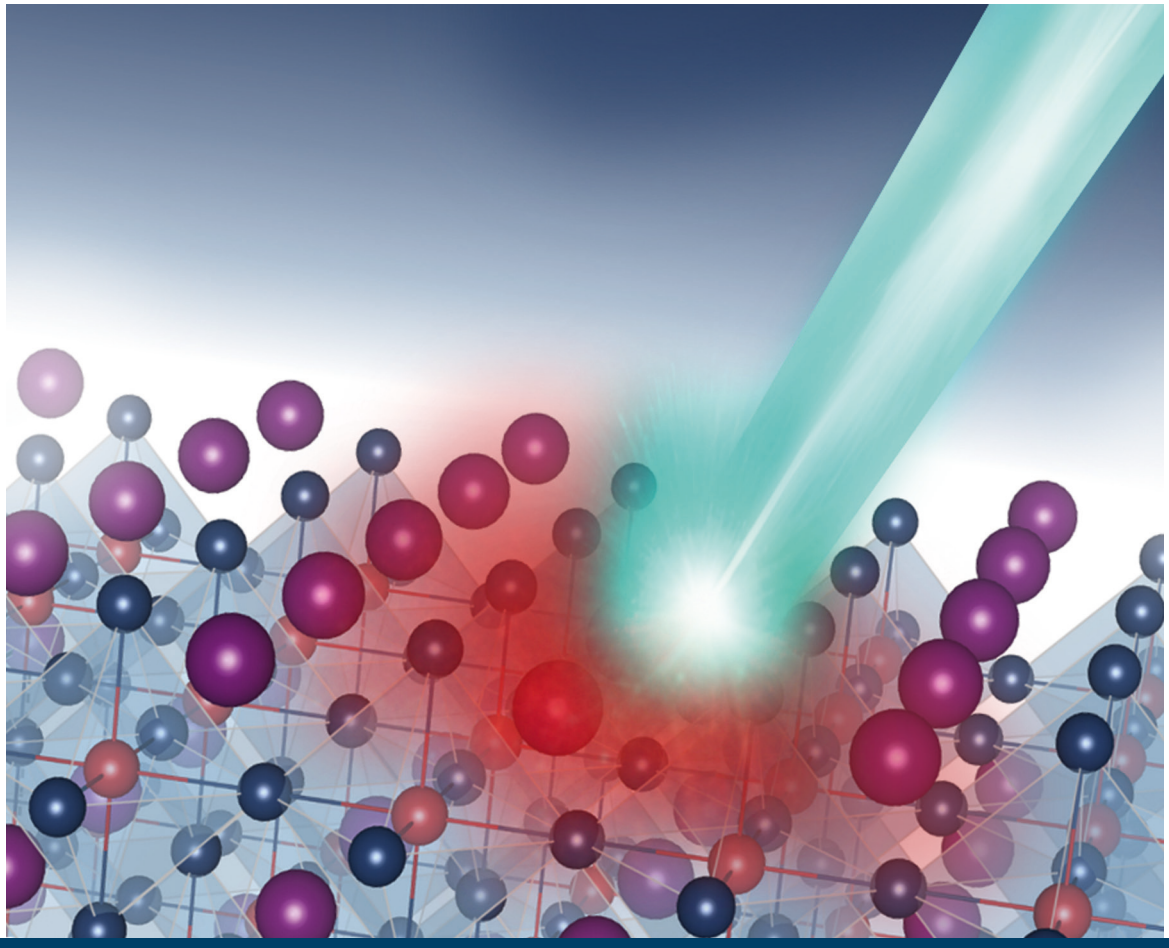

Quantifying Recombination Losses and Charge Extraction in Halide Perovskite Solar Cells

Lisa Krückemeier

Energie & Umwelt / Energy & Environment
Band / Volume 669
ISBN 978-3-95806-835-3

Mitglied der Helmholtz-Gemeinschaft

JÜLICH
Forschungszentrum

Schriften des Forschungszentrums Jülich
Reihe Energie & Umwelt / Energy & Environment Band / Volume 669

Forschungszentrum Jülich GmbH
Institute of Energy Materials and Devices (IMD)
Photovoltaik (IMD-3)

Quantifying Recombination Losses and Charge Extraction in Halide Perovskite Solar Cells

Lisa Krückemeier

Schriften des Forschungszentrums Jülich
Reihe Energie & Umwelt / Energy & Environment Band / Volume 669

ISSN 1866-1793 ISBN 978-3-95806-835-3

Bibliografische Information der Deutschen Nationalbibliothek.
Die Deutsche Nationalbibliothek verzeichnet diese Publikation in der
Deutschen Nationalbibliografie; detaillierte Bibliografische Daten
sind im Internet über http://dnb.d-nb.de abrufbar.

Herausgeber und Vertrieb:	Forschungszentrum Jülich GmbH Zentralbibliothek, Verlag 52425 Jülich Tel.: +49 2461 61-5368 Fax: +49 2461 61-6103 zb-publikation@fz-juelich.de www.fz-juelich.de/zb
Umschlaggestaltung:	Grafische Medien, Forschungszentrum Jülich GmbH
Druck:	Grafische Medien, Forschungszentrum Jülich GmbH
Copyright:	Forschungszentrum Jülich 2025

Schriften des Forschungszentrums Jülich
Reihe Energie & Umwelt / Energy & Environment, Band / Volume 669

D 82 (Diss. RWTH Aachen University, 2024)

ISSN 1866-1793
ISBN 978-3-95806-835-3

Vollständig frei verfügbar über das Publikationsportal des Forschungszentrums Jülich (JuSER)
unter www.fz-juelich.de/zb/openaccess.

Contents

Abstract

Due to their exceptional properties, halide perovskite materials have emerged as promising candidates for efficient and cost-effective photovoltaics, with some devices approaching the performance of silicon solar cells after a decade of research. Despite their remarkable progress, perovskite solar cells suffer from several loss mechanisms that limit their efficiency. However, the rapid development of perovskite research has outpaced advances in analyzing characterization techniques tailored to the unique properties of this material class. Thus, understanding and quantifying the losses within these devices remains difficult, especially in terms of recombination losses and charge-extraction dynamics. This work aims to bridge this gap by proposing innovative approaches and providing tools for analyzing charge-carrier dynamics, which will help correctly interpret and quantify experimental data for perovskite solar cells. The overarching motivation is to contribute to the advancement of perovskite solar cell technology by gaining a deeper understanding of fundamental processes.

Transient photoluminescence (TPL) and transient photovoltage (TPV) are popular techniques for monitoring charge-carrier dynamics and investigating recombination losses in perovskites. However, the low doping density of lead-halide perovskites often places the device in high-level injection during these measurements, leading to non-linear relationships between the recombination rates and carrier densities. This behavior leads to challenges in the use of a scalar charge-carrier lifetime as a figure of merit to quantify recombination. Furthermore, the interpretation of data from complete solar cells or multilayer samples is highly challenging due to the superposition of various effects that modulate the charge-carrier concentration. These effects include bulk and interfacial recombination, charge transfer and extraction, and capacitive charging or discharging. While theoretical work on TPL decays in full solar-cell devices has been published for other photovoltaic technolo-

gies, a comprehensive theory dealing with the specific situation in halide-perovskite devices is currently missing. In this work, improved spectroscopic techniques with a high dynamic range of data acquisition are combined with time-dependent, numerical simulations with Sentaurus TCAD to break down the complex behavior of charge-carrier dynamics in perovskite solar cells.

The dissertation contributes to the field by proposing new methods and analytical models for data analysis of perovskite solar cells. One major contribution involves a comprehensive analysis of transient photoluminescence and transient photovoltage decays, considering non-linear dependencies of the recombination rate on charge-carrier density. This multi-method quantitative data analysis of transient photoluminescence and transient photovoltage decays goes beyond traditional mono-exponential fitting methods, introducing an approach to derive differential decay times as a function of charge-carrier density and quasi-Fermi level splitting. Time-dependent, numerical drift-diffusion simulations of various sample structures, including perovskite films, multilayer systems, and complete devices, provide visualization and explanation of the injection dependence of the decay time and allow distinguishing between different carrier-density-dependent regimes. Building upon these insights, analytical equations are developed that serve as good approximations to the simulated and experimental decay-time functions. These analytical equations facilitate data analysis and the extraction of key material parameters, like trap-assisted Shockley-Read-Hall recombination coefficients, by removing the need to do extensive numerical simulations.

The analytical approach is further expanded to include the extraction of charge carriers by the interlayers and contacts, in addition to recombination. A two-component model for small-signal measurements is developed that is based on the analytical solution of coupled linear differential equations via the determination of eigenvalues. The model describes the transient behaviour of chemical and electrical potentials and allows us to connect the rise and decay times in small-signal transient-photovoltage experiments to recombination, extraction, and capacitive charging and discharging effects, providing quantitative values for recombination and extraction-time constants as a function of voltage.

Another part of this work is the development of a standardized framework for reporting voltage loss in perovskite solar cells, addressing the impact of perovskite

composition changes on the limiting open-circuit voltage, and proposing a consistent reference. This approach, approximating the radiative limit, requires only a single measurement of the external quantum efficiency for its calculation, and is therefore fast and easy to apply. The study compares different band gap definitions used in the literature, revealing a substantial impact on the ranking of the voltage losses. The proposal of referencing open-circuit voltages to the radiative limit enables a meta-analysis of previously published perovskite solar cells.

In addition, I present inverted, planar MAPI solar cells with open-circuit voltages exceeding 1.26 V. The combination of dry lead acetate and lead chloride precursors, along with optimized hole and electron transport layers, suppresses both bulk and surface recombination, which is confirmed by an exceptionally high photoluminescence external quantum efficiency exceeding 5 % in complete cells. These solar cells serve as the basis for subsequent investigations of device physics and characterization techniques.

These scientific contributions significantly expand the state-of-the-art by offering innovative methodologies for characterizing halide perovskite solar cells. The proposed frameworks and analytical approaches not only fill existing gaps in understanding the implications of unconventional material properties, but also pave the way for more accurate and comprehensive analysis in future perovskite research.

Zusammenfassung

Halogenid-Perowskit-Materialien haben sich aufgrund ihrer außergewöhnlichen Eigenschaften als vielversprechende Kandidaten für eine effiziente und kostengünstige Photovoltaik hervorgetan, wobei einige Bauelemente nach einem Jahrzehnt der Forschung an die Leistung von Silizium-Solarzellen heranreichen. Trotz ihrer bemerkenswerten Entwicklung leiden Perowskit-Solarzellen unter verschiedenen Verlustmechanismen, die ihre Effizienz mindern. Allerdings konnte die Weiterentwicklung von Analysemethoden in der Messtechnik, die auf die einzigartigen Eigenschaften dieser Materialklasse zugeschnitten sind, kaum mit dem raschen Fortschritt der Perowskit-Forschung mithalten. Daher ist es nach wie vor schwierig, die Verluste, insbesondere im Hinblick auf Rekombination und Ladungsträgerextraktion, in diesen eletronischen Bauelementen zu verstehen und zu quantifizieren. Ziel dieser Arbeit ist es, diese Lücke zu schließen und innovative Ansätze und Methoden zur Analyse der Ladungsträgerdynamik zu entwickeln, die eine verlässliche und eindeutige Interpretation experimenteller Messdaten von Perowskit-Solarzellen erlauben.

Transiente Photolumineszenz (TPL) und transiente Photospannung (TPV) sind beliebte Messmethoden zur Untersuchung der Ladungsträgerdynamik und der Messung von Rekombinationsverlusten in Perowskiten. Die niedrige Dotierstoffkonzentration von Bleihalogenid-Perowskiten führt jedoch häufig dazu, dass das Bauelement während dieser Messungen in Hochinjektion gebracht wird, was zu nichtlinearen Abhängigkeiten zwischen den Rekombinationsraten und Ladungsträgerdichten führt. Dadurch ist die Verwendung einer skalaren Ladungsträger-Lebensdauer als Kenngröße für die Quantifizierung der Rekombination ungeeignet. Darüber hinaus ist die Interpretation von Messdaten von Solarzellen oder Mehrschichtsystemen sehr komplex, da eine Überlagerung verschiedener Effekte stattfindet. Zu diesen Effekten gehören Bulk- und Grenzflächenrekombination, Ladungstransfer und -extraktion, so-

wie kapazitive Ladung oder Entladung von Kontakt- und Zwischenschichten. Während für andere Photovoltaik-Technologien theoretische Arbeiten zum Abklingverhalten der transienten Photolumineszenz von Solarzellen veröffentlicht wurden, fehlt derzeit eine umfassende Theorie, die sich mit der spezifischen Situation in Halogenid-Perowskit-Bauelementen befasst. In dieser Arbeit werden verbesserte spektroskopische Techniken mit einem hohen dynamischen Bereich in der Datenerfassung mit zeitabhängigen, numerischen Simulationen mit Sentaurus TCAD kombiniert, um das komplexe Verhalten der Ladungsträgerdynamik in Perowskit-Solarzellen zu entschlüsseln.

Die Dissertation leistet einen Beitrag zum Forschungsgebiet, indem sie neue Methoden und analytische Modelle für die Datenanalyse von Perowskit-Solarzellen entwickelt. Ein wichtiger Beitrag besteht in einer umfassenden Analyse der transienten Photolumineszenz und des transienten Photospannungsabfalls unter Berücksichtigung nichtlinearer Abhängigkeiten der Rekombinationsrate von der Ladungsträgerdichte. Die methodenübergreifende Analyse geht dabei über die traditionellen monoexponentiellen Fitting-Methoden hinaus und führt eine differentielle Abklingzeit als Funktion der Ladungsträgerdichte und der Quasi-Fermi-Niveau-Aufspaltung als neue Kenngröße ein. Zeitabhängige, numerische Drift-Diffusions-Simulationen verschiedenster Probenstrukturen, wie Perowskit-Filme, Mehrschichtsysteme und kompletten Bauelementen, ermöglichen die Visualisierung und Erklärung der Injektionsabhängigkeit dieser Größe und erlauben die Unterscheidung zwischen verschiedenen Regimen. Aufbauend auf diesen Erkenntnissen werden analytische Gleichungen entwickelt, die als gute Näherungen für die simulierten und experimentellen Abklingzeitfunktionen dienen. Diese analytischen Gleichungen erleichtern die Datenanalyse und die Extraktion charakteristischer Materialparameter aus den Observablen, wie z. B. der Shockley-Read-Hall-Rekombinationskoeffizienten, indem sie umfangreiche numerische Simulationen verzichtbar machen. Darüber hinaus wird ein konsistentes Gesamtbild aufgezeigt, dass die Diskrepanzen zwischen transienten Großsignal-Photolumineszenz- und transienten Kleinsignal-Photospannungs-Abklingzeiten vorstellt und erklärt. Diese Studie verbindet damit verschiedene 'Lebensdauerkonzepte' und schafft so die Grundlage für eine methodenübergreifende quantitative Datenanalyse. Der analytische Ansatz wird zusätzlich zur Rekombination auch auf die Extraktion von Ladungsträgern durch die Zwischenschichten und Kontakte erweitert. Es

wird ein Zweikomponentenmodell für Kleinsignalmessungen entwickelt, das auf der analytischen Lösung gekoppelter linearer Differentialgleichungen über die Bestimmung von Eigenwerten beruht. Das Modell beschreibt das transiente Verhalten chemischer und elektrischer Potenziale und ermöglicht es, die Anstiegs- und Abklingzeiten in transienten Kleinsignal-Photospannungsexperimenten mit Rekombinations-, Extraktions- und kapazitiven Lade- und Entladeeffekten in Verbindung zu bringen und quantitative Werte für Rekombinations- und Extraktionszeitkonstanten als Funktion der Spannung zu liefern.

Ein weiterer Beitrag diese Arbeit ist die Entwicklung eines standardisierten Verfahrens für die Berechnung von Spannungsverlusten in Perowskit-Solarzellen, welches die Auswirkungen von Variationen in der Perowskit-Zusammensetzung auf die maximal erreichbare Leerlaufspannung berücksichtigt und eine einheitliche Bezugsgröße vorschlägt. Dieser Ansatz, der eine Annäherung an das strahlende Limit darstellt, erfordert nur eine einzige Messung der externen Quanteneffizienz für die Berechnung und ist daher schnell und einfach anwendbar. Die Studie vergleicht verschiedene in der Literatur verwendete Bandlückendefinitionen und zeigt, dass die Wahl dieser Definition einen erheblichen Einfluss auf die Bewertung der Spannungsverluste hat. Die Methode ermöglicht außerdem eine Meta-Analyse der bisher veröffentlichten Perowskit-Solarzellen.

Darüber hinaus werden invertierte, planare MAPI-Solarzellen mit Leerlaufspannungen von mehr als $1,26\,\mathrm{V}$ entwickelt. Die Kombination aus wasserfreiem Bleiacetat- und Bleichlorid-Prekursoren, sowie optimierten Loch- und Elektronentransportschichten, unterdrückt sowohl die Bulk- als auch die Oberflächenrekombination, was durch die Messung von außergewöhnlich hohe absoluten Photolumineszenz-Quantenausbeuten von über $5\,\%$ bestätigt wird. Diese Bauteilentwicklung dient als Grundlage für nachfolgende Untersuchungen der Bauelementphysik und Weiterentwicklung von Charakterisierungsmethoden.

1 Introduction

The transition towards a carbon-neutral energy system based on renewable energy sources is urgently needed to tackle global greenhouse gas emissions and address anthropogenic climate change. Solar energy is one of the most promising sources of renewable energy, offering an abundant and sustainable alternative to fossil fuels. According to the Intergovernmental Panel on Climate Change (IPCC), photovoltaics (PV), which uses semiconductor materials to convert sunlight directly into electricity, is currently the most cost-effective way to avoid CO_2. [1] Photovoltaics is the fastest-growing technology for power generation and is a key player in providing a sustainable source of electric power. The global solar PV installations have grown exponentially in the last decade, and in 2022, the cumulative installed capacity surpassed 1 TW. However, despite its significant growth and cost reduction, PV remains a minor contributor to global electricity generation, accounting for only 4 to 5 %. Moreover, the window of opportunity to take large-scale action to reduce greenhouse gas emissions is closing. [2]

The largest share of the PV market is currently held by silicon wafer technology, which accounts for about 95 % of devices produced today. [3, 4] Among various photovoltaic technologies, silicon-based solar cells are the most mature and widely used due to their high efficiency and reliability. In 1954, Bell Laboratories scientists achieved a major milestone by creating the world's first operational silicon photovoltaic cell with around 6 % efficiency. [5] Since then, continuous research and optimization efforts have been made to improve silicon wafer technology, resulting in a current efficiency record of 26.8 %. [6, 7] Although silicon solar cells have proven to be efficient and cost-effective, their production process requires a large amount of energy, resulting in an energy payback time (EPBT) of around one to two years to compensate for the input energy. [3, 4] In addition, the performance is limited by

their fundamental material properties, like the indirect band gap. Therefore, developing alternative photovoltaic technologies that offer high efficiency at low cost and reduced energy consumption is highly desirable.

Perovskite solar cells (PSCs) are a relatively new photovoltaic technology that has shown great promise in recent years, offering the advantages of low-cost and low-temperature fabrication, flexibility, and lightweight. Perovskite solar cells use a hybrid organic-inorganic lead halide material as the light-absorbing layer, which features a tunable band gap and a significantly higher optical absorption coefficient as compared to silicon. In addition, these materials are defect-tolerant and show a high luminescence quantum yield. Their rare combination of favorable properties makes perovskites a promising class of optoelectronic material, [8–10] which has attracted considerable attention from the research community. Perovskite solar cells have achieved rapid progress in power conversion efficiency (PCE), with record efficiencies approaching the performance of silicon solar cells in just a few years. The PCE of PSCs has increased from 3.8 % in 2009 [11] to over 25 % in 2021, [12] which is the fastest efficiency improvement ever reported for any solar technology.

Despite their remarkable progress, perovskite solar cells suffer from several loss mechanisms that limit their efficiency and stability. Loss mechanisms in PSCs can arise from various sources, including charge recombination, non-radiative energy dissipation, trap-assisted recombination, ion migration, and interfacial charge transfer, among others. One of the most significant losses is due to charge-carrier recombination, which is the loss of carriers before they reach the electrodes, resulting in a lower current and voltage output. Also the extraction of charges from perovskite films is an issue that reduces efficiency. Understanding and mitigating the loss mechanisms in perovskite solar cells and their dependence on material properties, device structures, and operating conditions is also a key challenge to further enhancing their performance and reliability. Transient photoluminescence (TPL) and transient photovoltage (TPV) measurements have already been used as non-destructive and reliable techniques to study the fundamental properties of perovskite solar cells. However, this Ph.D. thesis proposes novel concepts directly tailored to PSCs and presents an improved understanding of these two techniques. By forming a deeper understanding of transient behaviour, this thesis aims to pave the way for the development of high-performance and stable perovskite solar cells.

While this thesis focuses on perovskite solar cells' device physics, it begins by introducing the fundamental concepts, definitions, and terminologies that form the foundation of all solar cell technologies. **Chapter 2** starts by deriving the upper efficiency limit of an ideal single-junction solar cell, known as the Shockley-Queisser model, which serves as a reference for actual solar cells. Subsequently, the more realistic radiative limit is presented, accounting for the real optical properties of the semiconducting absorber. Further exploration delves into additional loss mechanisms that affect the performance of real solar cells, along with experimentally measurable figures of merit that quantify deviations from the ideal model. Then, the material properties and working principle of metal-halide perovskite solar cells are introduced, with particular emphasis on recombination and open-circuit voltage losses.

In **Chapter 3**, the focus shifts to the characterization methods employed in this thesis. Alongside fundamental measurements such as voltage-dependent current (JV) and external quantum efficiency (EQE), transient methods such as time-resolved photoluminescence (TPL) and transient photovoltage (TPV) measurements are comprehensively covered. These transient techniques provide valuable insights into recombination dynamics, a key subject of investigation in this study.

The first two result chapters cover the development and optimization of perovskite solar cells fabricated within the scope of this thesis. **Chapter 4** explores the fabrication and characterization of solution-processed, inverted, planar methylammonium lead iodide (MAPI) solar cells. We achieved record open-circuit voltages exceeding 1.26 V by employing optimized fabrication techniques and carefully tailored hole- and electron-transport layers. Measurements of absolute photoluminescence and external quantum efficiencies validate the successful suppression of bulk and surface recombination, attaining impressive performance. The following **Chapter 5** outlines the technological development of coevaporated MAPI solar cells at the Jülich online semiconductor growth experiment for photovoltaics (JOSEPH) during the time of my dissertation. Here, the perovskite absorber layer is processed via an alternative fabrication routine, a vapor deposition called coevaporation.

Chapter 6 introduces a standardized framework for reporting voltage loss in perovskite solar cells. It addresses the challenge posed by varying perovskite compositions and band gaps, demonstrating how different band gap definitions used

in literature impact the calculated limit of the open-circuit voltage. The radiative open-circuit voltage, calculated from measured absorption and electroluminescence spectra, is compared with open-circuit voltages obtained through different definitions, enabling accurate referencing to the radiative limit.

The last three chapters expand the current understanding of the two measurement techniques, transient photoluminescence (TPL) and transient photovoltage (TPV), and build upon each other. First, **Chapter 7** delves into interpreting transient photoluminescence measurements on multilayer perovskite samples. A comprehensive understanding of this characterization method is achieved by combining numerical simulations, analytical solutions, and experimental data. The effects of bulk and interfacial recombination, charge transfer, and capacitive charging or discharging are analyzed, providing insights into the dominant processes for different sample types. **Chapter 8** addresses the discrepancies between large-signal transient photoluminescence (TPL) and small-signal transient photovoltage (TPV) decay times. I present a consistent framework to connect the different '*lifetime*' concepts and present the measurement conditions and data analysis methods necessary to obtain meaningful results. A comprehensive understanding of the different methods and their measurements is achieved by employing experimental data, numerical modeling and analytical equations. Finally, **Chapter 9** expands on the time-dependent behavior of charge carriers in perovskite solar cells, considering recombination, charge extraction, and the capacitive effects of electrode charging and discharging. A simplified analytical model is developed through transient drift-diffusion simulations to describe the transient characteristics of perovskite solar cells. An advanced two-component model is introduced to account for finite-speed of charge extraction and enables the determination of carrier recombination and extraction rates. Analyzing transient photovoltage measurements establishes a link between efficiency losses and the ratio of recombination and extraction rates, providing a comprehensive understanding of perovskite solar cell dynamics.

2 Fundamentals - Solar Cell Device Physics

A solar cell directly converts solar radiation into electrical energy using the internal photoelectric effect. [13, 14] Thermodynamically, the temperature difference between the earth and the sun's surface and its associated thermal radiations drive this process. The underlying operating principle requires a semiconductor that absorbs the solar spectrum as efficiently as possible and generates free electric charge carriers. Furthermore, it is necessary to selectively transport the photogenerated electrons and holes to their respective electrical contacts so that they get extracted and electric current flows without significant energy losses. [13–16]

While this thesis focuses on the device physics of metal-halide perovskite solar cells, this chapter begins by introducing the general and established concepts, definitions, and terminologies on which all solar cell technologies are built. First, the upper efficiency limit of an ideal single-junction solar cell in the Shockley-Queisser model is derived. This idealized model serves as a reference to evaluate the performance of actual solar cells. In this context, I also introduce the current-voltage characteristic and explain the different operating points of a solar cell. Subsequently, I present the more realistic radiative limit, which accounts for the actual optical properties of the semiconducting absorber. This radiative limit represents an actual thermodynamic efficiency limit discussed in section 2.2.

Section 2.3 discusses additional loss mechanisms that lower the performance of real-world solar cells. In addition, experimentally measurable figures of merit, quantifying how real-world solar cells differ from the ideal model, are introduced. In section 2.4 and 2.5, material properties and the working principle of metal-halide perovskite solar cells are introduced, with special attention to recombination.

2.1 Shockley-Queisser Model

The Shockley-Queisser model (SQ) [17] defines the maximum energy conversion efficiency η^{SQ} of a solar cell consisting of a semiconducting absorber with a single band gap $E_{\mathrm{g}}^{\mathrm{SQ}}$, using the basic thermodynamic principle of detailed balance. [18] This model is an idealized approach that neglects all avoidable losses, assuming that the solar cell is characterized by perfect extraction and idealized absorption properties. [19] An overview of the basic assumptions and settings is presented in Figure 2.1.

In the SQ model, the ideal solar cell interacts with the surroundings by exchanging photons with the sun and the ambient environment, electric charge with an external electrical circuit, and heat with a temperature reservoir, keeping the cell temperature T_{cell} constant and equal to the ambient temperature T_{amb}. While the original setting of the SQ model uses the black-body spectrum at 6000 K to describe the incoming solar radiation, [17] I will slightly modify this assumption by using the more realistic AM1.5g standard test spectrum [20] for further calculations.

The solar cell in the SQ model is defined only by its temperature T_{cell} and its band gap energy $E_{\mathrm{g}}^{\mathrm{SQ}}$, assuming that the quantum efficiency $Q_{\mathrm{e}}^{\mathrm{PV}}(E)$ equals the absorptance $a(E)$, which is a step-function depending on energy E with the band gap defining the position of the step, namely $a(E) = H(E - E_{\mathrm{g}}^{\mathrm{SQ}})$, where H is the Heaviside function. This assumption implies that photons with photon energies $E \geq E_{\mathrm{g}}^{\mathrm{SQ}}$ are absorbed, each generating exactly one electron-hole pair $a(E \geq E_{\mathrm{g}}^{\mathrm{SQ}}) = 1$. In contrast, the solar cell is transparent for photons with energies $E < E_{\mathrm{g}}^{\mathrm{SQ}}$ and no interaction occurs ($a(E < E_{\mathrm{g}}^{\mathrm{SQ}}) = 0$). Most absorbed photons have energies higher than the band gap, generating charge carriers deep in the band. These electrons and holes with excess kinetic energy thermalize to the same average energy in thermal equilibrium with the solar cell. This transmission of photons with energies below the band gap and thermalization to the semiconductor's conduction- or valence band edges represent two loss mechanisms that limit solar cell efficiency. The fraction of the incident power lost by transmission or thermalization is a function of the band gap energy, with the two loss mechanisms showing an opposite trend with the band gap. Transmission losses increase for high band gap energies, whereas thermalization losses decrease.

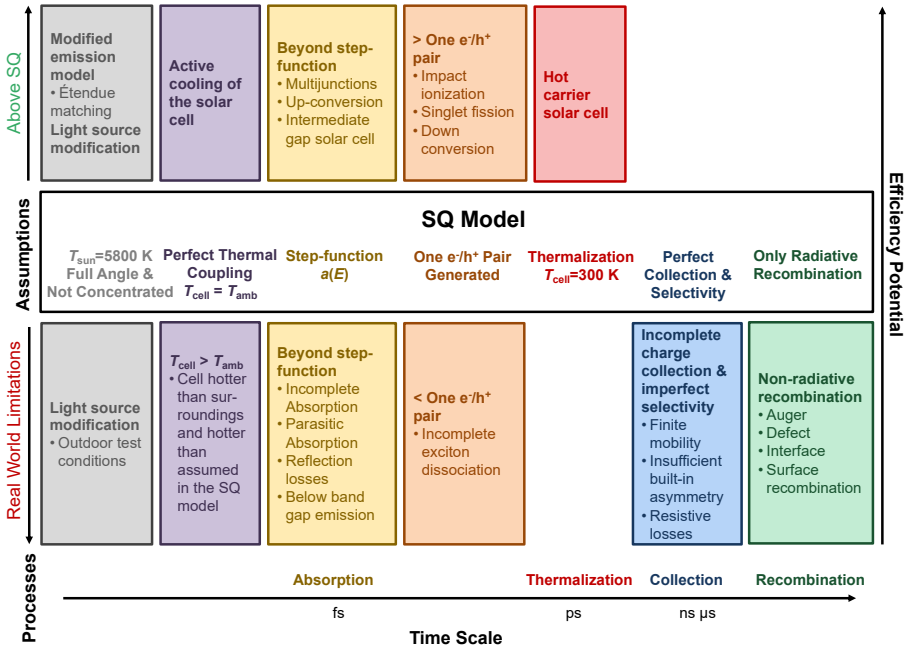

Abbildung 2.1: The Shockley-Queisser model calculates the upper efficiency limit of a single-junction solar cell, being defined by its band gap energy E_g^{SQ}, for a device temperature of 300 K and for the solar spectrum (ϕ_{sun}) parameterized by the black-body spectrum at 6000 K normalized to 100 mWcm^{-2}. [17] A restriction of the angle of optical interaction of the cell with the ambient is not considered. The SQ model consists of several assumptions that are relevant at different stages of the energy harvesting process. These four stages are absorption, thermalization, collection, and recombination. Any approach to achieve efficiencies above those predicted in the SQ model must bypass one of these assumptions or modify the setting. Frequently discussed concepts to achieve higher efficiencies are, for example, up- and down-conversion, singlet fission [21–23] and hot-carrier [24,25] or multijunction [26,27] solar cells. However, most photovoltaic R&D deal with the question of how to approach the assumptions of the SQ model as closely as possible to avoid additional losses in real-world devices, which further reduce solar cell efficiency.

Moreover, it is assumed in the SQ model that after the generation and thermalization of the electron-hole pairs, the charge carriers are either collected at their respective contacts or recombine radiatively by the emission of photons. The share of the respective processes depends on the operating point of the solar cell, which will be explained in more detail later in this section.

To study the interaction of the solar cell with the ambient, it is best to first consider the situation of the thermodynamic equilibrium of the solar cell with the ambient, where no voltage is applied to the solar cell and the ambient interacts with the cell only by radiation corresponding to the same temperature ($T_{\mathrm{cell}} = T_{\mathrm{amb}}$). We can then use the principle of detailed balance according to which each process is related to its inverse process. [28–30] With respect to the solar cell in the dark, i.e. without illumination from the sun, this principle means that the absorbed and emitted fluxes are equal. Thus, the absorptance $a(E)$ and the emitted photon flux $\phi_{\mathrm{em}}(E)$ are related via $\phi_{\mathrm{em}} = a(E)\phi_{\mathrm{bb}}(E,T)$. [31,32] Here, $\phi_{\mathrm{bb}}(E,T)$ is the black-body spectrum at temperature T in equilibrium ($T = T_{\mathrm{amb}} = T_{\mathrm{cell}}$) derived from Planck's radiation law. [33,34] The spectral dependence of the black-body radiation is given by

$$\phi_{\mathrm{bb}}(E,T) = \frac{2\pi E^2}{h^3c^2}\frac{1}{\exp\left(\frac{E}{k_{\mathrm{B}}T}\right) - 1} \approx \frac{2\pi E^2}{h^3c^2}\exp\left(\frac{-E}{kT}\right) \quad , \tag{2.1}$$

where h is Planck's constant, k_{B} Boltzmann's constant , and c denotes the speed of light in vacuum. The unit of the black-body radiation (ϕ_{bb}), as well as the emitted photon flux (ϕ_{em}), used here, is $\mathrm{cm}^{-2}\mathrm{s}^{-1}\mathrm{eV}^{-1}$. Since it is assumed that the solar cell is in thermal equilibrium, the recombination-current density at zero Volt is equal to the current density generated by the absorption of incoming photons from the ambient, being called saturation-current density

$$J_0^{\mathrm{SQ}} = q\int_0^\infty a(E)\,\phi_{\mathrm{bb}}(E,T)\,dE = q\int_{E_{\mathrm{g}}}^\infty \phi_{\mathrm{bb}}(E,T)\,dE \ . \tag{2.2}$$

In the following, we use the superscript SQ for quantities derived within the Shockley-Queisser model.

The recombination-current density $J_{\mathrm{rec}}^{\mathrm{SQ}}$ in non-equilibrium, which leads to

the emission of a photon flux $\phi_{\mathrm{em}} = J_{\mathrm{rec}}^{\mathrm{SQ}}/q$ by the ideal solar cell, depends on the voltage (V) and is given by [35]

$$J_{\mathrm{rec}}^{\mathrm{SQ}} = q \int_0^\infty a(E)\,\phi_{\mathrm{bb}}(E,T) \exp\left(\frac{qV}{k_{\mathrm{B}}T}\right) dE \tag{2.3}$$

$$= q \int_{E_{\mathrm{g}}^{\mathrm{SQ}}}^\infty \phi_{\mathrm{bb}}(E,T) \exp\left(\frac{qV}{k_{\mathrm{B}}T}\right) dE \tag{2.4}$$

$$= J_0^{\mathrm{SQ}} \exp\left(\frac{qV}{k_{\mathrm{B}}T}\right) . \tag{2.5}$$

To derive the current-density-voltage (JV) dependence of the ideal solar cell in non-equilibrium under illumination, the incoming current densities due to the illumination of the solar cell by the sun must also be considered. The total current density (J) is a superposition of all three contributions. The absorption of the incoming photon flux from the sun $\phi_{\mathrm{sun}}(E)$ generates the so-called short-circuit current density [34]

$$J_{\mathrm{sc}}^{\mathrm{SQ}} = q \int_0^\infty a(E)\,\phi_{\mathrm{sun}}(E)\,dE = q \int_{E_{\mathrm{g}}^{\mathrm{SQ}}}^\infty \phi_{\mathrm{sun}}(E)\,dE \ . \tag{2.6}$$

Finally, the total current density J is then given by

$$J = q \int_{E_{\mathrm{g}}^{\mathrm{SQ}}}^\infty \phi_{\mathrm{bb}}(E)\,dE \left[\exp\left(\frac{qV}{k_{\mathrm{B}}T}\right) - 1\right] - q \int_{E_{\mathrm{g}}^{\mathrm{SQ}}}^\infty \phi_{\mathrm{sun}}(E)\,dE \tag{2.7}$$

$$= J_{0,\mathrm{SQ}} \left[\exp\left(\frac{qV}{k_{\mathrm{B}}T}\right) - 1\right] - J_{\mathrm{sc}}^{\mathrm{SQ}} \tag{2.8}$$

$$= J_{\mathrm{dark}} - J_{\mathrm{sc}}^{\mathrm{SQ}} \ , \tag{2.9}$$

where the difference between the recombination-current density and saturation-current density equals the dark-current density J_{dark}, whose voltage dependence causes the diode-like behavior of the current-density-voltage characteristic. Additional solar irradiation produces a photocurrent that shifts the JV-characteristic to the fourth quadrant.

Figure 2.2a-c displays this JV-characteristic, resulting from the SQ model,

and additionally the different power losses and their fractions at different characteristic operating points, namely (a) short circuit (sc), (b) open circuit (oc) and (c) the point of maximum power (MPP). Transmission (yellow area) and thermalization losses (red area) are constant and depend only on the band gap. In this example, the band gap energy is set to 1.6 eV to match the value of the metal-halide perovskite used as the solar-cell absorber material in this thesis.

In short-circuit or open-circuit conditions, the solar cell does not convert any incoming radiative power into electric power. The transmitted power does not interact with the solar cell. In contrast, the absorbed part is converted and returned to the surroundings as heat or radiation with a modified spectral dependency. For example, in the thermalization process, energy is released in the form of phonons to the semiconductor lattice, followed by an immediate heat transfer from the cell to the ambient. At short circuit, the charge carriers generated by solar radiation are collected at the respective ideal contacts. Only a negligibly small portion of the overall absorbed photons recombine, matching the number of ambient-generated ones. During this collection process, the potential energy of the charge carrier is reduced from the band gap energy $E_{\mathrm{g}}^{\mathrm{SQ}}$ to qV, which is 0 eV at short circuit. This loss in total energy generates heat in the contact of the solar cell. It is called 'isothermal dissipation' as it generates heat in the solar cell without changing the temperature of electrons and holes. [19] This collection loss (blue area) is associated with entropy generation in the electron/hole system, which is highest at short circuit, decreases with increasing voltage and does not occur at open circuit, since here no net current flows and no charge carrier is extracted.

If the solar cell is at open circuit, as displayed in Figure 2.2b, all generated charge carriers must recombine, which is indicated by the green area. [17, 36, 37] Thus, the flux of absorbed photons equals the emitted one, which implies that

$$J_{\mathrm{rec}}^{\mathrm{SQ}}(V_{\mathrm{oc}}^{\mathrm{SQ}}) = J_0^{\mathrm{SQ}} + J_{\mathrm{sc}}^{\mathrm{SQ}} \ . \tag{2.10}$$

This radiation loss emitted by the solar cell can be recycled and, for example, reused by another solar cell. However, the solid angle of the emitted light increases compared to the solid angle of the absorbed solar radiation. This étendue expansion produces entropy because the directional order of the photons decreases (light green area). [38]

A restriction of the angle of optical interaction of the cell with the ambient could reduce this entropic recombination loss that limits the maximum achievable open-circuit voltage but is not considered in the SQ model. By setting the net current to zero and rearranging Equation 2.8 we can determine the respective open-circuit

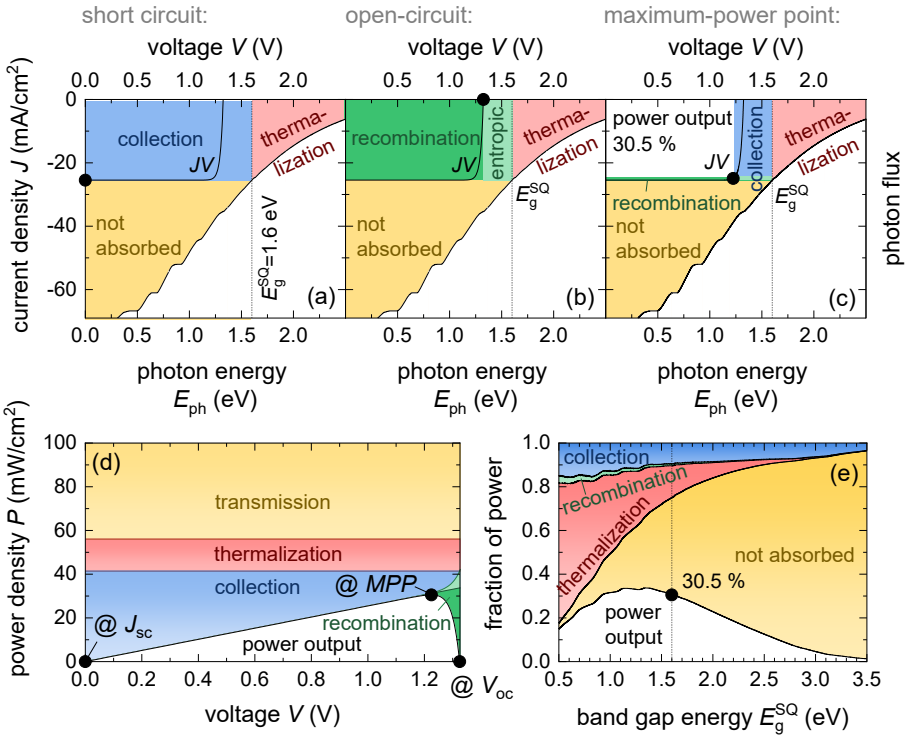

Abbildung 2.2: Visualization of power losses in the SQ model that occur during solar cell operation as a function of applied voltage V and band gap energy. These loss mechanisms are the loss of photons with energies smaller than the band gap which are not absorbed (yellow), loss of excess kinetic energy called thermalization (red)), the loss by emission of photons (green) and the isothermal dissipation loss during carrier collection (blue). (a-c) Current-density-voltage (JV) characteristic of the idealized solar cell in the SQ model with a band gap of 1.6 eV and a comparison of how the share of the four different loss mechanisms (transmission, thermalization, collection and recombination) differs at the three characteristic operating points, (a) short circuit, (b) open circuit and (b) the maximum-power point (MPP). (d-e) Share of the four different loss mechanisms and the harvested electrical power density, (d) as a function of voltage and (e) as a function of band gap energy examined at MPP.

voltage in the SQ model, which is given by

$$V_{\mathrm{oc}}^{\mathrm{SQ}} = \frac{k_{\mathrm{B}}T}{q} \cdot \ln \left(\frac{\int_{E_{\mathrm{g}}^{\mathrm{SQ}}}^{\infty} \phi_{\mathrm{sun}}(E)\, dE}{\int_{E_{\mathrm{g}}^{\mathrm{SQ}}}^{\infty} \phi_{\mathrm{bb}}(E)\, dE} + 1 \right) = \frac{k_{\mathrm{B}}T}{q} \cdot \ln \left(\frac{J_{\mathrm{sc}}^{\mathrm{SQ}}}{J_0^{\mathrm{SQ}}} + 1 \right) \quad . \tag{2.11}$$

Figure2.2c illustrates how the output power is maximized by the proper choice of the voltage, minimizing the loss by radiative recombination and isothermal dissipation through collection. Interestingly, at the maximum power point, the loss channel due to collection is much larger than that due to radiative recombination. This distribution is because the flux of collected electron-hole pairs pairs at the maximum power point far exceeds the flux of emitted photons. The electrical power density results from the product of the current density J and voltage V. With this, the efficiency limit in the SQ model results from the ratio of the maximum electrical power density $P_{\mathrm{out}}^{\mathrm{SQ}}$ to the incoming radiation power P_{in}, namely

$$\eta^{\mathrm{SQ}} = \frac{-\max\left(J(V)V\right)}{P_{\mathrm{in}}} = \frac{P_{\mathrm{out}}^{\mathrm{MPP}}}{P_{\mathrm{in}}} \quad . \tag{2.12}$$

In addition, I introduce the so-called fill factor

$$FF = \frac{J_{\mathrm{MPP}}V_{\mathrm{MPP}}}{J_{\mathrm{sc}}V_{\mathrm{oc}}} \quad , \tag{2.13}$$

which relates the product of current and voltage at the point of maximum power to the product of short-circuit current density $J_{\mathrm{sc}}^{\mathrm{SQ}}$ and open-circuit voltage $V_{\mathrm{oc}}^{\mathrm{SQ}}$. While the fill factor (FF) can not be derived analytically, there is an analytical function, which is suitable as an approximate equation to describe the idealized fill factor in the SQ limit [39]

$$FF^{\mathrm{SQ}} = \frac{v_{\mathrm{oc}}^{\mathrm{SQ}} - \ln\ v_{\mathrm{oc}}^{\mathrm{SQ}} + 0.72}{v_{\mathrm{oc}}^{\mathrm{SQ}} + 1} \tag{2.14}$$

with

$$v_{\mathrm{oc}}^{\mathrm{SQ}} = \frac{qV_{\mathrm{oc}}^{\mathrm{SQ}}}{k_{\mathrm{B}}T} \quad . \tag{2.15}$$

Its importance as a figure of merit (FOM) in real solar cell devices will be elaborated on later.

If the solar cell is operated at another working point than the MPP, the efficiency decreases, as summarized in Figure 2.2d. There, the share of the different loss mechanisms and the output-power density are plotted for a voltage scan. For the respective band gap of 1.6 eV, 30.5 % of the irradiated power can be used as electrical power at its best. This upper efficiency at the maximum power point is a function of the band gap energy with its respective relationship presented in Figure 2.2e. Additionally, Figure 2.2e depicts how the share of the four power losses changes with the band gap. Thermalization and transmission, in particular, show a significant change, yielding a maximum efficiency of 33 % for solar cell devices with band gap energy between 1.1 and 1.4 eV.

2.2 Thermodynamics of the Open-Circuit Voltage

The following section introduces a more realistic formulation of the upper efficiency limit. Although the simplifications in the Shockley-Queisser model are elegant and intuitive, real semiconductor materials do not have an infinitely sharp absorption edge, which would be required to reproduce the idealized, step-function-like absorptance in a material of finite thickness. Therefore, there is always a discrepancy between the calculated SQ efficiency η^{SQ} and the actual thermodynamic efficiency limit of a real-world solar cell with natural absorption properties. [40–42].

Adapting the general idea of the SQ model to real devices with non-step-function-like absorptances or quantum efficiencies leads us to a definition of the radiative limit. [41,43,44] As its name implies, it is assumed, just as in the SQ situation, that all recombination processes occur radiatively. In this case, the solar cell is explicitly defined only by its quantum efficiency ($Q_{\mathrm{e}}^{\mathrm{PV}}$) and temperature. Using these parameters in the framework of detailed balance enables us to derive a general expression for the short-circuit current density

$$J_{\mathrm{sc}} = q \int_0^\infty Q_{\mathrm{e}}^{\mathrm{PV}}(E)\, \phi_{\mathrm{sun}}(E)\, dE \ . \tag{2.16}$$

The radiative saturation-current density (J_0^{rad}) is derived using the optoelectronic reciprocity [45, 46] and is calculated via [47]

$$J_0^{\mathrm{rad}} = q \int_0^{\infty} Q_{\mathrm{e}}^{\mathrm{PV}}(E)\, \phi_{\mathrm{bb}}(E)\, dE \ . \tag{2.17}$$

In the following, I use the superscript 'rad' for quantities derived within the radiative limit. Finally, we calculate the radiative limit for the open-circuit voltage $V_{\mathrm{oc}}^{\mathrm{rad}}$ via [45]

$$V_{\mathrm{oc}}^{\mathrm{rad}} = \frac{k_{\mathrm{B}}T}{q} \ln \left(\frac{J_{\mathrm{sc}}}{J_0^{\mathrm{rad}}} + 1 \right) \ . \tag{2.18}$$

Note that the radiative limit of the open-circuit voltage ($V_{\mathrm{oc}}^{\mathrm{rad}}$) defined by Equation 2.18 does not need any value for the band gap energy. Nevertheless, Equation 2.16-2.18 can be connected to the SQ model by setting the quantum efficiency of the solar cell to $Q_{\mathrm{e}}^{\mathrm{PV}}(E) = a(E) = H\left(E - E_{\mathrm{g}}^{\mathrm{SQ}}\right)$ with the Heaviside function $H\left(E - E_{\mathrm{g}}^{\mathrm{SQ}}\right) = 1$ for $E \geq E_{\mathrm{g}}^{\mathrm{SQ}}$ and $H\left(E - E_{\mathrm{g}}^{\mathrm{SQ}}\right) = 0$ otherwise.

The radiative open-circuit voltage $V_{\mathrm{oc}}^{\mathrm{rad}}$ is always smaller than the value from the SQ model because additional radiative recombination losses occur due to the broadening of the absorption edge. The semiconductor should have a sharp and strong absorption coefficient to keep the losses in a real-world solar cell as small as possible and its respective thermodynamic efficiency limit high. In the limiting case, the radiation open-circuit voltage approaches the open-circuit voltage in the SQ model. Therefore, selecting an absorber material should consider the behavior of the absorption coefficient. Different solar cell technologies achieve this to varying degrees. However, because this is only one of the many selection criteria for a good absorber material, the task of building an excellent solar cell must always be tackled holistically.

Calculating the radiative limit requires an expression for the quantum efficiency. The direct measurement of the (photovoltaic) external-quantum efficiency ($Q_{\mathrm{e}}^{\mathrm{EQE}}$) of the solar cell, typically performed using a grating monochromator setup, usually does not cover the entire energy range of interest for the calculation of J_0^{rad} because its dynamic range is not sufficiently large to cover the relevant absorption edge. To calculate the saturation-current density, multiplication of the quantum efficiency with the black-body spectrum takes place (Equation 2.17). Thus,

in particular, the values of the quantum efficiency are weighted exponentially more at low energies and hence are decisive for the resulting value of J_0^{rad}. Therefore, the precise determination of J_0^{rad} requires an extended quantum efficiency data set that additionally contains values at low energies. This extended quantum efficiency can be obtained by applying the optoelectronic reciprocity theorem, [45] which connects the electroluminescent emission of a solar cell with its photovoltaic quantum efficiency and the voltage V via

$$\phi_{\mathrm{EL}}(E) = Q_{\mathrm{e}}^{\mathrm{PV}}(E)\,\phi_{\mathrm{bb}}(E) \quad \exp\left(\frac{qV}{k_{\mathrm{B}}T}\right) - 1 \quad . \tag{2.19}$$

This correlation enables the conversion of one parameter into another. Thus, it is possible to use a measurement of the electroluminescence (EL) spectrum $\phi_{\mathrm{EL}}(E)$ to obtain the missing values for the quantum efficiency of the solar cell for the low energy range and to combine them with the directly measured quantum efficiency $Q_{\mathrm{e}}^{\mathrm{EQE}}(E)$. [47, 48] The extension of the photovoltaic quantum efficiency using electroluminescence data via Equation 2.19 has previously been used for perovskite solar cells [49, 50] and other solution-processable semiconductors. [51, 52] An example is shown in Figure 2.3 for a perovskite solar cell fabricated in the scope of this thesis.

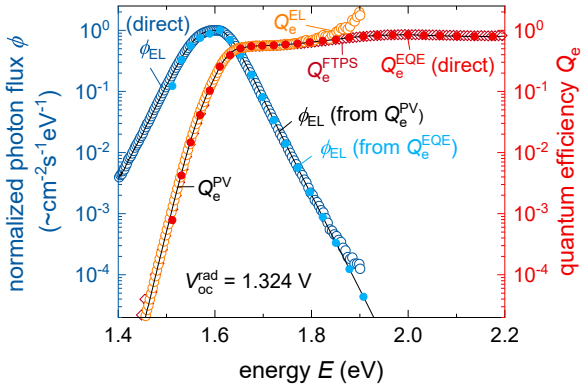

Abbildung 2.3: Electroluminescence spectrum $\phi_{\mathrm{em}}^{\mathrm{EL}}$ and quantum efficiency $Q_{\mathrm{e}}^{\mathrm{EQE}}$ from (EQE and FTPS) of measured on the same exemplary perovskite-solar cell to determine the radiative open-circuit voltage $V_{\mathrm{oc}}^{\mathrm{rad}}$ by using the optoelectronic reciprocity relation. The calculation gives a thermodynamic limit for the open-circuit voltage of 1.324 V for the respective solar cell device.

2.3 Losses in Real-World Solar Cells

In real-world solar cells, various efficiency-reducing loss mechanisms lead to discrepancies between the actual device efficiencies and theoretically possible values in the Shockley-Queisser model. Unfortunately, the idealized assumptions in the SQ model are highly difficult to meet and impose many requirements on the material properties of the absorber, interlayer and contact materials, as well as on their interfaces and their interplay in the device architecture. Thus, deviations from the ideal situation can easily occur. Figure 2.1 in section 2.1 shows a corresponding overview of the real-world limitations. In addition, Figure 2.4 provides an overview of the preferable properties of absorbers, interlayers and contact materials.

Optical losses occur, for example, due to reflection, transmission, and interference. Thus, in addition to selecting a suitable band gap, the absorber of a well-functioning solar cell should have a high and sharp absorption coefficient (α) to facilitate adequate light absorption even with thin film thicknesses. Besides, parasitic light absorption in the interlayer or contact material reduces the absorptance (a) and the photocurrent quantity generated by the solar cell. This portion of the radiation power is no longer available for the active layer, resulting in additional optical losses.

Likewise, the ideal extraction properties assumed in the SQ model can, at best, only be approximated with real materials. Additional collection losses occur, for example, because the mobility of electrons and holes is not infinitely high, and they recombine before reaching the contacts. Therefore, the diffusion length of charge carriers should be much greater than the absorber layer thickness. If this criterion is not met and the active layer of the solar cell is too thick, a large part of the generated charge carriers will not reach the contacts. These two opposing requirements for layer thickness call for a compromise between absorption and charge-carrier collection. A prerequisite for a good interlayer and selective contact is also a high mobility and conductivity to avoid resistive losses, which reduce the fill factor of the solar cell. It is also not trivial to achieve selective charge-carrier transport to the respective contacts. The interlayers have the function of letting one charge-carrier type pass without introducing significant energetic losses and blocking the other. This semipermeable behavior is, for example, achievable by a huge energetic barrier for

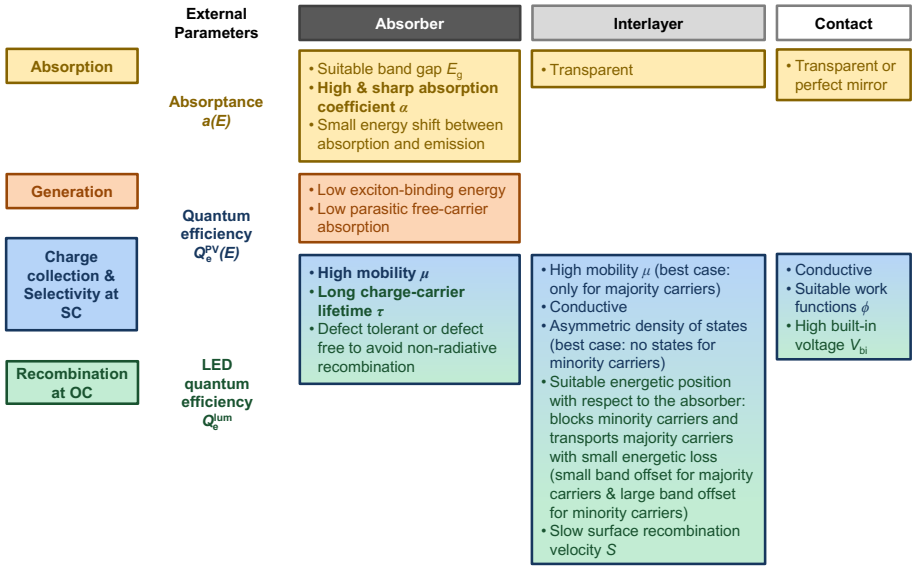

Abbildung 2.4: Overview of material properties of an absorber, interlayer, and contacts for a good solar cell. The respective internal material parameters are sorted according to their respective impact on the processes during energy harvesting. The relative importance of the three absorber material parameters for the solar cell performance is not trivial, and a strict separation as done here should only serve as a simplification for the reader.

minority carriers and similar energy levels between the absorber and the interlayer for majority carriers. Thus, a good energy-level alignment is beneficial and essential for preserving the potential energy of the charge carriers during charge transport from the absorber layer to the electrodes. Moreover, minimizing the equilibrium concentration of minorities at both contacts assists selectivity, which can be implemented, e.g., by doping densities of the used semiconductors [15,53] or a high built-in voltage, being set by the work-function difference of the contact materials. [54–57]

The non-radiative recombination of charge carriers represents another loss path in actual solar cells, which explicitly reduces the open-circuit voltage of the device. Several different mechanisms cause non-radiative recombination, where the energy of the recombining electron/hole pairs is dissipated by releasing phonons. I refer to section 2.5 for more details. However, defect recombination in the bulk material of the absorber, as well as at the interface to the adjoining interlayers, is critical and requires passivation strategies and defect-tolerant or defect-free absorber materials.

Consequently, suitable absorber materials should have long charge-carrier lifetimes, while the interfaces should feature slow surface-recombination velocities. In addition, a low surface-recombination velocity is one ingredient to obtain a high contact selectivity. The second ingredient is a low series resistance, according to the definition by Brendel and Peibst. [58] If this velocity is not sufficiently low, electrons recombine at the anode and holes at the cathode. An external quantity that enables the quantification of non-radiative losses of the solar cell is the external LED quantum efficiency ($Q_{\mathrm{e}}^{\mathrm{lum}}$), sometimes also denoted as external radiative efficiency [59,60] or LED quantum efficiency [36,45]. The potentially voltage-dependent ratio defines the external luminescence-quantum efficiency

$$Q_{\mathrm{e}}^{\mathrm{lum}} = \frac{J_{\mathrm{rad}}}{J_{\mathrm{nrad}} + J_{\mathrm{rad}}} = \frac{J_{\mathrm{rad}}}{J_{\mathrm{rec}}} \ , \tag{2.20}$$

comparing radiative recombination current (J_{rad}), which leads to the emission of photons, to the total recombination current (J_{rec}), where J_{rad} and non-radiative recombination current (J_{nrad}) add up. The external luminescence-quantum efficiency is crucial in explaining the power-conversion efficiency of a light-emitting diode. However, it is also important to understand photovoltaic power-conversion efficiency via its influence on open-circuit voltage (V_{oc}).

According to detailed balance, the voltage loss between the radiative limit of the open-circuit voltage $V_{\mathrm{oc}}^{\mathrm{rad}}$ introduced in section 2.2 and the actually measured open-circuit voltage V_{oc} should scale with the logarithm of the external luminescence-quantum efficiency $Q_{\mathrm{e}}^{\mathrm{lum}}$ via [45,61]

$$\Delta V_{\mathrm{oc}}^{\mathrm{nrad}} = V_{\mathrm{oc}}^{\mathrm{rad}} - V_{\mathrm{oc}} = \frac{-kT}{q} \ln \quad Q_{\mathrm{e}}^{\mathrm{lum}} \quad > 0 \ . \tag{2.21}$$

Equation 2.21 implies that if $Q_{\mathrm{e}}^{\mathrm{lum}} = 1$, the open-circuit voltage is equal to the radiative open-circuit voltage per definition of the latter. Hereby, the open-circuit voltage loss equals $k_{\mathrm{B}}T \ln\{10\} \approx 60\mathrm{meV}$ for every order of magnitude reduction in the external luminescence-quantum efficiency or increase in total the recombination current relative to the radiative one.

Combining the information about the radiative limit of the open-circuit voltage and $Q_{\mathrm{e}}^{\mathrm{lum}}$ allows the comparison of recombination limitation of different solar

cell technologies among each other. [40, 42, 59, 60] The recombination losses of the actual open-circuit voltage V_{oc} are split into two contributions. First, radiative losses due to the difference $\Delta V_{\mathrm{oc}}^{\mathrm{rad}} = V_{\mathrm{oc}}^{\mathrm{SQ}}(E_{\mathrm{g}}) - V_{\mathrm{oc}}^{\mathrm{rad}}$ between the SQ value, calculated for the idealized step-function-like quantum efficiency, and the radiative value corresponding to the actually measured $Q_{\mathrm{e}}^{\mathrm{EQE}}(E)$. The second contribution represents a non-radiative loss term $\Delta V_{\mathrm{oc}}^{\mathrm{nrad}} = V_{\mathrm{oc}}^{\mathrm{rad}} - V_{\mathrm{oc}}$. [40] Thus, the overall difference between $V_{\mathrm{oc}}^{\mathrm{SQ}}$ and V_{oc} is given by

$$\Delta V_{\mathrm{oc}} = V_{\mathrm{oc}}^{\mathrm{SQ}}(E_{\mathrm{g}}) - V_{\mathrm{oc}} = \Delta V_{\mathrm{oc}}^{\mathrm{rad}}(E_{\mathrm{g}}) + \Delta V_{\mathrm{oc}}^{\mathrm{nrad}} \quad . \tag{2.22}$$

It follows from Equation 2.22 that the actual value of ΔV_{oc} depends on the choice of band gap energy (E_{g}) used in the SQ model. For instance, a method that systematically determines lower values for the band gap than another method would also yield a lower estimate of open-circuit voltage loss. This problem motivates the meta-analysis and discussion in later chapter 6. For now, I use the inflection point (IP) of the photovoltaic quantum efficiency $Q_{\mathrm{e}}^{\mathrm{PV}}$ to define the band gap of the solar cell device. [40]

Following the introduction of additional loss mechanisms in real-world solar cells, Figure 2.5 compares the characteristic parameters from the SQ model vs. bang gap energy to a range of data points representing current efficiency records of different photovoltaic (PV) technologies. [62–67] In addition, Figure 2.5a shows how the external luminescence quantum efficiency $Q_{\mathrm{e}}^{\mathrm{lum}}$ reduces the thermodynamic efficiency limits to substantially lower values. Unfortunately, it is impossible to directly assign the difference in efficiency between the SQ limit and reality presented in Figure 2.5a to the different loss mechanisms. However, comparing the individual parameters, namely short-circuit current density (J_{sc}), fill factor FF and V_{oc} facilitates identifying the respective limitations of the different solar cell technologies. It becomes apparent that the photocurrent is not the most critical issue as J_{sc} deviates only slightly from the theoretical value compared to the losses in fill factor or open-circuit voltage. Furthermore, Figure 2.5e illustrates the normalized efficiency as a function of the external luminescence quantum efficiency $Q_{\mathrm{e}}^{\mathrm{lum}}$ for a range of devices, where the latter has been estimated based on available photovoltaic quantum efficiency data, using an approximation of the radiative V_{oc} that I will introduce in

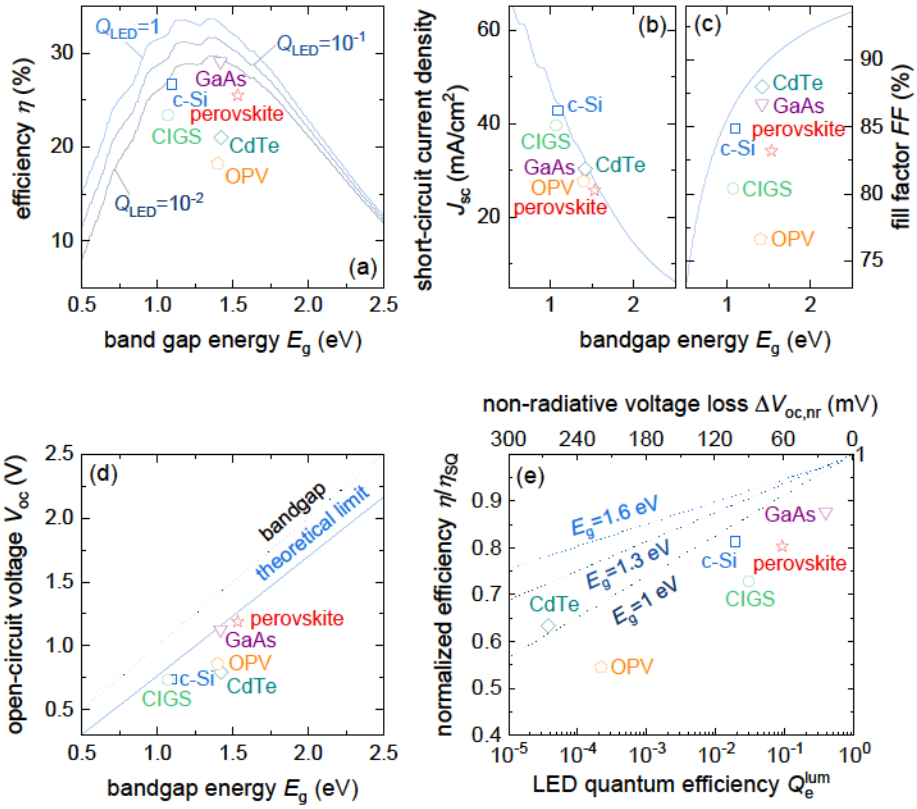

Abbildung 2.5: (a) Efficiency limit in the SQ model, and the other characteristic parameters (b) short-circuit current density, (c) fill factor and (d) open-circuit voltage as a function of the band gap energy. The data points represent the respective parameters of record devices from various established and emerging absorber materials. Furthermore, in panel (a), the external-luminescence quantum efficiency Q_e^{lum} is used as a parameter to depict its influence on the upper efficiency limit. (e) Normalized efficiency as a function of external luminescence quantum efficiency or non-radiative voltage loss, which are linked via Equation 2.21, stated for the record devices of various solar cell technologies. [62–67] The dashed lines are values of $\eta/\eta_S Q$ as a function of Q_e^{lum} calculated for three different band gap energies, assuming that only recombination losses are present.

chapter 6. One observation that emerges from Figure 2.5e is that the normalized efficiency η_{real}/η_{SQ} correlates empirically with Q_e^{lum}. Thus, the most efficient solar cells, such as GaAs and crystalline Si, also have the highest values of luminescence

quantum efficiency $Q_{\mathrm{e}}^{\mathrm{lum}}$ with the efficiency advantage of GaAs being mainly related to its direct band gap and higher luminescence. In the next section, I will introduce a more visually appealing presentation of the different loss contributions by specifying several figures of merit FOM.

2.3.1 Figures of Merit

Recently, it was shown how to break down the additional losses in a real-world solar cell into several factors, each of which can be considered as a figure of merit highlighting different physical loss mechanisms and, consequently, different optimization strategies. [19] The normalized efficiency used before in Figure 2.5e can be expressed as the product of five different contributions, which gives

$$\frac{\eta_{\mathrm{real}}}{\eta_{\mathrm{SQ}}} = \frac{V_{\mathrm{oc}}^{\mathrm{rad}}}{V_{\mathrm{oc}}^{\mathrm{SQ}}} \frac{V_{\mathrm{oc}}^{\mathrm{real}}}{V_{\mathrm{oc}}^{\mathrm{rad}}} F_{\mathrm{FF}}^{\mathrm{res}} \frac{FF_0 \;\; V_{\mathrm{oc}}^{\mathrm{real}}}{FF_0 \;\; V_{\mathrm{oc}}^{\mathrm{SQ}}} F_{\mathrm{sc}} \;\; , \tag{2.23}$$

and is discussed subsequently. Moreover, Figure 2.6 visualizes these five figures of merit for the current record-efficiency solar cells of different PV technologies presented in the last section. The losses in V_{oc} shown in different shades of green are split into two parts, namely into losses due to the discrepancy between the actual shape quantum efficiency and the ideal step-function assumed in the SQ limit, which is described by the ratio of $V_{\mathrm{oc}}^{\mathrm{rad,fit}}/V_{\mathrm{oc}}^{\mathrm{SQ}}$ (dark green) and losses due to non-radiative recombination $V_{\mathrm{oc}}^{\mathrm{real}}/V_{\mathrm{oc}}^{\mathrm{rad,fit}}$ (light green). Moreover, non-radiative losses always reduce the limit of the fill factor because FF is linked to the actual open-circuit voltage of the device, as specified by the relationship in Equation 2.14. [39, 68] The rationale behind this effect is that the difference between the voltage V_{mpp} at the maximum power point and the V_{oc} is relatively constant, which implies that the ratio $V_{\mathrm{mpp}}/V_{\mathrm{oc}}$ which controls the value of the ideal fill factor is not constant but a function of the open-circuit voltage. Hence, the fill factor losses in Equation 2.23 are also split into two parts, one $FF_0 \;\; V_{\mathrm{oc}}^{\mathrm{real}} \; / FF_0 \;\; V_{\mathrm{oc}}^{\mathrm{SQ}}$ (dark red) dealing with the fill factor loss due to the loss in open-circuit voltage and a second one called $F_{\mathrm{FF}}^{\mathrm{res}}$ taking into account additional losses which are mainly resistive in nature (light red). Here, the factor $F_{\mathrm{FF}}^{\mathrm{res}}$ is defined as the ratio $FF_{\mathrm{real}}/FF_0 \;\; V_{\mathrm{oc}}^{\mathrm{SQ}}$. Finally, the

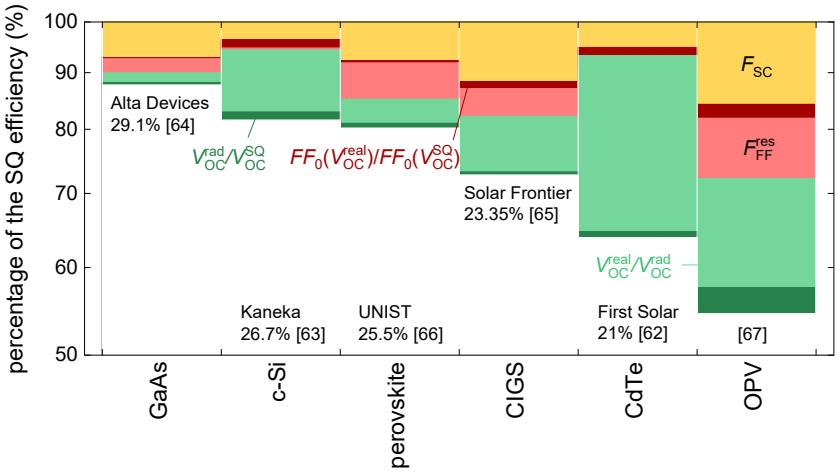

Abbildung 2.6: Visualization of efficiency losses in current record-efficiency cells of various solar cell absorber materials, [62–67] based on their band gaps, relative to the ideal, SQ-case, using partitioning of the efficiency losses, according to ref [19]. As a reference band gap, the photovoltaic band gap E_g^{ip} extracted from solar cell quantum efficiency data is used. [40] The following figures of merit (FOMs) are used and shown: F_{sc} and F_{FF}^{res}, $V_{oc}^{real}/V_{oc}^{rad,fit}$, $V_{oc}^{rad,fit}/V_{oc}^{SQ}$, and $FF_0\ V_{oc}^{real}\ /FF_0\ V_{oc}^{SQ}$. Only the two mature technologies GaAs and Si achieve $\eta^{real}/\eta^{SQ} > 80\%$.

figure of merit $F_{sc} = J_{sc}/J_{sc}^{SQ}$ compares the actually measured short-circuit current density with the theoretical one in the SQ model. The yellow bars in Figure 2.6 indicate the portion of this loss factor. A detailed description and discussion of all FOMs are available in ref. [19].

As the presentation in Figure 2.6 proves, the breakdown into different figures of merit facilitates the identification of the significant challenges regarding the solar cell's key parameters. Note, that the bar chart is plotted on a logarithm scale. Thereby, the area of the additive segments in the bar chart correctly represent the magnitude of the factors in equation 2.23. In addition, it allows the evaluation of the progress of emerging technologies, such as organic photovoltaic or perovskite solar cells, to more mature technologies, such as Si or GaAs. The two mature technologies, GaAs and Si, as well as the fairly new technology based on metal-halide perovskites, achieve 80% or more of the efficiency from the SQ model. This outstanding performance of the record perovskite solar cell, compared to other emerging PV, underlines

the potential of this material class. In particular, the losses in open-circuit voltage are already relatively small relative to other technologies.

2.4 Perovskite Solar Cells

This section provides an overview of the material properties that make metal-halide perovskites interesting for solar cell applications. Subsequently, the implementation and working principle are introduced.

2.4.1 Material Properties and Development

Generally, the term perovskite denotes a versatile crystal family with stoichiometry ABX_3 and many different polymorphs crystallizing, for example, in the cubic, tetragonal, or orthorhombic phase. Accordingly, perovskites exhibit a variety of different properties, ranging from metallic to semiconducting to insulating. However, only semiconducting metal-halide perovskites are interesting as absorber materials for solar cells since they stand out by their superior optoelectronic properties and the low material and energy input costs required for their fabrication. Thus, whenever the term 'perovskite' is used in this thesis, it refers exclusively to these metal-halide perovskites.

Figure 2.7 illustrates the ideal, cubic perovskite ABX_3 structure, consisting of a BX_6 octahedra in the middle of the cube formed by the A-site. This A-site is either a monovalent organic, charged molecule like methylammonium ($CH_3NH_3^+$, MA^+), formamidinium ($HC(NH_2)_2$, FA^+), or guanidinium ($CH_6N_3^+$, GA^+), or an inorganic cation such as Cs^+ or Ru^+. At the center of the cube, on the B-site positions, sits a divalent metal cation from elements such as lead (Pb^{2+}) or tin (Sn^{2+}) in six-fold coordination surrounded by monovalent halide anions such as iodide (I^-), bromide (Br^-) or chloride (Cl^-) (X-site). In this thesis, methylammonium lead iodide ($CH_3NH_3PbI_3$), also referred to as MAPI, is used, which is one of the most common and extensively investigated metal-halide perovskites.

Even though the first synthesis of methylammonium-lead halide perovskites dates back to 1978, [69] they were not used in photovoltaic devices until 2009. [11]

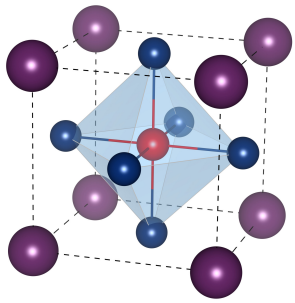

Abbildung 2.7: Schematic representation of the cubic perovskite structure with the chemical formula ABX_3. The A-site (purple) is occupied by methylammonium ($CH_3NH_3^+$), formamidinium ($HC(NH_2)_2$), guanidinium ($CH_6N_3^+$), or inorganic cations such as Cs^+ or Ru^+. The octahedra is built by halide anion (I^-, Br^-, Cl^-) on the X-site (blue) and usually (Pb^{2+}) on the B-side (dark red).

Initially, employed only as light-sensitizer in dye-solar cells in form of a very thin layer on a mesoporous scaffold of titanium dioxide, it became apparent that metal-halide perovskites also have exceptional electronic properties and function as an absorber and transport layer in a solid-state architecture. [70, 71] Since then, polycrystalline thin-film perovskite solar cells have attracted the attention of a growing number of scientists and have developed rapidly, bringing record cells closer and closer to the level of leading PV technologies. This unparalleled efficiency development is illustrated in Figure 2.8 with the current record efficiency being 25.5 %. [66] Still, two major concerns about lead-halide perovskites are the toxicity of the heavy metal lead and the current lack of long-term stability, which also holds back commercialization. [73, 74] The great success of this class of materials is attributed to its excellent optoelectronic properties, which cover many requirements for a good solar cell absorber material. [8–10]

Firstly, metal-halide perovskites are characterized by a high absorption coefficient in the visible range ($\sim 10^{-5}\,\mathrm{cm}^{-1}$), [75] yielding high absorptance even with very thin films of several hundred nanometres. The absorption onset of metal-halide perovskites is sharp and the sub-band gap absorption is low, which is beneficial for small radiative recombination losses. [40] Unlike organic absorber materials, lead-halide perovskites exhibit very low exciton-binding energies below $k_\mathrm{B}T$, [76] implying that the generated charge carries are dissociated and free at room temperature. This

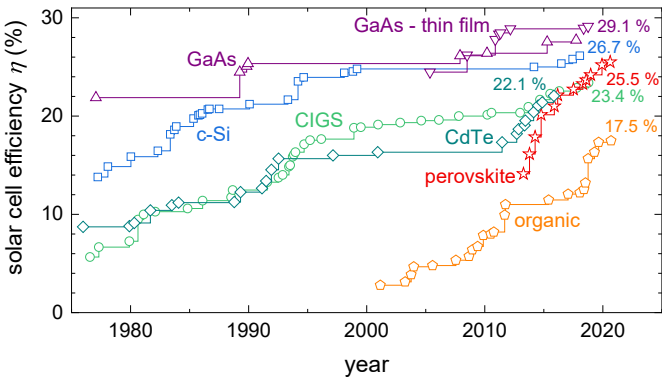

Abbildung 2.8: Chronological development of the highest confirmed efficiencies of single junction solar cells with different absorber materials. The current record efficiency of perovskite solar cells is 25.5 % Data is picked from the research-cell efficiency chart published by the National Renewable Energy Laboratory (NREL). [72]

property is related to their high static relative dielectric permittivity (ϵ_r) (~ 30). [77] In addition, charge-carrier lifetimes are exceptionally long for a polycrystalline material fabricated from simple low-temperature wet-chemical deposition. [78] Good charge-carrier transport to the contacts also requires high mobilities. In this regard, perovskites feature sufficiently high charge-carrier mobilities for electrons and holes in the order of $10 - 100\,\mathrm{cm^2V^{-1}s^{-1}}$ [79, 80] to provide diffusion lengths exceeding typical layer thicknesses. [81]

These exceptional electrical and optical properties of metal-halide perovskites result from their unusual electronic structure, which exhibits an anti-bonding valence-band maximum (VBM) constructed from 6s Pb electrons, coupled with 3p, 4p or 5p orbitals for Cl, Br or I, respectively. [82–85] A strong hybridization between these inorganic ions thereby results in low effective electron and hole masses. [86] With this, the halide anion (X-site) mainly dictates the valence-band energy, while the position of the conduction band maximum is barely altered. Thus, by changing the composition, it is possible to tune the optical band gap of these semiconductors, [87] making them highly interesting for tandem solar cell applications. Another peculiarity of the electronic structure is that lead and halide contributions dominate the electronic states at the conduction- and valence-band edges, while the impact of

the organic cation (A-site) on these relevant states for charge conduction and optical transitions is negligible. [83, 85] The A-site cation only influences the structural symmetry and needs the right size to allow a cubic perovskite lattice to form. [8] In addition, the A-site cation strongly affects the chemical stability. [88, 89]

The anti-bonding nature of the valence-band maximum is of particular relevance as it is associated with defect tolerance, [90, 91] thus explaining the long electron and hole bulk lifetimes. This defect tolerance occurs because the most abundant point defects in the bulk form energetically close states to the band edges or even in the energy bands rather than in the middle of the band gap. Thus, these defect states are less detrimental for non-radiative recombination. [90, 92–94] The few deep defects exhibit large formation enthalpies, which makes them occur in small concentrations. Additionally, phonon energies in lead-halide perovskites are quite small (16.5 meV) [77], making non-radiative recombination via multiphonon emission unlikely. [95] The deformation potential, which defines the energy required to adjust the lattice around a defect and screen it, is also small. [96] All these effects are beneficial for slowing down trap-facilitated recombination and predict a defect-tolerating system.

Even if the bulk material has all prerequisites for an excellent photovoltaic-absorber material, significant losses easily occur when the absorber, interlayer and contact materials interact. In particular, the interfaces between the layers can cause losses. An understanding of device physics and careful design is required to minimize these loss paths and further enhance efficiency.

2.4.2 Solar Cell Layer Sequence and Working Principle

There are several different stack configurations for perovskite solar cells, which differ, for example, in polarity or material choice. An overview illustrating some of the most common perovskite-solar cell device architectures is shown in Figure 2.9. Usually, a polycrystalline metal-halide perovskite layer of several hundred nanometres in thickness is sandwiched between two selective transport layers. One is semipermeable for electrons, called electron-transport layer (ETL), while the other so-called hole-transport layer (HTL) blocks electrons and allows holes to pass. Commonly, these transport layers are metal oxides, like titanium dioxi-

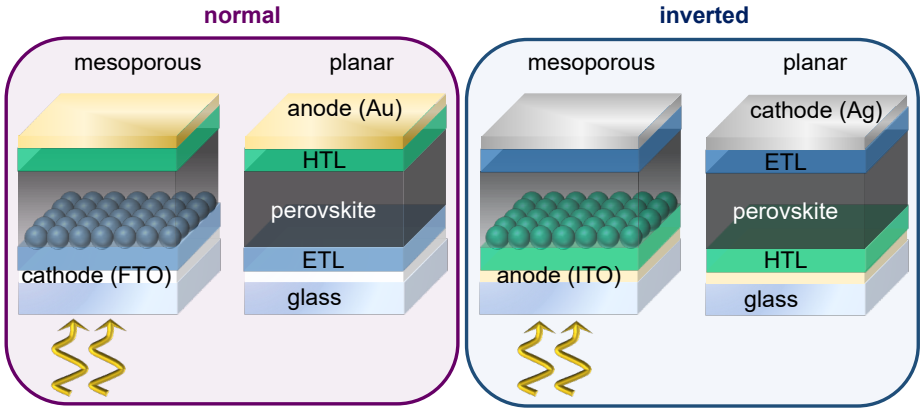

Abbildung 2.9: Schematic of different perovskite solar cell device architectures. The mesoporous, regular configuration is widely used and very efficient, but with the disadvantage that the fabrication of the commonly used ETL TiO_2 requires high temperatures. In this thesis, I used the inverted, planar structure.

de TiO_2, zinc oxide ZnO, tin oxide SnO_2 or organic semiconductors, like $2,2',7,7'$-tetrakis-(N,N-di-4-methoxyphenylamino)-$9,9'$-spirobifluorene (Spiro-OMeTAD) [97] or poly(3-hexylthio-phene- 2,5-diyl) P3HT. Furthermore, transparent conductive oxides (TCO) as transparent front and metal contacts as opaque rear electrodes form external contacts. Many high-performance devices have been fabricated in a mesoporous, regular architecture, where a mesoporous TiO_2 layer forms the electron-transport layer at the transparent cathode side, made from fluorine-doped tin oxide (FTO). [70, 98–101] The respective layout evolved from the dye-solar cell structure, in which perovskites were used for the first time. This architecture is still one of the most popular. The mesoporous ETL provides a scaffold with a large surface area infiltrated by perovskite crystals, assisting electron extraction.

However, all the devices used in this thesis are inverted, planar solar cells, discussed in more detail in the fabrication section 4.7. As its name implies, this architecture is electrically inverted with respect to the regular configuration that characterizes the most high-efficiency oxide-containing systems and employs a stack based on planar films. Apart from its simplicity, this structure has the advantage of being compatible with low-temperature processing. In addition, this structure is better suited for tandem applications with Si-solar cells. Here, fabricati-

on starts at the transparent anode side, usually made of indium-tin oxide (ITO) with an adjoining semipermeable hole-transport layer, like poly[bis(4-phenyl)(2,4,6-trimethylphenyl)amine] (PTAA), poly(3,4-ethylenedioxythiophene) (PEDOT:PSS), or poly(N,N'-bis-4-butylphenyl-N,N'-bisphenyl)benzidine (PolyTPD). On the other side of the perovskite absorber, an electron-transport layer hinders holes from moving to the cathode made of silver.

Figure 2.10 schematically depicts the respective inverted, planar perovskite solar cell stack and a schematic of the energy levels. In addition, exemplary energy-band diagrams in equilibrium, in the dark, and under illumination at the maximum power point are shown. These exemplary energy-band diagrams were generated with a numerical drift-diffusion device simulator using typical material parameters. In the following, I explain the functionality of the different layers and introduce important material parameters and quantities that mainly influence the energy-band diagram. The x-axis shows the cross-section of the solar cell with energy on the y-axis.

The band diagram describes the situation when different layers are brought into contact with each other. The layers exchange charge carriers to reach a thermal equilibrium state, characterized by equilibrated Fermi levels, which implies a zero net-current flow of electrons and holes. The equilibrium-Fermi level is given by E_{F} and controls the equilibrium electron and hole densities via

$$n_0 = N_{\mathrm{C}} \exp \quad \frac{E_{\mathrm{C}} - E_{\mathrm{F}}}{k_{\mathrm{B}} T} \tag{2.24}$$

and

$$p_0 = N_{\mathrm{V}} \exp \quad \frac{E_{\mathrm{F}} - E_{\mathrm{V}}}{k_{\mathrm{B}} T} \quad , \tag{2.25}$$

with E_{C} and E_{V} marking the edges of the conduction (CB), or valence band (VB) and N_{C} and N_{V} are the effective densities of state in these bands, respectively.

First, the three materials differ in their energy levels, as illustrated in Figure 2.10b. Thereby, the electron affinities, defined by the energy difference between the vacuum level E_{vac} and conduction-band edge, dictate the alignment of the conduction-band edges of the different layers in the final stack. Thus, for a tentative understanding of band alignment, the conduction- and valence-band offsets of the HTL, absorber and ETL layers can be used as the decisive quantities to understand

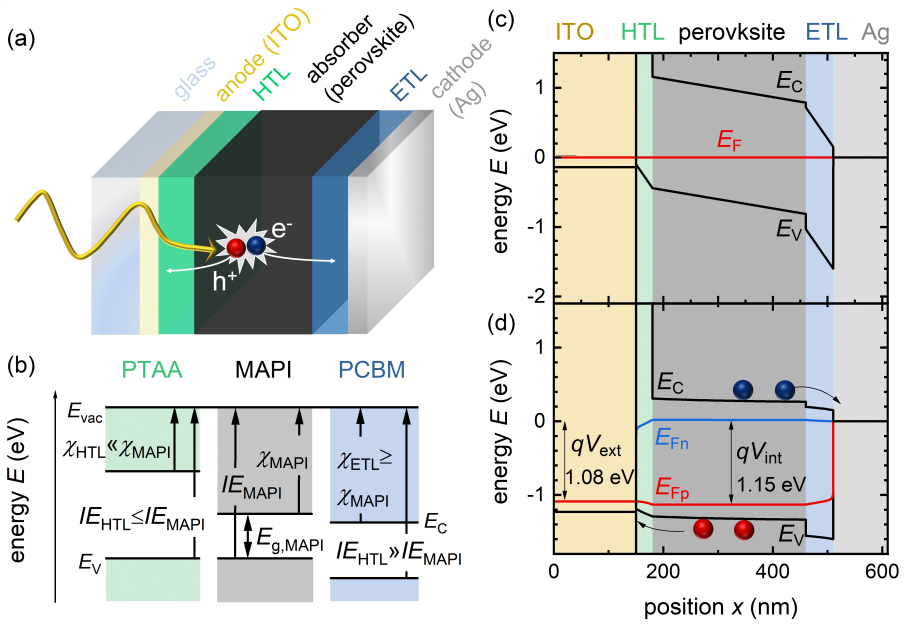

Abbildung 2.10: (a) Schematic of the inverted, planar solar cell device stack. (b) Trend of the energy levels. (c-d) Exemplary, simulated energy-band diagrams in the dark and under illumination at the maximum power point.

the band alignment. The hole-transport layer has a small electron affinity (χ) compared to the perovskite, which introduces an energetic barrier in the conduction band, hindering electron extraction. The electron current into the HTL depends exponentially on the height of this energetic barrier ($\exp(-\Delta E_C/k_B T)$). It is, therefore negligibly small for conduction-band offsets $\Delta E_C \gg k_B T$. At the same time, its ionisation energy (IE), which states the energy difference between the vacuum level and valence-band edge, is equal to or smaller than that of the perovskite, making it easy for holes to enter the HTL layer. The valence band difference should not be high to avoid losses in potential energy during transport to the contacts. The reverse is true for the electron-transport layer, which should create an energetic barrier at the valence-band edges for holes, adding selectivity to the contacts.

Furthermore, a work-function difference between the metal contacts is essential to induce a built-in asymmetry in this type of solar-cell device. The difference in electrostatic potential induces an electric field and a voltage drop across the sandwiched layers, causing tilting of the bands, as shown in Figure 2.10c. In addition, these contact materials (ITO, Ag) are far more conductive than the other layers. Generally, if different layers are brought into contact, charge-carrier injection from layers with a lower work function into layers with a higher work function occurs until the Fermi levels are equilibrated. Moreover, the perovskite absorber and organic semiconductors, usually used as transport layers, are only slightly doped or even intrinsic, [102]. This property implies that the equilibrium-majority carrier concentrations in all these layers are negligibly low relative to the concentrations of electrons or holes injected from the contacts. Thus, the position of the equilibrium-Fermi level in the energy-band diagram does not necessarily coincide with the work functions of the individual materials. Instead, charge-carrier injection from ITO and Ag strongly affects the position of the equilibrium-Fermi level in the energy-band diagram, reducing the equilibrium concentration of minorities at both contact sides. This asymmetry in the charge-carrier concentration benefits selectivity because it reduces the recombination current of electrons (holes) at the hole (electron) contact. Note that this high built-in voltage due to a work-function difference of the contact materials is only one way to implement this asymmetry. Other technologies use differences in doping densities or band gap grading towards the contacts. [53, 103, 104]

Figure 2.10d shows the non-equilibrium energy-band diagram under illumination and forward bias at the MPP. Light absorption generates excess-charge carriers in the perovskite, resulting in a higher occupation of electrons in the conduction band and holes in the valence band. This difference in carrier concentration is indicated by the respective quasi-Fermi levels E_{Fn} for electrons and E_{Fp} for holes setting the electron and hole densities via

$$n = N_{\mathrm{C}} \exp \quad \frac{E_{\mathrm{C}} - E_{\mathrm{Fn}}}{k_{\mathrm{B}} T} \tag{2.26}$$

and

$$p = N_{\mathrm{V}} \exp \quad \frac{E_{\mathrm{Fp}} - E_{\mathrm{V}}}{k_{\mathrm{B}} T} \quad . \tag{2.27}$$

Their quasi-Fermi level splitting (QFLS) is given by

$$\Delta E_{\mathrm{F}} = E_{\mathrm{Fn}} - E_{\mathrm{Fp}} = k_{\mathrm{B}} T \ln \frac{np}{n_{\mathrm{i}}^2} \quad . \tag{2.28}$$

Here, n_{i} denotes the intrinsic charge-carrier density, defined as $n_{\mathrm{i}}^2 = n_0 p_0$. The total electron and hole concentration can also be expressed as $n = n_0 + \Delta n$ and $p = p_0 + \Delta p$, respectively, with their corresponding excess-carrier concentrations Δn and Δp. As indicated in Equation 2.26 and 2.27, the distance between the respective quasi-Fermi level and the band edge correlates with the carrier density. This quasi-Fermi level splitting (ΔE_{F}) describes the chemical potential of electron-hole pairs that is built up inside the absorber of the solar cell. This splitting can also be considered as an internal voltage with $V_{\mathrm{int}} = \Delta E_{\mathrm{F}}/q$. Ideally, the internal voltage, and thus the chemical potential, remains the same throughout the solar cell up to the contacts, where it is converted into an electrostatic potential difference measurable as external voltage (V_{ext}). Unfortunately, real solar-cell devices usually experience losses, reducing the chemical potential of the charge carries across the transport layers, which is visible by a decrease in the QFLS. The gradient of the quasi-Fermi level is directly proportional to the electron and hole current densities via

$$J_{\mathrm{n}} = q D_{\mathrm{n}} \frac{dn}{dx} + q F \mu_{\mathrm{n}} n = n \mu_{\mathrm{n}} \frac{dE_{\mathrm{Fn}}}{dx} \tag{2.29}$$

and

$$J_{\mathrm{p}} = -q D_{\mathrm{p}} \frac{dp}{dx} + q F \mu_{\mathrm{p}} p = p \mu_{\mathrm{p}} \frac{dE_{\mathrm{Fp}}}{dx} \quad , \tag{2.30}$$

where μ_{n} and μ_{p} denote the mobilities and D_{n} and D_{p} are the diffusion constants for electrons and holes, respectively. These current densities J_{n} and J_{p} are a superposition of the drift-current density and the diffusion-current density. The drift-current density is driven by an electric field F visible as a gradient in the conduction- and valence band edges. In contrast, the gradient in charge-carrier concentration drives the diffusion-current density. If the product of the carrier density and mobility is too low at a given current density, a substantial gradient of the quasi-Fermi level is necessary to drive the current through the transport layers. In the example shown in Figure 2.10d, approximately 70 meV of accumulated Fermi-level gradient in the two contact layers is necessary to allow the extraction of a current J_{MPP}.

In addition, a comparison of the two band diagrams shows that at the maximum power point, the asymmetry due to the built-in voltage V_{bi} and the tilting of the bands nearly disappeared. Thus, the electric field, which assists charge transport to the contacts, is quite weak. In the worst-case scenario, the built-in voltage is smaller than the applied voltage at the maximum power point. Then, the charge carriers have to travel against the electric field, which creates a barrier for extraction.

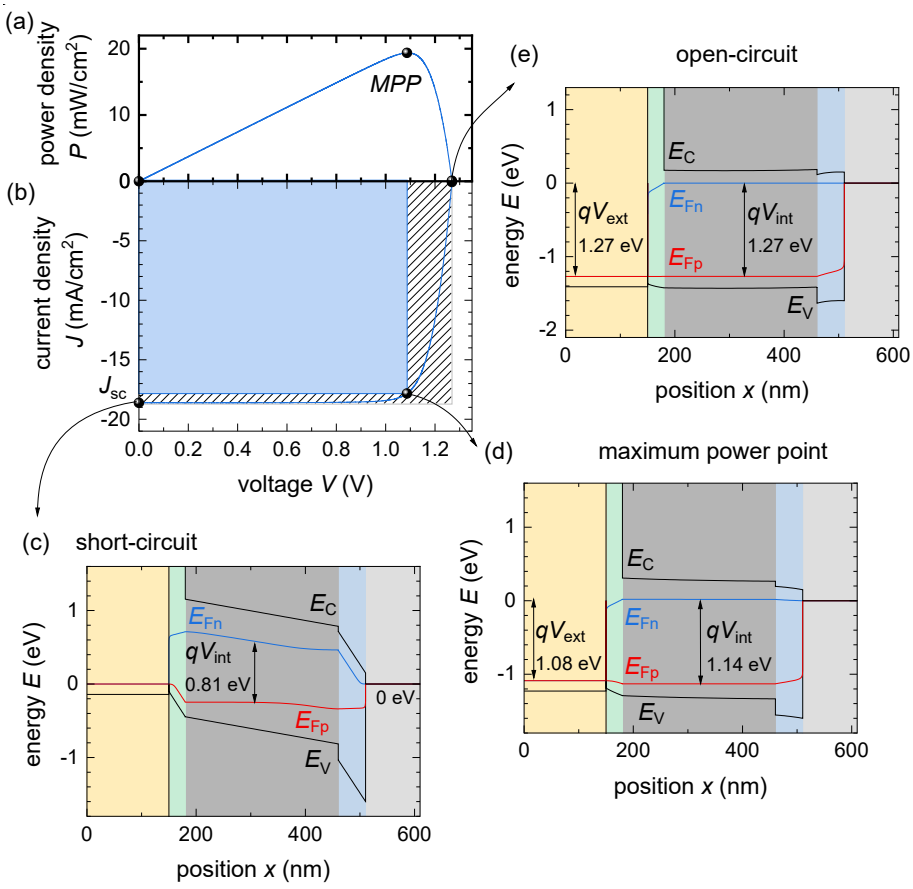

Abbildung 2.11: (a) Power- and (b) current density J as a function of voltage V, illustrating an exemplary solar cell behaviour. In addition, energy-band diagrams are at the three characteristic working points, namely (c) short circuit, (d) maximum-power point and (e) open circuit are shown.

For further explanation, Figure 2.11 shows exemplary band diagrams at three characteristic operating points during a JV-scan with a corresponding plot of the power output- and current-density voltage curve in (a-b). Mathematical expressions for the efficiency η and fill factor FF were already introduced in section 2.1 (Equation 2.12 and 2.13) and are also valid outside the SQ model if the actual quantities for J_{sc} and V_{oc} are inserted. Figure 2.11c presents the energy-band diagram at short circuit, (d) the situation at the MPP and (e) at open circuit. Short-circuit condition implies that the difference in the electrostatic potential between ITO and Ag is zero. At the same time, the extracted current density J_{sc} and the Fermi-level gradients are the highest compared to those at other working points in the fourth quadrant. However, even at short-circuit, a considerable amount of photogenerated charge carriers accumulate inside the absorber and the transport layers, as indicated by the internal voltage of approximately 0.9 V. This effect is caused by the transport materials' typically low mobility and reduces the solar cell's obtainable short-circuit current density. Furthermore, due to the low mobility in HTL and ETL, the Fermi-level gradients over the transport layers are larger than those over the absorber layer. At the MPP, the extracted current is only marginally smaller than that at short circuit, but the steady-state charge-carrier density is substantially higher. Thus, given the higher conductivity of all intrinsic layers in the system, the gradient of E_{Fn} and E_{Fp} will be much smaller than at short circuit. At open circuit, the net current through the transport layers is zero. Hence, all Fermi levels are flat, except for the electron-Fermi level in the HTL and the hole-Fermi level in the ETL. These have a slight gradient because a tiny minority-carrier current flows through these layers. However, due to their extremely low densities, these minority-carrier currents are basically irrelevant to the functionality of the device.

2.5 Recombination in Lead-Halide Perovskites

In this thesis, the electro-optical behavior of perovskite solar cells is simulated using numerical and analytical models. The numerical simulations are based on the drift-diffusion model, [105] where a set of coupled differential equations must be solved

together with the corresponding boundary conditions. This set of coupled differential equations consists of the Poisson equation and continuity equations for electrons and holes. In case of a one-dimensional system, the Poisson-equation, which governs the electrostatic potential (φ) induced by the net space-carrier density (ρ), is given by

$$\frac{\partial^2 \varphi}{\partial x^2} = -\frac{\rho}{\epsilon_0 \epsilon_\mathrm{r}} \ , \tag{2.31}$$

where ϵ_0 is the dielectric constant of vacuum and ϵ_r is the relative dielectric permittivity. The net charge density is the sum of all charges, expressed as $\rho = q(p - n + N_\mathrm{D} - N_\mathrm{A} + p_\mathrm{trapped} - n_\mathrm{trapped})$, which includes the carrier densities of free electrons n in the conduction band, free holes p in the valence band, the concentration of ionized donors and acceptors N_D and N_A, as well as localized charges n_trapped and p_trapped trapped in defects. The continuity equations follow from carrier conservation and account for how the free charge-carrier densities for electrons and holes change over time. The generation of charge carriers due to light absorption lets the densities of $n(x)$ and $p(x)$ increase, whereas recombination processes cause a reduction in carrier concentration. Additionally, a current flow can change the charge-carrier densities in both directions. Considering these different mechanisms in a homogeneous material without gradients in band gap or electron affinity allows us to write down the one-dimension continuity equation for electrons, resulting in

$$\frac{\partial n}{\partial t} = G_\mathrm{ext}(x,t) + G_\mathrm{int}(x,t,n,p) - R(x,t,n,p) + D_\mathrm{n}\frac{\partial^2 n(x,t)}{\partial x^2} + F\mu_\mathrm{n}\frac{\partial n(x,t)}{\partial x} \ , \tag{2.32}$$

and 1D-continuity equation for holes expressed via

$$\frac{\partial p}{\partial t} = G_\mathrm{ext}(x,t) + G_\mathrm{int}(x,t,n,p) - R(x,t,n,p) + D_\mathrm{p}\frac{\partial^2 p(x,t)}{\partial x^2} - F\mu_\mathrm{p}\frac{\partial p(x,t)}{\partial x} \ , \tag{2.33}$$

with the time t and total recombination rate (R). Note that at heterointerfaces, where, e.g., band gap, the density of states or electron affinity may change, additional terms must be added to the last terms on the right-hand side of Equation 2.32 and 2.33. References [106, 107] discuss this in more detail. For a description of the drift-diffusion equations in three dimensions, see ref. [105]. Moreover, G_ext denotes the generation rate due to external illumination, for example, sunlight, whereas the

internal generation rate G_{int} refers to generation due to reabsorption of photons generated by radiative recombination within the device itself. The latter process is called photon recycling, which is particularly relevant for absorber materials with a large energetic overlap between the emission spectrum and absorption profile. [108] This behavior is found in metal-halide perovskites. [109] Thus, if radiative recombination creates a photon within the perovskite absorber, it likely has a suitable photon energy to be absorbed again, generating an additional electron-hole pair. Thereby, p_{r} denotes the average probability of this recycling event and p_{e} the probability of emission and coupling out of the solar cell. Furthermore, the parasitic absorption probability p_{a} indicates how likely the photon is reabsorbed from another layer, such as the metal back reflector or transport layers. Since one of these processes must occur, $p_{\text{r}} + p_{\text{e}} + p_{\text{a}} = 1$ holds. [110]

In the simplest case, the external generation rate is assumed to be homogeneous and can be set to a constant and spatially independent value. In the case of transient experiments and their simulations, where the charge-carrier decay after a pulsed excitation is of interest, the generation rate is also time-dependent. Here, the simplest approach is to assume that the laser pulse creates an initial carrier concentration but not consider the laser pulse's generation profile and time dependence. In addition, calculating the generation rate requires information about the incoming photon flux and an optical model describing the absorption behavior of the solar cell. For example, one simple physical description follows from Lambert-Beer's law, assuming a generation rate that depends on the absorber layer depth and its absorption coefficient α. In this Lambert-Beer type model, the generation rate is given by $G = \phi\alpha(1 - \exp(-\alpha x))$. A more realistic model, which also considers interference effects and the optical material properties of all layers in the solar cell stack, is based on the transfer-matrix method (TMM). For more details, I refer to ref. [111]. The transfer-matrix method is applicable to simulate the optics of flat, planar films. Therefore, it is adequate to model the optics of an inverted, planar perovskite-solar cell. Thus, TMM is used to calculate the generation rate in the numerical drift-diffusion simulations performed in this thesis. The two last terms in Equations 2.32 and 2.33 represent the divergence of the drift and diffusion current, which were already introduced in the last section in Equation 2.29 and 2.30.

The total recombination rate R comprises several different mechanisms whose

individual rates add up. These mechanisms cover radiative and non-radiative processes, as schematically illustrated in Figure 2.12. To numerically solve the continuity equations, it would be necessary to express the rate R in terms of the concentrations n and p of free electrons and holes. The dependence of R on n and p differs for each of the mechanisms shown in Figure 2.12 and is therefore briefly introduced below. In addition, there are situations in which analytical solutions to the continuity equations are possible under certain assumptions. This is particularly the case when all bands and Fermi levels are flat and n and p are no longer a function of position. In this situation, the terms originating from the divergence of the current disappear. In addition, there is no space charge in this situation. Hence, the electrostatic potential is constant and the Poisson equation can be disregarded. I will make use of this simplification to introduce the respective recombination mechanisms didactically and to illustrate their behavior. Since this thesis especially focuses on understanding tran-

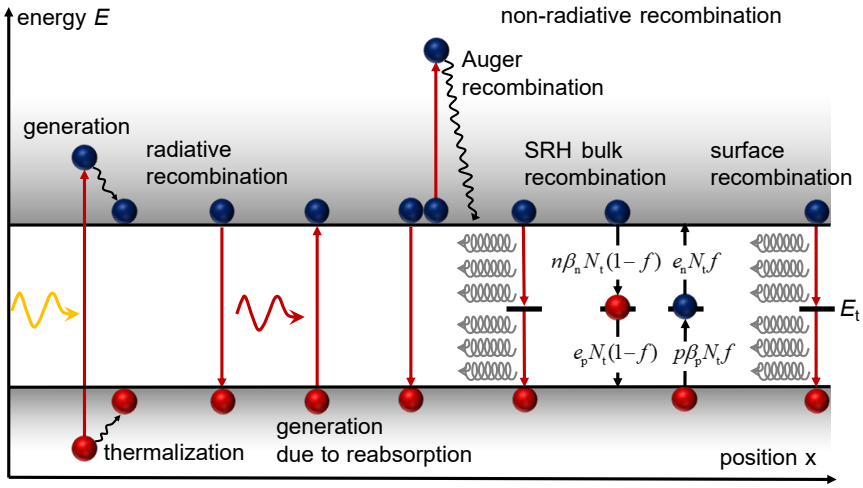

Abbildung 2.12: Schematic overview of different generation and recombination processes. Radiative recombination via band-to-band transition emits a photon, whereas non-radiative recombination processes release energy via phonons to the semiconductor lattice, as indicated by the grey springs. Thereby, three different non-radiative recombination mechanisms play a role in metal-halide perovskites, namely Auger recombination and defect recombination in the bulk or at the surface, as described by Shockley-Read-Hall (SRH) statistics. This model describes recombination via a defect as an interplay of four separate processes. These processes are electron capture, electron emission, hole capture and hole emission. The rates of these respective processes are stated above.

sient characterization methods regarding recombination dynamics, I will also focus on charge-carrier decays from an initial carrier concentration and the respective rate equations of the form $\frac{dn}{dt} = -R$.

2.5.1 Radiative Recombination

For metal-halide perovskites, it is justified to assume that radiative recombination is a bimolecular process. [112] Consequently, the internal recombination rate $R_{\mathrm{rad}}^{\mathrm{int}}$ at which the charge carriers recombine radiatively is proportional to the product of electron n and hole p concentration, resulting in

$$R_{\mathrm{rad}}^{\mathrm{int}} = k_{\mathrm{rad}}^{\mathrm{int}} \ np - n_{\mathrm{i}}^2 \quad . \tag{2.34}$$

Here, $k_{\mathrm{rad}}^{\mathrm{int}}$ denotes the internal radiative recombination coefficient. However, the externally accessible and measurable radiative recombination rate $R_{\mathrm{rad}}^{\mathrm{ext}}$ is slower because the internal generation due to photon recycling superimposes the decrease in charge-carrier density. [113] Hence, one can write

$$R_{\mathrm{rad}}^{\mathrm{ext}} = R_{\mathrm{rad}}^{\mathrm{int}} + G_{\mathrm{int}} = k_{\mathrm{rad}}^{\mathrm{int}} \left(1 - p_{\mathrm{r}}\right) \ np - n_{\mathrm{i}}^2 \ = k_{\mathrm{rad}}^{\mathrm{ext}} \ np - n_{\mathrm{i}}^2 \quad , \tag{2.35}$$

where $k_{\mathrm{rad}}^{\mathrm{ext}}$ is the external radiative recombination coefficient. This equation indicates that the external, radiative recombination rate depends on the optics of the solar-cell stack because the reabsorption probability p_{r} changes with the likelihood of the other two mechanisms. Note that the effect of photon recycling cannot be considered in the scope of the numerical simulations presented in later chapters. Therefore, the radiative coefficient k_{rad} is the corresponding external quantity used in the following.

2.5.2 Shockley-Read-Hall Recombination

In contrast to radiative recombination, non-radiative recombination involves the emission of phonons. Non-radiative recombination can occur via different mechanisms. However, this energy dissipation always represents a loss path that must be suppressed. One of the non-radiative recombination mechanisms represents recombination via defect states within the band gap of the absorber material. Whether

a defect contributes substantially to non-radiative recombination is often estimated by the Shockley-Read-Hall (SRH) statistics. [114, 115] Thereby, recombination via a singly charged defect is described as a combination of four separate processes, namely electron capture, electron emission, hole capture, and hole emission. Figure2.12 schematically illustrates these respective processes and also indicates their respective rates $r_{\mathrm{e,c}}$, $r_{\mathrm{e,e}}$, $r_{\mathrm{h,c}}$, $r_{\mathrm{h,e}}$. Under steady-state conditions, the occupation of the trap does not change. Thus, the net rate for electrons must be equal to the net rate for holes, resulting in the rate for Shockley-Read-Hall defect recombination

$$\begin{aligned} R_{\mathrm{SRH}} &= r_{\mathrm{e,c}} - r_{\mathrm{e,e}} = r_{\mathrm{h,c}} - r_{\mathrm{h,e}} \\ &= n\beta_{\mathrm{n}} N_{\mathrm{t}} (1-f) - e_{\mathrm{n}} N_{\mathrm{t}} f = p\beta_{\mathrm{p}} N_{\mathrm{t}} f - e_{\mathrm{p}} N_{\mathrm{t}} (1-f) \quad . \end{aligned} \tag{2.36}$$

N_{t} denotes the trap density of traps with energy E_{t}, $\beta_{\mathrm{n/p}}$ the capture coefficients and $e_{\mathrm{n/p}}$ is the emission coefficient for electrons and holes, respectively. The emission coefficients are connected to the capture coefficients via detailed balance and given by $e_{\mathrm{n}} = \beta_{\mathrm{n}} N_{\mathrm{c}} \exp\left((E_{\mathrm{t}} - E_{\mathrm{c}})/k_{\mathrm{B}}T\right)$ and $e_{\mathrm{p}} = \beta_{\mathrm{p}} N_{\mathrm{v}} \exp\left((E_{\mathrm{v}} - E_{\mathrm{t}})/k_{\mathrm{B}}T\right)$. Equation 2.36 allows us to determine the electron-occupation function

$$f = \frac{n\beta_{\mathrm{n}} + e_{\mathrm{p}}}{n\beta_{\mathrm{n}} + p\beta_{\mathrm{p}} + e_{\mathrm{n}} + e_{\mathrm{p}}} \quad , \tag{2.37}$$

which differs in non-equilibrium from the Fermi-Dirac distribution. Usually, this occupation function is valid to describe the occupation in the energy bands. Inserted in Equation 2.36, the rate for trap-assisted SRH recombination is determined as

$$R_{\mathrm{SRH}} = N_{\mathrm{t}} \beta_{\mathrm{n}} \beta_{\mathrm{p}} \frac{np - n_{\mathrm{i}}^2}{n\beta_{\mathrm{n}} + p\beta_{\mathrm{p}} + e_{\mathrm{n}} + e_{\mathrm{p}}} \quad . \tag{2.38}$$

The probability of a capture or emission event depends on the energetic position of the trap, as well as the Huang-Rhys factors of the individual defects [116, 117] and phonon energies within the semiconductor. [95, 118, 119] Traps located in the middle of the band gap are more recombination-active than those close to the band edges. For midgap traps, the probability that a hole and an electron are captured simultaneously is far more likely, than for traps near the band edges. In contrast, shallow defects capture one charge-carrier type less often, while the other one is more likely to be thermally reemitted. For a deep trap, the probability for reemission

and emission coefficients are negligibly small. Consequently, the SRH-recombination rate can be simplified, resulting in

$$R_{\mathrm{SRH}} = \frac{np - n_{\mathrm{i}}^2}{n\tau_{\mathrm{SRH,p}} + p\tau_{\mathrm{SRH,n}}} \quad . \tag{2.39}$$

Here, $\tau_{\mathrm{SRH,n}} = \tau_{\mathrm{n}}$ and $\tau_{\mathrm{SRH,p}} = \tau_{\mathrm{p}}$ are the SRH-bulk lifetimes for electrons and holes, respectively, defined by $\tau_{\mathrm{SRH,n/p}} = \left(\beta_{\mathrm{n/p}} N_{\mathrm{T}}\right)^{-1}$. To increase these SRH lifetimes, the trap density, particularly from deep defects, must be reduced. For instance, the fabrication routine and process parameters influence perovskite formation and, by this, the defect densities.

Non-radiative, trap-assisted recombination does not only occur in the perovskite bulk but also at the interfaces to the adjacent transport layer, at contacts, or if present at bare surfaces. Because these positions represent discontinuities within the ideal crystal symmetry, they often create additional electronic states within the band gap, introducing additional non-radiative recombination paths. Shockley-Read-Hall (SRH) statistic is also adequate to describe the occupation of these surface or interface traps. Thus, recombination at a surface can be expressed via a modified SRH rate. Then, a surface-recombination rate per unit area results in

$$R_{\mathrm{s}} = \frac{np - n_{\mathrm{i}}^2}{n/S_{\mathrm{p}} + p/S_{\mathrm{n}}} \quad , \tag{2.40}$$

where the inverse surface-recombination velocities S_{n} and S_{p} of electrons and holes replace all instances of the lifetime. This substitution implies that R_{s} is a rate per unit area and time rather than per unit volume and time as the SRH-bulk recombination rate.

Furthermore, this mathematical basis is suitable for describing recombination at interfaces at a heterojunction, such as a perovskite/ETL and HTL/perovskite transition. Figure 2.13 schematizes these two situations. In case of the perovskite/ETL interface, electrons n_{ETL} in the electron-transport layer recombine with holes p_{pero} in the perovskite, being reflected by the adjusted SRH rate

$$R_{\mathrm{int}}^{\mathrm{ETL}} = \frac{n_{\mathrm{ETL}} p_{\mathrm{pero}} - n_{\mathrm{i,int,E}}^2}{n_{\mathrm{ETL}}/S_{\mathrm{p,E}} + p_{\mathrm{pero}}/S_{\mathrm{n,E}}} \quad . \tag{2.41}$$

In this picture, $n_{\mathrm{i,int,E}}$ denotes the product of the electron and hole equilibrium concentrations on either side of the interface. Thus, for the specific case of the perovskite/ETL interface, one can write

$$\begin{aligned} n_{\mathrm{i,int,E}}^2 &= n_{0,\mathrm{ETL}} p_{0,\mathrm{pero}} \\ &= N_{\mathrm{c,ETL}} \exp\left(\frac{E_{\mathrm{F}} - E_{\mathrm{c,ETL}}}{k_{\mathrm{B}} T}\right) N_{\mathrm{v,pero}} \exp\left(\frac{E_{\mathrm{v,pero}} - E_{\mathrm{F}}}{k_{\mathrm{B}} T}\right) \\ &= N_{\mathrm{c,ETL}} N_{\mathrm{v,pero}} \exp\left(-\frac{E_{\mathrm{int,E}}}{k_{\mathrm{B}} T}\right) , \end{aligned} \tag{2.42}$$

with an interfacial band gap $E_{\mathrm{int,E}} = E_{\mathrm{c,ETL}} - E_{\mathrm{v,pero}}$.

For the case of the perovskite/HTL interface, the same principle is applicable, with the difference that electrons n_{pero} in the perovskite recombine with holes p_{HTL} from the hole-transport layer. This mechanism can be described by

$$R_{\mathrm{int}}^{\mathrm{HTL}} = \frac{n_{\mathrm{pero}} p_{\mathrm{HTL}} - n_{\mathrm{i,int,H}}^2}{n_{\mathrm{pero}}/S_{\mathrm{p,H}} + p_{\mathrm{HTL}}/S_{\mathrm{n,H}}} , \tag{2.43}$$

with

$$\begin{aligned} n_{\mathrm{i,int,H}}^2 &= n_{0,\mathrm{pero}} p_{0,\mathrm{HTL}} \\ &= N_{\mathrm{c,pero}} \exp\left(\frac{E_{\mathrm{F}} - E_{\mathrm{c,pero}}}{k_{\mathrm{B}} T}\right) N_{\mathrm{v,HTL}} \exp\left(\frac{E_{\mathrm{v,HTL}} - E_{\mathrm{F}}}{k_{\mathrm{B}} T}\right) \\ &= N_{\mathrm{c,pero}} N_{\mathrm{v,HTL}} \exp\left(-\frac{E_{\mathrm{int,H}}}{k_{\mathrm{B}} T}\right) . \end{aligned} \tag{2.44}$$

The interfacial band gap $E_{\mathrm{int,H}}$ between the HTL and perovskite is defined by $E_{\mathrm{int,H}} = E_{\mathrm{c,pero}} - E_{\mathrm{v,HTL}}$. Moreover, $S_{\mathrm{n,E/H}}$ and $S_{\mathrm{p,E/H}}$ are the recombination velocities at the interfaces. As highlighted by the two rate equations 2.41 and 2.43, interfacial recombination becomes faster for higher concentrations of the recombination-active charge-carrier densities at the interface and with higher interface-recombination velocities. As I will discuss in more detail in chapter 7, the key challenge for correctly including interface recombination in descriptions of transient experiments is that the concentration of charge carriers at interfaces is often strongly affected by Coulomb attraction. For this reason, analytical solutions to the problem are difficult or impossible. Thus, numerical approaches that consider the solution of the Poisson equation must be used.

2.5.3 Auger Recombination

Another non-radiative recombination mechanism is Auger recombination, where the energy of a recombining electron-hole pair is transferred to another charge carrier. This third particle gets excited within the conduction or valence band and subsequently thermalizes back to the band edge. In the course of thermalization, energy is released in the form of phonons to the lattice of the semiconductor. [120, 121] The rate of Auger recombination is

$$R_{\text{Auger}} = (C_{\text{n}} n + C_{\text{p}} p) \;\; np - n_{\text{i}}^2 \quad , \tag{2.45}$$

where C_{n} represents the Auger coefficient for electrons and C_{p} is the Auger coefficient for holes. These coefficients depend on the band structure of the material and typically change with the band gap. Compared with other materials of similar band gaps, metal-halide perovskites have relatively high Auger coefficients due to lattice distortions. [122] Since Auger recombination is a three-particle process, it depends on the injection level and becomes more likely at high charge-carrier densities. In addition, high doping densities enhance this mechanism. [123] Therefore, Auger recombination represents a significant non-radiative loss path in silicon-solar cells. In

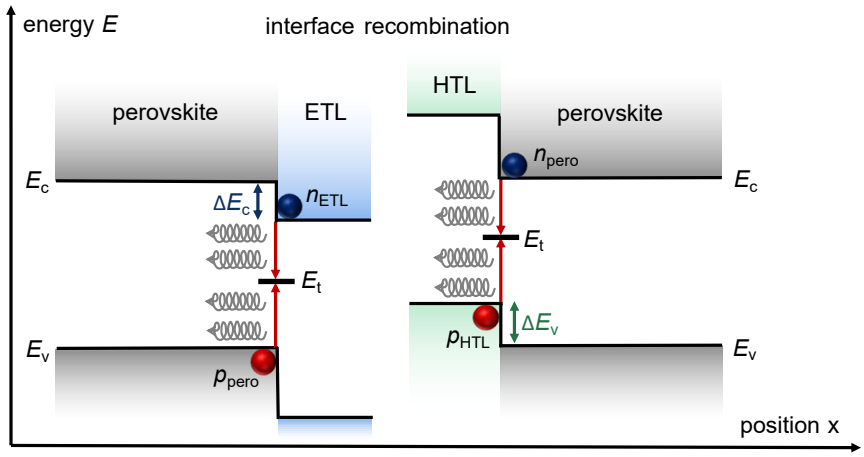

Abbildung 2.13: Schematic illustration of interface recombination processes picturing the two scenarios of perovskite/ETL- and a HTL/perovskite interface.

contrast, it plays only a minor role in metal-halide perovskites up to one sun conditions. [124] However, at higher injection levels or illumination intensities, Auger recombination is likely relevant.

2.5.4 High-Level Injection vs. Low-Level Injection

Besides, the injection level determines which of these different recombination mechanisms dominates the overall recombination dynamics. A comparison of the formulas of the different individual contributions indicates that they all differ in their dependency on carrier concentration. Furthermore, the ratio of electron and hole densities affects the Auger and SRH rates, whereas the radiative recombination rate is only controlled by the np-product. The different dependence of the recombination rates on the electron and hole concentrations implies that they would also have a different effect on the decay of the charge-carrier concentrations $n(t)$ and $p(t)$ after an initial concentration is left to decay via recombination. A typical assay of the charge-carrier concentration used in the literature and this thesis is time-resolved photoluminescence (TPL). The TPL signal results from measuring the emitted photons created by radiative recombination at a rate proportional to np. [29, 35] Accordingly, the TPL signal is proportional to the product of electron and hole concentration and not to n or p individually. At the same time, the time-resolved photoluminescence itself contains information about the entire recombination dynamics because the decrease in n and p results from the superposition of all recombination processes. In the following, I present analytical solutions to the rate equations for $n(t)$ that are valid in simple situations. Furthermore, I discuss how the observable used in this thesis, namely $\phi_{\mathrm{TPL}}(t) \propto np$, behaves.

While the radiative recombination and Auger coefficients are important material properties, the SRH lifetimes can vary substantially from sample to sample within a material system. This variation is because the SRH lifetime depends on defect concentrations which may vary, e.g., with processing conditions. Hence, while determining all recombination coefficients is important for a material system, the SRH lifetimes are the key sample-dependent property that might vary in a series of samples of the same material. Thus, TPL measurements on semiconducting materials are often performed to extract the non-radiative Shockley-Read-Hall re-

combination (SRH) lifetimes of individual samples. Given that the PL transient is affected by several recombination mechanisms, it is necessary to briefly discuss how to extract the SRH lifetimes from the PL transients and establish a common terminology that I use for the remainder of this thesis.

Next, two extreme cases regarding the injection level are discussed, referred to as low-level injection (LLI) and high-level injection (HLI). The latter is especially relevant for quite intrinsic lead-halide perovskites. The condition $n = p$ defines high-level injection, designating that during a TPL experiment, both types of carriers are present in roughly equal concentrations. In this situation, both types of carriers have finite lifetimes. Additionally, we keep the condition $\Delta n = \Delta p$ and therefore do not distinguish between the rate equations for electrons and holes. In high-level injection, the rate equation accounting only for SRH bulk recombination via a deep defect simplifies to

$$\frac{\partial \Delta n(t)}{\partial t} = -R_{\mathrm{SRH,HLI}} = -\frac{n(t)}{\tau_{\mathrm{SRH,n}} + \tau_{\mathrm{SRH,p}}} = -\frac{n(t)}{\tau_{\mathrm{n}} + \tau_{\mathrm{p}}} = -\frac{n(t)}{\tau_{\mathrm{SRH}}} \tag{2.46}$$

with the analytical solution of the form

$$n(t) = n(0)\exp(-t/\tau_{\mathrm{SRH}}) \ , \tag{2.47}$$

where $n(0)$ denotes the initial electron concentration. Using this analytical solution for the scenario, where SRH bulk recombination is the dominant mechanism and the injection level is HLI, results in Figure 2.14. Figure 2.14a illustrates the normalized PL decay, which behaves like the normalized decay of $n^2(t)$, for three different SRH bulk lifetimes. The decays are monoexponential, as implied by Equation 2.47.

Furthermore, I introduce the representation of the differential decay time τ_{TPL}, which results from the derivative of the photoluminescence with respect to time defined by

$$\tau_{\mathrm{TPL}} = \left(-\frac{1}{m} \frac{d\ln(\phi_{\mathrm{TPL}})}{dt} \right)^{-1} \tag{2.48}$$

with the factor m relating to the injection level. Here, $m = 1$ holds for low-level injection and $m = 2$ is for high-level injection, indicated by the indices 'HLI' and 'LLI'. This carrier-density-dependent decay time is an important and meaningful variable that serves as a generic quantity to interpret TPL decays in this thesis. For

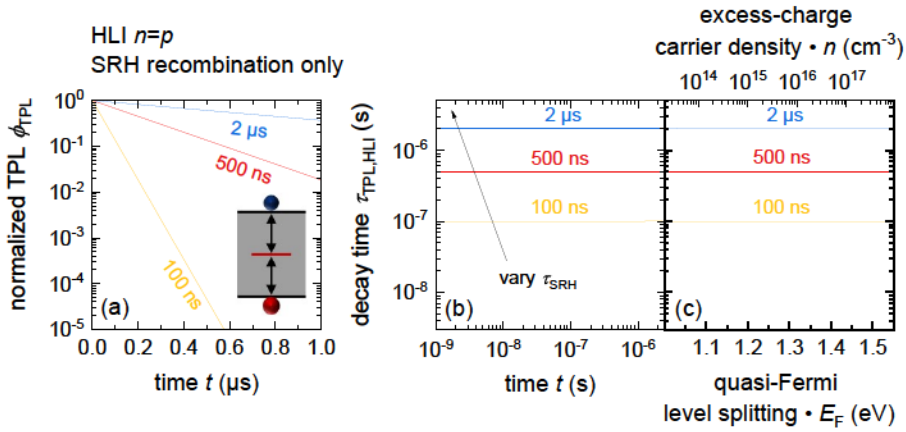

Abbildung 2.14: Illustration of the analytical solutions of the differential equations for high-level injection only considering SRH recombination. (a) Normalized transient photoluminescence decays ϕ_{TPL}, starting from similar initial charge-carrier concentration, for varying SRH lifetimes $\tau_{\mathrm{SRH}} = \tau_{\mathrm{SRH,n}} + \tau_{\mathrm{SRH,p}}$, namely 100 ns, 500 ns and 2 µs. (b) Differential decay time $\tau_{\mathrm{TPL,HLI}}$ as a function of time t or in (c) plotted versus excess-charge carrier density Δn and quasi-Fermi-level splitting.

the simple, zero-dimensional and analytically soluble scenarios described here, this differential decay time can also be expressed as

$$\tau_{\mathrm{TPL}} = -\frac{n(t)}{dn(t)/dt} \quad . \tag{2.49}$$

Figure 2.14b displays the decay time $\tau_{\mathrm{TPL,HLI}}$ resulting from the analytical solution of the TPL decay versus time. Figure 2.14c presents these decay times plotted as a function of the excess-electron density Δn, as well as the quasi-Fermi-level splitting ΔE_{F}, whose dependence on carrier concentration is stated in Equation 2.28. In the case of SRH recombination in HLI, the decay time $\tau_{\mathrm{TPL,HLI}}$ is constant with time and Fermi-level splitting and corresponds to $\tau_{\mathrm{SRH,n}} + \tau_{\mathrm{SRH,p}} = \tau_{\mathrm{SRH}}$.

In contrast, the decay time $\tau_{\mathrm{TPL,HLI}}$ in the scenario of solely radiative recombination in HLI, is described by

$$\frac{\partial \Delta n(t)}{\partial t} = -R_{\mathrm{rad,HLI}} = -k_{\mathrm{rad}} n(t)^2 \tag{2.50}$$

with the analytical solution

$$n(t) = \frac{n(0)}{k_{\mathrm{rad}} n(0) t + 1} \quad , \tag{2.51}$$

resulting in a differential decay time

$$\tau_{\mathrm{TPL,HLI}} = -\frac{n(t)}{dn(t)/dt} = \frac{1}{k_{\mathrm{rad}} n(t)} \tag{2.52}$$

that undergoes continuous change. This situation is illustrated in Figure 2.15. The PL exhibits a fast initial decay. Thus, the decay times at early times are short and increase continuously with time or decreasing carrier concentration. Higher radiative recombination coefficients k_{rad} enhance the decay and cause a parallel shift of the decay-time Fermi-level curve towards shorter decay times. Unfortunately, a different initial charge-carrier concentration, which could be set in a TPL experiment by the laser fluence, also changes the course of the transient PL decay. [125] Thus, different decays are no longer directly comparable because a fast decay does not necessarily

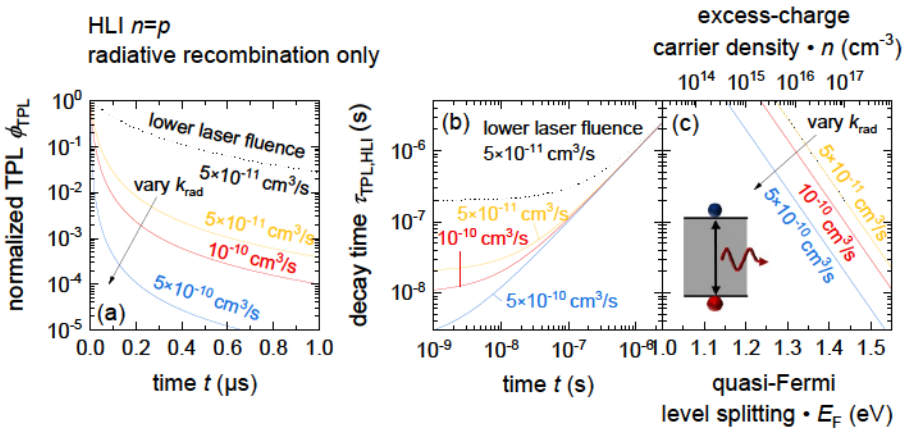

Abbildung 2.15: Illustration of the analytical solutions of the differential equations for high-level injection, assuming that radiative recombination is the only mechanism. (a) Normalized transient photoluminescence decays ϕ_{TPL}, starting from similar initial charge-carrier concentration, for varying radiative recombination coefficients, namely $k_{\mathrm{rad}} = 5 \times 10^{-11}\mathrm{cm^3 s^{-1}}$, $5 \times 10^{-10}\mathrm{cm^3 s^{-1}}$ or $10^{-10}\mathrm{cm^3 s^{-1}}$. (b) Differential decay time $\tau_{\mathrm{TPL,HLI}}$ as a function of time t or in (c) plotted versus excess-charge carrier density Δn and quasi-Fermi-level splitting ΔE_{F}.

correlate with a higher radiative recombination coefficient but could also be caused by a higher laser power. The representation of the decay time vs. Fermi-level splitting overcomes this ambiguity. With this, the information merges and the curves obtained for different initial carrier concentrations (yellow and black lines) complement each other.

Next, we study the low-level injection (LLI) case in more detail. In LLI, one charge-carrier species is present as the majority, for example, implemented by doping. In a p-doped semiconductor, holes represent the pre-existing majority carrier concentration which remains relatively unchanged. In contrast, the concentration of electrons, which are the less injected minority carriers in a p-doped material, sees a large relative increase due to excitation.
In low-level injection, the rate equation that only includes SRH-bulk recombination is given by

$$\frac{\partial \Delta n(t)}{\partial t} = -R_{\mathrm{SRH,LLI}} = -\frac{\Delta n(t)}{\tau_{\mathrm{SRH,n}}} \ . \tag{2.53}$$

The respective analytical solution is also a monoexponential decay function, namely

$$n(t) = n(0)\exp(-t/\tau_{\mathrm{SRH,n}}) \ . \tag{2.54}$$

However, only the lifetime of the minority carriers, in this example, electrons, is relevant. Also, the charge-carrier dependency for purely radiative recombination, described by the differential equation

$$\frac{\partial \Delta n(t)}{\partial t} = -R_{\mathrm{rad,LLI}} = -k_{\mathrm{rad}} \ \ n(t)N_{\mathrm{A}} - n_{\mathrm{i}}^2 \quad , \tag{2.55}$$

follows a monoexponential decay, given by

$$n(t) = n(0)\exp(-k_{\mathrm{rad}}pt) \ . \tag{2.56}$$

Thus, the decay time $\tau_{\mathrm{TPL,LLI}}$ is a constant, as depicted in Figure 2.16. This radiative lifetime in low-level injection is defined by $\tau_{\mathrm{TPL,LLI}} = \tau_{\mathrm{rad,LLI}} = (k_{\mathrm{rad}}p)^{-1}$ and is bounded by the doping density N_{A}. It is a particularity of the low-level condition that all the established recombination mechanisms become linear in minority carrier concentration. Accordingly, $n(t)$ for a combination of the recombination mechanisms

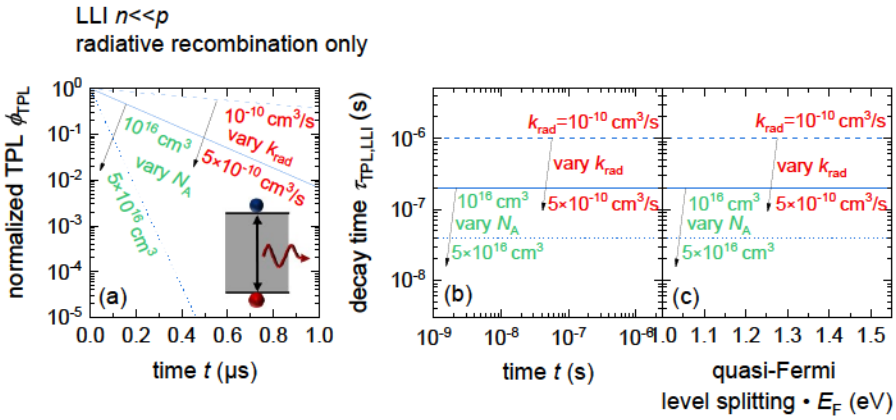

Abbildung 2.16: Illustration of the analytical solutions of the differential equations for low-level injection only considering radiative recombination. (a) Normalized, transient photoluminescence decays ϕ_{TPL} for two different radiative recombination coefficients, namely $k_{\mathrm{rad}} = 5\times10^{-10}\mathrm{cm}^3\mathrm{s}^{-1}$ or $10^{-10}\mathrm{cm}^3\mathrm{s}^{-1}$, as well as varying doping concentrations. (b) Differential decay time $\tau_{\mathrm{TPL,LLI}}$ as a function of time t or ΔE_{F} in (c). In this case, the decay time is the time constant from the monoexponential TPL decay, which decreases at higher doping densities or radiative recombination coefficients.

is easily specified and gives

$$n(t) = n(0)\exp\left(-t/\left(k_{\mathrm{rad}}p + 1/\tau_{\mathrm{SRH,n}}\right)^{-1}\right) \tag{2.57}$$

for the case of SRH and radiative recombination and

$$n(t) = n(0)\exp\left(-t/\left(C_{\mathrm{Auger}}p^2 + k_{\mathrm{rad}}p + 1/\tau_{\mathrm{SRH,n}}\right)^{-1}\right) \tag{2.58}$$

for SRH, radiative and Auger recombination in low-level injection with

$$\tau_{\mathrm{TPL,LLI}} = -\frac{n(t)}{dn(t)/dt} = \left(C_{\mathrm{Auger}}p^2 + k_{\mathrm{rad}}p + 1/\tau_{\mathrm{SRH,n}}\right)^{-1} . \tag{2.59}$$

In summary, in the case of high-level injection, different recombination mechanisms lead to differently shaped transient decays. Among the three typically studied bulk-recombination mechanisms (SRH, radiative and Auger) only SRH would lead to a monoexponential decay. [125] Hence, the situation where only SRH recombi-

nation occurs can be described by a single lifetime that is given for $n = p$ by the sum $\tau_{\mathrm{SRH}} = \tau_{\mathrm{SRH,n}} + \tau_{\mathrm{SRH,p}}$. Consequently, if any other recombination mechanism is considered, the decay is no longer monoexponential and cannot be described by a single lifetime. The term charge-carrier lifetime generally describes the dependence of the electron or hole concentration as a function of time after the generation of electrons and holes, e.g., by a laser pulse, has stopped. Often, the characteristic time constant of an exponential fit of the form $\phi_{\mathrm{TPL}} = \phi_{\mathrm{TPL}}(0)\exp(-t/\tau_{\mathrm{mono}})$ to TPL data is also called a '*lifetime*'. This lifetime concept is meaningful and suitable for a doped semiconductor film, crystal or wafer operated in low-level injection. In this case, all recombination mechanisms become linear in minority-carrier concentration. Then, a lifetime, which is often explicitly called the effective lifetime $\tau_{\mathrm{eff,LLI}}$ could easily be defined as the time-constant of minority-carrier decay. That is, if electrons are minority carriers, their decay would be monoexponential and follows $\Delta n = \Delta n(0)\exp(-t/\tau_{\mathrm{eff,LLI}})$ no matter what recombination mechanism dominates [126] and its effective lifetime $\tau_{\mathrm{eff,LLI}}$ is a constant, carrier-concentration independent value. This lifetime concept does not apply to intrinsic or low-doped semiconductors such as lead-halide perovskites, as discussed in more detail in the next section.

2.5.5 Perovskite Film on Glass

The next section discusses the charge-carrier recombination of a perovskite film. For a perovskite film on glass, three different bulk-recombination mechanisms are relevant, namely radiative band-to-band recombination [112, 127] and non-radiative recombination via Auger [122] or first-order Shockley-Read Hall. [128, 129]. First, I focus on recombination mechanisms in the bulk and exclude the effect of surface recombination, which is subsequently discussed in the end of this section. A perovskite film on glass whose surface is passivated, e.g., by an organic passivation layer, [78,130] would usually meet this case, because the interface between perovskite layers and glass substrates is typically quite inert and not particularly recombination active. [109] When a laser pulse photoexcites the semiconducting perovskite film, free excess-electrons Δn and equal density of holes $\Delta n = \Delta p$ are generated. The initial generation profile of these excess-charge carriers depends on the optical

properties of the perovskite, its thickness, and the excitation wavelength. The initially inhomogeneous distribution of the charge-carrier concentration is flattened by diffusion. Since the perovskite film is typically only a few hundred nanometres thick and the charge-carrier mobility (μ) is typically $> 1\,\mathrm{cm}^2/\mathrm{Vs}$, [79] an equilibration happens very fast and takes place in the first hundreds of pico- to nanoseconds after the laser pulse. For simplicity, we therefore assume that the system has no spatial gradients of electron or hole concentrations or electrostatic potential. This assumption leads us to a convenient situation where diffusion and drift currents can be neglected and the photogenerated charge carriers Δn vanish over time only through different recombination processes. The rate equation

$$\frac{\partial \Delta n}{\partial t} = -k_{\mathrm{rad}}\ \left(np - n_{\mathrm{i}}^2\right)\ - \frac{np - n_{\mathrm{i}}^2}{\tau_{\mathrm{SRH,p}} n + \tau_{\mathrm{SRH,n}} p} - C_{\mathrm{n}} n\ \left(np - n_{\mathrm{i}}^2\right)\ - C_{\mathrm{p}} p\ \left(np - n_{\mathrm{i}}^2\right) \tag{2.60}$$

accounts for the rates of these competing processes which will occur and describes the change in excess-charge carriers as a function of time. However, lead-halide perovskite films are typically intrinsic enough that during a TPL experiment, both types of carriers are present in roughly equal concentrations. Let us assume for simplicity that the electron and hole concentrations are precisely equal, that is $n = p$, meaning that the high-level condition applies. In this case, the rate equation for a film on glass can be simplified to

$$\begin{aligned} \frac{dn(t)}{dt} &= -\left(C_{\mathrm{n}} + C_{\mathrm{p}}\right) n(t)^3 - k_{\mathrm{rad}} n(t)^2 - \frac{n(t)}{\tau_{\mathrm{SRH,n}} + \tau_{\mathrm{SRH,p}}} \\ &= -C_{\mathrm{Auger}} n(t)^3 - k_{\mathrm{rad}} n(t)^2 - \frac{n(t)}{\tau_{\mathrm{SRH}}}\ , \end{aligned} \tag{2.61}$$

which can be solved analytically and results in the relation

$$\begin{aligned} t = \frac{1}{2}\tau_{\mathrm{SRH}} \ln\ & \frac{n(0)^2 + n(t) n(0)^2 k_{\mathrm{rad}} \tau_{\mathrm{SRH}} + n(t)^2 n(0)^2 C_{\mathrm{Auger}} \tau_{\mathrm{SRH}}}{n(t)^2 + n(t)^2 n(0) k_{\mathrm{rad}} \tau_{\mathrm{SRH}} + n(t)^2 n(0)^2 C_{\mathrm{Auger}} \tau_{\mathrm{SRH}}} \\ & - \frac{{k_{\mathrm{rad}} \tau_{\mathrm{SRH}}}^{2/3}}{\sqrt{4 C_{\mathrm{Auger}} - {k_{\mathrm{rad}}}^2 \tau_{\mathrm{SRH}}}}\ \tan^{-1}\ \frac{{\tau_{\mathrm{SRH}}}^{1/2} (2 C_{\mathrm{Auger}} n(0) + k_{\mathrm{rad}})}{\sqrt{4 C_{\mathrm{Auger}} - {k_{\mathrm{rad}}}^2 \tau_{\mathrm{SRH}}}} \\ & - \tan^{-1}\ \frac{{\tau_{\mathrm{SRH}}}^{1/2}\ 2 C_{\mathrm{Auger}} n(t) + k_{\mathrm{rad}}}{\sqrt{4 C_{\mathrm{Auger}} - {k_{\mathrm{rad}}}^2 \tau_{\mathrm{SRH}}}}\ . \end{aligned} \tag{2.62}$$

The example of Equation 2.62 demonstrates that the explicit solution of the DGL system can be lengthy and unwieldy. Thus, using implicit solutions that directly provide the decay time is advantageous. In this case, the dependence of the decay time on the actual carrier concentration is given by

$$\tau_{\mathrm{TPL,HLI}} = -\frac{1}{C_{\mathrm{Auger}} n(t)^2 + k_{\mathrm{rad}} n(t) + 1/\tau_{\mathrm{SRH}}} \quad . \tag{2.63}$$

For the more straightforward case without Auger recombination, the rate equation is

$$\frac{dn(t)}{dt} = -k_{\mathrm{rad}} n(t)^2 - \frac{n(t)}{\tau_{\mathrm{SRH,n}} + \tau_{\mathrm{SRH,p}}} = -k_{\mathrm{rad}} n(t)^2 - \frac{n(t)}{\tau_{\mathrm{SRH}}} \quad , \tag{2.64}$$

resulting in the time-dependent charge-carrier concentration

$$n(t) = \frac{n(0)\exp(-t/\tau_{\mathrm{SRH}})}{1 + n(0) k_{\mathrm{rad}} \tau_{\mathrm{SRH}} [1 - \exp(-t/\tau_{\mathrm{SRH}})]} \tag{2.65}$$

and the corresponding decay time

$$\tau_{\mathrm{TPL,HLI}} = -\frac{1}{k_{\mathrm{rad}} n(t) + 1/\tau_{\mathrm{SRH}}} \quad . \tag{2.66}$$

These two cases are illustrated in Figure 2.17. Thereby, the upper row shows a variation in the SRH bulk lifetime, whereas the second row of Figure 2.17 depicts the results for varying radiative recombination coefficients. The plots on the right-hand side, showing differential decay times as a function of charge-carrier density or quasi-Fermi-level splitting ΔE_{F}, highlight how the characteristics of the individual recombination processes superimpose and facilitate distinguishing the influences of the individual processes. Radiative and Auger recombination define the shape of the decay-time function at high Fermi-level splittings, which are present directly after the laser pulse. The comparison of the analytical solution with and without Auger recombination illustrates that Auger recombination steepens the increase of $\tau_{\mathrm{TPL,HLI}}$. In all cases, the saturation of the decay time at lower Fermi-level splittings on the value of the SRH lifetime is clearly visible. The choice of $m = 2$ for $n = p$ ensures that the decay-time function defined by Equation 2.48 will saturate towards $\tau_{\mathrm{TPL,HLI}} = \tau_{\mathrm{SRH,n}} + \tau_{\mathrm{SRH,p}}$ for long times or low ΔE_{F}. This representation method becomes even more relevant if TPL measurements at different excitation energies are compared because the photoexcited charge-carrier density dictates which recom-

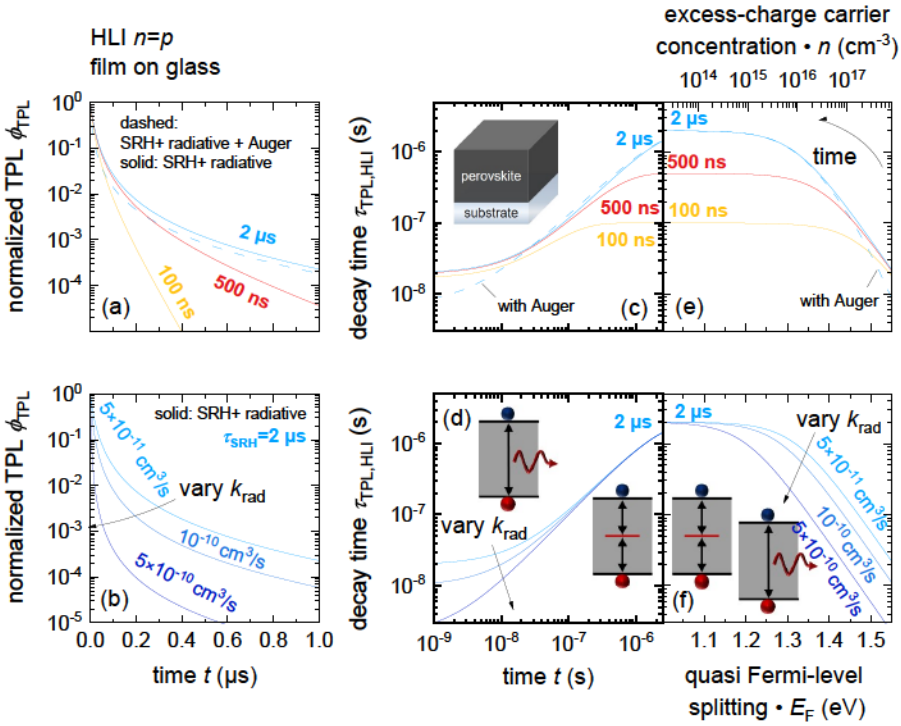

Abbildung 2.17: Illustration of the analytical solutions of the differential equations for high-level injection, which describe an undoped perovskite film on glass with a passivated surface. Different scenarios are selected to differentiate between the influence of the respective recombination mechanisms on the decay. The graphs in the top row show a variation of the SRH-bulk lifetime, namely $\tau_{SRH} = \tau_{SRH,n} + \tau_{SRH,p}$ equals 100 ns, 500 ns and 2 µs. The figures in the bottom row illustrate the results for varying radiative recombination coefficients ranging from $k_{rad} = 5 \times 10^{-11} \mathrm{cm^3 s^{-1}}$ to $5 \times 10^{-10} \mathrm{cm^3 s^{-1}}$. The total Auger coefficient was set to $C_{Auger} = 8.8 \times 10^{-29} \mathrm{cm^6 s^{-1}}$. (a-b) Normalized transient photoluminescence decays ϕ_{TPL}, starting from similar initial charge-carrier concentration. (c-d) Decay time $\tau_{TPL,HLI}$ as a function of time t or in panel (e-f) plotted versus quasi-Fermi-level splitting.

bination type dominates the TPL decay. Figure 2.18 presents a comparison of the simulated situation (a-c) and experimental data (d-f) of a perovskite film on glass, but now for varying laser fluences. Again, the results are shown as normalized TPL decays and their differential time constants over time or Fermi-level-splitting. Figure 2.18b and (e) reveal that using the time as the x-axis is not very informative because the decay time $\tau_{TPL,HLI}$ at a specific delay time after the pulse can have very dif-

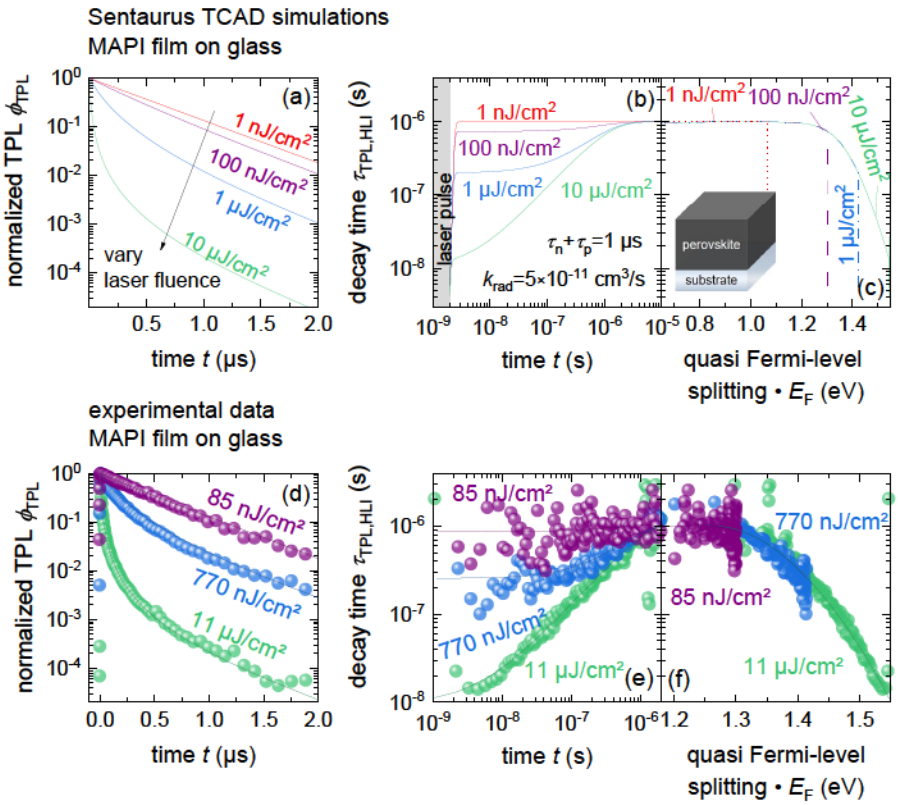

Abbildung 2.18: (a-c) Simulated data (Sentaurus TCAD) of transient photoluminescence measurements of a $CH_3NH_3PbI_3$ perovskite film with $\tau_n = \tau_p = 500$ns, $k_{rad} = 5 \times 10^{-11}$cm^{3}s^{-1} and $C_n = C_p = 4.4 \times 10^{-29}$cm^{6}s^{-1} for different laser-excitation fluences, namely 1 nJ/cm^2, 100 nJ/cm^2, 1 µJ/cm^2, 1 µJ/cm^2). (a) Normalized photoluminescence decays over time from measurements on a semi-logarithmic scale. For low laser fluences or later times, the exponential decay caused by SRH recombination dominates the normalized TPL decay. Higher-order recombination mechanisms such as radiative or Auger recombination dominate the decay at higher laser fluences. (b) Differential decay versus time and (c) versus Fermi-Level splitting. (d-f) Experimental data of transient photoluminescence measurements of a $CH_3NH_3PbI_3$ perovskite film on glass for different laser excitation fluences, namely 85 nJ/cm^2, 1 µJ/cm^2 and 10 µJ/cm^2, reused from ref. [109]. Panel (d) shows the normalized photoluminescence decays over time from measurements (open symbols). Solid lines represent global fits, including trap-assisted SRH, radiative and Auger recombination. (e) Decay times versus time and (f) versus Fermi-Level splitting extracted from experimental data.

ferent values depending on the excitation energy. The information only merges and the curves complement each other if one plots the time constant versus Fermi-level

splitting, which depends on the charge-carrier concentration. Finally, note that both the Sentaurus simulation and analytical solution reflect the trend of the experimental data and are therefore well-suited to describe a pure, passivated perovskite film on glass.

TPL measurements on unpassivated perovskite films on glass are often used to characterize not only the bulk, but also the surface. If the bulk properties of the perovskite are already known, this sample type can be used to extract the corresponding surface properties from the TPL measurement. In general, the rate of surface recombination may be limited either by the transport of charge carriers to the surface or by the surface-recombination velocities S_n and S_p of the electrons and holes at the interface itself. Including diffusion of charge-carriers to the surface in the differential equation only has an analytical solution for the low-level case. [131]

However, due to the relatively low thickness $d < 1$ m of perovskite thin films and the typically high mobilities of $\mu > 1\,\mathrm{cm}^2/\mathrm{Vs}$, the transport of electrons and holes to the surface can be considered fast compared to the rate of recombination at the surface, [109] which can be quite low relative to many other semiconductors. Therefore, it is a reasonable simplification to not distinguish between the average carrier concentration in the bulk of the perovskite-thin film and the carrier concentrations at either of the surfaces. This assumption implies that the rates of bulk and surface recombination can just be added up and it is not necessary to calculate the concentration of electrons and holes at the film surface. The surface-recombination rate per unit area in HLI is given by

$$R_\mathrm{s,HLI} = \frac{n}{1/S_\mathrm{p} + 1/S_\mathrm{n}} \ , \tag{2.67}$$

which is valid for $n = p$ and $np \gg n_\mathrm{i}^2$ and the simplified version of Equation 2.40. If it is additionally assumed for simplicity that the surface-recombination velocities for electrons and holes are equal, namely, $S_\mathrm{n} = S_\mathrm{p} = S$, the surface-recombination rate simplifies to $R_\mathrm{s,HLI} = S_\mathrm{n}/2$. To combine the surface-recombination rate per unit area with the bulk-recombination rates per volume and time, either all volume-recombination rates must be multiplied by the thickness d_pero of the perovskite film or the surface-recombination rate R_s must be divided by this thickness. Doing the

latter leads to

$$\frac{dn(t)}{dt} = -k_{\mathrm{rad}} n(t)^2 - \frac{n(t)}{\tau_{\mathrm{SRH}}} - \frac{Sn(t)}{2d_{\mathrm{pero}}} \tag{2.68}$$

for rate equation describing a perovskite film, including surface recombination at one surface with the other being perfectly passivated. Note that the bulk-SRH term and the surface-recombination term are both linear in electron concentration, which suggests defining a surface lifetime τ_{s} and an effective SRH lifetime

$$\tau_{\mathrm{SRH}}^{\mathrm{eff}} = \left(\frac{1}{\tau_{\mathrm{SRH}}} + \frac{1}{\tau_{\mathrm{s}}} \right)^{-1} = \left(\frac{1}{\tau_{\mathrm{SRH}}} + \frac{S}{2d_{\mathrm{pero}}} \right)^{-1}, \tag{2.69}$$

allowing to rewrite Equation 2.69 to obtain

$$\frac{dn(t)}{dt} = -k_{\mathrm{rad}} n(t)^2 - \frac{n(t)}{\tau_{\mathrm{SRH}}} - \frac{n(t)}{\tau_{\mathrm{s}}} = -k_{\mathrm{rad}} n(t)^2 - \frac{n(t)}{\tau_{\mathrm{SRH}}^{\mathrm{eff}}} \ . \tag{2.70}$$

where the analytical solution has the same mathematical form as Equation 2.65, substituting τ_{SRH} by $\tau_{\mathrm{SRH}}^{\mathrm{eff}}$. Additionally, I conducted numerical simulations using Sentaurus TCAD to check whether this analytical description of a film on glass with surface recombination is adequate. The resulting PL transients and their decay times as a function of the quasi-Fermi-level splitting for various surface-recombination velocities S are summarized in Figure 2.19a-c. Faster surface-recombination velocities S lead to faster TPL decays. Furthermore, the saturation value of the differential decay time at low Fermi-level-splitting decreases. These plateau values of $\tau_{\mathrm{TPL,HLI}}$ match the respective effective lifetime $\tau_{\mathrm{SRH}}^{\mathrm{eff}}$. How well the numerical and analytical solutions fit together is confirmed by Figure 2.19d, in which the corresponding plateau values of $\tau_{\mathrm{TPL,HLI}}$ are compared with the calculated values using Equation 2.48.

I conclude that the numerical results from Sentaurus TCAD and the analytical description fit pretty well and deviate only for a particularly large S. Therefore, the analytical model is suitable for analyzing the experimental TPL data of a perovskite film on glass with an unpassivated surface. The surface-recombination velocity S can then be extracted from the plateau value of the decay-time function if the SRH-bulk lifetime constant is already known from the measurement of a passivated sample.

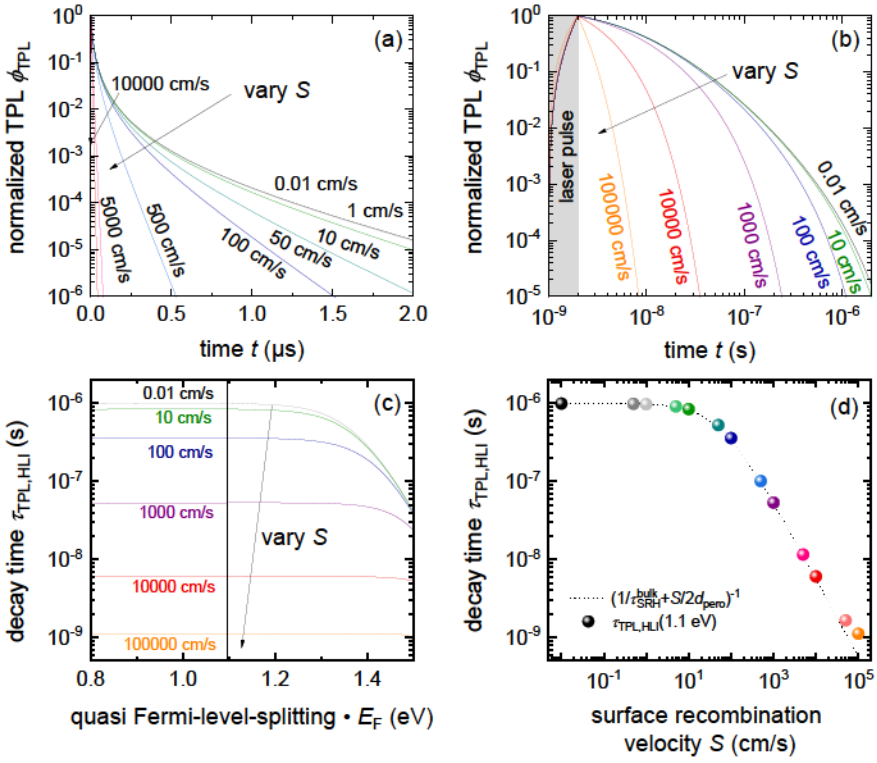

Abbildung 2.19: (a-b) Simulated, normalized photoluminescence decays ϕ_{TPL} versus time of a $CH_3NH_3PbI_3$ perovskite film with a constant bulk SRH lifetime of ($\tau_{SRH,n} + \tau_{SRH,p} = 1\,\mu s$ and a varying surface-recombination velocity S (Sentaurus TCAD). A laser excitation fluence of $10\,\mu J/cm^2$ was used. Table A.6 lists the additional simulation parameters. The higher the surface-recombination velocities, the faster the TPL decay. (b) Decay time $\tau_{TPL,HLI}$ over Fermi-Level splitting ΔE_F calculated from the normalized TPL decays via Equation 2.48. Panel (d) represents the correlation of the effective time constant with the surface-recombination velocity S. The dotted line represents the analytical solution. The colored data points belong to the saturated plateau values of the decay time $\tau_{TPL,HLI}$ for values at $\Delta E_F = 1.1\,eV$ from the numerical simulation.

3 Characterization Methods

In this chapter, I explain the basic principles and experimental setups of the characterization methods used in this thesis. In addition to covering the most fundamental measurements in photovoltaics, such as voltage-dependent current (JV) or external-quantum efficiency Q_e^{EQE} measurements, this chapter focuses on transient methods like TPL and transient photovoltage (TPV) measurements. These transient methods offer insides into the recombination dynamics, the quantification and qualitative understanding of which is one of the key subjects of this work.

3.1 Current-Voltage Characterization

Current-voltage measurements at different illumination intensities and in the dark are among the essential standard procedures used for solar-cell characterization, delivering, e.g., the solar-cell efficiency and the associated performance parameters short-circuit current J_{sc}, open-circuit voltage V_{oc} and fill factor FF. The current-voltage curves were measured on a calibrated AM1.5g spectrum of a class AAA solar simulator, WACOM-WXS-140S-Super-L2 with a combined xenon/halogen lamp-based system, providing a power density of $100\,\mathrm{mWcm}^2$. The devices are placed inside a sealed, nitrogen-filled measurement box with a quartz-glass window to prevent degradation of the perovskite sample due to air and humidity contact. The solar cell in the hermetic measurement box is electrically contacted with a 4-cable configuration and connected to an external switch box to automatically and sequentially measure all solar cells on the substrate. Each sample contains four solar cells with an active cell area of $0.16\,\mathrm{cm}^2$ defined by the overlap of orthogonal silver and ITO patterns, each 4 mm in width. A series 2420 SourceMeter from Keithley Instruments acts as a source-measurement unit by applying the desired voltage to the solar cell and re-

cording the output current flow. The forward scan ($-0.1\,\mathrm{V}$ to $1.3\,\mathrm{V}$) and subsequent reverse voltage scan ($1.3\,\mathrm{V}$ to $-0.1\,\mathrm{V}$) were each carried out at various scan speeds with a standard scan speed of $100\,\mathrm{mV/s}$.

A second solar simulator, which is directly integrated into the glovebox where the solar cells are fabricated, provides a preliminary function test of the devices and a first performance evaluation. Furthermore, the accompanying Delphi program offers various measurement modes, for example, a tracking function that records the maximum efficiency or open-circuit voltage over time. This second solar simulator uses only a white light-emitting diode (LED) (Cree XLamp CXA 3050) to mimic the solar spectrum but differs especially in the ultraviolet (UV) and infrared (IR) regions. A preconditioning of $10-30\,\mathrm{min}$ under this LED illumination was applied for an activation process discussed in section 4.

Measurement protocols for perovskite solar cells generally suggest using a shadowing mask to define the illuminated area precisely. [132] Since the illumination usually reaches the metal mask from a wide angle, light is spread and wave-guided through the glass substrate, distorting the measurement and questioning the validity of this approach. This interference is one reason I decided not to use a metal mask to measure the $JV-$curves shown in this thesis. However, I compared the J_{sc} values to the integrated values of the $Q_{\mathrm{e}}^{\mathrm{EQE}}$ measurements. Furthermore, masking the solar cell leads to underestimating the V_{oc} due to a geometric effect. This underestimation occurs if the ratio of the illuminated cell area A_{mask} to the cell area in the dark A_{cell} differ because they determine the measurable open-circuit voltage via [132]

$$V_{\mathrm{oc}} = \frac{k_{\mathrm{B}}T}{q} \ln \quad \frac{J_{\mathrm{sc}} A_{\mathrm{cell}}}{J_0 A_{\mathrm{mask}}} + 1 \quad . \tag{3.1}$$

3.2 External Quantum Efficiency

The external-quantum efficiency $Q_{\mathrm{e}}^{\mathrm{EQE}}$ gives the ratio of the extracted electric charge carriers to the number of externally irradiated photons, according to

$$Q_{\mathrm{e}}^{\mathrm{EQE}}(E) = \frac{1}{q} \frac{dJ(E)}{d\phi(E)} \ , \tag{3.2}$$

where $d\phi(E)$ is the incident photon flux in units of $\mathrm{cm}^{-2}\mathrm{s}^{-1}$ in the photon-energy interval dE, which leads to the current density $dJ(E)$. If each photon generates one electron-hole pair and the charge-carrier collection is ideal, the external-quantum efficiency equals one. However, optical and electrical losses reduce the external-quantum efficiency of real-world solar cell devices. Conducted at short circuit, the EQE is a spectrally resolved measurement of the short-circuit current, which offers information about the origin of J_{sc}-losses. These losses occur, for example, due to parasitic absorption of layers other than the perovskite absorber, reflection caused by differences in the refractive indices, interference effects due to adverse layer thicknesses and collection problems.

The external-quantum efficiency setup consists of a xenon-light source (Osram XPO150W) and a Bentham monochromator (TMC300) with a spectral range of $300-1100\,\mathrm{nm}$. This monochromatic light is focused on the solar cell, where it generates a current. The light intensity was calibrated using a calibrated silicon photodiode (Gigahertz-Optik SSO-PD100-04) as a reference. In this configuration, a spot smaller than the cell area illuminates the solar cells. The photon intensity for each energy interval is typically low. Consequently, the generated current is also small and must be amplified using lock-in technique. Since the lock-in amplifier requires a periodic signal, the light is chopped before entering the monochromator. The chopper frequency was set to 72 Hz and a wavelength step size of 10 nm was used. Furthermore, the lock-in amplifier needs a voltage as input. Therefore, the current collected from the solar cell is converted by a current-voltage converter for further processing.

Ideally, integration of the EQE gives the short-circuit current of the cell under illumination, via

$$J_{\mathrm{sc}} = q \int_0^\infty Q_{\mathrm{e}}^{\mathrm{EQE}}(E)\phi_{\mathrm{sun}}(E)dE \ . \tag{3.3}$$

Usually, this relation is used to confirm the short-circuit density from the JV-measurement, checking for reliability and measurement errors due to incorrect calibration. Unfortunately, in the case of perovskite solar cells, these two current densities often show a discrepancy with the EQE value, which is usually lower. The reason for these deviations is hard to pinpoint precisely. [133] Due to the low light intensities during the EQE experiment, the excess-charge carrier density is smaller than that

under the one-sun condition. Thus, the band diagrams of these two states are different. For example, the conductivity of the electron- and hole-transport layers will be affected by light intensity. Given that the conductivity of these layers can affect the efficiency of charge collection, the EQE may not reflect the same charge-collection efficiency as expected from a one-sun current-voltage measurement. Alternatively, bias light can be utilized to boost the excess-carrier density of a solar cell during the EQE measurement.

3.3 Steady State Luminescence

Luminescence describes the emission of photons after excitation. This excitation could arise because of the injection of a current called electroluminescence EL, or due to incident light called photoluminescence (PL). In this section, I introduce the steady-state versions of luminescence measurements, while the next section covers the transient measurement mode.

3.3.1 Steady State Photoluminescence

Photoluminescence PL spectroscopy is a non-destructive, contactless method applicable to pure perovskite films, interlayer stacks and complete solar-cell devices. During the PL experiment, the sample is photoexcited by light absorption, and its response by radiative emission of photons is detected. In this work, PL measurements are conducted at open circuit, implying that all the generated excess-charge carriers must recombine. Thus, at a given light intensity, the generation rate is fixed and equal to the sum of all recombination rates. Any other recombination process beyond radiative recombination will reduce the stationary concentration of excess-charge carriers and the associated quasi-Fermi level splitting achieved under steady-state illumination. Since PL measures the radiative part of the recombination, the intensity of the PL signal correlates with the external-luminescence quantum efficiency $Q_{\mathrm{e}}^{\mathrm{lum}}$. Thus, photoluminescence measurements can quantify recombination losses and deduce a sample's internal voltage or quasi-Fermi-level splitting. The PL flux scales with $\exp(\Delta E_{\mathrm{F}}/(k_{\mathrm{B}}T))$, which implies that every 58 meV reduction in

quasi-Fermi level splitting causes a decrease of one order of magnitude in the PL signal and external-LED quantum yield. Accordingly, the PL signal is quite sensitive to changes in the quasi-Fermi level splitting. Thus, it is well-suited for judging the optoelectronic quality of the sample without the need for electrical contacts.

Figure 3.1 schematically illustrates the steady-state PL setup used in this thesis. For steady-state PL spectroscopy, a continuous wave laser (Coherent Sapphire) with a wavelength of 532 nm optically excites the samples. A beam expander combined with a top-head profile widens the laser beam, yielding a homogeneous laser spot with a diameter of approximately 5.3 mm. This laser-beam adjustment ensures that the entire cell area, defined by a square of 4 mm × 4 mm, is homogeneously illuminated. The collimated macro-PL signal passes through a filter-wheel stage, which prevents the detection of reflected laser light and light of unwanted higher orders. The luminescence is then focused onto a spectrometer (Andor Shamrock 303), where the light gets spectrally resolved. The monochromator grating has 150 lines/mm and the central wavelength was set to 800 nm. For the subsequent light detection, an Andor Si (deep depletion) CCD camera (iDus Series) is used, whose 1024 pixels capture a full spectrum at once. An automated neutral density (ND) filter stage adjusts the laser intensity. I performed PL measurements for different applied laser-excitation powers impinging on the sample.

The respective steady-state PL setup was spectrally calibrated but not calibrated to absolute photon numbers, which is necessary to measure the absolute PL quantum yield directly. Nevertheless, to be able to compare and evaluate the PL intensities of different layer stacks, I measured the external open-circuit voltage $V_{\mathrm{oc}}(\phi_{\mathrm{laser,1sun}})$ of a completed solar-cell stack under laser illumination $\phi_{\mathrm{laser,1sun}}$. This laser illumination $\phi_{\mathrm{laser,1sun}}$ corresponds to the absorbed photon flux at 1 sun and $\phi_{\mathrm{PL,cell}}(\phi_{\mathrm{laser,1sun}})$ is respective PL. A relative calibration of the intensity uses both values. With this approach I can calculate the internal quasi-Fermi-level splitting ΔE_{F} at a given illumination ϕ_{laser} according to

$$\Delta E_{\mathrm{F}} = qV_{\mathrm{oc,imp}}(\phi_{\mathrm{PL}}) = qV_{\mathrm{oc}}(\phi_{\mathrm{laser,1sun}}) + k_{\mathrm{B}}T \ln \frac{\phi_{\mathrm{PL}}}{\phi_{\mathrm{PL,cell}}(\phi_{\mathrm{laser,1sun}})} \quad . \tag{3.4}$$

The symbol ϕ_{PL} denotes the photoluminescence flux of a certain unknown sample, whereas $\phi_{\mathrm{PL,cell}}(\phi_{\mathrm{laser,1sun}})$ is the photoluminescence flux of the reference cell, whose

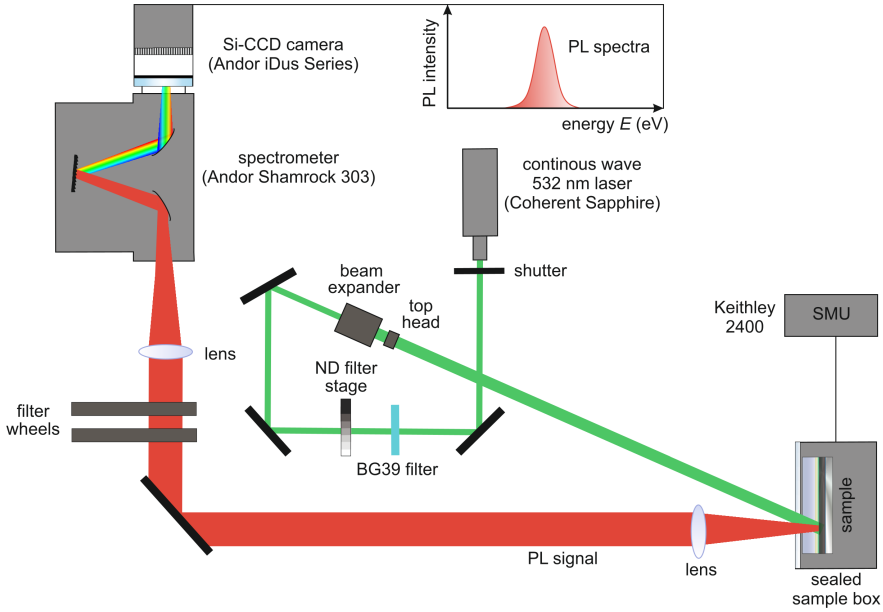

Abbildung 3.1: Schematic of the steady state photo- and electroluminescence setup used in this thesis.

open-circuit voltage under the same illumination is known. Note that the underlying assumption is that the system has no spatial gradients and flat quasi-Fermi levels. In this approach, the external-luminescence quantum efficiency $Q_{\mathrm{e}}^{\mathrm{lum}}$ is obtained via

$$Q_{\mathrm{e}}^{\mathrm{lum}}(\phi_{\mathrm{laser}}) = \exp\left(-\frac{qV_{\mathrm{oc}}^{\mathrm{rad}}(\phi_{\mathrm{laser}}) - \Delta E_{\mathrm{F}}(\phi_{\mathrm{laser}})}{k_{\mathrm{B}}T}\right) \tag{3.5}$$

with

$$V_{\mathrm{oc}}^{\mathrm{rad}}(\phi_{\mathrm{laser}}) = V_{\mathrm{oc}}^{\mathrm{rad}}(\phi_{\mathrm{laser,1sun}}) - \frac{k_{\mathrm{B}}T}{q}\ln\left(\frac{\phi_{\mathrm{laser,1sun}}}{\phi_{\mathrm{laser}}}\right), \tag{3.6}$$

where $V_{\mathrm{oc}}^{\mathrm{rad}}(\phi_{\mathrm{laser}})$ is the fluence-dependent radiative limit of the open-circuit voltage and ϕ_{laser} is the respective laser excitation flux.

To adjust this photon flux of the laser and to be able to correlate the laser power to the one-sun condition, the equivalent photon flux $\phi_{\mathrm{laser,1sun}}$ as absorbed under illumination with the AM1.5g spectrum needs to be determined. In the case of a semiconducting material with a band gap of 1.6 eV this absorbed photon flux is

equal to $1.6 \times 10^{17}\mathrm{cm}^{-2}\mathrm{s}^{-1}$ for an absorptance of one. This flux gives a corresponding power density of the green laser of $59.3\,\mathrm{mWcm}^2$. Under this illumination, the radiative limit of the open-circuit voltage is $V_{\mathrm{oc}}^{\mathrm{rad}}(\phi_{\mathrm{laser,1sun}}) = 1.324\,\mathrm{V}$.

3.3.2 Photoluminescence Quantum Yield

Hyperspectral absolute photoluminescence imaging was used to complement the approach described in section 3.3.1. Since this setup is calibrated to provide absolute quantum yields, the data provide additional evidence and independent validation of the quasi-Fermi level splitting. For a detailed description of the method and setup, I refer to reference [134, 135].

The samples are optically excited with blue light from two 450 nm LEDs equipped with diffuser lenses for these PL-imaging measurements. The intensity was adjusted to approximately 1 sun. The photoluminescence gets spectrally resolved using a liquid crystal tuneable filter. The wavelength step size was set to 5 nm. The PL images from 650 nm to 1100 nm were taken via a charge-coupled device (CCD) camera (Allied Vision) calibrated to pixel-wise detect the absolute photon number. To deduce the quasi-Fermi-level splitting and its distribution map from the PL image, the high-energy slope of the PL emission is fitted to every spectrum of the hyperspectral images using

$$\Delta E_{\mathrm{F}} = E + k_{\mathrm{B}} T \ln \frac{\phi_{\mathrm{PL}}(E)\, h^3 c^2}{2\pi E^2 a(E)} \quad . \tag{3.7}$$

For the evaluation, a step-function-like absorptance $a\,(\mathrm{E})$ of 1 was used for energies above the band gap. The global systematic error is approximately 20 meV, corresponding to a factor of two in the PLQY.

3.3.3 Steady State Electroluminescence

In the EL-measurement mode, the solar cell operates as a light-emitting diode LED, which is the reciprocal action to the standard operation of a solar cell. The EL is connected to the external-quantum efficiency via the optoelectronic reciprocity theorem. Therefore, electroluminescence reflects all important physical processes

influencing solar-cell performance, such as resistive, optical, or recombination losses. I use the EL-spectrum to calculate the radiative limit in this thesis, as described in section 2.2. Note that the shapes of the EL and PL spectra are typically similar for perovskite solar cells.

For electroluminescence measurements, a constant current is applied through the devices supplied by an external current/voltage source (Keithley SMU 2400). Apart from this difference in excitation, the EL experiment was carried out using the same setup used for PL, as shown in Figure 3.1.

3.4 Transient Methods

Transient photoluminescence TPL and transient photovoltage TPV measurements are used to monitor charge-carrier dynamics and analyze recombination losses, as theoretically discussed in section 2.5. Both methods measure the transient response to a short laser-pulse excitation. Transient photoluminescence measurements detect the PL emission, whereas transient photovoltage measurements track the external voltage decay. A special feature of this thesis is that the TPL and TPV measurements were performed simultaneously on the same integrated setup. This configuration opens the opportunity to compare both outputs directly. Figure 3.2 shows a simplified schematic of this setup for TPL (red) and TPV (blue). The next two sections introduce the basic measurement principles in more detail, describe the setup and discuss the details of data analysis.

3.4.1 Time-resolved Photoluminescence

Transient photoluminescence detects the emitted PL $\phi_{\mathrm{PL}} \propto np$ created by radiative recombination in the absorber material as a function of the delay time after a short laser pulse. Usually, TPL is performed as a large-signal method. In addition, the sample is in equilibrium before photoexcitation. Given that radiative recombination originates from the perovskite layer itself, this measurement provides an internal measure of recombination kinetics in the perovskite. The excess-charge carriers generated by the laser-pulse absorption cannot leave the sample and must recombine

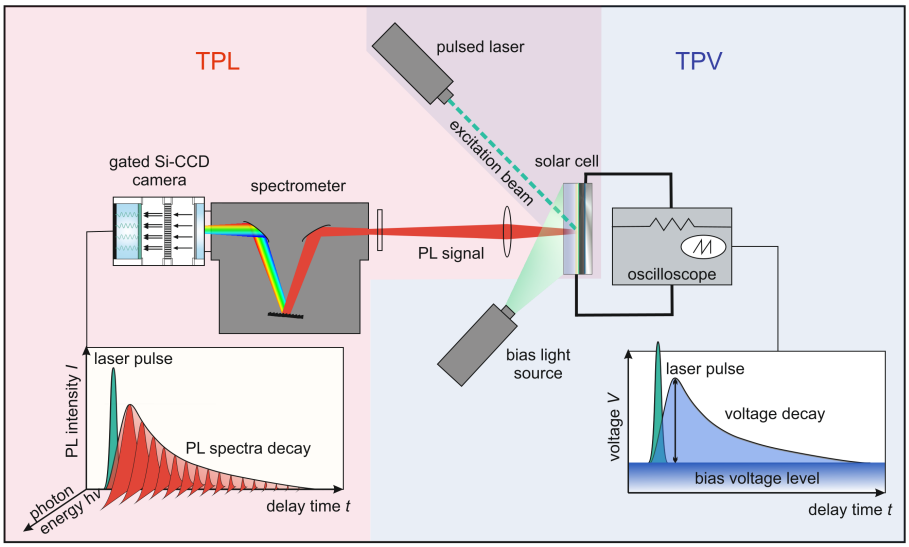

Abbildung 3.2: Schematic of the transient photoluminescence TPL (red) and transient photovoltage TPV (blue) setups.

at some point. Since TPL is a purely optical technique, no electrical connection is necessary. Therefore, it can be applied to any sample type, from pure films on glass to complete solar cell devices. Nevertheless, TPL is mainly measured on pure films because interpreting data from multilayer samples is challenging. A superposition of various effects occurs in complex multilayer stacks, which modulates the charge-carrier concentration in the perovskite layer and hence the measured PL. Chapter 7 deals with this topic. However, TPL measured on thin perovskite films on glass is a frequently used method to derive the key recombination rate constants of trap-assisted, SRH, bimolecular, and Auger recombination in the bulk material, [125] as derived in section 2.5.5. Note that this technique is also widely used in other solar cell technologies. [136–138]

For transient photoluminescence measurements, the samples are excited with a pulsed UV-solid-state laser, which serves as a pump laser for a dye laser. Usual-

ly, the pulse-repetition rate is set to 100 Hz. The pumped dye (Coumarin) emits down-converted, pulsed laser radiation of 498 nm. A pump system enables the continuous exchange of the dye in the laser cavity with a larger reservoir, decelerating the degradation of Coumarin. The laser radiation passes through an optical fiber. It impinges at an angle of 30°on the sample surface and illuminates an elliptically shaped spot with diagonal dimensions of 0.326 mm and 0.345 mm (0.353 mm^2). This spot size was chosen to illuminate a large part of the solar-cell area, thus minimizing lateral effects while ensuring that nearly all the laser power falls on the solar cell. The emitted photoluminescence is focused and coupled into a spectrometer (sPEX 270M from Horiba Jobin Yvon). An edge filter placed in front of the entrance slit of the spectrometer suppresses the pass-through of scattered laser light. In the spectrometer, the PL beam is diffracted by the grating unit (150 lines/mm, 500 nm blaze) and spectrally dispersed. Then, an intensified, gated CCD camera (iStar DH720 from Andor Solis) detects the spectrally resolved signal. This signal is first converted into an electrical signal by a (Multi Alkali) photocathode and amplified by a microchannel plate microchannel plate (MCP). After that, a phosphor (P43) screen back-converts the signal. Finally, the light is detected with a CCD chip consisting of an array of 1024×256 pixels. In order to perform time-resolved measurements, the inherent shutter-gate functionality of the camera is exploited by reverse poling of the voltages between the photocathode and MCP. A partial signal of the laser pulse triggers the gating times. Moreover, this technique uses different delay times between the trigger signal and the actual opening of the gate. In this way, we obtain a PL spectrum for different delay times after the initial laser pulse. In addition, the voltage applied across the microchannel plate, which is responsible for the acceleration of the photoelectrons and their multiplication, controls the amplification of the PL signal. This MPC gain, as well as the shutter-gate width, integration time and number of accumulations can be adjusted to maximize the intensity of the signal to use the detector optimally. Typically, the gate pulse width is kept constant at 2 ns and the intensity adjustment is implemented by changing the other parameters. The applied laser fluence is manually adjustable via neutral density (ND) filters with a maximum laser fluence of $\approx 800 nJ/cm^2$. The transient PL decay results from integrating the background-subtracted PL spectrum at each delay time over the energy region where the PL peaks are positioned. Finally, the TPL decay is normalized.

To increase the dynamic range of this method, I developed a routine in which

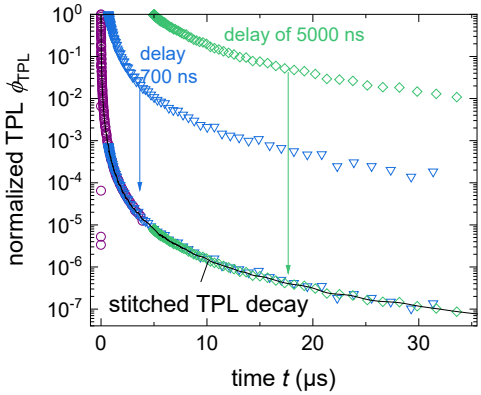

Abbildung 3.3: Illustration of the stitching routine used to increase the dynamic range of the TPL decay. TPV (blue) setups.

several measurements starting at different delay times after laser-pulse excitation are stitched together. Figure 3.3 illustrates this principle, where three different measurements with delay times of 0 ns, 700 ns and 5 s, as well as the resulting stitched data set are shown. Conducting additional measurements at later delay times (blue and green) allows me to adjust the measurement parameters like the MPC gain or camera-integration time, which goes along with a higher signal-to-noise ratio. The first measurement (purple), starting just before the laser pulse, is relatively fast and usually takes only a few minutes. Those at higher delay times between the trigger signal and the actual opening of the gate require a higher integration time to obtain a good signal because many of the generated charge carriers have already recombined. Therefore, I usually repeated the first measurement at the end to ensure that the decay did not change significantly .

In section 2.5.4, I introduced the representation of the TPL decay time τ_{TPL} as a function of the quasi-Fermi-level splitting ΔE_{F}. The proportionality between the PL intensity and quasi-Fermi-level splitting, given by $\phi_{\mathrm{PL}} \propto \exp(\Delta E_{\mathrm{F}}/(k_{\mathrm{B}}T))$, is exploited to calculate this x-axis. This proportionality implies that any order of magnitude decrease of the TPL decay corresponds to a relative change in the quasi-Fermi-level splitting of ≈ 60 meV. The initial excess-charge carrier density is required to provide the initial value of the Fermi-level splitting. To estimate the

latter, I measured the absorbed laser fluence and calculated the number of absorbed photons per laser pulse. The density can also be determined if the sample thickness is also known. In summary, the energy axis of ΔE_F for the experimental data is determined from knowledge of the laser-excitation fluences used in the measurement, providing the initial ΔE_F at time zero after the pulse. Furthermore, the dependency that the PL intensity scales with $\exp(\Delta E_\mathrm{F}/k_\mathrm{B}T)$ is used to calibrate the x-axis. [35] Alternatively, one could omit the absolute calibration of the x-axis and plot the decay time as a function of $\ln(\phi_\mathrm{PL})$, thereby leading to the same curve progression.

While taking the derivative defined by Equation 2.48 is a simple task for smooth, simulated data, extracting meaningful derivatives from noisy experimental data is quite challenging. Therefore, it is advisable to not or not only take the derivative of the background-corrected raw data but first fit the TPL decay with a function and then differentiate the fit. Additionally, I recommend smoothing the raw data. Smoothing enhances the quality of the calculated decay time, as shown by the comparison of (a-c) unsmoothed and (d-f) smoothed data in Figure 3.4. Note that given the multitude of non-exponential features affecting the transients, I opted to identify functions for which the fit algorithm converges quickly and leads to a good agreement with the experimental transients, even though the functional form of the fit functions bears no physical meaning. I observed that good candidates for fit functions are high-order polynomials that can be fitted to the logarithm of the PL. Alternatives are rational functions, i.e., ratios of higher-order polynomials. Thus, Figure 7.13 shows symbols and lines, where the symbols represent the background-corrected, stitched raw data. In contrast, the lines are fits to the experimental data. Both results agree within the accuracy of the method.

Note that a transient photoluminescence signal, which I detected in this thesis via an intensified, gated CCD camera with an inherent shutter-gate functionality, can also be recorded in another way. This second, frequently-used technique to detect the time-resolved PL signal is time-correlated single-photon counting (TCSPC), which uses a single-photon sensitive detector, e.g., a photomultiplier tube (PMT), combined with time-measuring electronics. The detection unit measures the time which passes in between the laser-pulse excitation and the first photon being emitted and recorded. Besides the measurement principle, these two TPL recording techniques differ in particular in their laser-pulse repetition rate. For a good signal-to-noise ra-

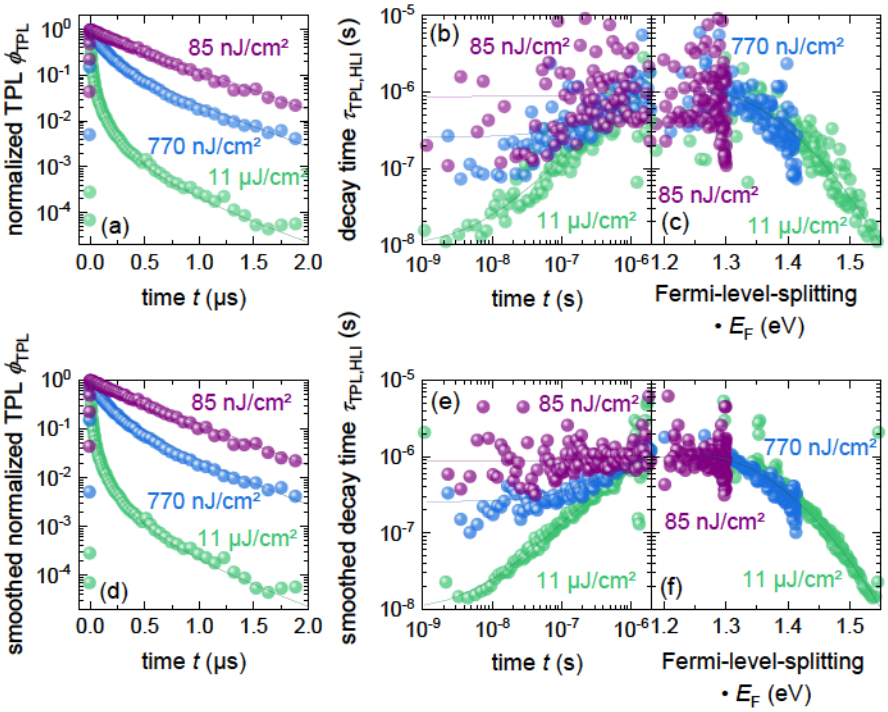

Abbildung 3.4: In order to reduce the noise in the derivatives of the raw transients, I decided to preprocess the data. First, I smooth the TPL raw data and then perform the derivative to calculate the decay time of the experimental data. A comparison is shown here, where (a-c) shows a version without smoothing, whereas in (d-f), the experimental TPL data is smoothed before calculating the decay time. Raw data is taken from ref. [109].

tio, TCSPC requires very high repetition rates between kHz and MHz. In contrast, the intensified, gated CCD-camera technique and typical repetition rates for TPV are only up to several hundred Hertz.

3.4.2 Transient Photovoltage

Transient photovoltage (TPV) is an external, electrical technique that requires contacts and that can only be applied to complete solar-cell devices. Furthermore, TPV is a small-signal method in which the solar cell is kept excited at open-circuit condition by permanent illumination with bias light even before the laser-pulse excitation.

For this purpose, I installed a steady-state laser with a wavelength of 532 nm at the setup, whose scattered light is blocked by the filter at the spectrometer entrance. This configuration also makes it possible to perform TPL measurements with bias-light excitation. The TPL and TPV were measured at one setup illustrated in Figure 3.1, using the same laser described in the previous section as the pulsed excitation source. An additional weak laser pulse is used in TPV to generate a small amount of additional excess-charge carriers, inducing a transient change in open-circuit voltage. The sample is electrically connected to an oscilloscope whose input impedance must be very high ($\approx M\Omega$) to ensure that the device is held at open-circuit. This oscilloscope records the photovoltage decay. The TPV method requires different bias-light intensities to obtain information at different injection levels. This light intensity often varies over orders of magnitude so that many different operating points with different levels of open-circuit voltage can be investigated. Figure 3.5a shows a series of photovoltage decays at different illumination intensities, which provides an overview of how the shape of the decay changes depending on the bias level. Here, it becomes apparent that the decay time increases with reduced bias-light intensity. The photovoltage transient due to the small laser perturbation is fitted to the slowest decay component using a monoexponential decay. With this approach, we obtain the small perturbation decay time constant $\tau_{\mathrm{TPV}}^{\mathrm{SS}}$, i.e.

$$\Delta V_{\mathrm{oc}}(t) = \Delta V_{\mathrm{oc,max}} \exp\left(-\frac{t}{\tau_{\mathrm{TPV}}^{\mathrm{SS}}}\right) , \tag{3.8}$$

where $\Delta V_{\mathrm{oc,max}}$ is the maximum excess open-circuit voltage. [139] Instead of fitting the decay with Equation 3.8, one can also calculate $\tau_{\mathrm{TPV}}^{\mathrm{SS}}$ from the derivative

$$\tau_{\mathrm{TPV}}^{\mathrm{SS}} = \frac{dt}{d\ln\left(\Delta V_{\mathrm{oc}}(t)\right)} . \tag{3.9}$$

The different TPV lifetimes obtained at varying bias illuminations are then typically plotted as a function of the open-circuit voltage corresponding to the bias illumination, as displayed in Figure 3.5b.

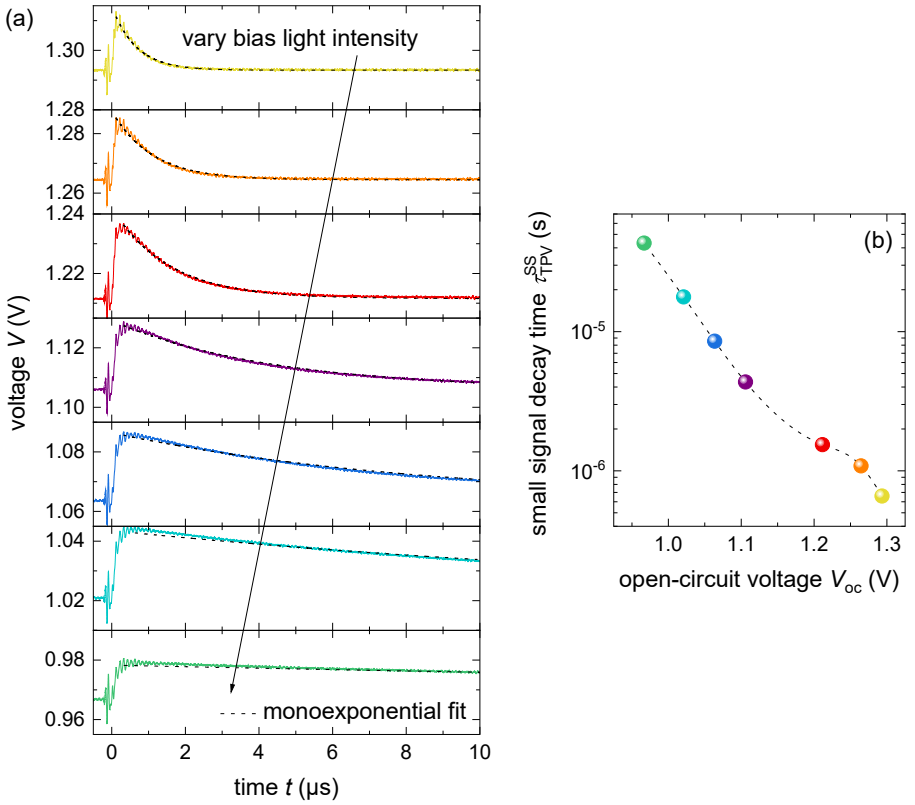

Abbildung 3.5: Exemplary measurement of transient photovoltage TPV and its analysis. TPV is a small-signal method that is performed at open circuit for different steady-state bias illumination intensities. An additional weak laser pulse creates a small perturbation and generates a small amount of extra excess-charge carriers, inducing an additional open-circuit voltage. Then, the corresponding photovoltage decay is measured and fitted with a monoexponential decay (dotted lines) to obtain the small perturbation lifetime associated with the steady-state V_{oc}. The time constants from the monoexponential fits are summarized in (b) for the different open-circuit voltages.

4 MAPI Solar Cells with High Open-Circuit Voltages

In this chapter, I present inverted, planar MAPI solar cells with open-circuit voltages exceeding $\sim 1.26\,\mathrm{V}$*, which were fabricated using a combination of dry lead acetate (*$\mathrm{Pb(CH_3COO)_2}$*) and lead chloride (*$PbCl_2$*) precursors leading to smooth films and large grain sizes. Surface recombination was suppressed by carefully optimizing the PTAA hole transport and PCBM electron-transport layers. Suppression of bulk and surface recombination was verified by measurements of absolute photoluminescence with external quantum efficiencies* $\sim 5\%$ *in complete cells, which was the highest reported value at that time (2018). In addition, the transient photoluminescence decays in full solar cells and layer stacks involving one or two contact layers are exceptionally long. This chapter is based on a joint first-author publication with Dr. Zhifa Liu. He was primarily responsible for the device fabrication and I was responsible for the characterization. [140] The fabrication routine and measured device characteristics of this sample type are discussed in the following. In the further course of this thesis, I repeatedly refer to this sample type as a basis to improve the understanding of device physics and characterization techniques.*

4.1 Introduction

One of the main reasons why metal-halide perovskites have attracted so much interest over the past years is their exceptional optoelectronic quality for a solution-processed, polycrystalline semiconductor, providing a bulk material that has the potential to approach the radiative limit of the open-circuit voltage by minimizing non-radiative recombination processes. Braly et al. have shown that a quasi-Fermi

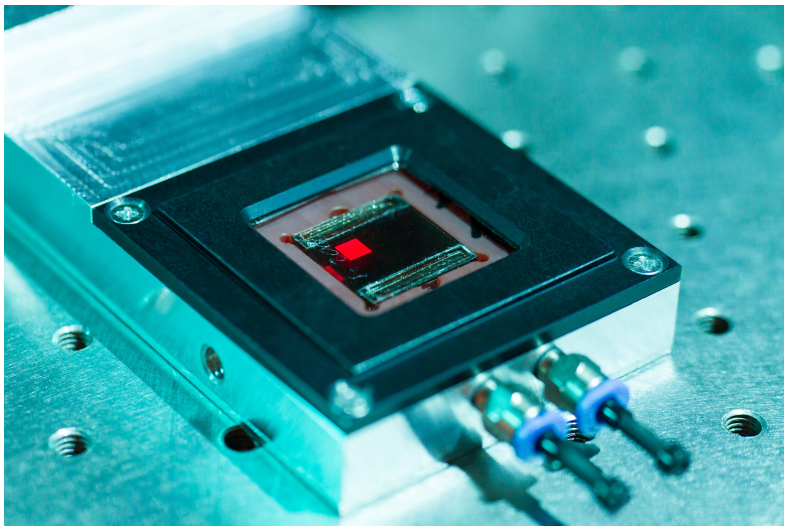

Abbildung 4.1: Photo, showing the bright electroluminescence of a MAPI-solar cell with an outstanding open-circuit voltage of 1.26 V. The V_{oc} correlates directly with the external luminescence-quantum efficiency Q_e^{lum}. Thus, a solar cell with low non-radiative recombination losses is also a good LED. Copyright Daniel Weigand.

level splitting corresponding to an internal open-circuit voltage of 1.28 V is possible in MAPI films on glass, proving that the bulk material has the potential to come within ~ 40 mV of its thermodynamic limit. [130] However, the presence of contacts typically limits the achievable open-circuit voltage V_{oc} in a complete device and introduces additional recombination paths. Note that from the beginning of their development, perovskite solar cells have demonstrated astonishingly high open-circuit voltages in relation to their band-gap energy. Already the first paper on $CH_3NH_3PbI_3$ (MAPI) based solar cells with $> 10\,\%$ efficiency, showed an open-circuit voltage $V_{oc} \approx 1.1$ V. [70] This behavior is atypical since other technologies, such as silicon solar cells, often require substantial technological efforts to suppress non-radiative recombination processes. [141] In contrast, perovskite solar cells can often generate considerable open-circuit voltages with little effort. Nevertheless, the manufacturing routine and the combination of materials in the solar cell stack significantly impact the amount of non-radiative losses. Any progress towards lower non-radiative recombination losses requires careful control of all non-radiative recombination pathways in the bulk and at the interfaces towards the electron- and

hole-extracting layers. Well-passivated grain boundaries and surfaces are needed, as well as the right choice of charge-transfer layer (CTL) for a good energy-level alignment.

Figure 4.2 shows an overview of the open-circuit voltage of lead-halide perovskite solar cells for varying chemical compositions as a function of band gap energy E_g^{ip} calculated for various publications. The surface-color plot represents the external quantum efficiency with isolines $10^{-6} - 1$ highlighted as black lines. This overview is certainly a non-exhaustive representation of the literature. However, I took care to include the results, which reported particularly high open-circuit voltages relative to their band gaps. The graphic also includes records that were published after this study in 2018. Additional information is summarized in Table A.1. The inverted, planar MAPI solar cell presented here has a radiative open-circuit voltage $V_{oc}^{rad} = 1.324\,V$

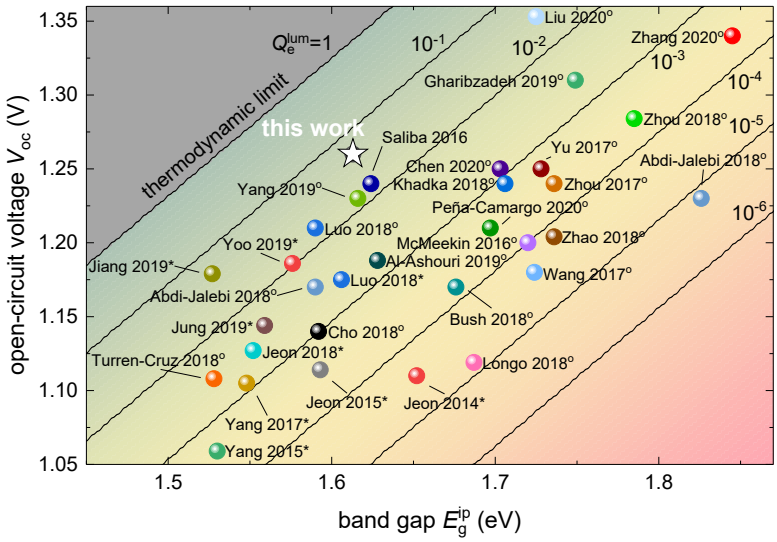

Abbildung 4.2: Overview of the open-circuit voltage of lead halide perovskite solar cells as a function of band gap energy E_g^{ip}, comparing current state in literature to the V_{oc} presented in this thesis. This comparison demonstrates the outstanding record value we have achieved through device optimization. This V_{oc} is substantially higher than the highest reported in 2018. Since then, further progress has led to continuous improvements and a further reduction of recombination losses. The surface plot and the black lines illustrate the limit for different external quantum efficiencies $10^{-6} - 1$ calculated with a step-function like absorptance.

and a band gap of 1.61 eV. Comparing this radiative open-circuit voltage with the actual open-circuit voltage of 1.26 V obtained in this study gives a value of 64 mV for the voltage loss due to non-radiative recombination. This voltage loss corresponds to an external luminescence-quantum efficiency of 8.4 %. Figure 4.2 puts this result in context. At the time Dr. Zhifa Liu developed the perovskite solar cells presented here, the highest external luminescence-quantum efficiency $Q_{\mathrm{e}}^{\mathrm{lum}}$ at injection conditions corresponding to one sun was $Q_{\mathrm{e}}^{\mathrm{lum}} \sim 1\,\%$ corresponding to voltage losses of about $\Delta V_{\mathrm{oc}}^{\mathrm{nrad}} \approx k_{\mathrm{B}}T/q \times \ln(100) \approx 120\,\mathrm{mV}$. Respective results were obtained for a Rb-containing perovskite solar cell with a band gap slightly above 1.6 eV. [142] However, one has to keep in mind that a quantum yield of 1 % means that 99 % of the electron-hole pairs recombine eventually non-radiatively, converting their energy into heat in the device and thereby leaving much room for improvement. The present work shows that this level can be substantially overcome in working devices of pure MAPI with $PbCl_2$ being used during fabrication without including molecules and elements such as K, [143] Rb, [142] or Cs, [101] that have previously been used to achieve the highest open-circuit voltages.

4.2 Solar Cell Device Stack

The perovskite absorber of the inverted, planar MAPI solar cells was fabricated from a mixture of $Pb(CH_3COO)_2$ (90 mol%) and $PbCl_2$ (10 mol%) that incorporate no other cations or anions in the crystal lattice. The organic charge-extraction layers poly(triaryl amine) (PTAA) was used for the hole extraction and [6,6]-phenyl-C_{61}-butyric acid methyl ester (PCBM) for the electron extraction. High open-circuit voltages around 1.26 V were achieved by small processing improvements, which substantially suppress recombination at interfaces and in bulk, presented in detail in section 4.7. Figure 4.3 shows (a) a schematic and (b) a cross-sectional scanning electron microscopy (SEM) image of the complete solar cell stack as used in this study, featuring ITO ($\sim 150\,\mathrm{nm}$) as the transparent conductive oxide, PTAA ($\sim 12-30\,\mathrm{nm}$) as the hole conductor, MAPI ($\sim 280-510\,\mathrm{nm}$) as the absorber, PCBM ($\sim 45\,\mathrm{nm}$) as the electron-transport material as well as bathocuproine (BCP) ($\sim 8\,\mathrm{nm}$) and Ag (80 nm) finishing up the cathode.

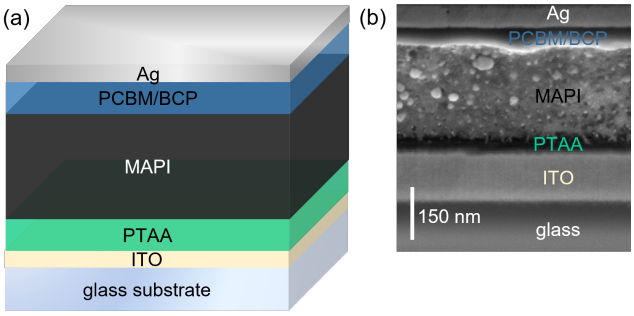

Abbildung 4.3: (a) Schematic drawing of the layer stack used in this study combined with (b) an SEM cross-section of a solar cell. [144]

4.3 Current-Voltage Characteristics

Figure 4.4a shows the current-density voltage ($JV-$) curve of a typical device optimized for high open-circuit voltages (blue line, device A) and a device further optimized for efficiency (red line, device B). All measurements were recorded at a scan speed of 100 mV/s with a class AAA solar simulator under forward (dashed line) and reverse (solid line) scan conditions. The efficiencies are around 18 % (device A) and 20 % (device B), but the most remarkable feature is in both cases the high open-circuit voltage $V_{\mathrm{oc}} \sim 1.26\,\mathrm{V}$. Figure 4.4b shows the efficiency and Figure 4.4c the open-circuit voltage measured as a function of time under white light provided by a LED adjusted to one sun conditions. These trackings confirm that the open-circuit voltage stabilizes above 1.26 V at an efficiency of $\sim 18\,\%$ and $\sim 20.2\,\%$, respectively. This high V_{oc} value is reproducible for a series of different devices fabricated using the recipe of device A, as illustrated by the histogram in Figure 4.4d. Furthermore, Figure 4.4f shows the photovoltaic external-quantum efficiency $Q_{\mathrm{e}}^{\mathrm{EQE}}$ of the same solar cells as a function of photon energy E providing further evidence for the measured short-circuit current density. Furthermore, comparing the two $Q_{\mathrm{e}}^{\mathrm{EQE}}$'s highlights the key differences between the two device preparation processes. Here, the integrated short-circuit density from $Q_{\mathrm{e}}^{\mathrm{EQE}}$ results in $18.2\,\mathrm{mA/cm^2}$ for device A and $20.2\,\mathrm{mA/cm^2}$ for device B. The absorber thickness of device A (blue curve) is around $\sim 280\,\mathrm{nm}$ implying that the quantum efficiency at the band gap is not perfectly sharp due to the kink in the absorption coefficient of MAPI. This feature

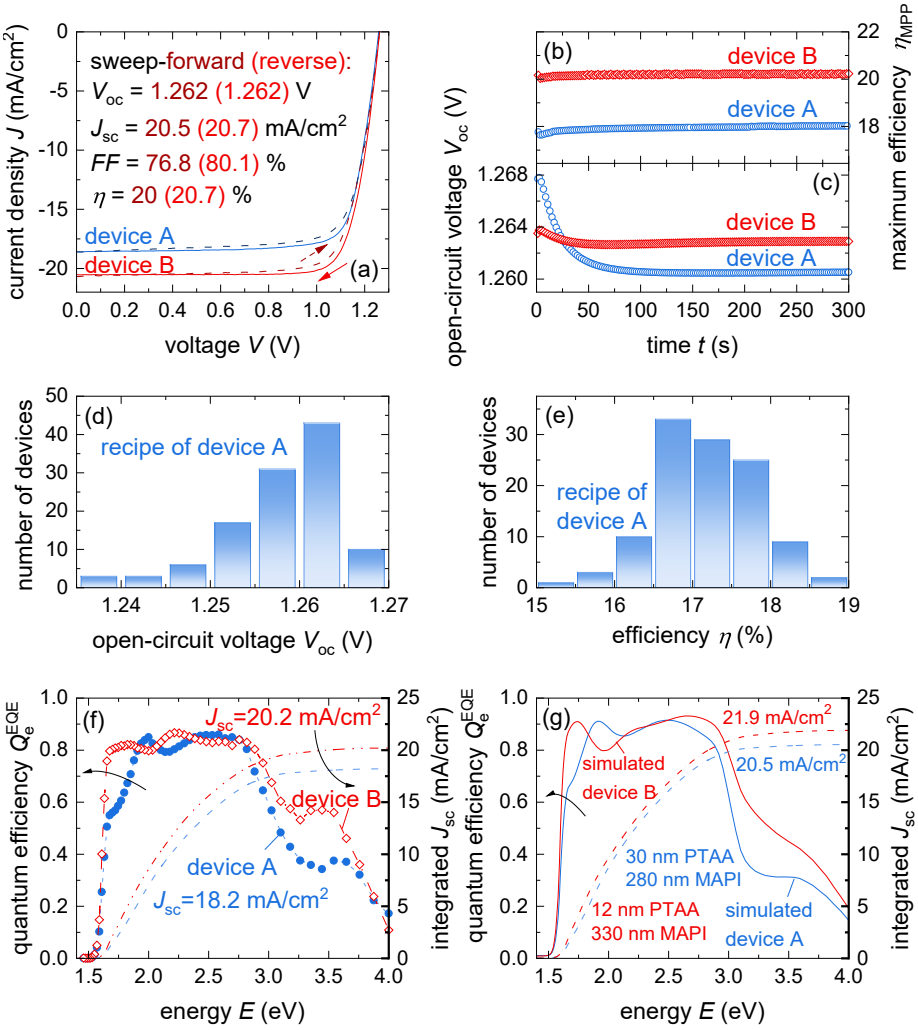

Abbildung 4.4: (a) Current density J as a function of voltage V measured under a class AAA solar simulator for two representative MAPI solar cells in this study. The scan speed of the measurement was set to 100 mV/s/. Device A (blue) was optimized for a high open-circuit voltage. In contrast, device B (red) was also optimized for efficiency by increasing the thickness of the absorber layer and making the PTAA layer thinner. (b) Tracking of the open-circuit voltage V_{oc} and (c) energy-conversion efficiency (η) for 300 s, measured with a white LED. The tracking results in a stabilized value > 1.26 V and around 18% (device A) and 20.2% (device B).(d-e) Histogram of the open-circuit voltage and efficiency for the number of devices using the recipe of device A. Figure panel (f) shows the measured Q_e^{EQE}, whereas Figure (g) the simulated quantum efficiency Q_e^{EQE} as a function of photon energy E. Moreover, the accumulated short-circuit current densities J_{sc} of the cells are added to the plots.

reveals that the perovskite layer is too thin to reach full absorption and partially transmits the incoming light. In addition, substantial losses in the blue spectral region can be partly associated with the $\sim 30\,\mathrm{nm}$ thick PTAA layer, which strongly absorbs in the UV-light range. Thus, we reduced the PTAA layer thickness for process B (red curve) to $\sim 12\,\mathrm{nm}$ in order to diminish resistive losses and parasitic absorption. The increased external quantum efficiency at energies $\sim 3.5\,\mathrm{eV}$ shows the successful reduction in parasitic absorption. Moreover, a slight increase in perovskite-layer thickness up to $\sim 330\,\mathrm{nm}$ increases the sharpness of the absorption onset of process B vs. process A. The formation of a thicker layer is enabled by using a more highly concentrated solution ($\sim 0.67\,\mathrm{M}$) combined with the addition of dimethylsulfoxid (DMSO) to the precursor solution to maintain a good quality of the film. The solvent additive DMSO in the $\mathrm{MAI-PbI_2-DMSO}$ phase retards the rapid reaction between lead iodide ($\mathrm{PbI_2}$) and MAI during evaporation of the solvent in the spin-coating process [99] and slows down crystallization speed. Note that just increasing the concentration of the precursor solution not only increases the layer thickness but changes the crystal growth, too. Thus, this spin-coating process forms very rough layers. To counteract the formation of pinholes in the perovskite layer, which results from the poorer wetting of the PTAA surface for a DMSO-doped perovskite solution, and to further improve grain sizes, the solution was heated to 75°C before spin-coating. [145] For more details regarding the fabrication routine and the device optimization process, I refer to section 4.7.

In addition, I performed electrical drift-diffusion simulations to demonstrate the impact of a thinner PTAA layer and estimate the achievable short-circuit current for the two device types by considering only optical losses and assuming ideal electronic properties. Figure 4.4g presents the respective simulations of the $Q_\mathrm{e}^\mathrm{EQE}$ conducted with the software Advanced Semiconductor Analysis (ASA). [146] ASA calculates the optical generation rate at every position in the active layer via the transfer matrix model using the optical data measured for MAPI and the contact layers. In addition to the optical simulation, I performed an electrical simulation using sufficiently high values for the charge-carrier mobility and low enough recombination coefficients to ensure that no recombination losses occur at short circuit. A comparison of Figure 4.4d and (e) highlights that the experimentally measured and simulated external-quantum efficiencies exhibit similar spectral dependencies. Thus,

the simulation reproduces the experimental features of the Q_e^{EQE} measurements, while the absolute values of the simulated external quantum efficiencies are higher. The integrated short-circuit current densities differ by $\sim 2\,mA/cm^2$, suggesting that this difference in short-circuit current is induced by collection losses rather than optical losses. The loss analysis depicted in Figure 4.5 compares the JV- and efficiency performance of device B to the three different cases. In this representation, the losses in fill factor, open-circuit voltage and short-circuit current are omitted one after the other. Additionally, Figure 4.5c visualizes the share of losses as a bar chart for the different figures of merit, introduced in section 2.3.1. Device B achieves $\sim 68\,\%$ of the theoretical efficiency limit resulting from the SQ model. Here it is clearly stated that the losses in the open-circuit voltage only make up a comparatively small proportion in this cell type, whereas losses in the short-circuit current density represent the lion's share.

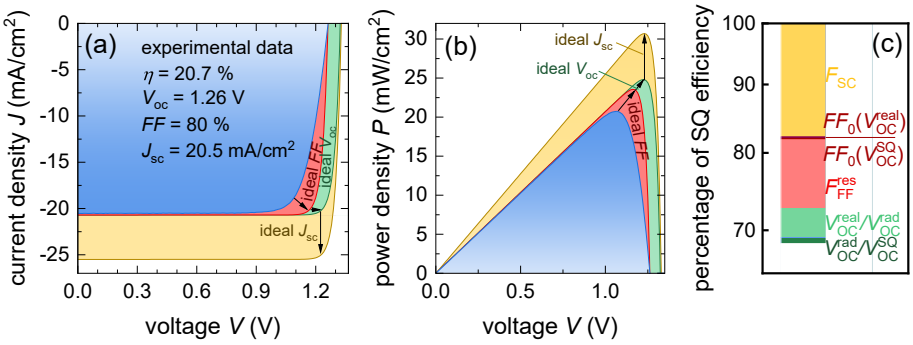

Abbildung 4.5: Analysis of losses and visualization of potential improvement of the MAPI solar cell device. (a) Current-voltage curves and (b) power density P of the real solar cell device (blue) compared to the ideal solar cell in different steps of ideality, ideal fill factor (red), Shockley-Queisser V_{oc} (green) and complete SQ model (yellow). (c) Percentage of Shockley-Queisser efficiency in current loss, fill factor losses and radiative and non-radiative voltage loss.

4.4 Photoluminescence Quantum Yield

As has recently been shown by Stolterfoht et al. [135, 147] in a similar device stack, interface recombination between the perovskite-absorber layer and the electron- and hole-transport layers [6,6]-phenyl-C_{61}-butyric acid methyl ester (PCBM) and PTAA

is a critical factor in achieving the highest possible open-circuit voltages. In order to study interfacial recombination, I use steady-state and transient photoluminescence on different sample configurations. I analyze completed solar cells and different layer stacks with only one contact layer (PTAA) or with both contact layers (PTAA and PCBM) but without metal back contact. Additionally, I show the steady state PL of a MAPI layer grown on PTAA, being passivated with n-trioctylphosphine oxide (n-trioctylphosphine oxide (TOPO)), which allows me to evaluate the quality of the perovskite itself, as well as its interface to PTAA and the uncovered surface. The results of the steady-state measurements are presented in this section, while the subsequent one presents those of the transient method. Figure 4.6a-c summarise the results from the steady-state PL measurement conducted in Jülich with the setup described in section 3.3.1. Furthermore, Figure 4.6e-h serves as independent confirmation of my results, being recorded with a calibrated hyperspectral imaging setup at the Helmholtz-Zentrum Berlin with the help of Dr. José A. Márquez.

In Figure 4.6a, the reader finds a comparison of the calculated implied open-circuit voltage at one sun condition for the different sample stacks. Untypically, all implied V_{oc} values are very close to each other, implying that the additional PCBM interface does not introduce significant recombination paths. This trend is also evident for the steady-state photoluminescence signal as a function of the laser power used for the sample excitation for the four investigated stacks. These four cases are a passivated perovskite, perovskite with hole contact only, as well as with both interlayer materials and a complete solar cell. While the left y-axis of Figure 4.6b shows the photoluminescence counts in arbitrary units, the right y-axis shows the quasi-Fermi level splitting that corresponds to the photoluminescence counts on the y-axis using the luminescence of the solar cell at one sun to calibrate the quasi-Fermi level axis as described in section 3.3.1. Note, that any difference in PL intensity of a factor of 10 corresponds to $k_{\mathrm{B}}T\ln 10 \approx 60\,\mathrm{meV}$ change in quasi-Fermi level splitting ΔE_{F}. I find that the TOPO-passivated sample (grey) has the highest quantum efficiency and a Fermi-energy splitting of $\sim 1.27\,\mathrm{eV}$ at $\sim 1\,\mathrm{sun}$. This value is comparable to the $\sim 1.28\,\mathrm{eV}$ previously reported by Braly et al. [130] for a TOPO passivated film on glass. However, as an electrically insulating interface minimizing recombination, TOPO does not meet the key requirement for a functional solar cell with reasonably low resistive losses. Nevertheless, using TOPO as

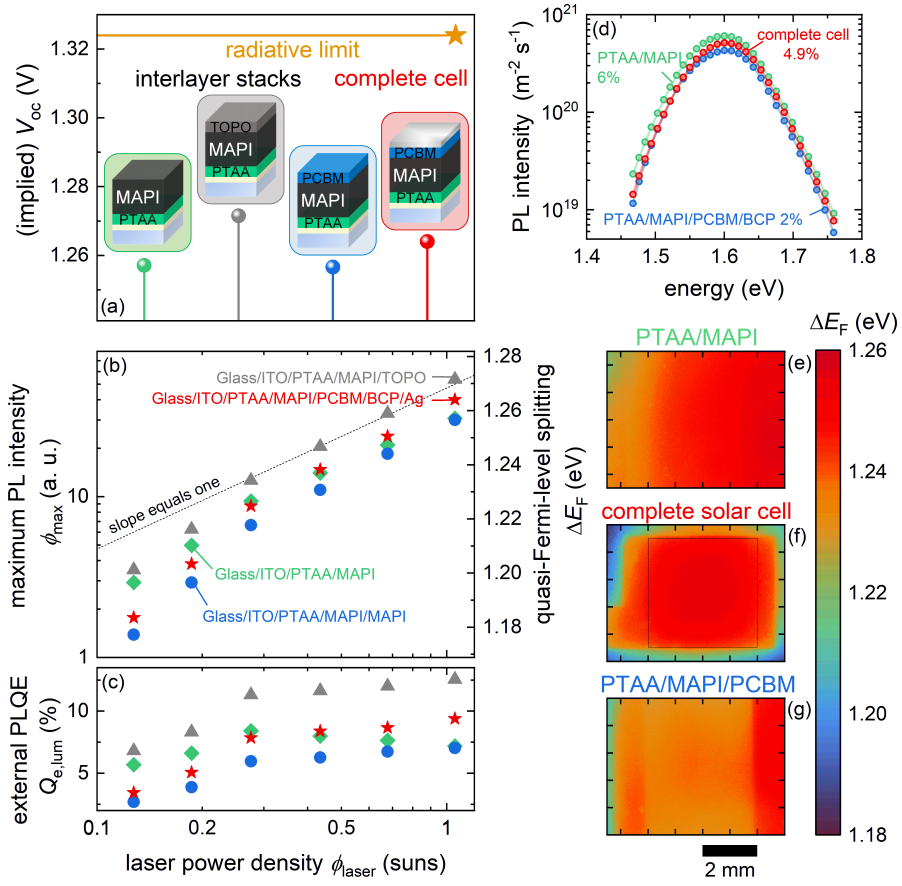

Abbildung 4.6: (a-c) Results obtained from steady-state PL measurements on different interlayer stacks measured in Jülich with the setup described in section 3.3.1. (a) Implied open-circuit voltage of the four different layer stacks compared to the radiative limit at one-sun illumination. (b) Maximum of the PL intensity peak, converted into the quasi-Fermi level splitting ΔE_F and (c) the external photoluminescence-quantum yield (PLQY) Q_e^{lum} as a function of laser excitation. (d-g) Additionally, intensity-calibrated PL measurements and PL-images were measured at the Helmholtz-Zentrum Berlin with Dr. José A. Márquez to provide independent confirmation of the internal quasi-Fermi level splitting.

a passivation experiment [78] demonstrates that the perovskite bulk material used in this study, stands out by its high optoelectronic quality and exhibits very low non-radiative recombination. When comparing the passivated sample to the other samples, it stands out that the quasi-Fermi level splitting in the solar cell (red)

and in the other layer stacks is only about $\sim 10-20\,\mathrm{meV}$ smaller. This very small difference demonstrates how well the interlayers in these samples are adapted and suggests that there are only minor non-radiative losses due to surface recombination. Note that the solar cell even has a slightly higher quasi-Fermi level splitting than their two respective layer stacks without metal. This apparent superiority of the device relative to the other two samples may at first seem surprising since in previous publications, [135,143,147,148] the addition of contacts always led to reduced luminescence and quasi-Fermi level splitting. This is no longer the case in the MAPI samples presented here, at least if the detectable luminescence emitted through the front surface is compared. This observation may be because photon recycling has to be a substantial factor in devices being that close to the radiative limit. Thus, the presence of a back reflector, which increases the reabsorption of light relative to outcoupling towards the back, may increase the concentration of charge carriers in the device and the detectable luminescence.

The high quasi-Fermi level splitting is linked to a high external luminescence quantum efficiency $Q_\mathrm{e}^\mathrm{lum}$ via Equation 3.5, being depicted in Figure 4.6c. The external luminescence-quantum efficiency decreases for lower excitation densities in all four sample types. With this, I obtain values between $\sim 3-8.4\,\%$ for the solar cell device and the $Q_\mathrm{e}^\mathrm{lum}$s of the interlayer stacks in the same range. The PL images of the layer systems measured on a hyperspectral absolute photoluminescence imaging setup, being calibrated to provide absolute quantum yields, provide independent validation and additional evidence of these high external luminescence-quantum yields or high quasi-Fermi level splittings. Figure 4.6d displays exemplary PL spectra, while Figures 4.6e-g map the quasi-Fermi level splitting over a section larger than the cell area. The image section in Figure4.6f shows one solar cell of the four existing on the substrate, marked by the black square. In the case of the layer system without ETL and silver, a contrast between the areas without and with ITO is visible. This calibrated measurement confirms an external luminescence-quantum efficiency of 5 % for the solar cell, which is smaller than the results depicted in Figure 4.6c, but it still represents the highest value reported at that time for a full lead-halide perovskite solar cell device. However, higher external luminescence-quantum efficiencies of up to 15 % have been reported for perovskite light-emitting diodes back then. [149–153] Todays records achieve over 20 %. [154–156]

4.5 Time-Resolved Photoluminescence

Figure 4.7 presents the results that emerge from transient photoluminescence measurements for a sample series. This series consists of one sample with the hole contact only, one with both charge-transfer layers and the full solar cell. Contact layers typically quench the luminescence. This quenching should also be clearly visible in transient photoluminescence experiments, with the expectation being that the transient becomes substantially faster in the presence of contacts. In the past, the longer time-decays of luminescence of samples with at least one electron- or hole-accepting layer have been analyzed and interpreted in terms of surface-recombination velocities. [135, 157, 158] However, in the present case, the contacts do not lead to any substantial quenching of the steady-state luminescence. Thus, it is not surprising to see that also the transients of all three types of samples decay quite slowly after a quick initial decay. Although the transients of the two samples with the additional PCBM interface drop faster, the PL is still measurable for several microseconds.

Plotting the decay time from TPL in low-level injection ($\tau_{\mathrm{TPL,LLI}}$), introduced in Equation 2.48 in section 2.5.4, facilitates the comparison of the recombination dynamics in these three different samples. Figure 4.7b shows the decay time as a function of time t and Figure 4.7c shows the decay time over quasi-Fermi level splitting ΔE_{F}. All decay times $\tau_{\mathrm{TPL,LLI}}$ increase for longer times or lower Fermi-level splittings and saturate for long times in the low s range for all three scenarios. At early times or corresponding high quasi-Fermi level splitting, the decay time is associated with higher-order recombination mechanisms like Auger or radiative recombination. The decay time at longer times or corresponding low Fermi-level splitting may be affected by a combination of non-radiative SRH bulk or interface recombination. Section 2.5.4 in the fundamentals of this thesis provides a detailed introduction. The decay time vs. ΔE_{F} plot reveals that the ITO/PTAA/MAPI transient is dominated by radiative recombination, implying the effective SRH lifetime must be very long. Thus, the bulk lifetime is long and the PTAA/MAPI interface-recombination velocity must be slow. In the samples with PCBM as the second interlayer, SRH recombination seems more prominent, as indicated by the shorter decay time at small Fermi-level splittings. Nevertheless, the decay time values of ~ 2 s are exceptionally high for samples with two charge-extracting layers,

suggesting slow recombination at the PCBM side, too. This observation is consistent with the high external luminescence-quantum efficiencies that also last in the

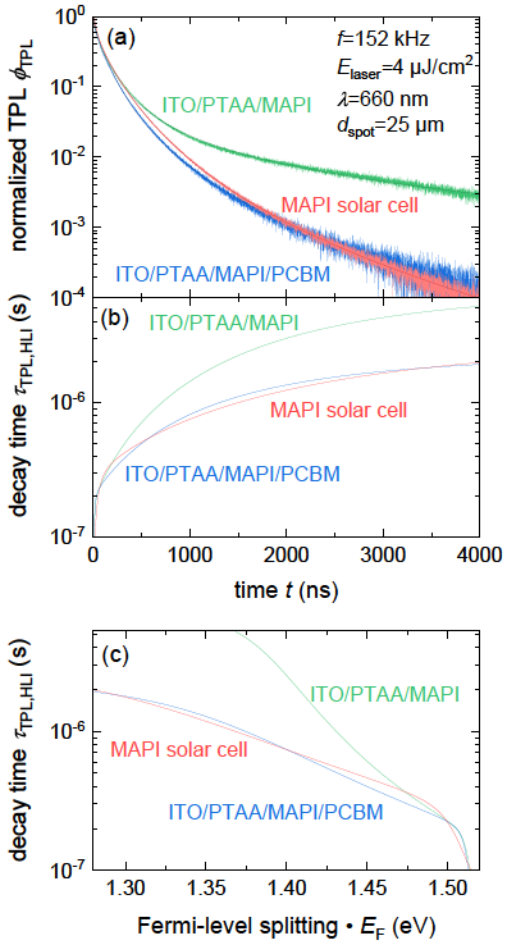

Abbildung 4.7: (a) Transient photoluminescence TPL measurements on different layer stacks, namely the full solar cell (red) and MAPI grown on PTAA without (green) and with PCBM/BCP (blue) as ETL. This data set was measured with a time-correlated single photon counting setup at the Helmholtz-Zentrum Berlin with the help of Dr. Sergiu Levcenko. (b) Differential decay time $\tau_{\mathrm{TPL,HLI}}$ obtained by taking the derivative of the curves in (a) for every time t. To obtain a smoother derivative, the data in (a) was fitted first (thin lines shown in (a)) and then the derivate was computed from the fitted data according to Equation 2.48. (c) Decay time as a function of the quasi-Fermi level splitting.

presence of selective contacts. The quantitative interpretation of PL transients of layer stacks involving charge-extracting layers is complicated by the multitude of competing mechanisms that need to be taken into account. A detailed consideration is the content of the chapter 7.1.

4.6 Photoactivation

In order to reach these high open-circuit voltages, all devices need photoactivation. This action process is achieved by measuring several current-voltage curves for $\sim 10\,\text{min}$ or keeping the device under open-circuit condition by a white light LED. There have been various propositions to explain the improvement of electronic properties by light soaking, such as defect passivation by redistribution of halide ions, [159,160] lattice expansion reducing local strain in the crystal [161] and doping of the fullerene-based electron contact layers. [162] Here, I do not aim to further elucidate the mechanisms for light-induced performance improvements. However, I note that while I observe improvements in V_{oc} similar to the ones presented by Tsai

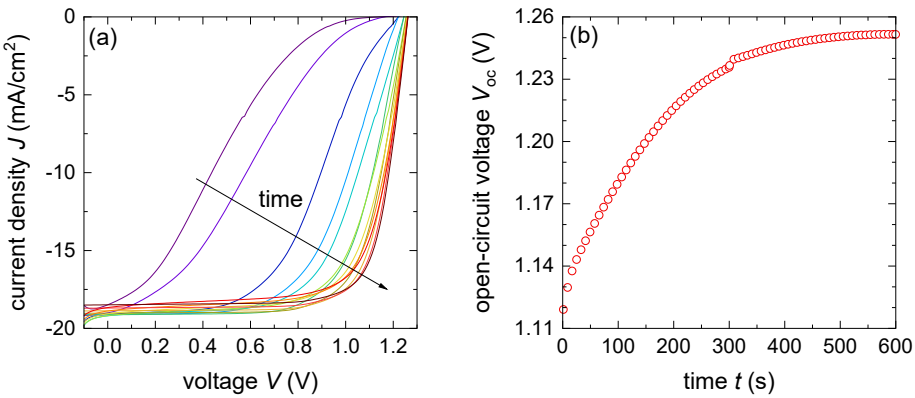

Abbildung 4.8: (a) Exemplary series of $JV-$curves over time showing the change in cell performance during light activation, starting with a fresh solar cell (purple line). Initially, the $JV-$curves are s−shaped and the open-circuit voltage is low. The light activation improves the cell performance and increases the fill factor FF. With this routine, exceptionally high open-circuit voltages are achieved. (b) Example of the light activation process. Tracking of the open-circuit voltage over 10 min of light activation at the LED-solar simulator, showing the continuous increase in V_{oc}.

et al. [161], I do not observe any changes in band gap that were suggested to be a result of photoinduced lattice expansion. [161] In contrast, the observations of defect passivation and reported fullerene doping [159, 160, 162] are fully in agreement with our results of improved fill factor and Voc after light soaking.

4.7 Fabrication via Solution-Processing

This section describes the fabrication routine of the solution-processed, inverted, planar MAPI solar cells with high open-circuit voltages, with the general layout being schematically pictured in Figure 4.9. In addition, Table A.2 in the appendix provides an overview of all relevant recipes in this thesis.

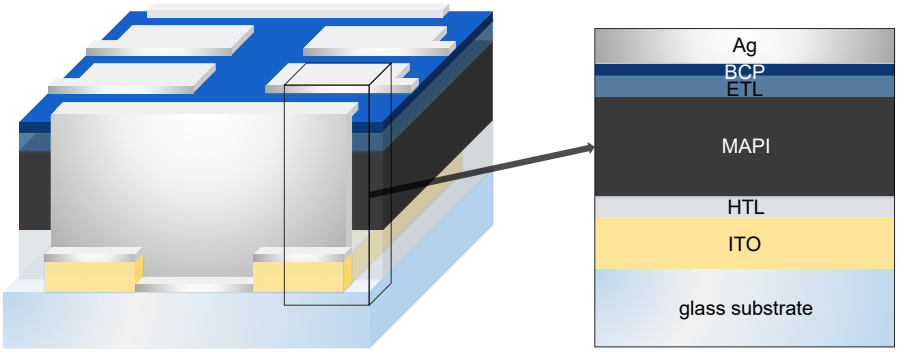

Abbildung 4.9: Schematic of the planar, inverted perovskite solar cell structure. On each glass substrate are four solar cells with a cell area that is defined by the overlap of the ITO stripes and the Ag pads.

4.7.1 Substrate Cleaning

The pre-patterned ITO substrates ($2.0 \times 2.0\,\mathrm{cm}^2$) were ultrasonically cleaned with soap (Hellmanex III), deionized water, acetone and isopropanol (IPA) in succession for 10 min. The as-cleaned ITO substrates were treated with oxygen plasma for 12 min and directly transferred to a nitrogen-filled glovebox for further processing.

4.7.2 Fabrication of the PTAA Layer

The solution-processed solar cells use PTAA as hole-transport layer (HTL). Toluene (T) was used as a solvent to prepare a PTAA solution with a concentration of $3.0\,\mathrm{mgml}^{-1}$ (device A) and $1.5\,\mathrm{mgml}^{-1}$ (device B). The PTAA solution was stirred overnight at room temperature (RT) and was not filtered or heated before use. The first part of Table A.2 in the appendix lists the different PTAA recipes used in this thesis. For the recipes presented in this chapter, 120 l PTAA solution was spin-coated onto the pre-patterned ITO substrates with a two-consecutive step program at 500 rpm for 4 s with a ramping rate of $500\,\mathrm{rpms}^{-1}$, and 4500 rpm for 20 s with a ramping rate of $800\,\mathrm{rpms}^{-1}$. Then the samples were thermally annealed at 110 °C for 10 min. Afterward, the samples were cooled down to room temperature. The PTAA layer thickness is $\sim 30\,\mathrm{nm}$ for the more concentrated solution and $\sim 12\,\mathrm{nm}$ for the less concentrated one.

4.7.3 Fabrication of the MAPI Film

The process to deposit the MAPI layers by spin-coating involved a solution of $Pb(CH_3COO)_2$, $PbCl_2$ and MAI in DMF or DMF/DMSO combined with a very short annealing time of 2 min at 75 °C. Lead-acetate-based precursors have previously been shown to yield smooth, [163], high-quality, pinhole-free layers [164] and were therefore chosen to achieve highest open-circuit voltages. The addition of $PbCl_2$ has been shown to lead to substantially increased photoluminescence lifetimes [165, 166] and increased grain sizes and improved crystallinity due to methylammonium chloride (MACl) in the perovskite precursor solution. [76, 167] Figure 4.10 compares exemplary SEM pictures of MAPI films spin-coated from different precursor solutions. This comparison highlights the grain size increase due to chloride use in perovskite fabrication. The perovskite precursor solution was prepared by mixing water-free $Pb(CH_3COO)_2$ (0.54 M) , $PbCl_2$ (0.06 M) and MAI (1.8 M) in DMF (device A) or $Pb(CH_3COO)_2$ (0.6 M), $PbCl_2$ (0.067 M), DMSO (0.067 M) and MAI (2 M) in DMF/DMSO (device B). The precursor solution was stirred at room temperature for 60 min and filtered with a 0.45 m PTFE filter prior to use. To fabricate the perovskite layer, 180 l (device A) or 135 l preheated to 75 °C (device B) precursor solution was spin-coated on the top of PTAA layer by a two-consecutive step program at

2000 rpm for 10 s with a ramping rate of 500 $rpms^{-1}$ and 6000 rpm for 8 s with a ramping rate of 800 $rpms^{-1}$ (device A). The second spin-coating step for device B was prolonged to 30 s because the crystallization speed is slower when using DMSO

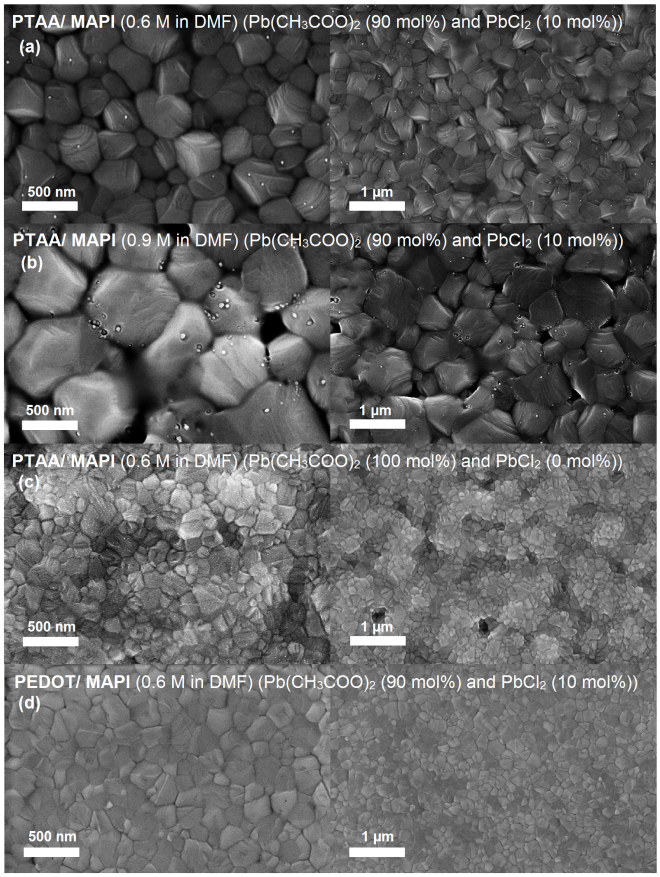

Abbildung 4.10: SEM pictures of MAPI films spin-coated from different precursor solutions and on different HTL materials, showing that grain size and the crystallization process of the perovskite are influenced by the bottom layer. Figures (a-c) show the perovskite grown on PTAA with (a, b) and without (c) using $PbCl_2$, which increases the grain size. Moreover, using non-wetting PTAA as HTL results in larger grains, compared to the perovskite layer shown in (d) on PEDOT:PSS. For the methylammonium-lead iodide $CH_3NH_3PbI_3$ (MAPI) films in (a) and (b) different concentrations (0.6 M and 0.9 M) of the precursor solution were used to increase the layer thickness from ~ 280 nm to ~ 510 nm. A comparison of (a) and (c) highlights the impact of $PbCl_2$ on the grain size. These SEM pictures were conducted with the help of Dr. Benjamin Klingebiel.

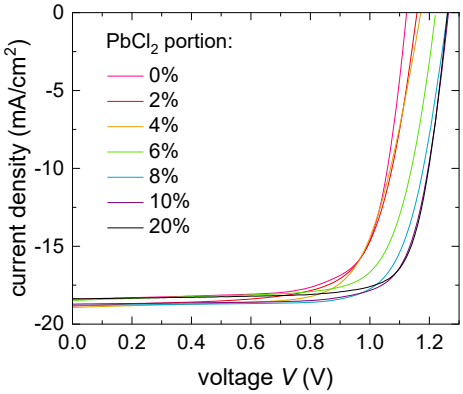

Abbildung 4.11: $JV-$curves of perovskite solar cells using the same parameters for the device fabrication (recipe A), but different ratios of $Pb(CH_3COO)_2$ to $PbCl_2$. $PbCl_2$ concentrations higher than 8% lead to high open-circuit voltages. Lower values lead to reduced open-circuit voltages. While higher $PbCl_2$ values than 10 % make the devices less stable during MPP-tracking in a N_2 filled glovebox.

than for pure DMF. Then the samples were immediately annealed on a hotplate at 75 °C for 2 min. Afterwards, they were cooled down to room temperature.

In this study, Dr. Zhifa Liu found a continuous improvement in open-circuit voltages when the concentration of $PbCl_2$ was increased from 0 % to 8 %, while the optimal concentration of $PbCl_2$ in term of efficiency is in the range of $8-10\,\%$. The JV-curves from a respective sample series are shown in Figure 4.11. We noted that while $PbAc_2$ and $PbCl_2$ based precursors have both been shown to be beneficial for suppressing recombination, [163] there is a comparably small amount of literature on these precursors. As far as we are aware, a mixture of these two precursors has not been used with the combination of PTAA- and PCBM-based contact materials before. Although, this interlayer combination has shown very low voltage losses with multication-based perovskites already. [147] However, the combination with our MAPI absorber seems to currently have an even higher potential to achieve high open-circuit voltages. Moreover, Figure 4.12 shows the JV-curve and the external quantum efficiency Q_e^{EQE} resulting from a thickness series of the absorber layer made to find the optimum.

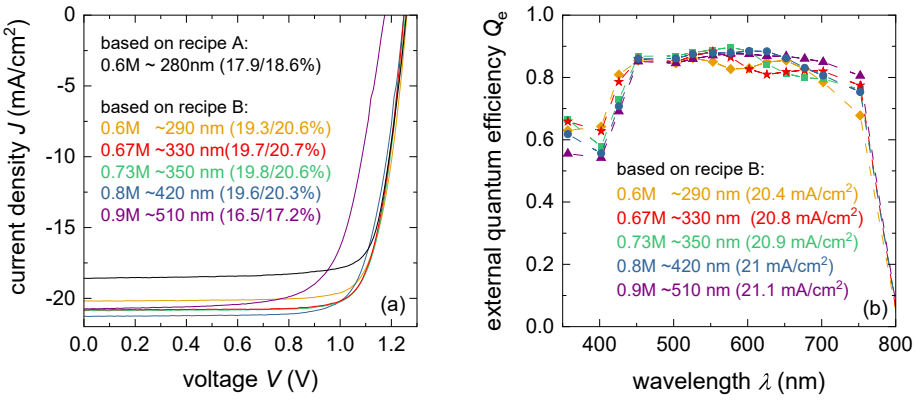

Abbildung 4.12: (a) $JV-$curves of perovskite solar cells comparing the performance of the two different standard recipes (device A and B) and with differently thick absorber layer taken at an AAA class solar simulator. For the thickness series (based on recipe B), the concentration and the amount of DMSO in the perovskite precursor solution was changed while keeping the $Pb(Ac)_2$ to $PbCl_2$ ratio constant at (9:1). Note, that the nomenclature 0.6 M means: $(Pb(CH_3COO)_2$ (0.54 M), $PbCl_2$ (0.0 M), DMSO (0.6 M) and MAI (2.8 M) in DMF/DMSO) and (0.9 M) means: $(Pb(CH_3COO)_2$ (0.81 M), PbCl2 (0.9 M), DMSO (0.9 M) and MAI (2.7 M) in DMF/DMSO)). The perovskite thickness varies between $\sim 290-510$ nm. Thicker perovskite layers achieve higher short-circuit currents with an efficiency optimum for a thickness of 330 nm. (b) Corresponding external quantum efficiency Q_e^{EQE} measurements as a function of wavelength.

4.7.4 Fabrication of the PCBM Layer

PCBM is used as an electron-transport layer (ETL). The PCBM solution was spin-coated on the top of the perovskite layer at a speed of 1200 rpm for 60 s with a ramping rate of 400 rpms^{-1}. Recipe A uses 80 l of a solution with 20 mg/ml PCBM in CB. In contrast, recipe B uses 65 l with a concentration of 20 mg/ml dissolved in CB and T (1 : 1) being preheated to 75 °C for the spin-coating step. The PCBM spin-coating was performed statically, with a time delay of ~ 10 s for recipe B. Typically, the PCBM solution is stirred at 70 °C for at least four hours and filtered with a 0.2 m PTFE filter prior to use. For the drying of the PCBM layer, the samples were left in an open petri dish for at least 20 min without additional annealing.

Since high open-circuit voltages require well-passivated surfaces, the optimization also had to include the right choice of processing conditions for PCBM. There are various degrees of freedom in processing the PCBM layer that we can use to

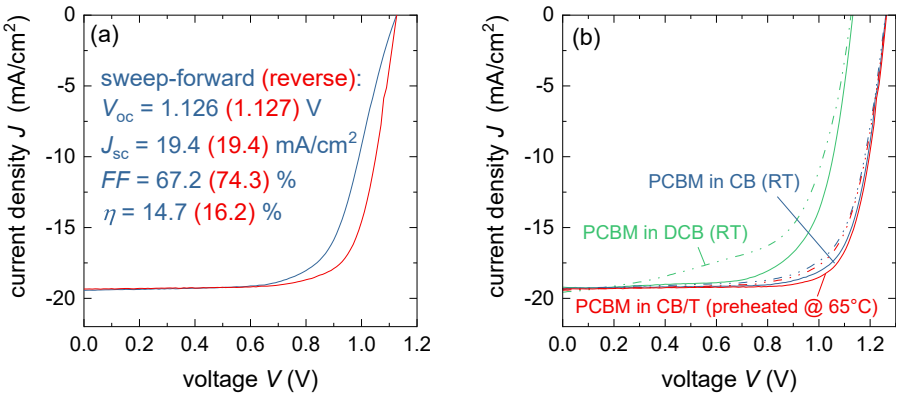

Abbildung 4.13: (a) $JV-$curves of a MAPI perovskite solar using the same parameters for the device fabrication (recipe A), except from the perovskite-precursor solution ($Pb(CH_3COO)_2$ (0.6 M), $PbCl_2$ (0 M) and MAI (1.8 M) in DMF). The MAPI film without $PbCl_2$ as precursor has a different morphology (see Figure 4.10a and (c)) with reduced grain size. $JV-$characteristic of these devices show a reduced open-circuit voltage, smaller fill factor and stronger hysteresis. (b) $JV-$curves of perovskite solar fabricated with PCBM dissolved in different solvents (DCB, CB and CB/T), demonstrating the impact of small changes in the fabrication process on device performance. Note that all other fabrication parameters are similar to the one described for device A.

optimize the MAPI/PCBM interface for the lowest possible recombination rates. These degrees of freedom include, besides the spin-coating parameters, the choice of solvent, the post-deposition annealing treatment and the atmosphere during spin-coating and subsequent annealing. It was reported [166] that higher boiling-point solvents can lead to more ordered layers because the solvent has more time to evaporate when compared to lower boiling-point solvents. In addition, by annealing, preheating the solution or solvent-assisted annealing, crystallization of the absorber layer can be accelerated or slowed down. As part of device optimization, various solvents were used for PCBM, namely the lower boiling-point solvents toluene (T) (110.6 °C) and chlorobenzene (CB) (130 °C) and the higher boiling point (180.5 °C) solvent 1,2-dichlorobenzene (1,2-DCB). Shao et al. [168] have previously reported an improvement in V_{oc} in a very similar device stack when using DCB as a solvent for PCBM combined with solvent-vapor annealing in DCB vapor. In contrast, our PCBM films deposited using the lower boiling-point solvent (CB) or a mixture of CB/T on top of our PTAA/MAPI stack lead to substantially higher open-circuit

voltages. Note that PCBM is not entirely soluble in pure toluene in the desired concentration. During our studies, we also noted that the ideal processing conditions for the PCBM did vary depending on the choice of hole-transport material but also on the MAPI processing conditions. If $1,2-$DCB is used as a solvent for PCBM, substantial losses in V_{oc} occur, yielding in open-circuit voltages lower than 1.2 V. Figure 4.13 summarizes these results. We observed the opposite trend of V_{oc} with PCBM processing conditions when another HTL layer (PEDOT:PSS) was chosen on which the perovskite crystallizes differently. Therefore, we assume that the ideal process parameters must always be considered holistically and have to be individually adjusted to each other in order to achieve the best possible results.

4.7.5 Fabrication of the Cathode

For the solution-processed solar cell devices 120 l BCP solution with a concentration of 0.5 mg/ml in IPA was spin-coated at 4000 rpm for 30 s with a ramping rate of 800 rpm/s. The BCP solution was not filtered or heated but got an ultrasonic treatment for one hour. Finally, 80 nm Ag was thermally evaporated in a separate vacuum chamber ($< 5 \times 10^{-6}$ mbar) with a rate of 2 Å/s. A metal shadow mask defined an aperture area of 0.16 cm^2 by the overlap of the ITO stripe and the Ag. As part of device optimization, it has become apparent that the temperature in the glove box and the atmosphere in the spin-coater influence the crystallization and drying. Thus, the atmosphere impacts the quality of the different layers. The fabrication process was optimized to a temperature of 20 °C and an integrated spin-coater for the MBRAUN glovebox.

4.8 Summary

In conclusion, I have shown that by using a combination of $Pb(CH_3COO)_2$ and $PbCl_2$ based precursors and process optimization of the contact layers PTAA and PCBM, the open-circuit voltage of simple MAPI can be tuned up to 1.26 V without any addition of passivating alkali metals such as Cs, K or Rb. In addition, extremely low surface-recombination velocities have been observed that are required in

order to rationalize the high open-circuit voltage. A detailed quantitative analysis of the recombination behaviour and the resulting lifetime coefficients of this solar cell type with very high open-circuit voltages is discussed in chapter 7.6. While the optimization in the current study focused on eliminating and characterizing losses due to bulk and interface recombination, future improvements in open-circuit voltage will require optimizing the layer stack for minimum parasitic absorption and maximum efficiency of photon recycling, [109,169,170] in a similar way as efficiency optimization in GaAs solar cells has been achieved in the past. [171]

5 Coevaporated Solar Cells

In this chapter, I summarize the technological development of coevaporated MAPI solar cells at the cluster tool - Jülich online semiconductor growth experiment for photovoltaics (JOSEPH), which I managed scientifically during the years of my Ph.D.. Within the scope of this project, I supervised two master's theses [172, 173] and a bachelor's thesis. [174] JOSEPH is a double-cluster UHV system consisting of two central chambers, which are connected to several satellite chambers. One half of JOSEPH comprises a series of deposition chambers specialized for the fabrication of thin film materials for photovoltaic applications. The other half comprises various surface analysis tools facilitating chemical and physical analysis without a vacuum break. One of these deposition chambers is designed for fabricating perovskite-absorber layers by vapor-deposition, also called coevaporation, as an alternative to solution-processing introduced in chapter 4. Chemical analysis via XPS measurements in the analysis cluster assists in process optimization. This second sample type is also used in the further course of this thesis, serving as an example of a MAPI solar cell with high non-radiative recombination losses and low open-circuit voltage. Therefore, I will introduce the corresponding device characteristics of our coevaporated, inverted MAPI solar cells and give an overview of the process development.

5.1 Introduction to Fabrication via Coevaporation

The vacuum-based thin-film fabrication routine of metal-halide perovskites, where multiple materials are thermally evaporated simultaneously, is a rarely used technique compared to the common solution-processing by spin-coating. One reason for this rare use is that coevaporation requires a rather complex and expensive infra-

structure. Additionally, the deposition of the perovskite layer via this method takes several hours, which is quite long considering that spin-coating takes a few minutes at most. However, this technology has some advantages and provides an alternative if conventional spin-coating or other solution-processing techniques are unsuited or challenging to implement. This case applies, e.g., for covering microscopically textured substrates. [175,176] Since vacuum-based perovskite deposition produces highly conformal, pinhole-free and very smooth layers, [177,178] it is a promising route for the development of high-quality perovskite films [179] on double-side textured substrates for monolithic perovskite/silicon tandem solar cells, enabling optimum light management. [175, 180] In addition, vacuum deposition is an attractive method, which is already widely adopted in the semiconductor and coating industry due to the ease of scalability of the device area and excellent homogeneity. [179] Other benefits are the material purity of the sublimed precursors and the solvent-free fabrication, avoiding the toxic solvents generally employed for solution-processing perovskites. Furthermore, coevaporation has a low substrate-fabrication temperature and is therefore compatible with temperature-sensitive plastic electronics. [181,182]

The dual-source coevaporation of the two perovskite precursors lead iodide PbI_2 and methylammonium iodide (MAI) is most employed. [175, 177, 182–187] Best-performing coevaporated MAPI solar cells reach an efficiency of 20.6 %, achieved through continuous device optimization and fine-tuning of the precursor ratio, the development of process know-how, as well as the use of new interlayer materials. [187] However, many other precursor combinations have also been tested, producing various perovskites with different chemical compositions. Unfortunately, these attempts have so far achieved only lower power conversion efficiencies. All-inorganic variants using cesium iodide (CsI) [188] or cesium bromide (CsBr) [189, 190] were tried out, yielding efficiencies below 15 %. Furthermore, also the fabrication of triple-cation mixed-halide perovskite with complex stoichiometry was realized by simultaneous vacuum deposition of MAI, CsBr, formamidimium iodide (FAI), and PbI_2. [191]. Since we only used dual-source coevaporation of the organic salt MAI and the metal-halide source PbI_2, I focus the following discussion on this material system.

While efficiencies of coevaporated perovskites still lack behind those of solution-processed perovskite solar cells, there are recent promising results, e.g., with regard

to high thermal stability achieved via coevaporation. [192] A key open question is the efficiency potential of coevaporated perovskites. Given the substantially lower research effort that has gone so far in optimizing coevaporated perovskites rather than spin-coated, it would be natural if efficiencies trail behind. However, there may also be more fundamental reasons why efficiencies in solution-processed perovskite solar cells are higher than in coevaporated devices.

5.2 Fabrication of the MAPI Film via Coevaporation

This section describes our standard fabrication routine that has evolved over time and gives the best solar cell performance. There were three main challenges in optimizing the perovskite layer, process control and reproducibility, control of the stoichiometry of the layer optimized by XPS, and improvement of the optoelectronic properties of the MAPI film.

The coevaporated MAPI perovskite is deposited by coevaporating lead iodide (PbI_2) and methylammonium iodide MAI powder in a coevaporation chamber from CreaPhys. Figure 5.1 illustrates a schematic drawing of the coevaporator. The chamber was pumped down to a base pressure of at least $\sim 10^{-6}$ mbar. Both materials evaporate from current-heated, ceramic crucibles. Two quartz-crystal microbalances (QCMs), being located ~ 25 cm above each source, control the deposition rates of the individual materials. We tried out various deposition-rate ratios to fine-tune the stoichiometry of the perovskite absorber. A third QCM sensor near the substrate monitors the combined deposition rate and the film thickness of the perovskite layer. The PbI_2 and MAI powder in the crucibles is exchanged each time and refilled with new chemicals prior to the process, keeping the filling level constant to increase reproducibility. The PbI_2 quartz sensor is renewed each time, too. The lifetime of the MAI sensor decreases slowly, so a replacement is not often necessary. Furthermore, the software SQC-310Comm from Inficon controls the deposition rates. First, the PbI_2 and the MAI sources are preheated, then the PID control loop of the SQC controls the output power reaching stabilized rates before the substrate shutter opens. The precursors are heated by the TCU230S temperature control unit to their corresponding sublimation temperatures with a source temperature around 330 °C for of

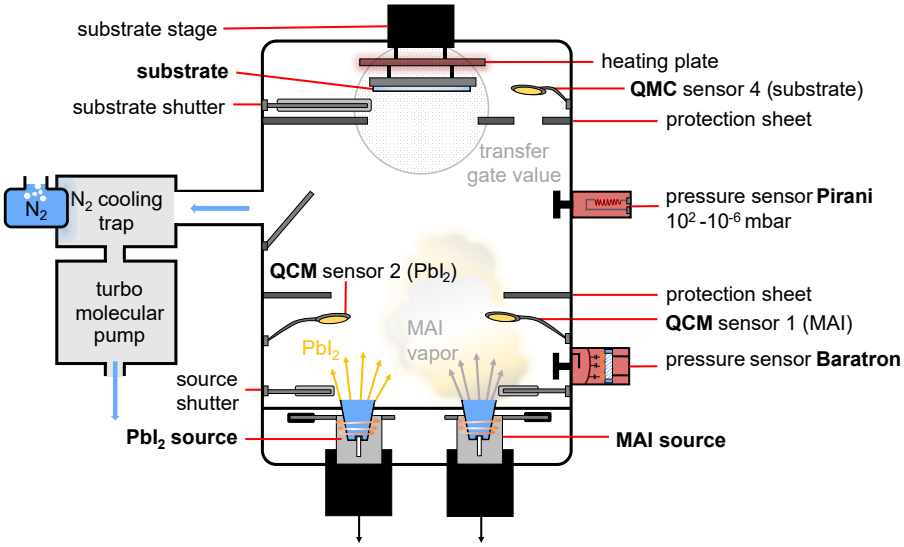

Abbildung 5.1: Schematic drawing of the coevaporator vacuum chamber at the clustertool JOSEPH used for the fabrication of MAPI perovskite films.

PbI_2 and around 150 °C for of MAI. The PbI_2 has a geometric tooling factor 14 % (100 %, 14 %), a density of 6.16 gcm^{-3} and a Z-factor of 0.55. A calibrated deposition rate of 0.3 Å/s is used for the evaporation of lead iodide.

The main challenge in this coevaporation process is the controlled evaporation of the MAI compound. This volatile organic salt can decompose easily and has a very high vapor pressure, leading to non-directed evaporation in cloud formation. Thus, MAI deposits everywhere in the chamber. We noticed, for instance, that MAI also coats the backside of the substrate, which is opposite to the MAI source. Furthermore, the low vapor pressure causes the MAI to detach from the surfaces in the evaporation chamber, influencing the process conditions. Thus, it is challenging to evaporate MAI in a reproducible and controlled way. Other research groups in the field also experience this behavior, [175, 179, 181, 183, 193, 194] who have used different strategies to address this problem. Some tried to bypass this problem by keeping the temperature of the MAI source constant. [180, 183, 185] This approach was not suited for us, because a constant temperature led to a fluctuating MAI rate, which implies that the ratio of the two components changes during the coevapora-

tion process. Hence, no control of the stoichiometry is possible. Another strategy is to choose a fixed PbI_2 rate and set the background-process pressure of the MAI constant. To maintain a constant pressure, a gate valve is used. [179, 186] Unfortunately, we could not apply this approach to our system because we could not observe any significant correlation between pressure changes and temperature and deposition rates of the MAI source. Note that our process pressures are with values in the range of 10^{-6} mbar orders of magnitudes below the pressures reported in some other publications. [186] Hence, we installed a barathron as a second pressure sensor close to the MAI source to expand our understanding and gain process control. This pressure is also decoupled from the temperature and indicated rate on the quartz-crystal microbalances (QCM) sensor. Instead, the pressure depends on the ambient temperature and the liquid nitrogen level of the cold trap installed in our setup to protect the turbomolecular pump by holding back the organic compounds. Consequently, we could not include the pressure as a control parameter and must control the MAI evaporation via the rate at the quartz sensor. Moreover, the tooling of the QCM sensor above the MAI source is very complicated because the MAI film is very soft and unstable in air. Thus, determining the layer thickness of a pure MAI film was not possible and hindered the calibration of the sensor. Other groups have similar problems, [177, 183, 185, 195] whereas some managed to determine a tooling factor for the MAI sensor. [187, 191]. However, we could only use the sensor as a relative indicator in the rate control. For the tooling factors of this sensor, we chose the highest possible values that could be set in the software in order to maximize the resolution of the MAI deposition rate. We obtained the best results with a relative deposition rate of 1.5 Å/s with a tooling factor of 150 % (399 %, 150 %), a density of 0.99 gcm^{-3} and a Z-factor of 3.26. The total deposition time was ~ 240 min. The PbI_2 sensor showed a final thickness of 400 nm, the MAI sensor of 200 nm and the substrate sensor of 500 nm of perovskite. The coevaporated perovskite layer was ~ 465 nm thick in profilometer measurements. XPS analysis yielded a perovskite stoichiometry for $MA_{1.01}Pb_1I_{3.06}$. Subsequently, the samples were thermally annealed at 100 °C for 10 min on a hotplate in glovebox atmosphere. This post-annealing step supports the formation of the black phase, if the perovskite is formed with an excess of methylammonium iodide. [181]

The reproducibility of the process could be better, but we were able to produce

MAPI solar cells with very similar efficiencies in many experiments. The perovskite is very tolerant to slight changes in the ratio of the process rates. Also, MAPI films with stoichiometries, determined from XPS, that deviate from the ideal one yield comparably good solar cell efficiencies, as presented in the next section.

5.3 Device Characteristics of Inverted, Coevaporated MAPI Solar Cells

Figure 5.2 gives an overview of the device performance of our coevaporated MAPI solar cells, testing different hole transport materials, namely PEDOT:PSS, a double layer of PEDOT:PSS and PolyTPD or PTAA. These results summarize the work from Rene Krimmel, [172], who helped to establish an efficient coevaporation process in our group for the first time (2018). The use of PEDOT:PSS as a hole-transport layer was our starting point and a common choice in inverted, planar solar cells at that time. However, employing only PEDOT:PSS as the HTL was not successful, as the $JV-$curve of this device (green line) shows. This cell type leads to efficiency below 5 %. The cell performance suffers particularly from heavy losses in the open-circuit voltage. In addition, the short-circuit current is with $10\,\mathrm{mA/cm^{-2}}$ also extremely low and could be significantly higher with a $\sim 300\,\mathrm{nm}$ thick perovskite absorber layer. Employing an additional organic hole blocking layer on top of the PEDOT:PSS made from PolyTPD, which serves as a substrate for the coevaporation process and is in direct contact with the coevaporated perovskite, improves the efficiency up to 12.8 %. Malinkiewicz et al. has obtained similar trends. [183, 184, 194]. We were able to achieve the best results with the use of the polymer PTAA as selective interlayer material (red line), yielding efficiencies above 15 %. The coevaporated cells show significant losses in open-circuit voltage compared to the solution-processed inverted MAPI solar cells presented in chapter 4, whose device stack comprises the same materials. The highest open-circuit voltages we observed for the coevaporated cells were around 1.1 V, typically even up to 60 meV lower, with a radiative $V_{\mathrm{oc}}^{\mathrm{rad}}$ of 1.322 V (Figure 5.2c). The significant differences in open-circuit voltage raise the question of whether bulk or interfaces dominate recombination losses and how to reduce these losses. A repeatedly observed distinguishing feature of coevaporated perovskite films

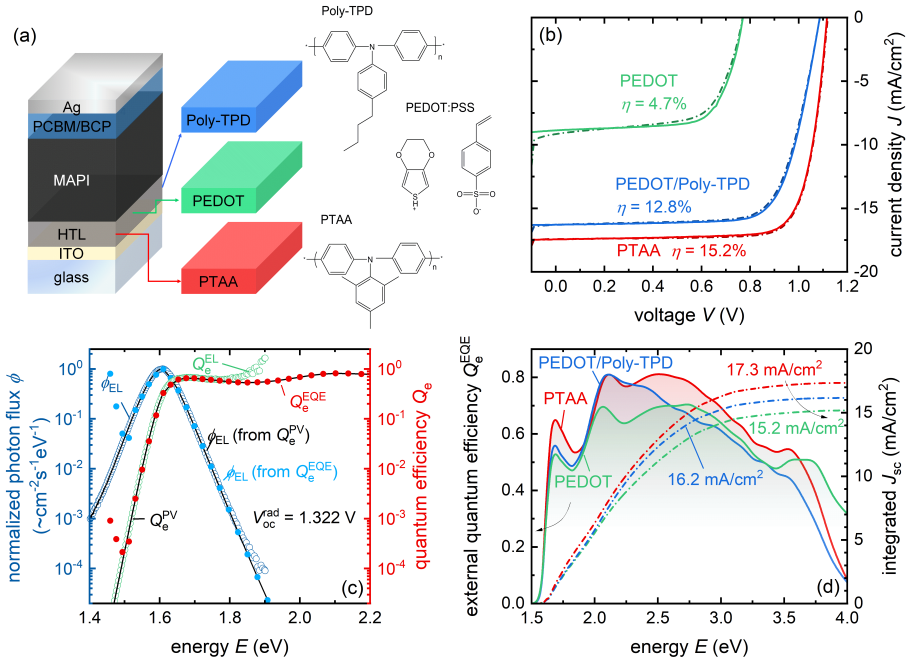

Abbildung 5.2: Overview of the device performance of coevaporated MAPI solar cells grown on three different hole transport materials, namely PEDOT:PSS (green), PolyTPD (blue) and PTAA (red). Figure (a) illustrates the device-stack options, while (b) depicts the up- and down scans of the current-voltage curves. (c) Exemplary calculation of the radiative limit of the open-circuit voltage for the coevaporated solar cell with PTAA, yielding similar results as for the solution-processed sample type. Figure (d) compares the external quantum efficiency measurements of all three devices. The kinks in the EQE near the absorption edges indicate that current losses evoke by incomplete absorption. In addition, strong optical interference effects occur in all three cases.

compared to solution-processed samples is their compact and homogeneous morphology, consisting of tiny crystal grains. [181] Figure 5.3 shows a comparison of SEM images for those different sample types. The crystal structure in the SEM images differs visibly, with the crystallites of the liquid-processed samples produced with and without chlorine in the precursor solution being larger in diameter. This bigger grain size indicates that the initial bulk quality of the solution-processed samples is higher. Later in chapter 7.1, I will analyze and discuss the differences between the coevaporated and solution-processed MAPI solar cells in more detail using TPL measurements. Furthermore, the smoothness of the coevaporated perovskite film

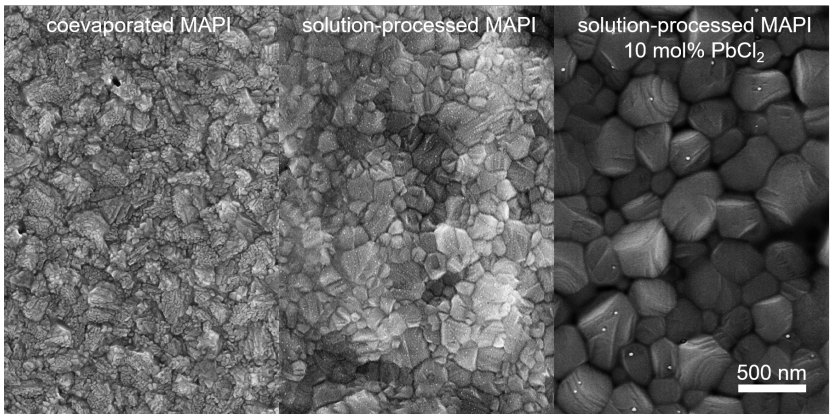

Abbildung 5.3: SEM images of coevaporated (left) and solution-processed MAPI films fabricated without (middle) and with (right) $PbCl_2$ in the precursor solution. These SEM images were conducted with the help of Dr. Benjamin Klingebiel.

enhances optical interference effects that occur in the layer stack, whose layers have dimensions in the range or below the visible wavelengths. These optical interference minima and maxima appear prominently in the measurements of the external quantum efficiencies shown in Figure 5.2d, reducing the short-circuit current densities of the coevaporated solar cells.

We investigated the influence of the chemical nature of the substrates on the perovskite growth to understand the significant variation in device performance for the different hole-transport layers. Figure 5.4 shows SEM pictures of perovskite films grown in the same coevaporation process but on different HTLs. The morphology of the perovskite differs slightly. However, the SEM images do not pinpoint a clear trend that explains the differences in the $JV-$curves. This finding implies that the low performance of the PEDOT:PSS originates from the actual interface between the HTL and the perovskite absorber and not from causing poor growth conditions for the perovskite. As was shown later by Stolterfoht et al., [196] the energy-level alignment of PEDOT:PSS to lead-halide perovskites is unsuitable for efficient charge extraction. In this material combination, PEDOT:PSS does not block electrons efficiently, leading to massive recombination losses throughout the whole voltage range. [182, 190]

Figure 5.5 shows the current-voltage characteristic and the corresponding ex-

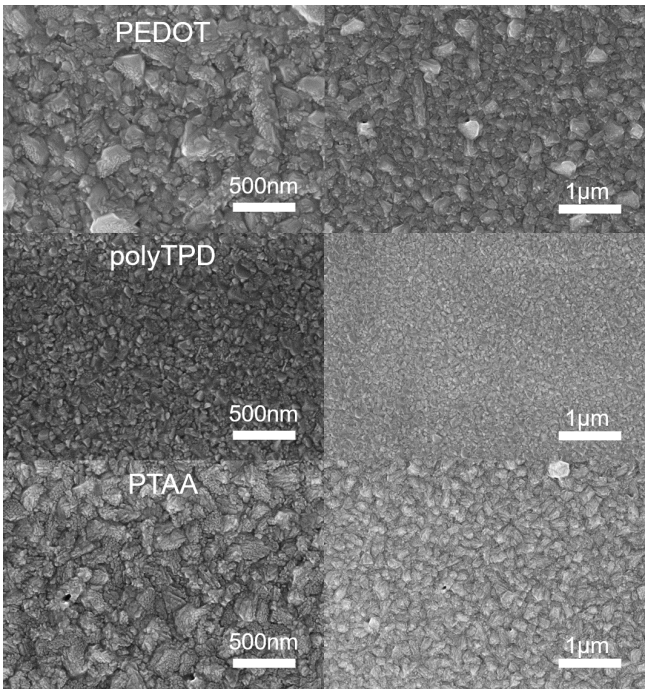

Abbildung 5.4: SEM pictures of coevaporated MAPI films grown on different hole transport materials, namely (a) PEDOT:PSS, (b) PolyTPD and (c) PTAA. These SEM pictures were conducted with the help of Dr. Benjamin Klingebiel.

ternal quantum efficiency of the best-performing coevaporated MAPI cell that we have obtained so far. The solar cell has an efficiency of 17.3 %. However, our optimization efforts only helped increase the short-circuit current density of the coevaporated MAPI cells. Unfortunately, all efforts to suppress non-radiative recombination and increase the open-circuit voltage failed. Since the solar cells presented in Figure 5.2 with perovskite layer thicknesses in the first optical interference maximum of around $\sim 300\,\text{nm}$ suffered from incomplete absorption, we increased the thickness of the coevaporated perovskite absorber by prolonging the coevaporation process. By using layer thicknesses of $\sim 500\,\text{nm}$ around the second interference maximum, we were able to increase J_{sc}. Combined with the optimization of stoichiometry using X-ray photoelectron spectroscopy (XPS), as well as reducing parasitic absorption in the stack, we obtained an increase in short-circuit current of $\sim 4\,\text{mA}$.

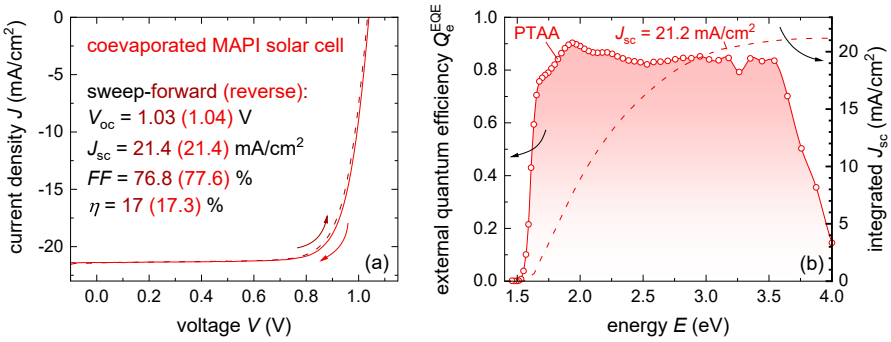

Abbildung 5.5: (a)Current-voltage curve and (b) external quantum efficiency measurement of the best-performing coevaporated MAPI solar cell in this study.

5.4 Rating the Device Performance of Coevaported Solar Cells

In section 2.3.1, I introduced the representation of the losses in a solar cell as a bar chart composed of several figures of merit, each representing a different physical loss mechanism. [19] In the following, I apply this method to a dataset of coevaporated solar cells presented in Figure 5.5, to the record coevaporated solar cell at the time this study ended, [197] and to the solution-processed, MAPI solar cell with high V_{oc} presented in the previous chapter 4. Figure 5.6 illustrates the respective loss analysis of these six devices. Note that the y-axis, representing the normalized efficiency, is a logarithmic axis, implying that the order of the loss factors can be exchanged without changing the relative size of the boxes, which would not be the case with a linear axis. The voltage losses are depicted in green, fill factor losses due to resistive losses in red, whereas the yellow bars show losses in short-circuit current. This representation outlines the progress and the device improvement of the coevaporated solar cells in our research group during the time of my thesis. In addition, it ranks its performance to our best solution-processed device and the record for coevaporated solar cell in literature.

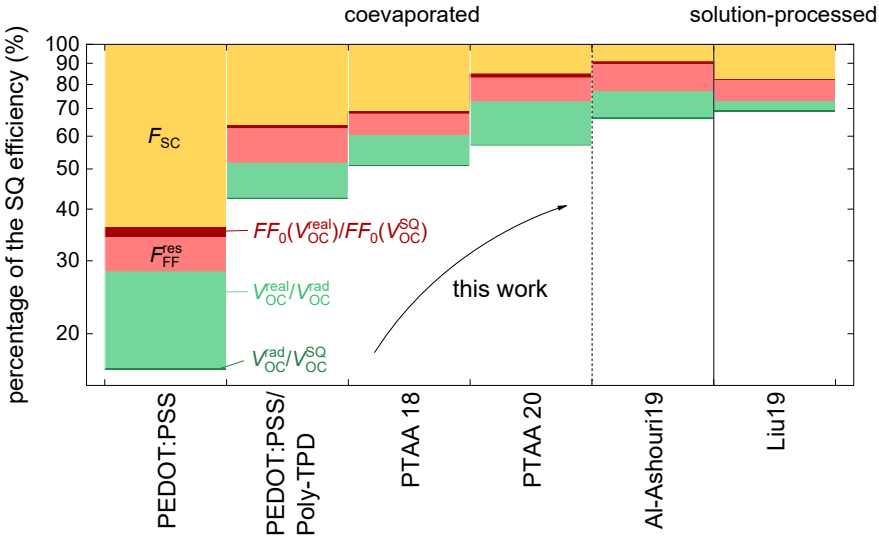

Abbildung 5.6: Loss analysis showing the development of the coevaporated MAPI solar cells. For comparison, the loss analysis of the coevaporated perovskite solar cell published by Al-Ashouri et al., [197] which constituted a record at the time of this study, as well as of the solution-processed sample with a record open-circuit voltage, being introduced in chapter 4 and published as a shared first authorship with Dr. Zhifa Liu, [140] are also shown.

The bar chart plot shows that in the beginning, the most significant improvement from 16 % to > 50 % of the SQ-efficiency limit was realized. This progress results from using new contact materials as a hole-transport layer in the device stack. Since the coevaporated solar cells with PTAA in 2018 suffered from substantial losses in short-circuit current, as illustrated by the yellow bar, we increased the thickness of the coevaporated MAPI layer. The loss analysis of the coevaporated solar cell with PTAA from 2020 shows that this strategy was successful. Thus, the size of the yellow bar is diminished. However, non-radiative losses in V_{oc}, displayed as green bar, are still high and make up the most extensive loss path. Overall, our best coevaported solar cell achieves 57 % of the theoretical limit. The loss in V_{oc} is also the main difference between the coevaporated and our solution-processed solar cell, as the comparison of the two bar charts demonstrates. We put a lot of effort into optimizing the open-circuit voltage of our coevaported solar cells and the process conditions of the

coevaporation process. Besides improving reproducibility by automating the process control and feedback loop during the coevaporation process and implementing data tracking, we tried out a post-treatment in a climate box. This treatment aims to passivate the perovskite surface and increase the crystallinity of the coevaporated MAPI film. The climate box makes the precise adjustment and control of the moisture content possible. It was used previously to improve the quality of MAPI films on glass substrates. [198] In addition, we tried out the new hole-selective contact material ([2-(3, 6-dimethoxy-9H-carbazol-9-yl)ethyl]phosphonic acid) (MeO-2PACz), as self-assembling monolayer molecule (SAM). Unfortunately, we could not achieve an increase in V_{oc} in our experiments.

This respective material MeO-2PACz was introduced by Al-Ashouri et al. [197] at the end of 2019 and outperforms the polymer PTAA in versatility, scalability and power-conversion efficiency. MeO-2PACz is based on a carbazole body with phosphonic acid anchoring groups and can form self-assembled monolayers on various oxides. They reached a new record efficiency of 19.6 % for a coevaproated MAPI solar cell by replacing the PTAA with MeO-2PACz in the layer stack. The respective loss analysis of this solar cell is also shown in Figure 5.6.

6 How to Report Record Open-Circuit Voltages

In this chapter, I present a standardized framework to report voltage loss in perovskite solar cells. As perovskite composition changes, also the band gap does. Thus, higher V_{oc} values are not necessarily better because the reference point changes with the size of this band gap. This solar cell band gap is a model parameter that can be derived and defined in various ways. Therefore, it is not unique. Here, I compare the different band gap definitions used in the literature and show how the thermodynamic limit of the open-circuit voltage based on the Shockley-Queisser model [17] varies widely depending on the definition used. Accordingly, referencing the open-circuit voltage of an actual device to the SQ case is subject to large uncertainty, being introduced by choice of band gap definition. Next, I compare these open-circuit voltages with the so-called radiative open-circuit voltage, [47] derived from the measured absorption and electroluminescence spectra. Thanks to the sharp band edge and the small variations in the Urbach-tail slope, a standard external photovoltaic quantum efficiency of the solar device holds all the information to calculate the radiative open-circuit voltage with an accuracy of a few meV. Therefore a meta-analysis of previously published perovskite solar cells with high open-circuit voltages relative to their band gap becomes possible, where all devices are compared using an identical way of referencing the open-circuit voltages to their radiative limit.

6.1 Definitions of Band Gap Used in Literature

Publications in the research field of perovskite solar cells currently use a variety of different band gap definitions for solar cell devices based on different approaches

and measurement methods. [140, 143, 160, 199–203] The band gap that is determined by one of these different methods, is often used to calculate a reference open-circuit voltage $V_{\mathrm{oc}}^{\mathrm{SQ}}(E_{\mathrm{g}})$. Then, these reference is compared to the actual value V_{oc} in order to rate the loss ΔV_{oc}. With this approach, our research community intends to compare different solar cell types to rank the results from various research groups. [130, 140, 199] In this section, I will explain and compare different methods for defining the band gap of a solar cell that are commonly used in literature. By applying these methods to an exemplary data set, belonging to the MAPI solar cells introduced in chapter 4, I will show that the calculated value for the band gap varies substantially, depending on the chosen method. Subsequently, I calculate the open-circuit voltages in the SQ limit for the different band-gap definitions to demonstrate that the corresponding difference propagates further and affects the V_{oc} limit even more in relative terms.

The first method I will introduce is the Tauc method [204, 205], which is in contrast to most other methods, based on the use of absorption coefficient data. The absorption coefficient α is a material property that results from the characteristic energy-band structure. For an ideal, defect-free semiconductor with a direct band gap, the absorption coefficient is related to the bang gap energy via $\alpha \propto \sqrt{h\nu - E_{\mathrm{g}}}/h\nu$, [206] with the frequency ν. Based on this theoretical shape of the absorption coefficient α, mathematical transformation yields

$$(\alpha h\nu)^2 \propto h\nu - E_{\mathrm{g}} \ . \tag{6.1}$$

For the Tauc method, $(\alpha h\nu)^2$ is then plotted as a function of energy $h\nu$. This approach fits linear region so that the band gap results from an extrapolation of this linear fit to the x-axis [204, 205]. Figure 6.1a shows an example of a Tauc plot. The course of the data illustrates that the actual shape of the absorption coefficient of metal-halide perovskites, in this case of MAPI, does not fit well with the theoretical one. [207–209]. Inherent structural disorder of a material creates absorption tail states toward lower photon energies, which become apparent as an exponential tail in the absorption coefficient. This characteristic is called Urbach tail. [210, 211] The slope of this exponential part varies with the degree of disorder and is characterized by the Urbach energy E_{Urbach}. [42, 211, 212] Besides the shape mismatch between

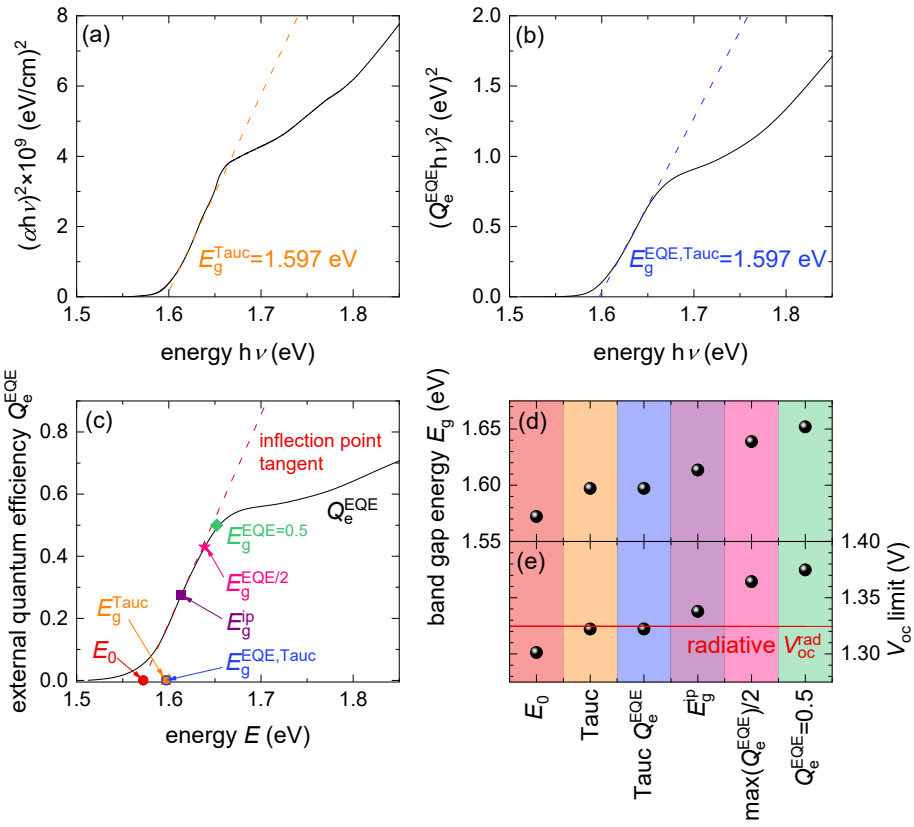

Abbildung 6.1: (a-c) Determination of the band gap energy for an exemplary data set [140] (optical data of MAPI and quantum efficiency data of a respective MAPI solar cell) using different methods that are applied in literature. Figure panel (a) shows the Tauc plot method (orange), extracting the band gap E_g^{Tauc} from absorption coefficient data. (b) Example of Tauc plot method, adapted to quantum efficiency data, yielding in $E_g^{Tauc,EQE}$ (blue). (c) Several methods that use characteristic points of the external quantum efficiency Q_e^{EQE} of the solar cell to determine a band gap energy. These respective characteristic energy values, stated in (c), are the inflection point E_g^{ip} of the Q_e^{EQE} (purple), the x-axis intercept of the inflection point tangent E_0 (red), the energy $E_g^{EQE/2}$ for which the Q_e^{EQE} reaches half of its maximum value, or the energy $E_g^{EQE=0.5}$ for which the Q_e^{EQE} reaches 50 %. (d) Comparison of the resulting band gap energy values for all presented methods revealing a huge deviation. (e) In addition, I calculate the limit of the open-circuit voltage for respective band gaps in the SQ limit and the radiative limit V_{oc}^{rad}.

the theoretical and experimental absorption coefficients, the band gap determined by the Tauc method represents an internal property of the photovoltaic material.

Thus, it is not an external property of the solar cell device, as it is assumed in the SQ limit. However, the application of the Tauc method can be extended and applied to external quantum efficiency $Q_\mathrm{e}^\mathrm{EQE}$ data if we assume that quantum efficiency equals absorptance for efficient charge collection. Furthermore, we must assume that a simple Lambert-Beer model suits to describe the absorptance. Under these assumptions, the $Q_\mathrm{e}^\mathrm{EQE}$ and the absorption coefficient should be proportional to each other for low photon energies and absorption coefficients. The Taylor expansion of the absorptance $\alpha(E)\,d \to 0$ yields

$$Q_\mathrm{e}^\mathrm{EQE} \propto a(E) = 1 - \exp(-\alpha(E)\,d) \approx \alpha(E)\,d \tag{6.2}$$

Figure 6.1b shows the result of the Tauc method that is applied to quantum efficiency $Q_\mathrm{e}^\mathrm{EQE}$. Both data sets in Figure 6.1a and Figure 6.1b yield similar values for the band gap. Note that the values for $E_\mathrm{g}^\mathrm{Tauc,EQE}$ and $E_\mathrm{g}^\mathrm{Tauc}$ do not necessarily agree with each other, as we will see later during the discussion of literature data.

Other common methods, which are applied to determine the band gap of a solar cell, use different characteristic points of quantum efficiency $Q_\mathrm{e}^\mathrm{EQE}$. Thereby, they indicate an external property of the solar cell device. Figure 6.1c gives an overview of these characteristic points, calculated for the exemplary data set. The energy $E_\mathrm{g}^\mathrm{EQE/2}$ at which the quantum efficiency $Q_\mathrm{e}^\mathrm{EQE}$ reaches half its maximum value or the energy $E_\mathrm{g}^\mathrm{EQE=0.5}$ at which the quantum efficiency is 50 % are for instance such characteristic points. [200] Another convention, henceforth referred to as the E_0 method, defines the energy E_0, where the inflection-point tangent intersects the x-axis, as band gap. [143, 203, 213] A related approach is to use the inflection point E_g^ip itself, [200]. It has the advantage that a constant inflection point often leads to small differences in J_sc for differently sharp absorption onset because gains and losses are roughly compensating. The inflection point for fairly sharp and symmetric onsets, as present in halide perovskites, is also identical to the concept of the photovoltaic band gap introduced in ref. [40] and used in recent overviews of photovoltaic technologies. [60, 214]

Figure 6.1d compares all different band gap energies, which I obtained by analyzing absorption and quantum efficiency data for an exemplary data set. This summary reveals how decisive the choice of the method is for the determined band

gap value. The band gap differs in this example by approximately 80 meV, with the E_0 method leading to a rather small band gap value. In contrast, characteristic points, such as the half maximum of the Q_e^{EQE}, yield larger band gap energies, whereas using the inflection points yields a medium value. Subsequently, I calculate the SQ limit for the different band-gap definitions. The corresponding limit of the open-circuit voltage is plotted in Figure 6.1e. This overview of different V_{oc}^{SQ}'s shows a similar spread as the band gap energies, i.e., roughly 80 mV. Thus, it has a huge impact, which V_{oc} limit is compared to the actually measured open-circuit voltage of 1.26 V and used to state the non-radiative voltage losses. This distinction becomes especially relevant for small losses, as in this example. Depending on the method, the losses are ~ 40 meV in the best case and up to 115 mV for the most conservative estimate of the band gap. Hence, if one were to estimate Q_e^{lum} from the different voltage losses mentioned above, the variation in Q_e^{lum} would range from 1 % to 50 %. Thus, the different band gap definitions lead to a spread in band gap energies that is similar to the energy losses under investigation. Accordingly, comparisons between different solar cells become meaningless. As a result, the research community should agree on one suitable and consistent method of referencing to enable a comprehensive, simple, fair and meaningful comparison of non-radiative voltage losses. This consistency would then allow a rating of the measured V_{oc} values among various perovskite compositions.

6.2 A Standardized Method to Report Voltage Losses

In the following section, I propose such a standardized method to state the V_{oc} limit and voltage losses that is meaningful and, at the same time, convenient and easy to apply. My approach is an approximated version of the radiative limit that only requires a single measurement of the external quantum efficiency of the solar cell for its calculation. A detailed introduction of the radiative limit and its calculation can be found in section 2.2. Usually, the external quantum efficiency $Q_e^{EQE}(E)$ and EL emission data $\phi_{EL}(E)$ are both needed to aprecisely determine the radiative open-circuit voltage. Figure 6.2a shows respective Q_e^{EQE} and EL measurements for

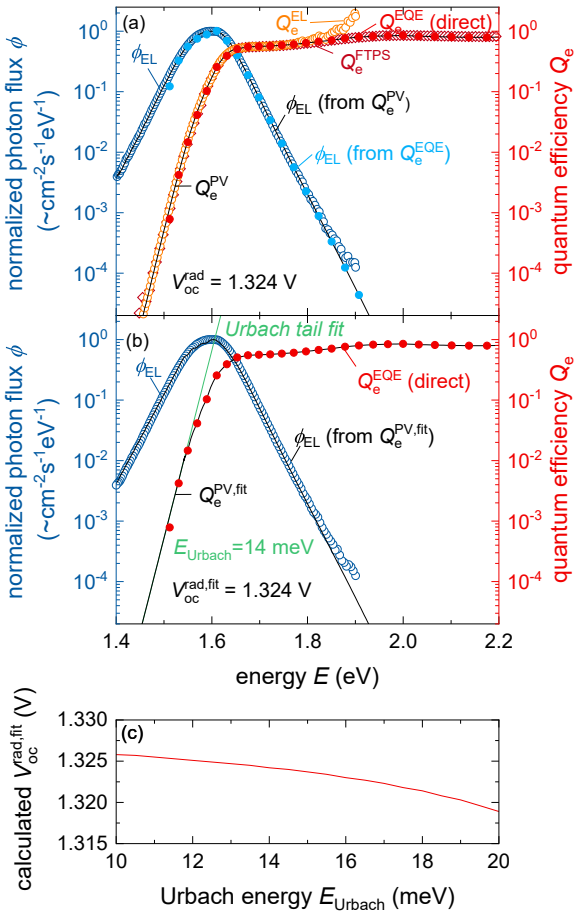

Abbildung 6.2: (a) Electroluminescence spectrum $\phi_{EL}(E)$ (dark blue) and quantum efficiency $Q_e^{EQE}(E)$ from EQE (red) and $Q_e^{FTPS}(E)$ from Fourier transform photocurrent spectroscopy (FTPS) (dark red) of the exemplary solution-processed MAPI cell, being introduced in c. chapter 4. Respective EL and Q_e^{EQE}-data is converted via the reciprocity relation in one another (light blue and orange), and finally combined to an extended $Q_e^{PV}(E)$, Then, the extended $Q_e^{PV}(E)$ is used to calculate the radiative open-circuit voltage V_{oc}^{rad}. This calculation results in a thermodynamic limit for the open-circuit voltage of 1.324 V for this respective device. Reprinted with permission from Liu et al. [140] Copyright 2019 American Chemical Society. (b) Calculation of the radiative limit from measured quantum efficiency $Q_e^{EQE}(E)$ data, to which a fit of the Urbach tail was attached to obtain $Q_e^{PV,fit}(E)$. An Urbach energy of 14 meV fits best to the exponential decay and yields the same V_{oc} limit of 1.324 V. (c) The radiative open-circuit voltage $V_{oc}^{rad,fit}$ as a function of Urbach energy E_{Urbach}.

our exemplary MAPI solar cell. Note, that the photovoltaic quantum efficiency and the electroluminescent emission are reciprocal quantities, which can be converted into one another by using the reciprocity relation introduced in section 2.2 and stated in equation 2.19. Thus, the measured spectrum of the EL photon flux ϕ_{EL} (dark blue spheres) can be converted into a quantum efficiency by the reciprocity relation via

$$Q_{\mathrm{e}}^{\mathrm{EL}}(E) = \frac{\phi_{\mathrm{EL}}(E)}{\phi_{\mathrm{bb}}(E) \quad \exp \quad \frac{qV}{k_{\mathrm{B}}T} \quad -1} \quad . \tag{6.3}$$

Combining the resulting $Q_{\mathrm{e}}^{\mathrm{EL}}$ (orange spheres) at small energies with the the $Q_{\mathrm{e}}^{\mathrm{EQE}}$ (red spheres) gives a data set of the photovoltaic quantum efficiency $Q_{\mathrm{e}}^{\mathrm{PV}}$ (black line) that covers a wide the energy range. Calculating the radiative limit for the open-circuit voltage for this particular data set, using

$$V_{\mathrm{oc}}^{\mathrm{rad}} = \frac{k_{\mathrm{B}}T}{q} \ln \quad \frac{J_{\mathrm{sc}}}{J_0^{\mathrm{rad}}} + 1 \quad , \tag{6.4}$$

results in $V_{\mathrm{oc}}^{\mathrm{rad}} = 1.324\,\mathrm{V}$. Here, the calculation of the short-circuit current density J_{sc} and the radiative saturation-current density J_0^{rad} requires the data set of the photovoltaic quantum efficiency, namely

$$J_0^{\mathrm{rad}} = q \int_0^{\infty} Q_{\mathrm{e}}^{\mathrm{PV}}(E)\, \phi_{\mathrm{bb}}(E)\, dE \tag{6.5}$$

$$= q \int_0^{E_{\mathrm{x}}} Q_{\mathrm{e}}^{\mathrm{EL}}(E)\, \phi_{\mathrm{bb}}(E)\, dE + q \int_{E_{\mathrm{x}}}^{\infty} Q_{\mathrm{e}}^{\mathrm{EQE}}(E)\, \phi_{\mathrm{bb}}(E)\, dE \quad . \tag{6.6}$$

In this equation, E_{x} denotes the energy at the transition point, where the data sets of EL and EQE are stitched together. The short-circuit current density can be determined in the same way, whereby the black-body spectrum ϕ_{bb} must be replaced by the solar spectrum ϕ_{sun}.

The course of the overall $Q_{\mathrm{e}}^{\mathrm{PV}}(E)$ at the band edge, follows a sharp, exponential tail with a slope that is already apparent in the measured $Q_{\mathrm{e}}^{\mathrm{EQE}}(E)$ data and no other characteristics occur. This characteristic is called Urbach tail, where the

absorption edge is dominated by

$$\alpha(E) \propto B \cdot \exp\left(E/E_{\mathrm{Urbach}}\right) \quad . \tag{6.7}$$

Here, E_{Urbach} denotes the Urbach energy and B is a prefactor. The room-temperature Urbach energy is usually around 15 meV for metal-halide perovskites. [75, 160] Utilizing this simple behavior opens up the possibility of generating the missing quantum efficiency values at low energies through a fit of an Urbach tail. Next, I apply this idea to our exemplary $Q_{\mathrm{e}}^{\mathrm{EQE}}(E)$ data set. This allows me to approximate the short circuit-current and the radiative saturation-current density, e.g. via

$$J_0^{\mathrm{rad,fit}} = q \int_0^{E_{\mathrm{x}}} Q_{\mathrm{e}}^{\mathrm{Urbach}}(E)\,\phi_{\mathrm{bb}}(E)\,dE + q \int_{E_{\mathrm{x}}}^{\infty} Q_{\mathrm{e}}^{\mathrm{EQE}}(E)\,\phi_{\mathrm{bb}}(E)\,dE \tag{6.8}$$

$$= q \int_0^{\infty} Q_{\mathrm{e}}^{\mathrm{PV,fit}}(E)\,\phi_{\mathrm{bb}}(E)\,dE \quad , \tag{6.9}$$

with

$$Q_{\mathrm{e}}^{\mathrm{Urbach}}(E) = Q_{\mathrm{e}}^{\mathrm{EQE}}(E_{\mathrm{x}}) \cdot \exp\left(\frac{E - E_{\mathrm{x}}}{E_{\mathrm{Urbach}}}\right) \quad . \tag{6.10}$$

With this approach, I obtain from the fit a value for the radiative open-circuit-voltage

$$V_{\mathrm{oc}}^{\mathrm{rad,fit}} = \frac{k_{\mathrm{B}}T}{q} \ln\left(\frac{J_{\mathrm{sc,fit}}}{J_0^{\mathrm{rad,fit}}} + 1\right) \tag{6.11}$$

that is in good agreement with $V_{\mathrm{oc}}^{\mathrm{rad}}$. Figure 6.2b shows the fitted Urbach tail as green line and the resulting overall $Q_{\mathrm{e}}^{\mathrm{PV,fit}}(E)$.

Furthermore, I evaluated this approximated radiative limit for different Urbach energies, pointing out that the accuracy of the slope of the Urbach tails has no significant influence on the determined $V_{\mathrm{oc}}^{\mathrm{rad,fit}}$ value. As shown in Figure 6.2c, the $V_{\mathrm{oc}}^{\mathrm{rad,fit}}$ deviates by a few millivolts, when E_{Urbach} is varied by 10 meV. This variance is negligible compared to the deviation of 80 mV that could occur when different band gap definitions are mixed and not only one consistent referencing method is used. Concluding, the quality of the fit is therefore not decisive for the determination of $V_{\mathrm{oc}}^{\mathrm{rad,fit}}$. Moreover, Figure 6.3 points out that displaying these fit results for Urbach

tails with different energies in the EL spectrum plot facilitates the choice of a suitable Urbach energy because differences become more apparent. In this example, the slopes of the Urbach tails with Urbach energies E_{Urbach} of 10 meV (yellow line) and 20 meV (back line) are clearly unsuitable and do not fit the experimental data (red line) in Figure6.3b .

In summary, I conclude that an approximate determination of the radiative limit that results from combining the measured $Q_{\mathrm{e}}^{\mathrm{EQE}}$ with an Urbach tail fit, is a suitable method to determine the theoretical limit of the open-circuit voltage of metal-halide perovskite solar cells. Furthermore, this method is easily done, but still precisely enough. Thus, determining the radiative open-circuit voltage becomes possible as long as a measurement of the external photovoltaic quantum efficiency is available for the specific device. Since this EQE measurement is already a well-established method in the perovskite solar cell research community, my proposed method can be applied without any additional metrological effort and still provides a meaningful, cross-literature comparability of losses in the open-circuit voltage.

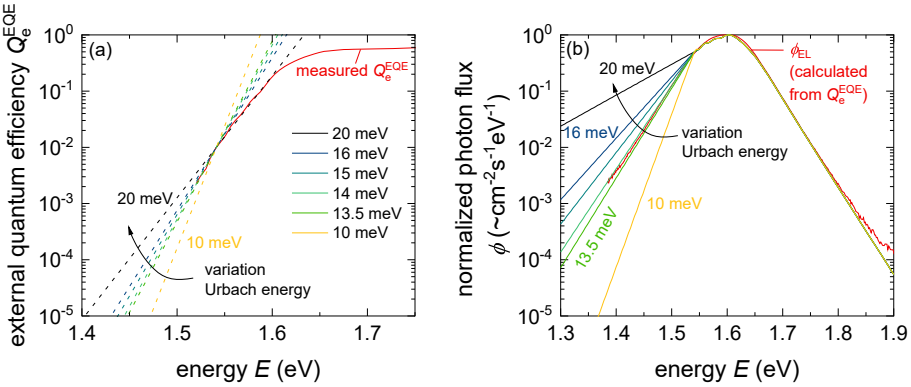

Abbildung 6.3: Variation of the Urbach energy E_{Urbach} that changes the slope of the Urbach tail. Panel (a) shows this variation for the external quatum effiency plot, whereas panel (b) depicts the same data set but converted into the electroluminescence spectrum using the reciprocity relation introduced in section 2.2 and stated in equation 2.19. The radiative open-circuit voltage increase for steeper tails, but only about a few millivolts. Thus, the calculated $V_{\mathrm{oc}}^{\mathrm{rad,fit}}$ is still quite accurate, even if I use a not well-fitting Urbach tail.

6.3 Meta-Analysis of Literature Data

The last section has provided an overview of various methods used in the literature to determine the band gap, its corresponding SQ limit of $V_{oc,\,SQ}$ and the radiative limit, too. In addition, I have calculated all corresponding quantities for an exemplary data set. In this section, I apply all these introduced methods to external quantum efficiency data and, if available, to absorption data of previously published perovskite solar cells with exceptionally high open-circuit voltages. [140, 143, 160, 199–202, 213] In Figure 6.4a, the different values of band gap energy are plotted. Figure 6.4b compares the corresponding voltage losses ΔV_{oc}, defined by the difference between the values of the calculated V_{oc} limits and the stated V_{oc}. Just as for the exemplary data set in Figure 6.1, the resulting values for E_g and ΔV_{oc} are quite different and widespread, depending on the applied method. The E_0 method leads in each case

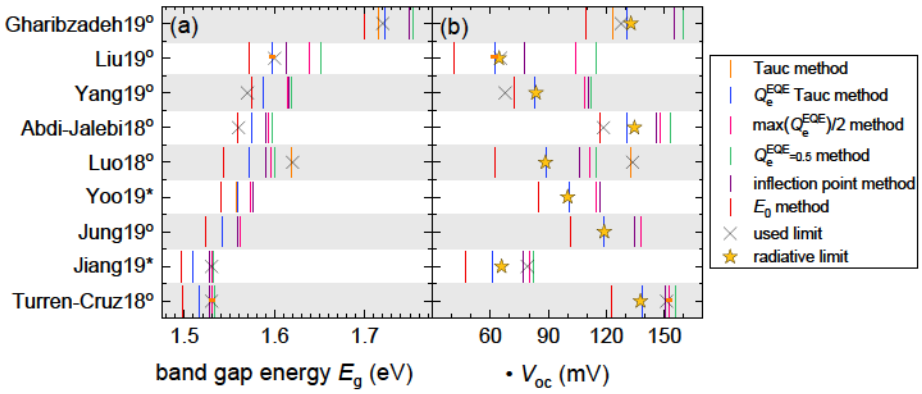

Abbildung 6.4: Comparison of solar cells from the literature with exceptionally high V_{oc}'s, [140, 143, 160, 199–203, 213] which were evaluated with the different methods for band gap determination introduced in section 6.2. Figure (a) shows the different band gap energy values determined using various methods introduced in the last section. Furthermore, panel (b) shows the corresponding voltage losses, calculated by subtracting the reported V_{oc} from the SQ limit of the open-circuit voltage for the band gap values resulting from each method. In addition, this plot states the losses with regard to an approximation of the radiative open-circuit voltage. This approximation combines the measured quantum efficiency data from the respective publications with a fit of the Urbach tail to an extended quantum efficiency. Moreover, I quote the voltage losses stated in literature for each solar cell record. Since the perovskite composition and accompanying the band gap changes, these literature values are neither comparable nor meaningful because different methods were used for the analysis.

to rather small band gap values and thus to minimal voltages losses. So, it is a very optimistic calculation, which always yields smaller values than the radiative limit. All other methods are not so clearly arranged and do not always show the same trend for all considered high-performance devices. Values for the band gap energy such as $E_g^{EQE=0.5}$can be rather different, since the layer thickness, which changes the transparency, and optical interference effects in these layer stacks, modify the shape of the quantum efficiency. In addition to the calculated values ot the energy band gap and voltage losses, I added the actually stated values from the respective publications to Figure 6.4. These used limits are plotted as crosses. Since various perovskite compositions and the whole range of different methods are used, some results are rather optimistic in their assessment of voltage losses, e.g. Yang et al. [203] or Abdi-Jalebi et al. [143]). While others are quite conservative, like Jiang et al. [200] or Turren-Cruz et al. [202], who overestimate their losses. Comparisons of values between different papers is hence either misleading or only possible if the differences are huge, i.e. much larger than the band gap range caused by the different definitions.

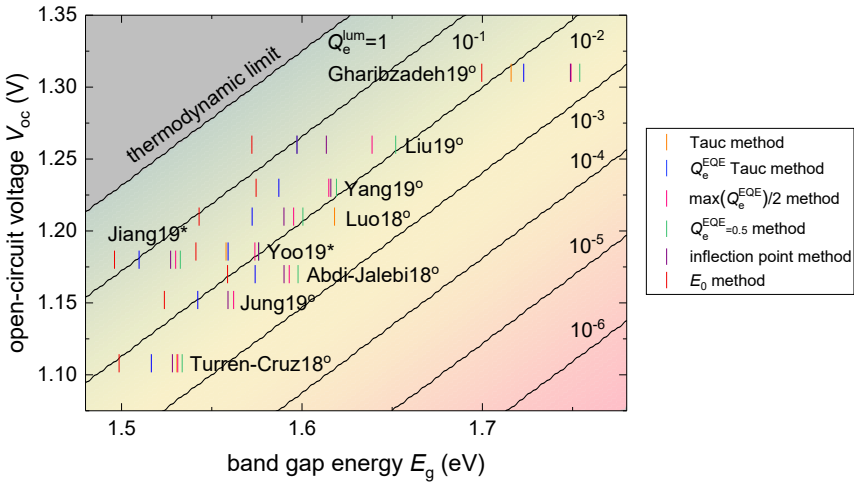

Abbildung 6.5: Overview of the open-circuit voltage of lead halide perovskite solar cells as a function of band gap energy E_g. Here, this band gap energy is calculated for various definitions of band gap used in literature, which were introduced in section 6.2. Thus, the energy value on the x-axis shifts, which also changes the ranking in relation to the external quantum efficiency significantly. This overview shows a comparison of solar cells from the literature with exceptionally high V_{oc}'s, [140, 143, 160, 199–203, 213].

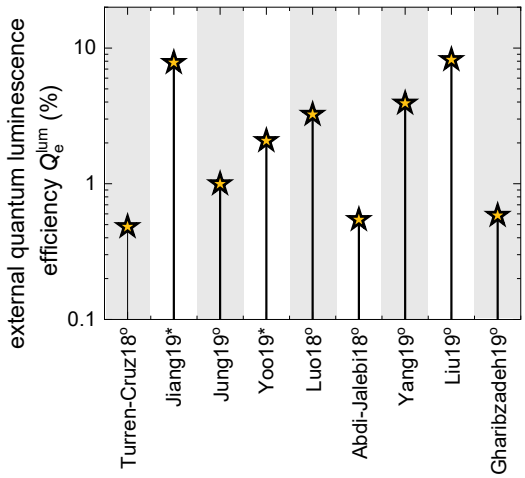

Abbildung 6.6: Comparison of the external luminescence quantum efficiency Q_e^{lum} of solar cells from the literature with exceptionally high V_{oc}'s, [140, 143, 160, 199–203, 213], calculated with the help of the standardized method introduced in section 6.2

Figure 6.5 illustrates the results from Figure 6.4 in a different representation. This illustration highlights the extent to which changes in the band gap energy influence the ranking of the open-circuit voltage value in relation to the external luminescence quantum efficiency Q_e^{lum}. In addition, Figure 6.6 shows a ranking of the external luminescence quantum efficiency Q_e^{lum} of these solar cell devices.

6.4 Figures of Merit for Perovskite Solar Cells

In the following, I use an identical way of referencing to compare all devices and to enable an unbiased, comprehensive comparison, which reveals the respective device limitations. Figure 6.7 gives an overview of the resulting losses in J_{sc} and V_{oc} for the high-performance solar cells studied in our meta-analysis. As a figure of merit (FOM) for the limitations due to non-radiative voltage losses the difference between their respective radiative limits, which were calculated from the extended quantum efficiencies $Q_e^{PV,fit}(E)$ and the reported open-circuit voltages, is used. Moreover, we have a look at the reported short-circuit current densities J_{sc}, which mainly indicates

how good the respective devices absorb light, and consider them in relation to the one in the SQ limit J_{sc}^{SQ}. The performance of the device from Jiang et al. [200] stands out, because it has both extremely small losses in short-circuit current density and in open-circuit voltage, and the voltage losses were rated too pessimistic in the actual publication. In addition, it is curious to note that the solar cell published by Gharibzadeh et al. [199] was advertised in the title of the paper because of its high V_{oc}, despite the fact that if band gap and radiative V_{oc} are considered, the cell actually excels in J_{sc}. Only an identical way of referencing perovskite solar cells with varying compositions helps to explicitly highlight these peculiarities or limitations, which otherwise remain unnoticed. In addition, comparison of losses as done in Figure 6.7 is important because it allows us to better identify which aspects to target for further efficiency improvements. For instance, work on surface passivation would be highly valuable if open-circuit voltage losses are substantial but would be less relevant if the losses appear mainly in J_{sc}. The use of a consistent definition of band gap (via the inflection point method) also allows us to make a historical analysis of efficiencies, normalized efficiencies and band gaps as shown in Figure 6.8

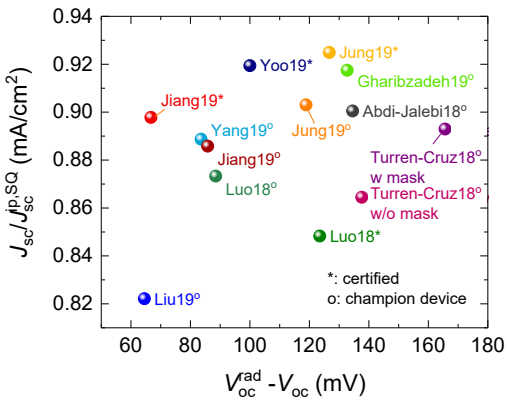

Abbildung 6.7: Comparison of the limitations of the different record perovskite solar cells from literature, [140,143,160,199–203,213] all being analysed by using one consistent method to determine the band gap and the limit of the open-circuit voltage. In this way, the losses are comparable with each other and an unbiased comparison is possible. The performance with regard to the short-circuit current density is indicated by the ratio of experimental J_{sc} compared to the Shockley-Queisser (SQ) limit. For calculating the non-radiative voltage losses, I subtract the measured open-circuit voltage from the radiative limit $V_{oc}^{rad,fit}$.

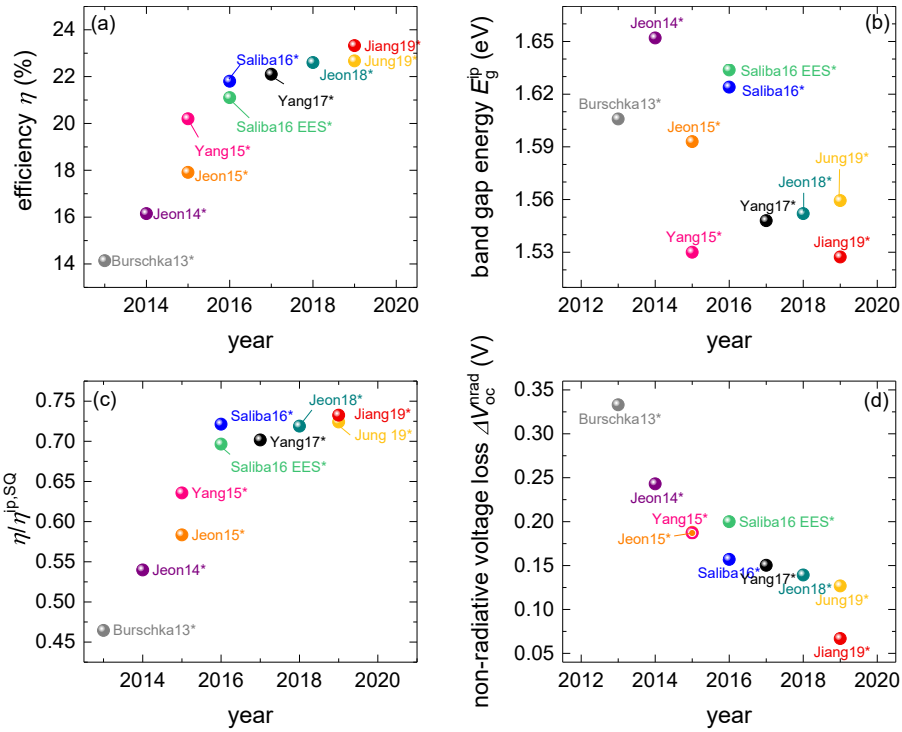

Abbildung 6.8: Overview over the development of certified record devices characteristics [99–101, 142, 200, 201, 215–218] over time. Most of these record cells are stated in the NREL solar cell efficiency tables. [219] In (a) the progress of record efficiency is shown. Furthermore, Figure (b) presents the respective band gap energy E_g^{ip}, being calculated via the inflection point method from the external quantum efficiency, and (c) the ratio of efficiency to the one in SQ limit calculated for E_g^{ip}. (d) Trend of the non-radiative losses in open-circuit voltage ΔV_{oc}^{nrad} over time.

for the material class of lead-halide perovskites. While not all efficiency record over the years was published in a scientific journal, it is at least possible to trace the key developments during the years based on published data that I can analyse in the same way as discussed above. Figure 6.8a shows the evolution in efficiency, starting with 15 % $MAPbI_3$ solar cells in 2013 and ending in 2019, when I conducted this study, with $> 23\%$ efficiency devices based on $FA_{0.92}MA_{0.08}PbI_3$. As shown in Figure 6.8b, part of the development towards higher efficiencies was driven by a reduction of the band gap by adding different amounts of formamidinium (FA) and sometimes

Cs to double or triple cation blends. Due to the different amounts of Br added to the initially purely I-based perovskites, the band gap continuously varied. Figure 6.8c shows the development of the efficiency normalized to the SQ efficiency for the given band gap. Thereby, I used the inflection point of the quantum efficiency to calculate the efficiency in the SQ limit. While good MAPI cells in 2013 were still below 50 % of the band-gap specific SQ limit, values exceeded already 72 % in 2016 and have risen only moderately in the three following years up to $\sim 73\,\%$. Most of the efficiency gains relative to the quadruple cation perovskites presented by Saliba et al. [142] are mainly due to a reduction in band gap. It is clear that while this is a valid path to go for increasing single junction efficiencies, any efforts towards tandem solar cells benefit from either substantially lower (1.25 eV or lower) [220] or slightly higher band gaps ($\sim 1.65 - 1.85\,\mathrm{eV}$). [221, 222] Figure 6.8d shows the development of non-radiative voltage losses $\Delta V_{\mathrm{oc}}^{\mathrm{nrad}}$ as a function of time for the same set of cells. The voltage losses decrease continuously until again about 2016, where the data published in ref. [142] already achieves a level of $\Delta V_{\mathrm{oc}}^{\mathrm{nrad}}$ typical also

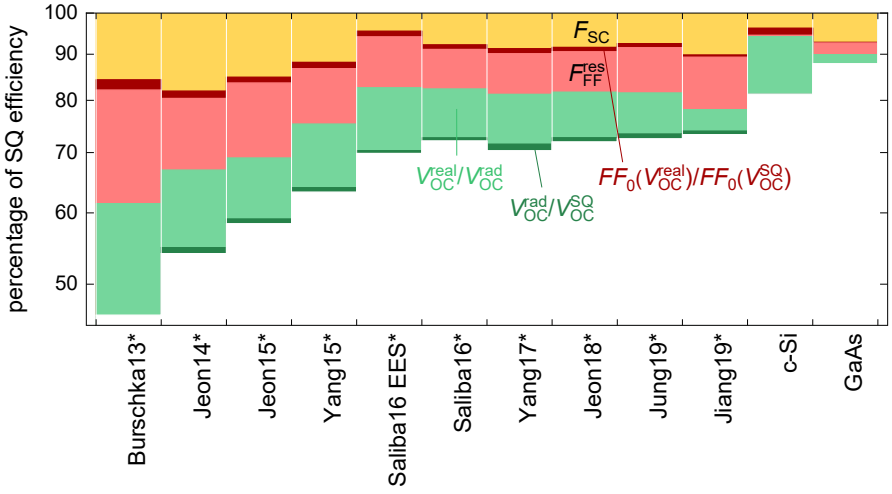

Abbildung 6.9: Visualization of potential improvement of record-efficiency metal-halide perovskite solar cells over time, and current record-efficiency cells of c-Si and GaAs from literature, based on their band gaps, relative to the ideal, SQ-case, using partitioning of the efficiency losses, introduced in section 2.3.1. As a reference band gap, I used the photovoltaic band gap $E_{\mathrm{g}}^{\mathrm{ip}}$ extracted from solar cell quantum efficiency data.

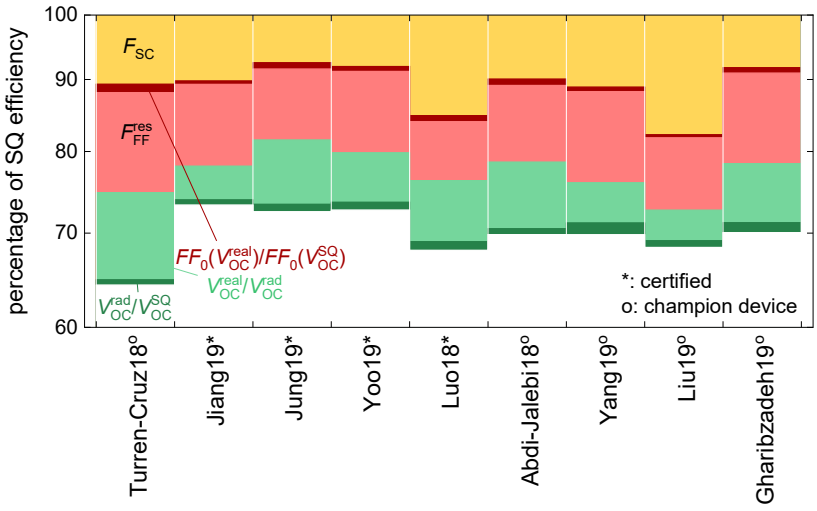

Abbildung 6.10: Visualization of potential improvement of top-performing metal-halide perovskite solar cells from literature, based on their band gaps, relative to the ideal, SQ-case, using partitioning of the efficiency losses, according to ref. [19]. A detailed discussion of these different figures of merit (FOMs) is available in section 2.3.1. As a reference band gap, I used the photovoltaic band gap E_g^{ip} extracted from the inflection point of the solar cell quantum efficiency data.

for later record cells. Note, that I used the highest efficiency cell from ref. [142] and not the highest V_{oc} cell for this comparison, which implies that even lower voltage losses were possible with this layer stack. During recent years, among the highest efficiency cells, only the data in the paper by Jiang et al. [200] stands out in terms of extremely low ΔV_{oc}^{nrad} as previously mentioned.

In section 2.3.1, I introduced the representation of the losses in a solar cell as a bar chart, composed of several figures of merit each representing a different physical loss mechanism. [19] Applying this method to the data set of efficiency record solar cells over the years gives us Figure 6.9, which summerises the finding from the discussion of Figure 6.8. Furthermore, Figure 6.10 compares the different loss terms as bar chart among the range of recent perovskite solar cells already discussed in Figure 6.4 and 6.7. Note that the y-axis representing the normalized efficiency is a logarithmic axis, implying that the order of the loss factors can be exchanged without changing the relative size of the boxes which would not be the case with a linear axis. A lot of effort has already been invested in minimizing non-

radiative recombination explaining that in the case of high-performance devices, the green bar is no longer the largest in terms of area. Rather, Figure 6.10 reveals that resistive losses, reducing the fill factor (red), make up the largest share for almost all perovskite solar cells and are the limiting factor. Thus, the comparatively rarely discussed resistive losses [223] stand out as providing the highest potential for further improvement and are substantially higher than in more mature technologies such as GaAs, Si or $Cu(In,Ga)Se_2$. [19]

7 Understanding Transient PL of Layer Stacks and Solar Cells

While transient photoluminescence measurements are a very popular tool to monitor the charge-carrier dynamics and investigate these recombination losses in perovskite films [224–226], interpretation of data obtained on multilayer samples is highly challenging due to the superposition of various effects that modulate the charge-carrier concentration in the perovskite layer and thereby the measured PL. These effects include bulk and interfacial recombination, charge transfer to electron or hole transport layers and capacitive charging or discharging.

In this chapter, I combine numerical simulations with Sentaurus TCAD, analytical solutions and experimental data with a dynamic range of around seven orders of magnitude on various sample geometries to present an improved understanding of this method. I will discuss their respective peculiarities and show how adding further layers and interfaces modifies the PL transients and causes physical effects that must be considered. With this consecutive step-by-step approach to increasingly complex systems, I aim to create an understanding of which processes dominate and are important for different sample types. In addition, I explain how these different processes affect the transient PL decay and their extracted differential decay time, introduced in section 2.5.4 for a perovskite film on glass. Plotting this decay time as a function of the time-dependent quasi-Fermi level splitting enables distinguishing between the different contributions of recombination, charge extraction, as well as capacitive effects to the decay.

7.1 Introduction

Technological development of halide-perovskite solar cells towards even higher efficiencies requires ways of understanding and quantitatively analyzing the main loss processes. [227, 228] Non-radiative recombination is one of the main loss processes in basically any solar-cell technology [60, 214] including perovskites that leads to reduced open-circuit voltages at a given illumination condition. [42, 50, 229, 230] TPL measured on thin perovskite films on glass is a well-understood and frequently-used method to derive charge-carrier lifetimes and recombination coefficients, [109, 231] which are seen as important metrics to quantify the photovoltaic absorber layer.

For a film on glass, the only mechanism that reduces the concentration of excess-charge carriers after the laser-pulse excitation is the recombination of charge carriers in the bulk or at the surfaces of the perovskite. In this case, faster recombination will lead to a faster decay of charge carriers and, hence, a faster photoluminescence decay after a pulsed excitation. Unfortunately, this clear correlation between recombination and transient decay only applies to perovskite films on glass but not to more complex sample structures.

However, interfaces to charge-extracting layers and electrical contacts can substantially affect the recombination dynamics of perovskite solar cells [125, 231] and typically dominate recombination losses in complete perovskite solar cells. Hence, developing methods to measure and understand recombination dynamics in layer stacks and complete devices is paramount. [232–236] TPL measurements on samples with more than one semiconductor layer or even on solar-cell devices are challenging to characterize and interpret because many different mechanisms coincide and decays are affected by various effects. The reason for this is that adding contact layers to the perovskite film not only adds additional recombination paths but also leads to effects like charge-carrier separation, transfer- or interface-charging effects [157, 233, 237] that may change the recombination kinetics fundamentally. Therefore, a fast TPL decay is not necessarily caused by recombination losses but is rather influenced by a combination of effects such as energy-level alignment of the material combination, charge-carrier mobilities, transfer velocities, thicknesses, and interfaces of the additional layers. Given that this combination of these effects is difficult to describe analytically, the state-of-the-art interpretation of transient

PL decays of perovskite-layer stacks or even complete solar-cell devices is currently still at an early stage. In experimental practice, the information contained in the decay curve is often reduced to a single value – the characteristic time constant of a monoexponential decay. However, this reduction of the transient to a single value will cause a loss of information, making a misinterpretation of experimental data more likely and impeding a deeper understanding of the information contained in PL transients. While theoretical work on TPL decays on full solar-cell devices has been published for other photovoltaic technologies, using III–V semiconductors, [238], $Cu(In,Ga)Se_2$, [138, 239] or CdTe [240] as absorber material, a theory dealing with the specific situation in halide-perovskite devices is currently missing. A distinctive feature of halide perovskites is their low doping density, which implies

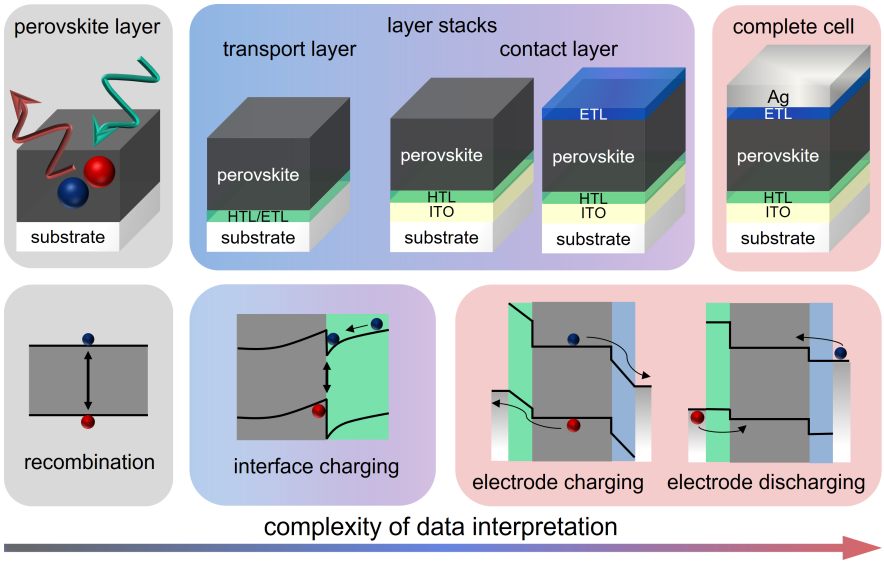

Abbildung 7.1: Overview of the different halide perovskite sample types that are investigated with transient photoluminescence. Depending on the sample type, i.e., absorber layer on glass or absorber layer with one or two contact layers attached, the complexity of the interpretation of data increases from left to right. The second row illustrates typical mechanisms affecting the PL decay in different sample geometries. While the film on glass is only affected by bulk and surface recombination, samples with interfaces to charge extraction layers are affected by charge accumulation and recombination at the interfaces between the absorber and charge-extraction layer. On fully contacted devices, charging and discharging the electrodes also affect the global band diagram and the transients measured on full devices.

that the absorber is in high-level injection during the transient experiment. Thus both charge-carrier types equally matter. Furthermore, contact layers, especially in the inverted geometry, where illumination takes place through the anode, are often low-conductivity organic materials such as PTAA or fullerenes that may take up a substantial part of the built-in voltage of the device [56] and that can decouple the internal quasi-Fermi-level splitting from the external voltage, particularly during early times of the transients.

Therefore, this chapter proposes an alternative approach to analyze TPL data from different layer stacks and perovskite solar cells. I will transfer the concept of plotting the differential decay as a function of the corresponding quasi-Fermi level splitting, first introduced in section 2.5.4 of this thesis, to these more complex sample structures. In the case of an absorber layer on glass, the presentation of decay time versus Fermi-level splitting ΔE_{F} helps to distinguish between the different radiative and non-radiative recombination mechanisms, since each dominates at different levels of charge-carrier concentration, thus different quasi-Fermi level splittings. On this subject, I refer to Figure 2.17 in chapter 2, which summarizes the corresponding results. Based on these findings, this presentation of TPL data will also allow a better understanding of the more complex recombination dynamic that results from the interplay between charge extraction and interface or contact charging and recombination. Figure 7.1 depicts the different sample types of interest. The following section 7.2 deals with the sample type of a perovskite layer in combination with a selective charge-transport layer. Based on this, section 7.3 looks at the layer-stack configuration consisting of one electrode, charge-transport layer and perovskite absorber. Afterward, section 7.4 continues with the TPL characteristics of a complete cell. Finally, section 7.6 presents experimental TPL for different sample types and stacks.

7.2 Perovskite Layer with Charge-Extraction Layer

Surface recombination is an important loss mechanism, but the surface to ambient air is usually not particularly interesting because it does not appear within a perovskite-solar cell. Instead, research is interested in analyzing interfaces between the perovs-

kite film and charge-extracting layers to evaluate and compare the quality of contact materials and assign recombination losses relevant for the actual solar cell. There is a range of additional effects - not related to recombination - that will affect the shape of the TPL decay and that I am going to illustrate in the following by using the example of a perovskite/PCBM bilayer. The parameters that influence the shape of the TPL decay most strongly are the energetic offset $\Delta\chi$ of the conduction bands, the surface-recombination velocity S_{PCBM} and the thickness d_{PCBM} of the charge-extracting PCBM layer. In the following, I will start with an exemplary situation to visualize the effect of charge accumulation if interface recombination is slow, with the help of energy-band diagrams of this bilayer stack. Later, I will discuss the influence of these parameters on the decay time versus Fermi-level curves.

Figures 7.2a-d show band diagrams of a simulated TPL experiment on such a bilayer, while Figures 7.2e-g show the TPL data at different fluences and the differential decay time $\tau_{\mathrm{TPL,LLI}}$ vs. time t and vs. quasi-Fermi level splitting ΔE_{F}, calculated via Equation 2.48. After the laser pulse has hit the sample, the equilibrium-Fermi level (E_{F}) splits up into a quasi-Fermi level for holes ($E_{\mathrm{F,p}}$) and quasi-Fermi level for electrons ($E_{\mathrm{F,n}}$), as shown in Figure 7.2b. Simultaneously, electrons are transferred to the PCBM, which is visible by the increase of the Fermi-level split inside the fullerene layer. Due to its reasonably low mobility of about $\mu_{\mathrm{PCBM}} = 5 \cdot 10^{-2}\,\mathrm{cm}^2/\mathrm{Vs}$, [241] this increase is slower than in the perovskite. Moreover, this increase is also position-dependent, as the comparison of the conduction and valence band in the PCBM region of Figure 7.2b and (c) reveals. The injection of electrons into the PCBM leads to a reduction of the *np*-product in the perovskite and, by this, to a reduction in the PL at early times that is not caused by recombination. In Figure 7.2c, depicting the situation 35 ns after the pulse, the quasi-Fermi levels are flat throughout the sample. At the same time, the energy bands are bent close to the MAPI/PCBM interface. This bending implies that high densities of electrons accumulate in the PCBM close to the interface. This accumulation requires high fluences and low interfacial recombination velocities to happen. Thus, a quantitative description of interfacial recombination is only possible by including the effect of Poisson's equation in addition to the continuity equations for electrons and holes. [157] After the quasi-Fermi levels have equilibrated, recombination leads to a further reduction in PL. Figure7.2e-f illustrates the respective normalized transient PL decay and the

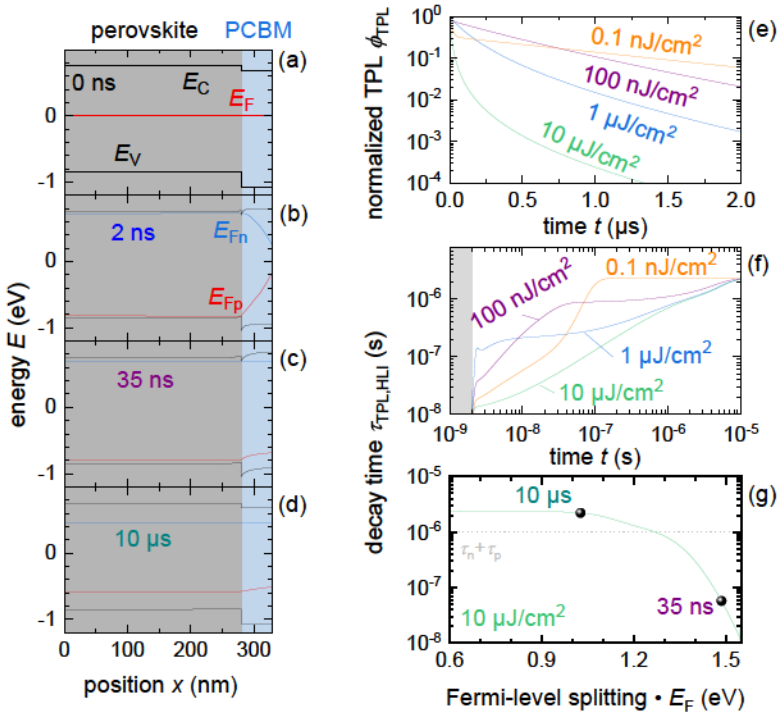

Abbildung 7.2: (a-d) Band diagrams of a perovskite film on glass with a charge-extracting PCBM layer on top before and at different time delays after the laser-pulse excitation simulated with Sentaurus TCAD. (a) Equilibrium-band diagram before the sample gets photoexcited. The band diagram in Figure (b) shows the situations directly after the end of the laser pulse when the quasi-Fermi level splitting in the perovskite is the highest but a negligible density of electrons has been transferred to the PCBM. In panel (c) substantial transfer of electrons to the PCBM has happened, resulting in electron accumulation and band bending in the PCBM close to the perovskite/PCBM interface (35 ns). (d) After 10 µs, this band bending has vanished again and the Fermi-level splitting has visibly decreased. (e) Normalized PL and (f) decay time over time for different laser fluences. In Figure (g), the decay time $\tau_{TPL,LLI}$ for the highest fluence is shown again, but here as a function of the average quasi-Fermi-level-splitting in the perovskite layer. The SRH-bulk lifetimes were set to $\tau_n + \tau_p = 1\,\mu s$ with $\tau_n = \tau_p$. The perovskite/PCBM junction is a type-II heterojunction. The difference in electron affinity is 70 meV and the interface-recombination velocity is set to $S = 0.01\,cms^{-1}$.

calculated decay time $\tau_{TPL,LLI}$ as a green line.

Depending on the properties of the bilayer, recombination may preferentially proceed (i) via interfacial recombination of electrons in the PCBM with holes

in the perovskite, (ii) via re-injection of electrons from the PCBM layer into the perovskite and subsequent recombination in the perovskite bulk. The first scenario is more likely if the interfacial recombination velocities are high and the conduction band offsets $\Delta\chi$ are large. The second scenario dominates in the opposite case of low recombination velocities and small energetic offsets. In both cases, additional aspects, e.g., the thickness d_{PCBM} of the PCBM layer, will affect the TPL decay.

Figure 7.3a-b helps us to study the impact of the conduction-band offset, which is defined by the difference in electron affinity χ_{PCBM} of the PCBM and the perovskite χ_{pero}, for the two scenarios. In this example $\Delta\chi$ is varied between $40\,\mathrm{meV} - 220\,\mathrm{meV}$, while the thickness d_{PCBM} of the PCBM is set to 50 nm, similarly to the simulations in Figure 7.2. Figure 7.3c-d illustrates the impact of a thickness variation of the PCBM layer.

First, I discuss scenario (i) by showing decay-time curves calculated for a non-negligible interface-recombination velocity of $S_{\mathrm{PCBM}} = 50\,\mathrm{cms}^{-1}$, as it is assumed for the two panels on the left-hand side of Figure 7.3. The decay-time curves show differently pronounced S-shapes depending on the band offset $\Delta\chi$. After the fast decay times at high ΔE_{F} due to charge transfer to the PCBM and normal radiative and Auger recombination in the bulk, an initial plateau at around 1.2 to 1.4 eV of quasi-Fermi level splitting occurs in the $\tau_{\mathrm{TPL,LLI}}$-curves. For even lower ΔE_{F} values, the decay time $\tau_{\mathrm{TPL,LLI}}$ saturates at a second plateau value, which differs only slightly for different energy offsets. In contrast to this behavior, the first plateau nearly disappears for small offsets and is particularly pronounced in the opposite case. For an offset of only 40 meV, illustrated by the grey line, the shape of the decay time approaches the simple case of an unpassivated perovskite film where no additional effects besides recombination define the decay time. From now on, this decay time is called recombination lifetime (τ_{R}). The explanation for the first plateau at higher ΔE_{F} is the effect of charge accumulation in the PCBM close to the interface. This effect reduces $\tau_{\mathrm{TPL,LLI}}$ relative to longer times after the pulse excitation, where charge accumulation has been reduced to a point where all bands and Fermi levels are flat. This situation was depicted in the band diagram in Figure 7.2d. The effect of charge-carrier accumulation gets more severe for higher energy-band offsets because the misalignment of the conduction bands leads to larger electron densities in the PCBM. It also reduces the rate of re-injection into the perovskite.

Next, the thickness of the PCBM layer is varied between $10-150\,\mathrm{nm}$ for a medium-large energy offset of $150\,\mathrm{meV}$. Figure 7.3c represents the respective decay times $\tau_{\mathrm{TPL,LLI}}$ as lines in different shades of purple with lighter colors belonging to thinner layers.This variation allows us to analyze the impact of the PCBM thickness in more detail. For example, the first plateau gets more pronounced for thicker PCBM layers. Furthermore, higher charge-extraction layer thickness also increases

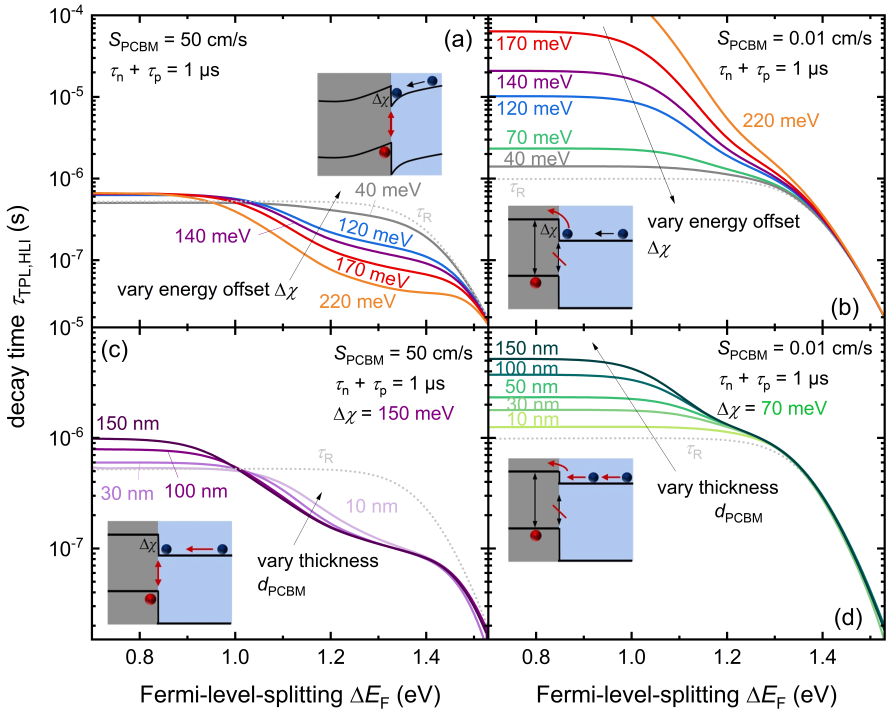

Abbildung 7.3: Decay time $\tau_{\mathrm{TPL,LLI}}$ versus Fermi-level splitting ΔE_{F} for the two scenarios, of (a, c) a high interfacial recombination velocity of $S_{\mathrm{PCBM}} = 50\,\mathrm{cms}^{-1}$ at the perovskite/PCBM interface and (b, d) a negligible interfacial recombination velocity of $S_{\mathrm{PCBM}} = 0.01\,\mathrm{cms}^{-1}$. Figures (a-b) show a variation of the energy offset $\Delta\chi$ of the conduction bands and its impact on the decay time for each scenario. (c-d) Decay time plotted for a variation of the PCBM layer thickness d_{PCBM}. The dotted, grey lines show the simulation result of the pure perovskite film where only the combination of the different recombination processes defines the course of the decay time, named recombination lifetime τ_{R}. The comparison allows us to distinguish between pure recombination processes and the impact of additional effects, e.g., interfacial charging, re-injection, or diffusion limitation. Additional simulation parameters can be found in the Appendix in Table A.6.

the impact of band bending due to a pronounced electrostatic interaction. For a given charge-carrier density, any change in electrostatic potential of $k_{\mathrm{B}}T/q$ will occur over one Debye length, where k_{B} is the Boltzmann constant, T the temperature and q the elementary charge. Hence, thicker layers allow for a larger change in electrostatic potential over the PCBM and, therefore, stronger band bending. The fullerene thickness also strongly affects the saturation value of the second plateau of $\tau_{\mathrm{TPL,LLI}}$ at small Fermi-level splittings or longer times. At longer times after the laser-pulse excitation, recombination will be limited by the time the electrons take to diffuse through part of the PCBM layer before they can recombine at the interface. This diffusion limitation leads to longer decay-time values at small ΔE_{F}. This effect is especially relevant for materials with low charge-carrier mobility, like organic semiconductors.

Figure 7.3b shows the scenario (ii) for varying energy offsets, where interfacial recombination is negligibly small and the decay at longer times must be due to re-injection of electrons into the perovskite absorber layer. Now, decay-time values at longer times or small ΔE_{F} can substantially exceed the Shockley-Read-Hall bulk lifetime (τ_{SRH}) of 1 s. This phenomenon occurs because electrons are injected into the PCBM and cannot escape from there other than by re-injection over a barrier of a certain height. This re-injection process is the rate-limiting step at longer times, leading to prolonged decay times at small ΔE_{F}. I expect energy-activated de-trapping from shallow defects to exhibit similar behavior, although this topic is not systematically investigated in this thesis. Again, PCBM thickness has the same effect as before for the saturation value of the decay time. Larger thicknesses lead to longer $\tau_{\mathrm{TPL,LLI}}$ due to the longer diffusion time through the PCBM, as depicted in Figure 7.3d.

Note that an analytical solution can no longer describe the effect of band bending and, thus, charge-carrier dynamics in a perovskite layer in contact with a charge-extraction layer. Just for thin charge-extracting layers with small energy offset, it is still reasonable to use the saturation value of the decay time $\tau_{\mathrm{TPL,LLI}}$ at small quasi-Fermi level splittings as an effective lifetime. With this, we can use Equation 2.69 in order to estimate interface-recombination velocities and SRH-bulk lifetimes. Only then does the decay time roughly correspond to the pure recombination lifetime τ_{R}. When interpreting data from TPL measurements on samples with

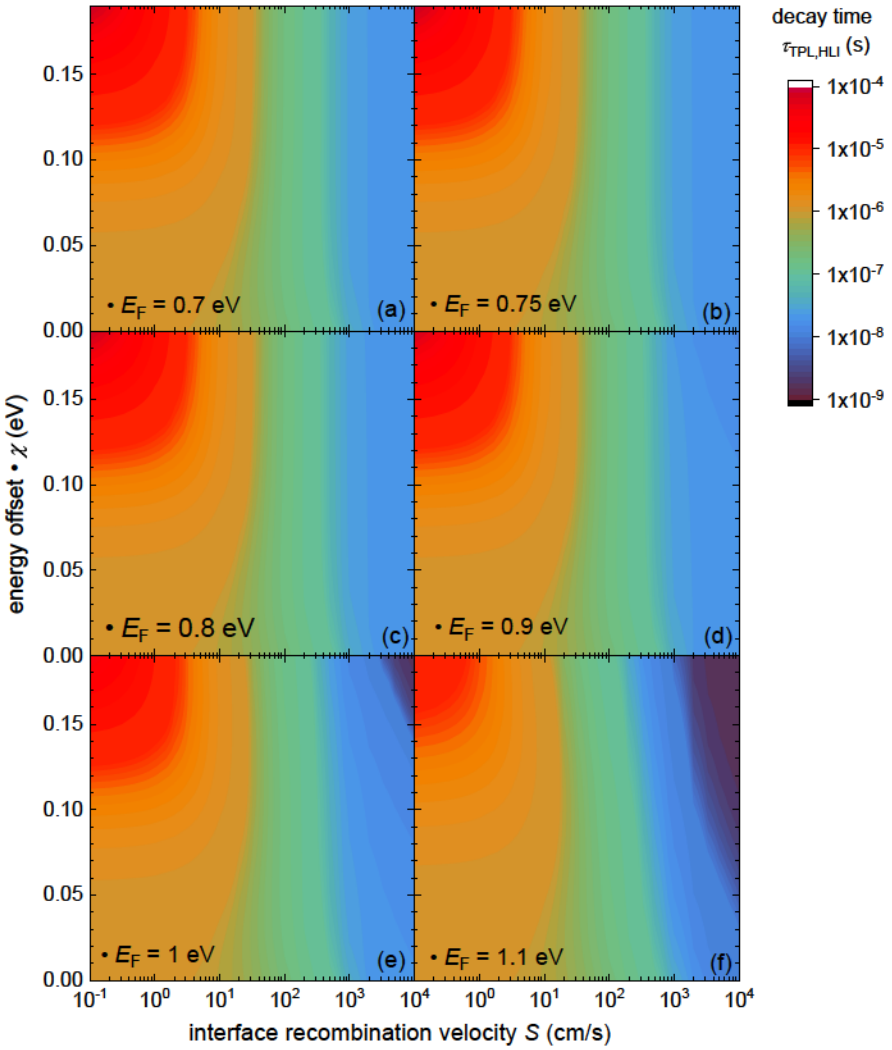

Abbildung 7.4: Surface plots of the decay time $\tau_{\mathrm{TPL,LLI}}$ at various Fermi-level splittings ΔE_{F} from $0.7-1.1\,\mathrm{eV}$ as a function of the energy offset $\Delta\chi$ and the surface-recombination velocity S used in the transient device simulation.

thick transport layers or those with high energetic offsets, the presented effects and their impact on the decay time $\tau_{\mathrm{TPL,LLI}}$ cannot be ignored. Otherwise, one assigns

interface and bulk lifetimes, which can differ by orders of magnitude from the actual one.

In addition to the individually selected curves in Figure 7.3, I have chosen a second way of displaying the influence of the energy offset $\Delta\chi$ and the interfacial recombination velocity of S_{PCBM} on the decay time. Figure 7.4 and 7.5 show surface-colour plots of the simulated decay time $\tau_{\mathrm{TPL,LLI}}$ as a function of these two parameters, being extracted at different levels of quasi-Femi level splitting. The energy offset $\Delta\chi$ is varied between $0-190\,\mathrm{meV}$, while the S_{PCBM} changes by five orders of magnitude. The SRH-bulk lifetime is set $\tau_{\mathrm{n}}+\tau_{\mathrm{p}}=1\,\mu\mathrm{s}$ with $\tau_{\mathrm{n}}=\tau_{\mathrm{p}}$, which is equal

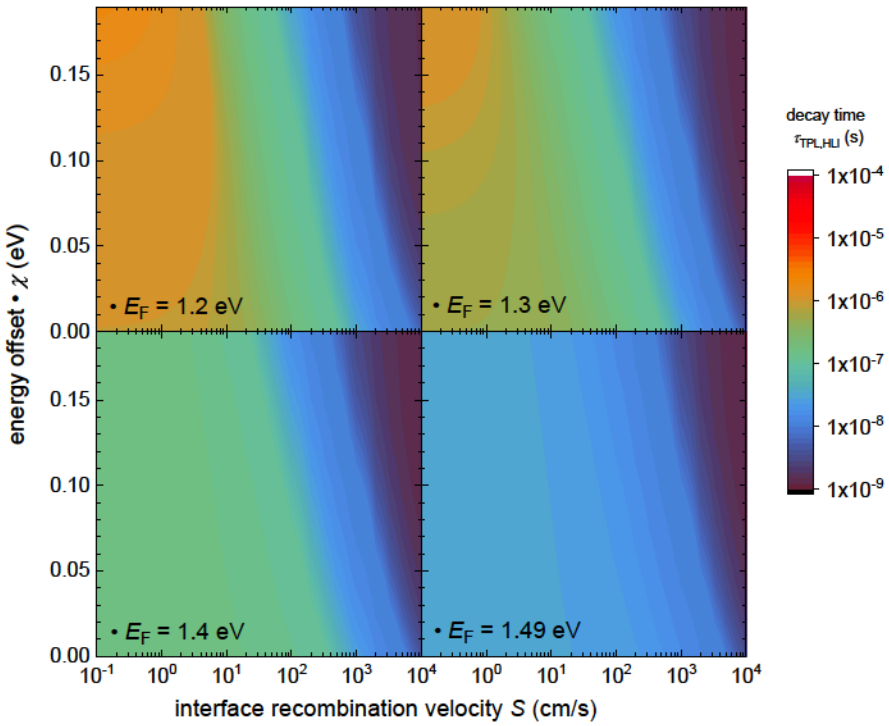

Abbildung 7.5: Surface plots of the decay time $\tau_{\mathrm{TPL,LLI}}$ at various Fermi-level splittings ΔE_{F} from $1.2-1.49\,\mathrm{eV}$ as a function of the energy offset $\Delta\chi$ and the interface-recombination velocity S used in the transient device simulation. The thickness of the PCBM layer is kept constant at 50 nm. Furthermore, I used a SRH-bulk lifetime of $\tau_{\mathrm{n}}+\tau_{\mathrm{p}}=1\,\mu\mathrm{s}$ with $\tau_{\mathrm{n}}=\tau_{\mathrm{p}}$. The Appendix shows additional simulation parameters in Table A.6.

to the pure recombination lifetime τ_R at low Femi-level splittings ΔE_F, when lower-order recombination processes dominate. The first surfaces plots in Figure 7.4a-d, for quasi-Femi-level splittings of $0.7 - 0.9\,\mathrm{eV}$, present this respective situation and show how the decay time behaves around what I have called second plateau so far. The colour maps of 7.4e-f and 7.5a picture the intermediate state of Fermi-level splittings, whereas the last three show the change of the differential decay time with $\Delta\chi$ and S_{PCBM} at high ΔE_F's. Additional simulation parameter can be found in Table A.6 in the Appendix.

7.3 Perovskite Layer with Charge-Extraction Layer and Electrode

In the previous section, I have discussed the relevant case of a type-II heterojunction between the perovskite and a charge-transport layer – in this case, the ETL. Of course, similar simulations could be done for hole transport layers that form a type-II interface with the perovskite. However, two aspects that may appear in practice are missing in section 7.2. One is the case where type-I heterojunction is formed, and the second aspect is that an electrode, anode or cathode, may be present in addition to the ETL or HTL. In this section, I am going to combine these two issues and simulate transient PL experiments on the layer stack glass/ITO/PTAA/perovskite. Results from ultraviolet photoelectron spectroscopy (UPS) measurements suggest that the hole-transport material PTAA may have a negligible valence band offset to MAPI at least for the samples prepared with the recipe presented in ref. [140]. As in the previous section, we first look at the corresponding band diagram in equilibrium and at different delay times after laser-pulse excitation, represented in Figure 7.6a-d. Following, I vary the SRH-bulk lifetime and the interface-recombination velocity and investigate their impact on the differential decay time $\tau_{TPL,LLI}$ for this layer-stack combination.

When comparing the equilibrium-band diagrams of Figure 7.2a and 7.6a, it is directly apparent that the equilibrium Fermi-level E_F is no longer roughly in the middle of the perovskite-band gap but is rather pinned by the ITO contact. When

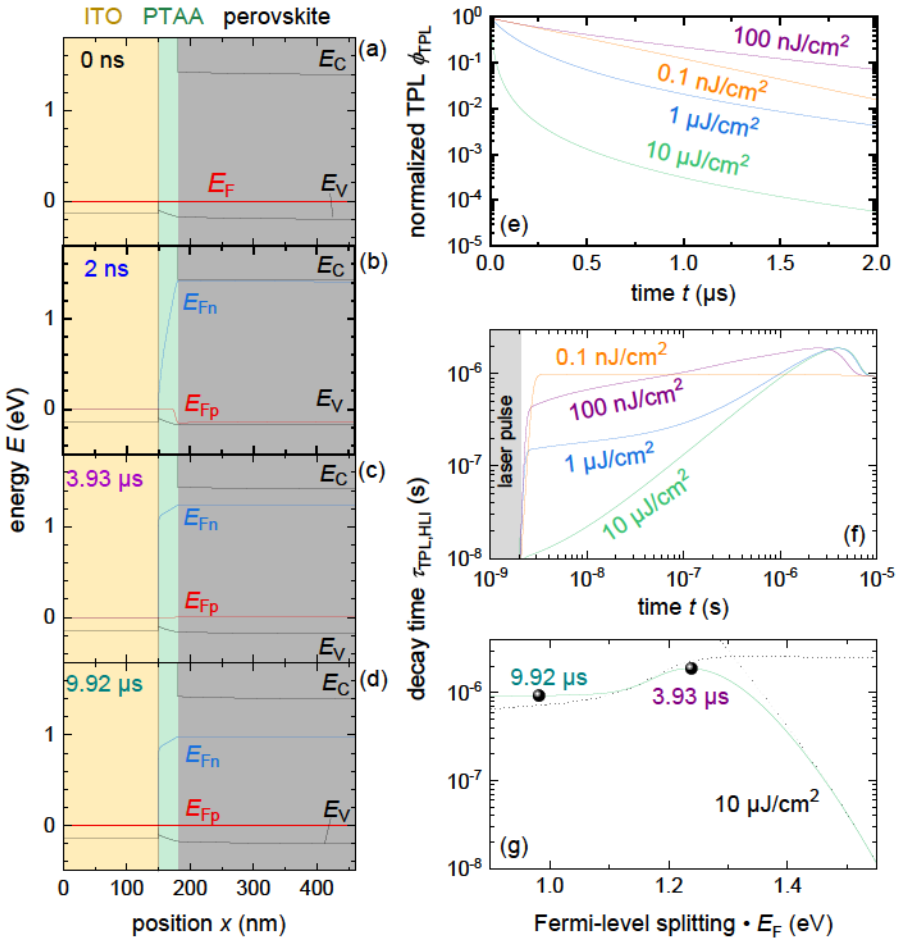

Abbildung 7.6: (a-d) Simulated band diagrams of a glass/ITO/PTAA/perovskite-layer stack at different time delays before and after the laser pulses. These times are (a) before the laser pulse, (b) directly after the end of the laser pulse, (c) at a delay of 3.93 µs when the quasi-Fermi level for holes $E_{F,p}$ is flat with the perovskite still being in high-level injection. Figure (d) shows the transient experiment after 9.92 µs, when the concentration of electrons in the perovskite is much lower than that for holes, corresponding to low-level injection. (e) Normalized PL transients and (f) decay time over time t for different laser fluences. Figure (g) shows again the decay time $\tau_{TPL,LLI}$ for the highest fluence, but as a function of the average quasi-Fermi-level splitting in the perovskite layer. The respective time steps for which the band diagrams are shown are highlighted. The perovskite/PTAA junction is a type-I heterojunction with interface-recombination velocities of $S_n = S_p = 0.01\,\mathrm{cms}^{-1}$. Moreover, the SRH-bulk lifetimes were set asymmetric to $\tau_n = 500\,\mathrm{ns}$ and $\tau_p = 2\,\mu\mathrm{s}$ enabling us to see the transition for high-level injection (HLI) to low-level injection (LLI).

different layers are brought into contact, charge-carrier injection from layers with higher electron or hole concentrations into layers with lower concentrations occurs. Since ITO is much more conductive than the organic semiconductor PTAA and the perovskite, the work function of the ITO sets the position of the Fermi level in the layer stack. As a result, holes are transferred into the PTAA and the perovskite. Therefore, the Fermi-level in the perovskite is much closer to the valence band edge energy level of valence band (E_V) than to the conduction band edge energy level of conduction band (E_C), which implies that the equilibrium-hole concentration (p_0) is substantially higher than the intrinsic charge-carrier concentration (n_i). Thus, the situation is comparable to the one in a doped semiconductor, even though the perovskite itself is assumed to be perfectly intrinsic. This behavior caused by the ITO contact leads to a transition between high- and low-level injection during the TPL measurement. Directly after up to 3.93 s after the laser-pulse excitation (Figure 7.6b-c) roughly equal densities of electrons and holes are present in the perovskite ($n \approx p$, HLI). In contrast, the density of electrons becomes much smaller compared to hole ($n \gg p$, LLI) at later times. Then the position $E_\mathrm{F,p}$ relative to the valence band E_V is approximately constant. Only $E_\mathrm{F,n}$ moves towards $E_\mathrm{F,p}$, further reducing the quasi-Fermi level splitting. This change in injection level also has an impact on the recombination rates. Since the ratio of electrons and holes is not constant and also not explicitly known, it is no longer possible to simplify the differential equation in Equation 2.60 for high- or low-level injection (e.g. $n = p$ or $n \gg p$). This lack of information complicates the interpretation of the decay time in terms of bulk or surface lifetimes. In order to better see the transition from HLI to LLI, I use asymmetric SRH-bulk lifetimes of $\tau_\mathrm{n} = 500\,\mathrm{ns}$ and $\tau_\mathrm{p} = 2$ s for the transient drift-diffusion simulations. In high-level injection ($n \approx p$) the lifetime from SRH recombination is given by $\tau_\mathrm{n} + \tau_\mathrm{p} = 2.5$ s. At lower Fermi-level splitting (LLI), the situation in this example can be described in a simplified manner by the rate equation

$$\frac{dn\,(t)}{dt} = -\frac{n\,(t)}{\tau_\mathrm{n}} \tag{7.1}$$

with the solution $\Delta n = \Delta n\,(0) \exp(-t/\tau_\mathrm{n})$. With p being approximately constant and fixed by the ITO work function, the photoluminescence flux will be only proportional to the minority-carrier density, i.e., $\phi_\mathrm{TPL} \propto n$. Thus, the decay time given

by Equation 2.48 will give $2\tau_n = 1\,\mu s$, with the factor 2 originating from the choice $m = 2$ that I use throughout this thesis. I observe this transition from $\tau_n + \tau_p$ to $2\tau_n$ when looking at the decay time curve vs. Fermi-level splitting (Figure 7.6g). A deviation from the value $\tau_{TPL,LLI} = \tau_n + \tau_p$ occurs because the transition from higher order recombination (radiative and Auger) to SRH recombination is not yet complete when the transition to LLI begins. The grey lines indicate this behavior.

Figure 7.7 summarize these findings by comparing the decay times for different ratios of electron and hole bulk lifetimes, highlighting the transition from HLI to LLI. The dotted lines are a guide-to-the eye and mark the respective lifetime values of $\tau_n + \tau_p$ (red) and $2\tau_n$ (blue). The dotted white lines show the simulations scenarios where only SRH or only radiative recombination is active. Note that these transitions from high- to low-level injection that may occur due to doping of the absorber or Fermi-level pinning due to the low or high work function of a contact layer create a dilemma for the definition of the decay time. I can either choose $m = 1$ or $m = 2$. No matter how I decide, it will affect the translation between decay time and lifetime in either of the two regimes.

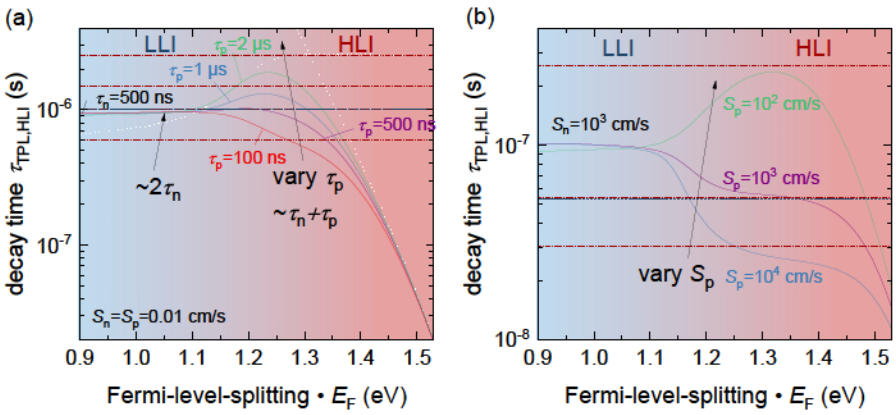

Abbildung 7.7: Decay times vs. quasi-Fermi level splitting from simulated transient PL of a glass/ITO/PTAA/perovskite stack, which result from drift-diffusion simulation conducted with Sentaurus TCAD. (a) Variation of the SRH-bulk lifetime for holes Shockley-Read-Hall bulk lifetime of holes ($\tau_{SRH,p}$) from 100 ns (red) to 2 µs (green) at a constant electron lifetime $\tau_n = 500$ ns, while the interface-recombination velocity is negligibly slow ($S_n = S_p = 0.01\,cms^{-1}$). (b) Variation of the surface-recombination velocity for holes (S_p) at a constant bulk lifetime and surface-recombination velocity for electrons of $S_n = 1000\,cms^{-1}$. Both changes translate into observable changes in the decay time, illustrating the transition from high- to low-level injection.

Figure 7.7b shows the corresponding situation for a case where interface recombination at the perovskite/PTAA becomes relevant. Here, I fix the SRH-bulk lifetime at $\tau_n = 500\,\text{ns}$ and $\tau_p = 1$ s, as well as the interface-recombination velocity for electrons at $S_n = 10^3\,\text{cms}^{-1}$, and vary the interface-recombination velocity S_p for holes. Likewise, I also see a change of the decay time $\tau_{TPL,LLI}$ at a Fermi-level splitting of ΔE_F of around 1.2 eV due to the transition from high- to low-level injection. In HLI, both interface-recombination velocities surface-recombination velocity for electrons (S_n) and S_p are relevant for the recombination rate, whereas in LLI, only S_n plays are role. Thus, the three curves converge to the same decay time value at very low Fermi-level energies. Since the bulk lifetimes are high, interface recombination is the dominant non-radiative process. Thus, $\tau_{TPL,LLI}$ should saturate to $2d_{pero}/S_n = 56\,\text{ns}$ but the actual value is almost twice as high. In addition, I would not expect to see any transition for the case of symmetrically chosen lifetimes $\tau_n + \tau_p$ and surface-recombination velocities $S_n + S_p$. The influence of space charge is the reason why the decay time at very low Fermi-level splitting differs from this estimation is the influence of space charge. In low-level injection, the high work function of the ITO leads to the creation of positive charge due to free holes inside the PTAA and the perovskite that is counterbalanced by negative charge at the ITO surface. This positive charge in the perovskite leads to band bending and, therefore, a slightly higher concentration of holes and lower concentration of electrons at the PTAA/perovskite interface as compared to the bulk of the perovskite. At the PTAA/perovskite interface, electrons are the minority carriers in low-level injection. Hence, the reduction of electron concentration leads to a slight increase in the decay time in low-level injection relative to high-level injection.

The situation is illustrated in Figure 7.8 in more detail. For the sake of clarity, I have chosen symmetrical bulk and surface lifetimes in this example. For this choice, I have expected that the decay time saturation values in HLI and LLI would be similar. Instead, the decay time vs. Fermi-level curve in Figure 7.8e also shows a clear transition from lower to higher decay time values. The representation of the carrier concentration of electrons and holes shown for the different times after the laser pulse in Figure7.8f-h confirms the explanation given above.

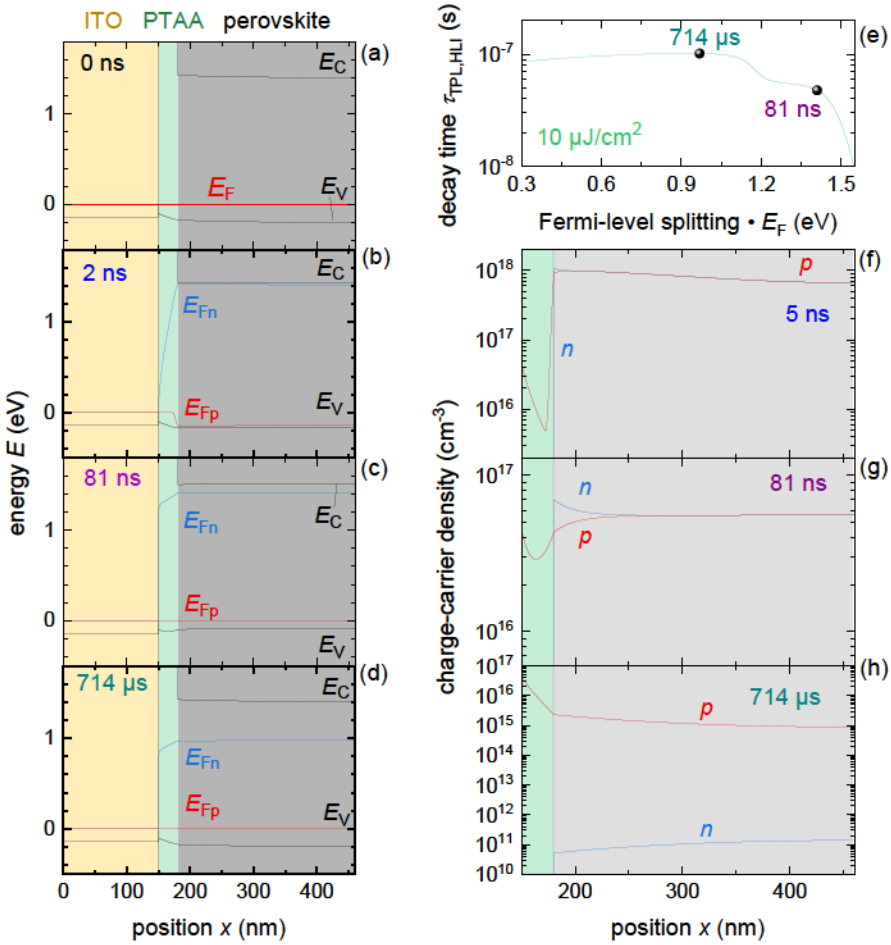

Abbildung 7.8: (a-d) Simulated band diagrams of a glass/ITO/PTAA/perovskite layer stack at different time delays before and after the laser pulses and (e) the corresponding decay time. The perovskite/PTAA junction is a type-I heterojunction with a high interface-recombination velocity of $S = 1000\,\mathrm{cms}^{-1}$. (e-f) Charge-carrier density of holes $p(x)$ and electrons $n(x)$ for the three exemplary times steps. For longer times (714 µs) there is a slightly higher concentration of holes and thereby lower concentration of electrons at the perovskite/PTAA interface as compared to the bulk of the perovskite. At the PTAA/perovskite interface, electrons are the minority carriers in low-level injection. Hence, the reduction of electron concentration leads to a slight increase in the charge-carrier lifetime in low-level injection relative to high-level injection. as shown by the decay time behavior. Table A.6 lists the other simulation parameters.

7.4 Complete Solar Cell Device Stack

This section presents the results from transient PL simulations of a planar, inverted MAPI solar cell, which material stack is discussed in detail in section 4.2. In the case of the TPL of complete perovskite solar cells, the charging and discharging of the device electrodes apparently add an additional effect, modifying the shape of the TPL decay. The mathematical problem can still be approximately described by an ordinary differential equation in time without any spatial dependences. This differential equation could be written as

$$\frac{dn\,(t)}{dt} = -k_{\mathrm{rad}} n(t)^2 - \frac{n\,(t)}{\tau_{\mathrm{SRH}}^{\mathrm{eff}}} - \frac{C_{\mathrm{area}}}{q d_{\mathrm{pero}}} \frac{dV_{\mathrm{ext}}\,(t)}{dt} \quad , \tag{7.2}$$

where C_{area} is the area-related capacitance in $\mathrm{F/cm^2}$, d_{pero} the thickness of the perovskite layer, V_{ext} the voltage between the electrodes. If I assume that the electron and hole densities scale with voltage as $n(t) = p(t) = n_{\mathrm{i}} \exp\left(qV_{\mathrm{ext}}\,(t)/2k_{\mathrm{B}}T\right)$, I can solve Equation 7.2 analytically, as shown later. The first two terms are well-known and represent radiative and non-radiative SRH recombination. The last term in Equation 7.2 represents a current that is necessary to charge and discharge the electrodes of the solar cell. It accounts for the change in surface-charge density on the cathode and anode of the device.

To illustrate these effects that occur in complete devices more clearly, Figure 7.9a-f presents the band diagrams, simulated by using the full differential equations that include charge transport, at different delay times during a TPL experiment. Figure 7.9b depicts the band diagram directly after the pulse has hit the sample, showing a substantial internal quasi-Fermi level splitting in the perovskite layer. In contrast, the external voltage V_{ext} at the outer contacts of the solar cell is still zero. In order to recognize this, one has to compare the Fermi levels in the ITO on the left, relative to the one in the silver contact on the right-hand side of Figure 7.9b. Figure 7.9c pictures the situation 5 ns after the laser pulse. At this stage, the quasi-Fermi level splitting in the perovskite is substantial and an external voltage has also been built up. However, there is still a substantial difference between the quasi-Fermi level splitting inside the perovskite absorber and the external quasi-Fermi splitting $\Delta E_{\mathrm{F,ext}} = qV_{\mathrm{ext}}$. Furthermore, there are large gradients dE_{Fn}/dx and dE_{Fp}/dx in

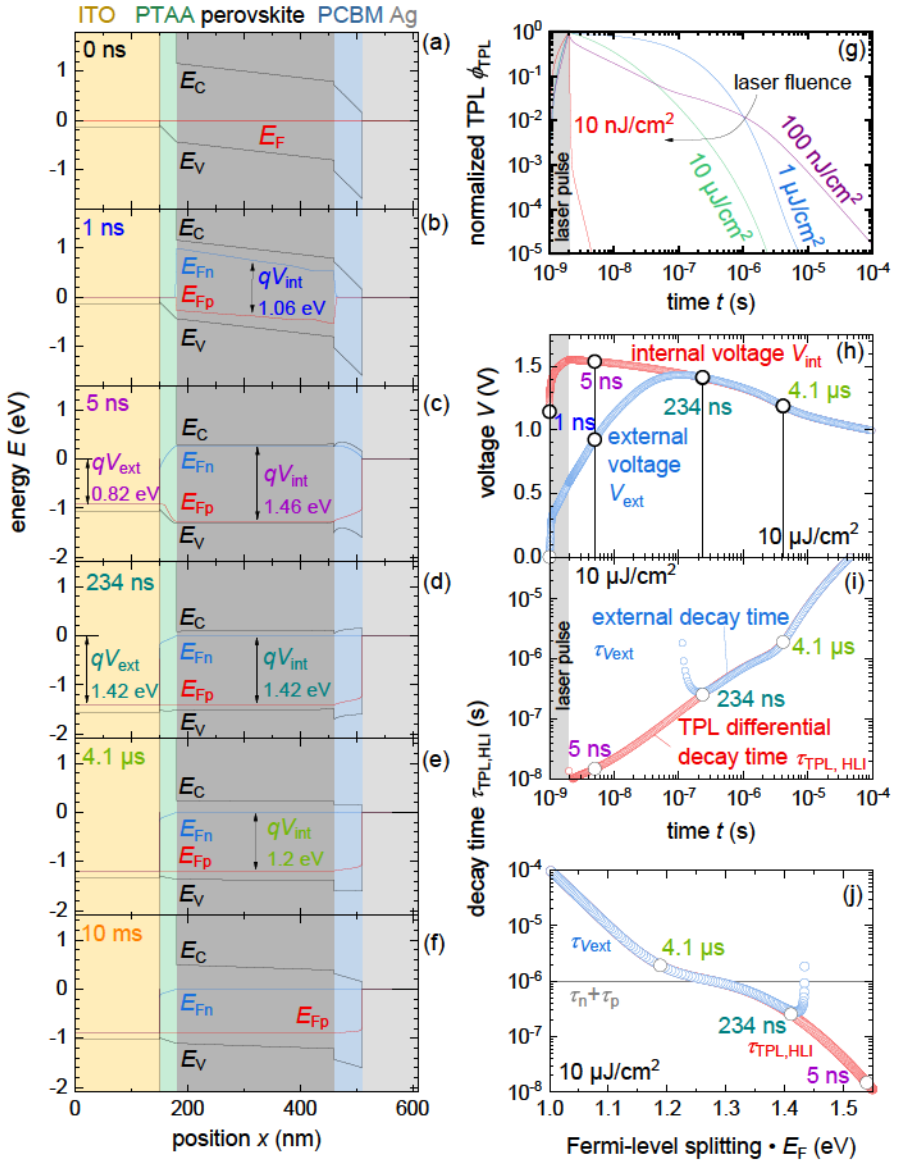

Abbildung 7.9: Numerical simulation results of a TPL experiment on a complete solar cell stack. (a-f) Band diagrams of the glass/ITO/PTAA/perovskite/PCBM/Ag stack for different time delays. (g) Normalized TPL transients for different laser fluences. Figure (h) illustrates how the externally measurable voltage $V_{ext} = \Delta E_{F,ext}/q$ between the contacts needs time to build up, while the internal Fermi-level-splitting $\Delta E_{F,int} = qV_{int}$ inside the cell is already present. (i) Differential time constant $\tau_{TPL,LLI}$ as a function of time or in (j) plotted versus ΔE_F for the highest excitation fluence of $10\,\mu J/cm^2$.

the quasi-Fermi levels inside the electron and hole transport materials. These gradients are necessary to drive the electron- $J_\mathrm{n} = n\mu_\mathrm{n} dE_\mathrm{Fn}/dx$ and hole-current density $J_\mathrm{p} = n\mu_\mathrm{p} dE_\mathrm{Fp}/dx$ that have to flow from the absorber to the contacts to change the amount of charge stored on the electrodes. Hence, the average internal voltage V_int is still substantially higher than the external voltage. Figure 7.9d shows the situation where the quasi-Fermi levels have equilibrated. Now the gradients dE_Fn/dx and dE_Fp/dx are nearly zero, which indicates that there is very little current flow to or from the electrodes. The internal and external voltage are equal and both will decay over time in the same way.

Suppose I simulate the photoluminescence transients for the device geometry presented in Figure 7.9a-f. In that case, I observe a strong dependence of the decay curve on the pulse energy of the laser. Figure 7.9g shows the decays normalized to their maximum. For the low pulse fluence of $10\,\mathrm{nJ/cm^2}$, the PL decays quickly and directly after the laser pulse has hit the sample. In this case, nearly all electrons and holes generated by the laser pulse are necessary to change the amount of charge on the device electrodes for a sufficient external voltage to build up. If, however, the pulse energy is higher, no abrupt fast decay at early times is visible because only a small fraction of photogenerated electrons and holes are needed to build up the external voltage. However, the initial decay is still not monoexponential because Auger- and radiative recombination in the absorber will now matter at early times. The combination of these effects leads to a difficult-to-interpret situation, where fast decays at early times are visible for very low and very high pulse energies but for completely different reasons.

Figure 7.9h summarizes the charging and discharging of the capacitance of the solar cell by showing how external and internal voltage change with time. The external voltage needs several hundred nanoseconds to build up. The reason for this delay is that electrons take a while to diffuse from the perovskite, where they were generated, through the ETL to the cathode (Ag) and holes through the HTL to the anode (ITO). This capacitive charging changes the surface-charge density on the cathode and anode of the device until the external voltage $V_\mathrm{ext} = \Delta E_\mathrm{F,ext}/q$ and the internal quasi-Fermi splitting $\Delta E_\mathrm{F,int} = qV_\mathrm{int}$ have equilibrated. Then, no further current is flowing. At longer times, when the charge-carrier concentration in the absorber decreases due to recombination, the reversed process takes place and

charge carriers are re-injected from the contacts into the interlayers. The electrode capacitance and the differential resistance of the solar cell limit this step.

Furthermore, Figure 7.9i-j presents the decay time plotted as a function of time or Fermi-level splitting. For the complete solar-cell device stack, the decay time $\tau_{\mathrm{TPL,LLI}}$ vs. ΔE_{F} consists of three regions discussed in the following. As mentioned before, if I assume high-level injection, it is still possible to derive an analytical relation describing the transient behavior that includes radiative recombination, SRH recombination and discharging of a constant capacitance. This most simplified model of the time-dependent processes in a complete solar cell can be described by the differential Equation 7.2. In this case, the solution of Equation 7.2 has to be expressed as time as a function of the Fermi-level splitting via

$$\begin{aligned} t = & \quad 1 - \frac{2k_{\mathrm{B}}T}{q}\frac{C_{\mathrm{area}}}{qd_{\mathrm{pero}}}k_{\mathrm{rad}}\tau_{\mathrm{SRH}}^{\mathrm{eff}} \quad \tau_{\mathrm{SRH}}^{\mathrm{eff}}\ln \quad \frac{n(0)+n(t)\,n(0)\,k_{\mathrm{rad}}\tau_{\mathrm{SRH}}^{\mathrm{eff}}}{n(t)+n(t)\,n(0)\,k_{\mathrm{rad}}\tau_{\mathrm{SRH}}^{\mathrm{eff}}} \\ & + \frac{2k_{\mathrm{B}}T}{q}\frac{C_{\mathrm{area}}}{J_0} \quad \exp \quad -\frac{\Delta E_{\mathrm{F}}(t)}{2k_{\mathrm{B}}T} \quad -\exp \quad -\frac{\Delta E_{\mathrm{F}}(0)}{2k_{\mathrm{B}}T} \\ = & \quad 1 - n_{\mathrm{Q}}k_{\mathrm{rad}}\tau_{\mathrm{SRH}}^{\mathrm{eff}} \quad \tau_{\mathrm{SRH}}^{\mathrm{eff}}\ln \quad \frac{n(0)+n(t)\,n(0)\,k_{\mathrm{rad}}\tau_{\mathrm{SRH}}^{\mathrm{eff}}}{n(t)+n(t)\,n(0)\,k_{\mathrm{rad}}\tau_{\mathrm{SRH}}^{\mathrm{eff}}} \\ & + \frac{n_{\mathrm{Q}}}{n_{\mathrm{i}}}\tau_{\mathrm{SRH}}^{\mathrm{eff}} \quad \exp \quad -\frac{\Delta E_{\mathrm{F}}(t)}{2k_{\mathrm{B}}T} \quad -\exp \quad -\frac{\Delta E_{\mathrm{F}}(0)}{2k_{\mathrm{B}}T} \end{aligned} \tag{7.3}$$

with $J_0 = qd_{\mathrm{pero}}n_{\mathrm{i}}/\tau_{\mathrm{SRH}}^{\mathrm{eff}}$, $n(t) = n_{\mathrm{i}}\exp\left(\Delta E_{\mathrm{F}}(t)/2k_{\mathrm{B}}T\right)$ Moreover, $n(0)$ equals the initial charge-carrier density due to the generation of the laser-pulse excitation. In addition, $n_{\mathrm{Q}} = 2k_{\mathrm{B}}TC_{\mathrm{area}}/\ q^2d_{\mathrm{pero}}$ is the charge per volume that is induced on the capacitor by two times the thermal voltage. Thus, in the situation $n < n_{\mathrm{Q}}$ would be fewer charge carriers in the absorber than in the contact. While I am not aware that Equation 7.3 has been previously presented in the literature, similar equations neglecting radiative recombination have been derived and used in the context of analyzing open-circuit voltage decay (OCVD) decays. There, the equation was used to derive a time-dependent open-circuit voltage and, subsequently, a differential time constant of a large-signal V_{oc} decay. [242–244] This explicit solution, stated in Equation 7.3 of the DGL system established in Equation 7.2, can become long and unwieldy. Thus, using an implicit solution that directly provides the decay time $\tau_{\mathrm{TPL,LLI}}$ is advantageous. Rewriting Equation 7.2 using relation $dV_{\mathrm{ext}}/dn =$

$2k_{\mathrm{B}}T/(qn)$ gives a functional dependence of the total kinetics of the charge-carrier density, namely

$$\begin{aligned}\frac{dn(t)}{dt} &= -k_{\mathrm{rad}}n(t)^2 - \frac{n(t)}{\tau_{\mathrm{SRH}}^{\mathrm{eff}}} \qquad 1+\frac{2k_{\mathrm{B}}T}{qn(t)}\frac{C_{\mathrm{area}}}{qd_{\mathrm{pero}}} \\ &= \frac{-k_{\mathrm{rad}}n(t)^2 - n(t)/\tau_{\mathrm{SRH}}^{\mathrm{eff}}}{1+n_{\mathrm{Q}}/n(t)} \quad .\end{aligned} \tag{7.4}$$

In this case, the dependence of the decay time on the actual carrier concentration is given by

$$\tau_{\mathrm{TPL,\ HLI}} = \tau_{\mathrm{cell,\ HLI}}^{\mathrm{LS}} = -\frac{n(t)}{dn(t)/dt} = \frac{n_{\mathrm{Q}}/n(t)\ +1}{k_{\mathrm{rad}}n(t)+1/\tau_{\mathrm{SRH}}^{\mathrm{eff}}} \quad . \tag{7.5}$$

Figure 7.10 illustrates Equation 7.3. Here, panel (a) shows the normalized TPL decays and panel (b) their decay times calculated via Equation 7.5 for three different SRH-bulk lifetimes $\tau_{\mathrm{SRH}}^{\mathrm{eff}} = \tau_{\mathrm{SRH}}^{\mathrm{bulk}} = \tau_{\mathrm{n}} + \tau_{\mathrm{p}}$, respectively 100 ns (yellow), 500 ns (red) and 2 s (blue). Furthermore, the external external radiative recombination coefficient (k_{rad}) is varied for a constant SRH lifetime of 2 s. Respective solutions are plotted in Figure 7.10b-c. Finally, I also vary the capacitance C_{area}, which controls the amount of charge that needs to be added to or subtracted from the electrodes to accommodate a change in V_{ext}. Its impact on the decay time is shown in the last two panels.With shorter SRH lifetimes and higher radiative coefficients, the PL transients on the left-hand side show a faster decay. However, one can hardly note any systematic differences or peculiarities in shape compared to the case of perovskite on glass. This picture changes when considering the decay times $\tau_{\mathrm{TPL,LLI}}$ versus quasi-Fermi-level splitting as in the panels on the right-hand side of Figure 7.10. In these plots, three different regions appear in the decay-time curve. This trend corresponds to the behavior shown in Figure 7.9j. At early times and high Fermi-level-splitting, I observe a charge-carrier-dependent lifetime that is already familiar to us and indicative of radiative recombination. Looking at Equation 7.4 confirms that the decay time of the solar cell approaches $\tau_{\mathrm{TPL,HLI}} \ \ n \gg 1/\ \ k_{\mathrm{rad}}\tau_{\mathrm{SRH}}^{\mathrm{eff}} \ \ \approx 1/(k_{\mathrm{rad}}n)$ for high carrier concentration, similar to the case without considering the capacitance. At slightly longer times and lower Fermi-level-splitting, $\tau_{\mathrm{TPL,LLI}}$ reaches a plateau and becomes approximately constant at a value $\tau_{\mathrm{SRH}}^{\mathrm{eff}} = \tau_{\mathrm{SRH}}^{\mathrm{bulk}} = \tau_{\mathrm{n}} + \tau_{\mathrm{p}}$. Further mathe-

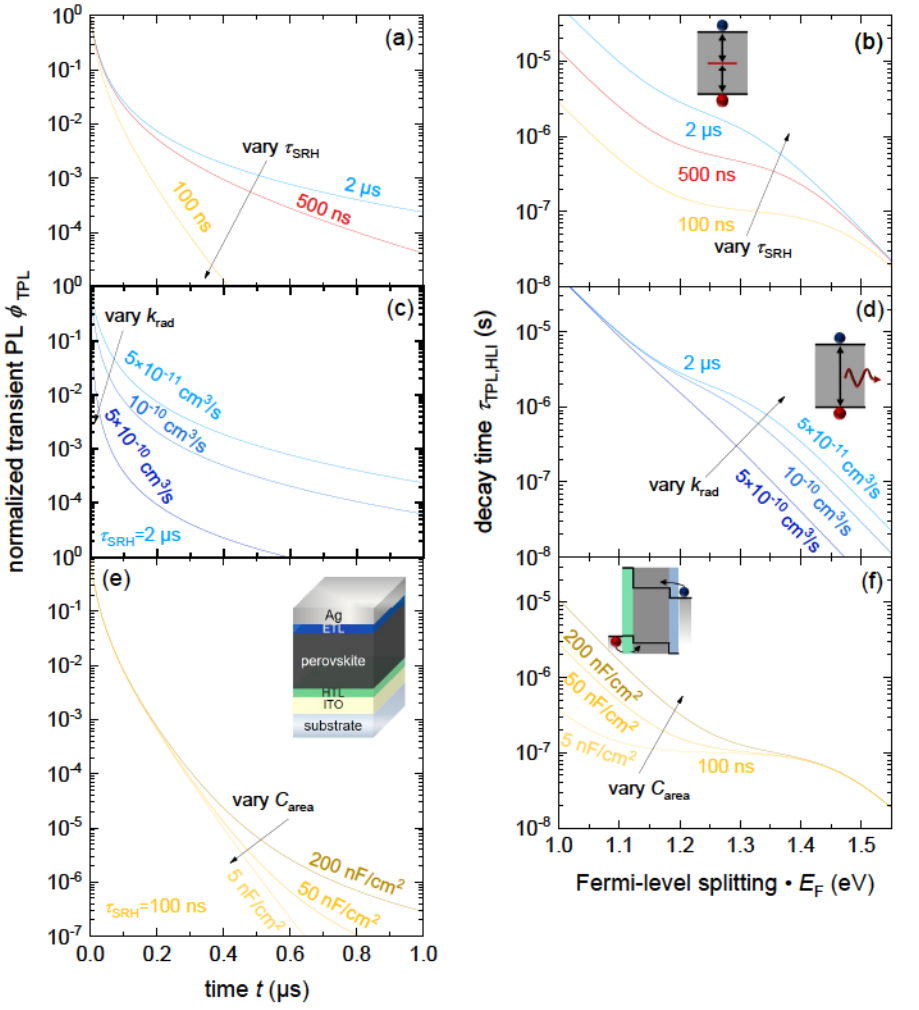

Abbildung 7.10: Illustration of normalized transient photoluminescence decays (left) calculated from the analytical solution of the simplified differential equation in Equation 7.3 and the decay time over quasi-Fermi level splitting (right) resulting from the implicit solution from Equation 7.4. The solution is valid for the case of high-level injection HLI and neglected Auger recombination, applicable to demonstrate the charge-carrier dynamics in a perovskite solar cell. (a-b) Results for varying SRH-bulk lifetimes $\tau_{SRH} = \tau_n + \tau_p$, namely 100 ns (yellow), 500 ns (red) and 2 µs (blue) are shown. (c-d) Effects due to changes of the radiative coefficients ($10^{-10}\,cm^{-3}s^1$, $5 \cdot 10^{-10}\,cm^{-3}s^1$, $5 \cdot 10^{-11}\,cm^{-3}s^1$). (e-f) Variation of the capacitance ($5\,nF/cm^2$, $50\,nF/cm^2$, $200\,nF/cm^2$) and its impact on the shape of the decay time at low ΔE_F. The discharging of the electrode capacitance prolongs the decay time.

matical analysis of Equation confirms that the inflection point (ip) of the decay time equals $\tau_{\mathrm{TPL,HLI}}(n_{\mathrm{ip}} = n_{\mathrm{Q}}/k_{\mathrm{rad}}\tau_{\mathrm{SRH}}^{\mathrm{eff}}) = \tau_{\mathrm{SRH}}^{\mathrm{eff}}$. New is the third region in the decay-time vs. ΔE_{F} plot at low Fermi-level splittings or carrier concentrations. The decay times for even smaller Fermi-level splitting further increase instead of staying on or near this plateau value of $\tau_{\mathrm{SRH}}^{\mathrm{eff}}$. Here, the SRH-dominated regime transitions into the exponentially voltage-dependent regime controlled by the ratio C_{area}/J_0. In this situation, charge-carrier recombination is limited by discharging of the electrodes and all curves exhibit an asymptotic behavior to $\tau_{\mathrm{SRH}}^{\mathrm{eff}} n_{\mathrm{Q}}/n$. Thus, the decay time $\tau_{\mathrm{TPL,LLI}}$ at small ΔE_{F} is higher for higher capacitances, demonstrated by the yellow curves in Figure 7.10f. The decay time $\tau_{\mathrm{TPL,LLI}}$ at low ΔE_{F} can be understood as an RC-time constant with the C being formed by the electrode capacitance of the contacts and the R being determined by the recombination resistance of the solar cell that increases exponentially towards smaller voltages as predicted by the diode equation. Hence, $\tau_{\mathrm{TPL,LLI}}$ is also increasing exponentially towards smaller ΔE_{F} as previously observed for large- and small-signal V_{oc} decays. [242–245]

The purpose of transient photoluminescence measurements is to determine recombination parameters in finished devices. Thus, the region at low times and medium to high quasi-Fermi level splittings ΔE_{F} is the relevant region that one would like to assess and use to extract parameters, such as bulk lifetimes, interface-recombination velocities and radiative recombination coefficients. This preference implies that the initial value $\Delta E_{\mathrm{F}}(0)$ of the Fermi-level splitting and hence also, the charge-carrier concentration $n(0)$ has to be high enough to observe the relevant range. Unfortunately, the different regimes can also merge into one another, making a clear separation no longer possible. This overlap occurs, e.g., for a combination of high radiative recombination coefficients and high bulk lifetimes. Then the decay time $\tau_{\mathrm{TPL,LLI}}$ is radiatively limited. The corresponding case is illustrated by the blue curves in Figure 7.10d that belong to a SRH-bulk lifetime of 2 s. For a radiative recombination coefficient of $k_{\mathrm{rad}} = 10^{-10}\,\mathrm{cm^3 s^{-1}}$, the plateau of the $\tau_{\mathrm{TPL,LLI}}$-curve is fully gone and the decay time runs almost straight. At this point, it is no longer possible to determine whether there is a limitation due to capacitive effects or fast radiative recombination. This means that identifying the recombination processes becomes particularly difficult for excellent devices with long effective SRH lifetimes.

With Figure 7.11, I confirm that numerical drift-diffusion simulations of a solar

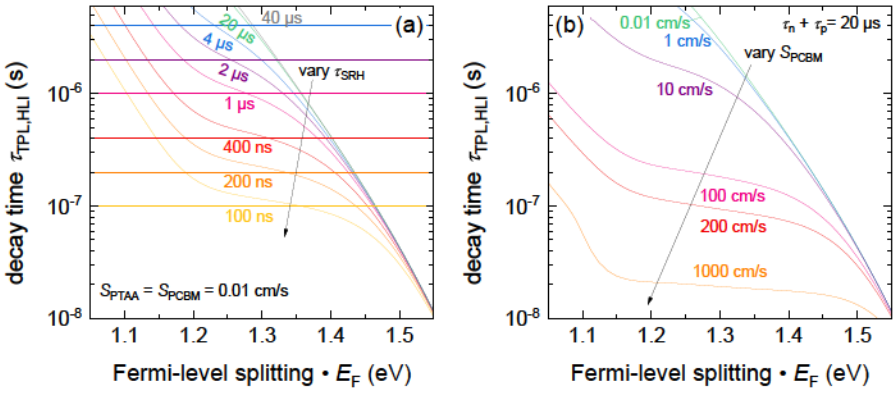

Abbildung 7.11: Decay times $\tau_{\mathrm{TPL,LLI}}$ vs. Fermi-level splitting resulting from numerical simulations of a transient PL of solar cell stack conducted with Sentaurus TCAD. (a) Simulation series where the SRH bulk lifetime is varied from 100 ns (yellow) to 40 µs (grey), while the interface-recombination velocities are low ($S = 0.01$ cm/s) for both absorber-transport layer interfaces. In panel (b) the opposite case is presented by keeping $\tau_n + \tau_p = 20$ µs constant and varying the interface-recombination velocity S_{PCBM} of perovskite/PCBM. Both changes translate into observable changes in the decay time. Additional simulation parameters are listed in Table A.6.

cell give a similar trend as the analytical relation. Figure 7.11a shows a variation of the SRH-bulk lifetime, varing from 100 ns to 40 µs. In this example, the interfaces between the perovskite absorber and the charge-extracting layers are chosen to be nearly ideal, using slow interface-recombination velocities and small energetic band offsets in the simulation. The transient simulations in Figure 7.9 use similar simulation parameters. Here again, the SRH-bulk lifetime correlates with the value of the decay time $\tau_{\mathrm{TPL,LLI}}$ near the inflection point of the curve and also the radiative limitation for high $\tau_n + \tau_p$ becomes apparent. Figure 7.11b deals with the case of varying interface-recombination velocities S_{PCBM} on the perovskite/PCBM side, while the SRH-bulk lifetime is high, namely $\tau_n + \tau_p = 20$ µs . For higher S_{PCBM} the decay time in the middle region around 1.2 to 1.4 eV drops.

7.5 Summary of Simulation Results

Finally, Figure 7.12 gives an overview of some exemplary effects that we have so far observed in the transient drift-diffusion simulations from Sentaurus TCAD of

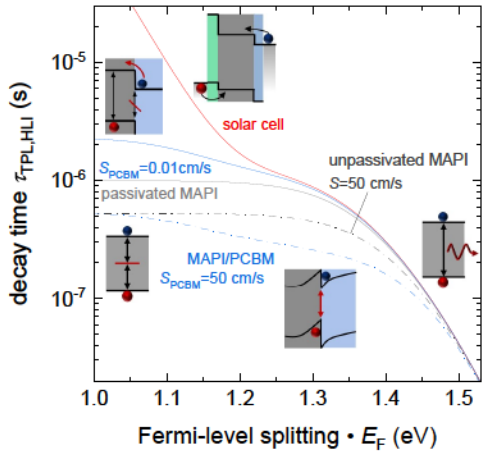

Abbildung 7.12: Summary of the fundamentally different effects that modify the decay time in different sample geometries. Bulk recombination (radiative and SRH) is the sole factor influencing the decay in a passivated perovskite layer (solid grey line)– the simplest possible sample geometry discussed here. In the presence of surface recombination (dot-dashed dark grey line), the decay time $\tau_{TPL,LLI}$ at low ΔE_F is reduced. In the case of a perovskite/ETL bilayer (blue curves), the shape of the decay time is fundamentally changed due to effects such as interface charging (dash-dotted blue line) and electron re-injection (solid blue line) from the ETL into the perovskite. In addition to interfacial charging, I also observe electrode charging and discharging when analyzing complete devices (red line). For those, $\tau_{TPL,LLI}$ increases exponentially towards lower values of ΔE_F.

the different sample types. This comparison illustrates how the sample type affects the charge-density-dependent decay time $\tau_{TPL,LLI}$. The simplest case of a passivated perovskite film on glass, plotted as a solid grey line, shows that fast radiative recombination dominates at high ΔE_F and the bulk lifetime of SRH recombination at low ΔE_F. For less well-passivated surfaces, the $\tau_{TPL,LLI}$-curve is essentially only shifted to lower decay times at lower values of ΔE_F, as the dot-dashed grey curve shows. An additional dip is observed for combinations of absorber with charge transfer layer, as illustrated by the dot-dashed blue curve. Here, interface charging and Coulomb-induced charge accumulation at the MAPI/PCBM interface lead to increased interface recombination and decay times that are reduced relative to the case of a MAPI layer with the same surface-recombination velocity but without the PCBM layer attached. For perovskite/ETL bilayers with substantial conduction-band offset but a recombination-inactive interface, I would observe additional effects due to

electron re-injection into the perovskite. This re-injection depends on the energetic barrier at the perovskite/ETL interface and leads to $\tau_{\mathrm{TPL,LLI}}$ values that can substantially exceed the SRH-bulk lifetimes of the perovskite itself. The decay time belonging to this case is the solid blue line. Finally, the solid red line represents the decay-time curve of a relatively well-behaved perovskite solar cell, where charging and discharging the electrode capacitance further influences $\tau_{\mathrm{TPL,LLI}}$. At open circuit, the capacitor can only discharge via recombination in the absorber layer or at its interfaces. Since the recombination resistance of the solar cell increases exponentially towards lower voltages, the decay time associated with electrode discharging increases exponentially, too.

7.6 Comparison to Experimental Data

Next, I want to apply and transfer our findings from the numerical simulations to experimental TPL data. Figure 7.13 shows experimental data obtained from photoluminescence measurements for two sample series, each featuring different multilayer stacks from the film on glass to the complete device. One sample series is based on solution-processed MAPI, while the second sample series uses coevaporated MAPI as absorber material (right side). Chapter 4 and 5 introduce these different device types and their solar cell performance. The results of the solution-processed samples are shown in the panels on the left, whereas the panels on the right-hand side belong to those of the coevaporated sample series. Note that the open-circuit voltages of the two solar cells are substantially different, even though the stack and the materials are nearly identical. The coevaporated, inverted, planar MAPI solar cell has an open-circuit voltage V_{oc} of only 1.05 V, while the solution-processed MAPI solar cell has a very high open-circuit voltage of 1.25 V. A more detailed discussion on this topic can also be found in chapter 4 and 5. Each sample series comprises a sample of glass/MAPI/TOPO that should be well passivated. The molecule n-trioctylphosphine oxide TOPO has been shown to strongly reduce surface-recombination velocities. [78, 130] Moreover, each sample series includes one sample with the hole-transport layer PTAA in addition that serves to characterize recombination losses at the PTAA/MAPI interface. The respective stack sequence is

glass/PTAA/MAPI/TOPO present in green. Finally, the complete cells are included,

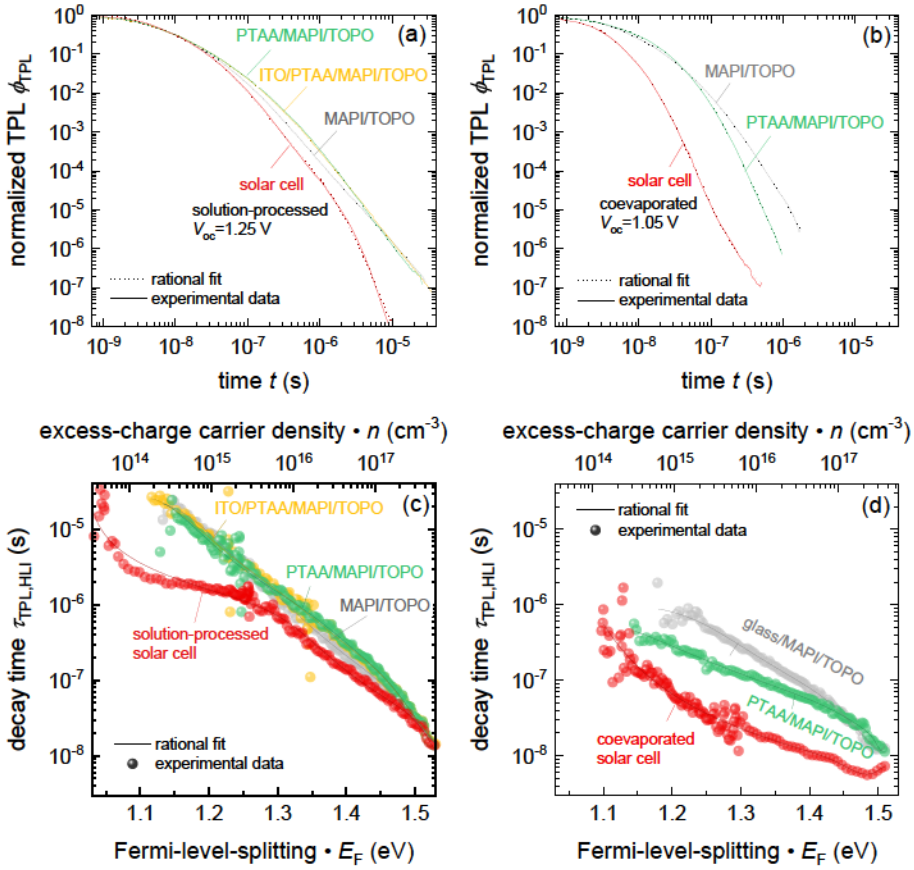

Abbildung 7.13: Experimental data of transient photoluminescence measurements on two different sample series, comparing coevaporated and solution-processed devices. The series starts with the passivated perovskite film (grey), goes further to MAPI with charge-extracting layer (PTAA (green), and finally shows the complete solar-cell device (red). A laser excitation fluence of $7.2\,\mu J/cm^2$ with a spot diameter of 3.8 mm was used for the measurements. Furthermore, a gated CCD camera detects the time-resolved PL. Stitching several measurements, recorded at different delay times after the laser pulse with different gains and integration times, enables a higher dynamic range. The method section presents further details. (a-b) Normalized photoluminescence decays over time. (c-d) Decay time $\tau_{TPL,LLI}$ assuming HLI ($m = 2$) versus quasi Fermi-level splitting ΔE_F. Solid lines are a guide-to-the eye, representing the derivative from TPL fits using a fifth-degree rational function.

which additionally feature the MAPI/ETL interface as another source of recombination. Figures 7.13a-b compare the normalized transient PL intensities ϕ_{TPL} and (c-d) the respective decay times $\tau_{\mathrm{TPL,LLI}}$ vs. quasi-Fermi level splitting ΔE_{F} for the two sample series described above. Each data set results from stitching several measurements recorded with a gated-CCD camera starting at different delay times after the laser pulse and using different gains and integration times. This approach is described in more detail in section 3.4.1 and enables a very high dynamic range of up to seven orders of magnitude. Note that this high dynamic is necessary to observe the wide range of physical phenomena discussed before.

Given the differences in V_{oc} of the two cells, I expect that the two sample series should differ in the recombination losses that occur either in the bulk or at interfaces. Thus, these differences should be reflected in differences in the decay times $\tau_{\mathrm{TPL,LLI}}$. If you look at Figures 7.13a-b, this qualitative expectation is confirmed already by studying the PL transients for the two sample series. In this comparison, all samples based on coevaporated perovskite layers have a substantially faster TPL decay. In order to obtain additional insights, I first determine the decay times shown in Figure 7.13c and (d) for the different samples of both sample series. Note that Figure 7.13 contains symbols and lines, where the symbols represent background-corrected and stitched and smoothed raw data, while the lines are the fits to the data. Both agree within the accuracy of the method. Further details regarding the data processing are stated in the method section 3.4.1, too.

From comparing the decay-time curves of the glass/MAPI/TOPO (grey) samples from the coevaporated and the solution-processed sample series in Figure 7.13c and (d), it is directly apparent that the quality of the bulk differs substantially. In addition, the coevaporated cell suffers from increased interface recombination relative to the solution-processed cell. I conclude this from the substantial reduction in $\tau_{\mathrm{TPL,LLI}}$ for the samples with interfaces (green and red) relative to the passivated layer on glass (grey). Furthermore, the comparison in Figure 7.13 demonstrates that the representation of the decay time $\tau_{\mathrm{TPL,LLI}}$ via Fermi-level-splitting ΔE_{F} is advantageous compared to the usual representation of the decay itself. This new type of graph highlights differences and similarities between the samples more clearly and allows for an estimation of recombination parameters.

The TPL data sets were fitted with transient simulations from Sentaurus

TCAD to quantify and extract these material and device parameters. Figure 7.14 presents the experimental data for $\tau_{\mathrm{TPL,LLI}}$ of the two sample series compared with the simulations that best reproduce the experimental data. First, I simulated the glass/perovskite/TOPO stacks (grey) to determine the recombination coefficients of the perovskite bulk material. The decay time $\tau_{\mathrm{TPL,LLI}}$ of experimental data is dominated by radiative recombination over the complete range of quasi-Fermi level splitting that is experimentally accessible and constantly increases for smaller ΔE_{F}. This behavior implies that SRH lifetimes must be extremely long. The matching simulations use SRH-bulk lifetimes of $\tau_{\mathrm{n}} + \tau_{\mathrm{p}} = 80$ s. Furthermore, Figure A.3a in the Appendix displays what the simulations with lower SRH lifetimes look like. From Figure A.3a, I conclude that the agreement between simulation and experiment deteriorates substantially for lifetimes $\tau_{\mathrm{n}} + \tau_{\mathrm{p}} < 40$ s. SRH-bulk lifetimes as high as 80 s would allow an open-circuit voltage of 1.31 V under AM1.5g illumination, i.e., a value very close to the radiative limit of 1.32 V. [246] The solution-processed samples with PTAA (green, yellow) do not suffer from additional losses. The decay times are similar to the passivated sample with the glass/perovskite interface. Therefore, the band offset between perovskite and PTAA and the surface-recombination velocity must be negligibly small. With Figure A.3 in the Appendix, I demonstrate that a surface-recombination velocity must be around $S_{\mathrm{PTAA}} = 1\,\mathrm{cms}^{-1}$. Also, the band offset and surface recombination at the PCBM/perovskite interface must be quite small to explain the data. Nevertheless, the PCBM/perovskite interface is the only interface that causes visible deviations of the PL transients from the behavior expected in the radiative limit. I find that an interface-recombination velocity $S_{\mathrm{PCBM}} = 17\,\mathrm{cms}^{-1}$ and an offset of 70 meV lead to the best agreement with the experimental data. Note that the decay-time curve for the solution-processed cell reproduces the typical curve shape, being predicted by Equation 7.4.

Moreover, it should be noted that the corresponding current-voltage characteristic of a simulated solar cell device calculated with these stated simulation parameters also agrees well with the measured JV-characteristic. Figure A.5 in the Appendix presents a respective comparison. Another implication from the data shown in Figure 7.14a is that for perovskite films and layer stacks with small recombination losses, the measured differential time constants may assume nearly any value (from tens of ns to tens of ms), depending on the range of carrier concentrations and

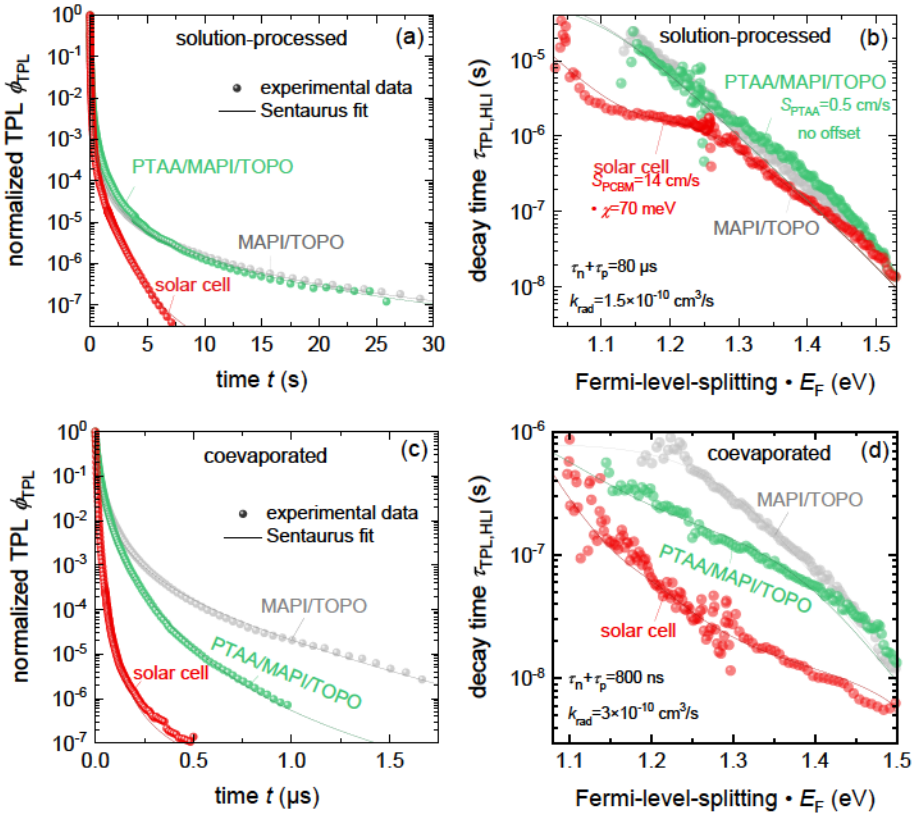

Abbildung 7.14: Experimental data of transient photoluminescence measurements of the solution-processed sample series and fits from Sentaurus TCAD allow us to state the material parameters that best describe the sample behavior. All simulation parameters are listed in Table A.7 and A.8.

quasi-Fermi level splitting that are set by the laser fluence. Without the additional information on the laser fluence and without high dynamic range data as shown here, the information obtained from TPL data on many high-quality layers or layer stacks would be either difficult to compare or entirely meaningless.

In the following paragraph, I want to discuss the fitting of the coevaporated sample series, representing an example of samples with a higher degree of non-radiative recombination. A SRH-bulk lifetime of about $\tau_n + \tau_p = 750\,\text{ns}$ best describes the experimental TPL data of coevaporated bulk passivated with TOPO in the

glass/MAPI/TOPO stack (grey). This SRH-bulk lifetime would allow much higher open-circuit voltages than the 1.05 V the coevaporated solar cell has. If no additional recombination losses would occur in the stack, a SRH-bulk time of 750 ns and an effective radiative recombination coefficient of $k_{\mathrm{rad}} = 2 \times 10^{-10}\,\mathrm{cm^3 s^{-1}}$, would allow an open-circuit voltage of about 1.23 V. The simulations suggest that these additional recombination losses of 180 mV of the coevaporated solar cell are caused by misaligned energy levels and enhanced recombination at both interfaces. Interface recombination at the PTAA/MAPI interface of the coevaporated sample leads to slightly shorter decay times at small Fermi-level splitting (green), as opposed to the samples without extra charge-extracting layers (grey). Note that these two decay time curves overlap well at high ΔE_{F}, where radiative and Auger recombination dominate $\tau_{\mathrm{TPL,LLI}}$. A band offset of $\Delta\chi = 100\,\mathrm{meV}$ and a surface recombination velocity of $S_{\mathrm{n}} = S_{\mathrm{p}} = 100\,\mathrm{cm^3 s^{-1}}$ best explain the trend of the PTAA/perovskite interface. Since the PTAA layer is very thin, I would expect that $\tau_{\mathrm{TPL,LLI}}$ saturates for small ΔE_{F} at around 400 ns. However, the decay time at small ΔE_{F} is much higher and increases beyond the bulk lifetime. If I assume shallow, neutral defects, I also observe this behavior in our simulations. Thus, in the simulation that best fits the experimental data, the defects are shallow and positioned only 150 meV away from the valence band edge. These parameters would still allow a Fermi-level splitting of 1.18 V in simulated PTAA/perovskite stack. Also, the properties of the perovskite/fullerene (C_{60}) interface in the solar cell (red) are quite complex. In this case, the decay time is roughly two orders of magnitudes lower, suggesting the additional interfacial losses in V_{oc} must be higher. Only for smallΔE_{F} does the decay time increase again, indicating that the loss is caused by a huge conduction band offset,e.g., $\Delta\chi = 200\,\mathrm{meV}$. In order to explain the shape of $\tau_{\mathrm{TPL,LLI}}$ vs. ΔE_{F} curve that deviates from the typical S-shape, I had to assume at least two different defect states. A deep-level defect is responsible for the loss in open-circuit voltage. A second shallow defect is added in the simulations to match the shape of the differential decay curve. While I note here that various defect properties such as its charge, concentration, or energetic and spatial position affect the TPL, it is beyond the scope of this thesis to present a systematic investigation of the influence of these parameters on the decay time $\tau_{\mathrm{TPL,LLI}}$.

7.7 Conclusions

Transient photoluminescence experiments are abundantly used in the field of halide perovskite photovoltaics to study charge-carrier recombination in the bulk and at interfaces. While the interpretation of TPL on thin films on glass has been thoroughly discussed and used in the literature, [125, 226, 246] the most substantial recombination losses are often occurring at the interfaces between the absorber and the charge-transfer layers. [196] Moreover, the presence of charge-transfer layers can also impact how the perovskite films grow, affecting the bulk and surface quality of the perovskite layer. Thus, there is a clear need to extend our theoretical understanding to TPL measurements done on various sample geometries, including zero, one, or two charge-transfer layers in contact with the perovskite absorber. In addition, it is important also to understand how contact layers, such as ITO or Ag, affect the TPL decay and to be able to comprehend measurements done on complete devices.

This chapter provided an extensive account based on a combination of experimental data, numerical simulations with Sentaurus TCAD and analytical solutions to differential equations that allows the reader to understand the mechanisms affecting a TPL decay in a variety of sample geometries. I introduced the concept of a decay time displayed as a function of the time-dependent quasi-Fermi level splitting as a key tool to analyze the data. This plot allows us to combine data conducted at different laser fluences in one Figure. Furthermore, the stitching improves the comparability of different data sets. The carrier-density dependent decay time of a full device is affected by various recombination mechanisms (radiative, Auger and SRH recombination), by charge transfer between the absorber and the charge-transport layers and by capacitive charging and discharging of the electrodes. I have shown how to distinguish these different mechanisms by their appearance at different values of the quasi-Fermi level splitting and by their characteristic slope in the decay time vs. quasi-Fermi level splitting diagram.

After introducing the general concepts via numerical simulations, I applied my findings to experimental data sets on different sample geometries and absorber deposition methods: solution-processed vs. coevaporated fabrication. I determined the TPL decays over seven orders of magnitude in dynamic range. Furthermore, this chapter demonstrated that our previously presented recipe for MAPI layers allows

bulk lifetimes of several tens of s, as a value of 80 s for the sum of electron and hole lifetimes yielding the best fits. In addition, the TPL transients clearly indicate negligible losses at the MAPI/PTAA interface and only moderate losses with surface-recombination velocities of $17\,\mathrm{cms}^{-1}$ for the MAPI/PCBM interface.

8 Consistent Interpretation of Optical and Electrical Transients

Transient photoluminescence (TPL) and transient photovoltage (TPV) measurements are popular and frequently applied methods to study recombination dynamics and charge-carrier lifetimes in the field of halide-perovskite photovoltaics. However, large-signal TPL and small-signal TPV decay times often correlate poorly and differ by orders of magnitude. A theory that explains this huge discrepancy is so far missing. Usually, these differences are not further discussed.

In this chapter, I present a consistent framework of the different "lifetime" concepts, which connects the small-signal and large-signal decay time and reveals that suitable measurement conditions and data-analysis methods are essential for getting meaningful results. A combination of experiment, numerical modeling and description of data via simple analytical equations helps to understand what the different methods actually measure and to demonstrate that a consistent multi-method quantitative data analysis is possible.

8.1 Meta-Analysis of Literature Data

Transient photoluminescence TPL is only one of the various other transient methods used to study the charge-carrier dynamics in metal-halide perovskite films, layer stacks and solar cells. Unfortunately, in most cases, charge-carrier concentrations are not directly measured. Instead, various observable quantities are detected as a function of time after excitation, being more or less closely related to the charge-carrier concentration. These measurable quantities include luminescence, [136, 137] voltage, [243,247,248]conductivity [158,165,249] as well as the amount of free carrier

absorption. [231, 250] In addition, time constants related to recombination are also extracted from frequency domain methods. [251–253]

Among these different options, two rather common and jointly used modes of detection in the field of metal-halide perovskite research are measurements of transient photoluminescence TPL and the transient photovoltage TPV. While TPL measurements are preferably performed on pure perovskite films, electrical detection via TPV requires complete solar cell devices. The PL signal during a TPL experiment is proportional to the product np of electrons and holes, [29, 35] while TPV as a small-signal measurement measures an excess voltage ΔV_{oc} that is assumed to be proportional to the laser-induced excess-carrier concentration $\Delta n_{\mathrm{laser}}$. [139] I refer to section 3.4 for a detailed description of these two methods. In both cases, it is common in literature to report decay-time constants that result from exponential fits to the TPL or TPV data. Usually, the authors report an improved "lifetime" constant in both methods if comparing, for example, a novel process or interlayer with a reference. Figure 8.1 presents data collected from literature, [186, 200, 203, 254–270] which compares decay times extracted from these two techniques plotted against each other. Figure 8.1 shows that these two decay-time constants from exponential fitting differ by up to four orders of magnitude, with the correlation between the decay times being extremely poor. This level of discrepancy cannot easily be explained by the detection mode alone. While there is an abundance of studies that uses both techniques to characterize perovskite films or devices, [186, 200, 203, 254–270] a theory that connects the two decay times with each other is so far missing. The community has seemingly accepted that values are always compared from sample to sample but never from method to method. The lack of understanding what these decay-time constants mean, how they are related to each other and their variation by several orders of magnitude undermines the ability of the research community to understand and compare recombination and the concept of charge-carrier lifetimes.

One of the most obvious differences is that TPV is an electrical technique measured on devices. In contrast, TPL is typically measured on perovskite layers or layer stacks but rarely on full devices. While a perovskite layer has two surfaces that may potentially cause substantial recombination losses, the glass/perovskite interface is usually of high electronic quality. Alternatively, the perovskite surface can easily be passivated using insulating molecules such as TOPO [78] or (3-

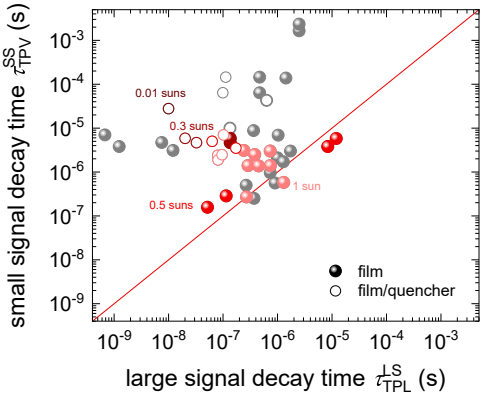

Abbildung 8.1: Data collection from literature, comparing the decay time τ_{TPL}^{LS} of the transient PL measured on perovskite films (filled symbols) or on perovskite/transport layer stacks (blank symbols) with the stated decay-time constant τ_{TPV}^{SS} resulting from transient photovoltage measurements on the respective solar cell device. The color code represents the bias-light intensity during the TPV experiment ranging from light red (1 sun) to dark red (0.01 suns). No information about the bias illumination level is available for the grey data points. The bisecting line (red) is a guide-to-the-eye and highlights where both decay-time constants are equal. The comparison of these decay times highlights that they correlate poorly and can differ by orders of magnitude. Interestingly, the time constant from the TPV measurement is usually longer, although recombination losses are expected to be higher in the complete solar cell than in the pure perovskite film. Table A.9 lists the publications from which the meta-data were extracted.

aminopropyl)trimethoxysilane (APTMS). [271] In contrast, completed devices have additional layers and interfaces that have to support charge extraction and, therefore, cannot easily be passivated with electrically insulating molecules. Thus, one might expect that recombination in devices is always enhanced relative to a well-passivated perovskite film on glass. Consequently, time constants measured on devices in TPV should generally be shorter than in TPL on films. However, Figure 8.1 shows that the opposite is true, with decay times from transient photovoltage often drastically exceeding those measured from time-resolved photoluminescence. This result may be partly due to the lack of good surface passivation for the films measured in TPL. Nevertheless, the major contribution will be the influence of slow capacitive effects originating from the electrode discharging via the perovskite diode. [243, 245, 272, 273] While the resulting long decay times are still related to recombination, they are much longer than the actual charge-carrier lifetimes of the

bulk material. Note that I have already introduced and elaborated on this capacitive effect in more detail in the previous chapter in the section 7.4 about the TPL signal of complete solar cell devices.
In this chapter, I will study and explain the discrepancies between the two methods and show that quantitatively consistent results are obtained if suitable measurement conditions and data analysis methods are used. In order to compare the meaning of the decay times extracted from the two experimental methods, it is first necessary to establish the key differences between them. TPV and TPL differ in potentially three major aspects. These three major differences are (i) the sample type, e.g., single layer, layer stack or full device, (ii) the type of perturbation, namely large-signal vs. small-signal analysis, and (iii) the mode of detection, which could be either optical or electrical. I have already described the impact of the sample type on the TPL in detail in the last chapter. Therefore, I will focus less on these specifics here. I will start with the general differences between large- and small-signal analysis. Afterwards, I will discuss the impact of the different observables, namely voltage and luminescence, on the decay times.

8.2 Large-Signal versus Small-Signal Analysis

To help understand the different measurement principles and conditions, Figure 8.2 compares simulated band diagrams of a perovskite solar cell for both situations. These transient simulations were also conducted with TCAD Sentaurus by Synopsys, which uses the finite element method to solve several differential equations, including the continuity equations for electrons and holes and the Poisson equation. The band diagrams on the left-hand side of Figure 8.2 belong to the large-signal TPL, the ones on the right to the small-signal TPV measurement condition at different delay times after the laser-pulse excitation. Figures 8.2a-b depict the respective band diagram for the initial situation before the laser pulse impinges on the sample. The comparison of these two band diagrams already shows a decisive difference between the two methods.

In TPL, the sample is in thermal equilibrium in the dark, which can be recognized by the equilibrium-Fermi level before it is excited by the laser beam. However,

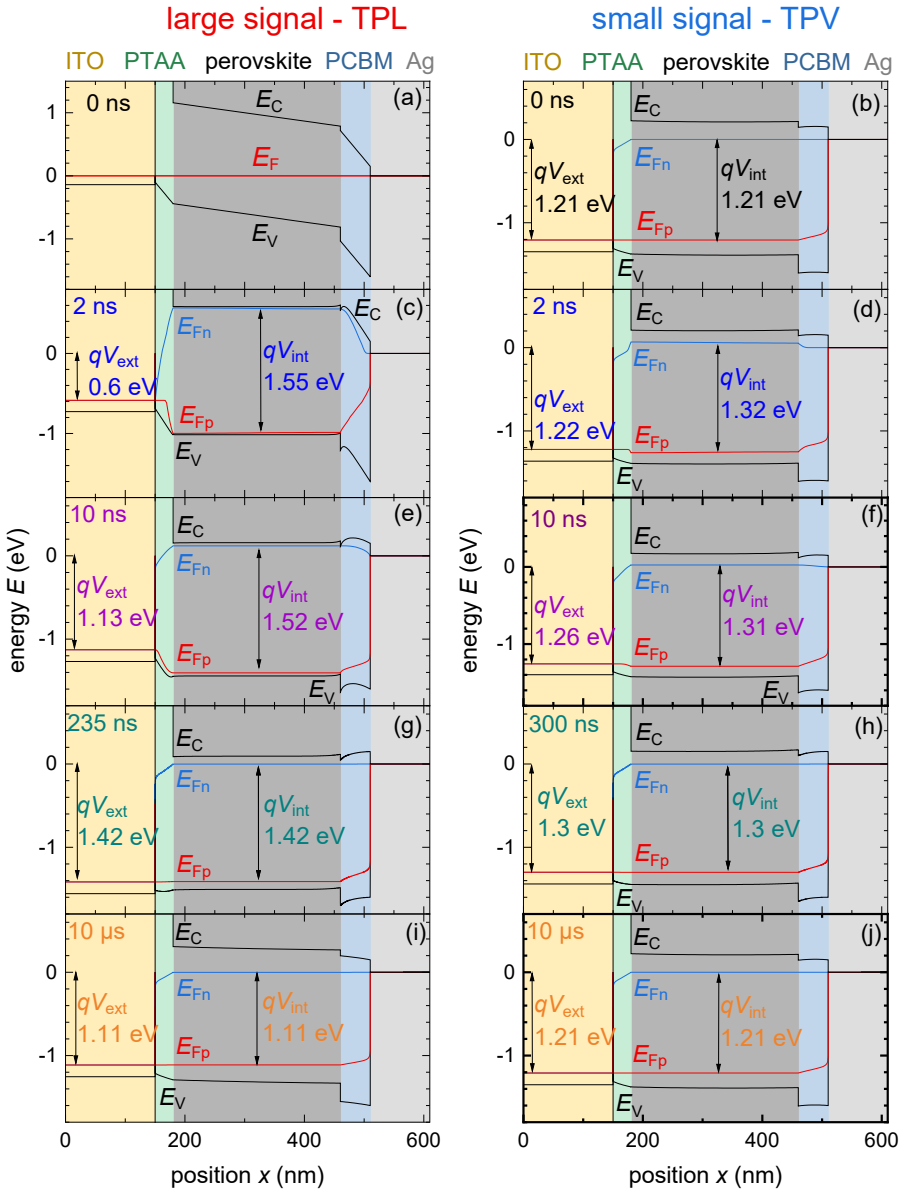

Abbildung 8.2: Band diagrams of a perovskite solar cell before and at different time delays after the laser-pulse excitation for transient photoluminescence (right side) compared to a transient photovoltage experiment (left side). (a-b) Situation before the sample get photoexcited by the laser pulse (100 nJ/cm^2). In the TPL experiment, the sample is initially in the dark, while for TPV the sample is kept at open circuit at a certain bias-light intensity. (c-d) Situations directly after the end of the laser pulse, (e-f) after 10 ns, (g-h) after several hundreds of nanoseconds and (i-j) after 10 s.

the solar cell in the TPV situation is already in an excited, but stationary, state due to the illumination with a bias-light intensity of, e.g., 0.1 suns. This bias causes an internal quasi-Fermi level splitting and externally measurable voltage of 1.21 V. Figures 8.2c-d show the band diagrams directly after the laser-pulse excitation. For TPV, only a small laser fluence of $100\,\mathrm{nJcm^{-2}}$ is used to meet the small-perturbation condition. Therefore, the increase in internal quasi-Fermi level splitting $\Delta E_{\mathrm{F,int}} = qV_{\mathrm{int}}$ in the perovskite is hard to recognize, whereas in the TPL experiment a massive change from zero to 1.55 eV is directly visible. In both cases, it takes some time for the generated charge carriers in the absorber to spread over the entire solar cell and reach the external contacts. Thus, the external voltage V_{ext} has not changed significantly yet compared to the change in internal voltage. The gradients dE_{Fn}/dx and dE_{Fp}/dx in the quasi-Fermi levels inside the electron- and hole-transport materials drive the electron- $J_{\mathrm{n}} = n\mu_{\mathrm{n}} dE_{\mathrm{Fn}}/dx$ and hole-current density $J_{\mathrm{p}} = n\mu_{\mathrm{p}} dE_{\mathrm{Fp}}/dx$ from the absorber to the contacts to change the amount of charge stored on the electrodes. How fast this equilibration takes place depends on the transfer velocity and mobility of the contact-layer materials, as well as on the capacity of the electrodes.

In this example, it takes several hundred nanoseconds for the large-signal and small-signal case to adjust with the corresponding band diagrams depicted in Figures 8.2g-h. Concerning the TPV, it should be noted that some excess-charge carriers have then already recombined before the actual decay of the photovoltage even begins. This delayed alignment between the internal and external state of the solar cell can affect the result of the measurement and can make data interpretation even more difficult. This additional challenge will be the subject of the next chapter. However, this study focuses on the decay behavior at longer times where the assumption of equilibrated Fermi levels over the contact layers is more likely to be accurate than at shorter times. For the analytical description of the methods, I even go one step further and assume that the coupling between the interior and exterior of the solar cell is ideal.

The last two band diagrams plotted in Figure8.2i-j show the situations for TPL and TPV after 10 s. The solar cell in the TPV experiment is back to its initial state, which is determined by the steady-state illumination intensity. In contrast, the quasi-Fermi level splitting in the TPL situation continues to decrease. The electrons and holes flow back from the electrodes through the ETL and HTL

to the perovskite. This process depends on the RC time constant. The electrode forms the capacitance C. The recombination resistance of the solar cell determines $R = dV/dJ$ that increases exponentially towards smaller voltages as predicted by the diode equation.

8.2.1 Analytical Description

Metal-halide perovskites stand out due to their very low doping densities. [102] Thus, both charge-carrier types, electrons and holes, are typically present in approximately the same concentrations during TPL and TPV experiments. This behavior complicates data interpretation compared to other solar-cell technologies. Usually, high doping densities ensure at all times that only minority carriers dominate the charge-carrier dynamics and all recombination rates are linear in minority-carrier concentration. As I will show in the following, this missing universal linear dependency has the consequence that large- and small-signal lifetime definitions are no longer identical in the case of high-level injection HLI. Note that in the current literature on perovskites [243], it is sometimes stated that the small-signal and large-signal approaches lead to similar solutions. This statement is generally incorrect and especially for perovskites, where nonlinear radiative terms will dominate at higher voltages and carrier densities. In contrast, the fact that small-signal and large-signal decay times are different by a factor as long as recombination rates are nonlinear in carrier concentration is a well-known fact in the literature dealing with TPV transients in organic or dye-sensitized solar cells. [274–277] Here this factor is often called reaction order.

For simplicity, this study starts with a comparison of the small- and large-signal definitions for the more straightforward case of a perovskite film on glass and discusses the implications for the perovskite solar cell afterwards. For small-signal analysis, the sample is examined at a particular working point. For example, this stationary bias-point state is set by a continuous bias-light illumination of the sample, creating a respective steady-state carrier density n_{bias} for this given excitation level. A small perturbation, e.g., due to a short laser pulse, creates a small amount of additional charge-carriers $\Delta n_{\mathrm{laser}}(t)$ that recombine with time. Figure 8.2d shows this small perturbation in the band diagram. If a bias illumination is present, we

must consider the steady-state photogeneration rate G of excess-charge carriers. Therefore, the differential equation describing the charge-carrier dynamics in the perovskite absorber must be adjusted for the small-signal situation. It follows that

$$\frac{dn(t)}{dt} = -R(n) + G = -k_{\mathrm{rad}} n(t)^2 - \frac{n(t)}{\tau_{\mathrm{SRH}}^{\mathrm{bulk}}} + G \ , \tag{8.1}$$

where t is the time passed after the end of the laser pulse. Due to the bias illumination, the carrier density $n(t) = n_{\mathrm{bias}} + \Delta n_{\mathrm{laser}}(t)$ consists of these two contributions, namely the constant, steady-state carrier density n_{bias} at a given time independent bias-photogeneration rate G and the additional time-dependent part given by $\Delta n_{\mathrm{laser}}(t)$.
The small-signal decay time $\tau_{\mathrm{film,HLI}}^{\mathrm{SS}}$ at a given carrier concentration n_{bias}, resulting from a linearization at this operating point, is then given by

$$\tau_{\mathrm{film,HLI}}^{\mathrm{SS}} = -\frac{dn(t)}{d(dn(t)/dt)} = \frac{1}{dR/dn} = \frac{1}{2k_{\mathrm{rad}} n_{\mathrm{bias}} + 1/\tau_{\mathrm{SRH}}^{\mathrm{eff}}} \ . \tag{8.2}$$

The continuous generation rate G can be omitted for a large-signal experiment. Thus, inserting $G = 0$ gives the DGL system we are already familiar with. In this case, the dependence of the large-signal carrier concentration decay time on the actual carrier concentration $n(t)$ is defined by

$$\tau_{\mathrm{film,HLI}}^{\mathrm{LS}} = -\frac{dt}{d\ln(n(t))} = -\frac{n(t)}{dn(t)/dt} = \frac{1}{k_{\mathrm{rad}} n(t) + 1/\tau_{\mathrm{SRH}}^{\mathrm{eff}}} \ . \tag{8.3}$$

Note that Equation 8.3 gives the large-signal decay for a film on glass as a function of carrier density $n(t)$ varying as a function of time. Therefore, it could also be presented as a function of time, carrier density or even Fermi-level splitting, using the relation $\Delta E_{\mathrm{F}} = k_{\mathrm{B}} T \ln\ n^2/n_{\mathrm{i}}^2$.

Comparing the implicit expressions for the large- and the small-signal decay in Equations 8.2 and 8.3 directly reveals that the decay times are only equal in the linear regime at small charge-carrier densities, when SRH recombination dominates. In contrast, the large- and small-signal decays differ by a factor of 2 once radiative recombination dominates. This factor would go up to 3 if Auger recombi-

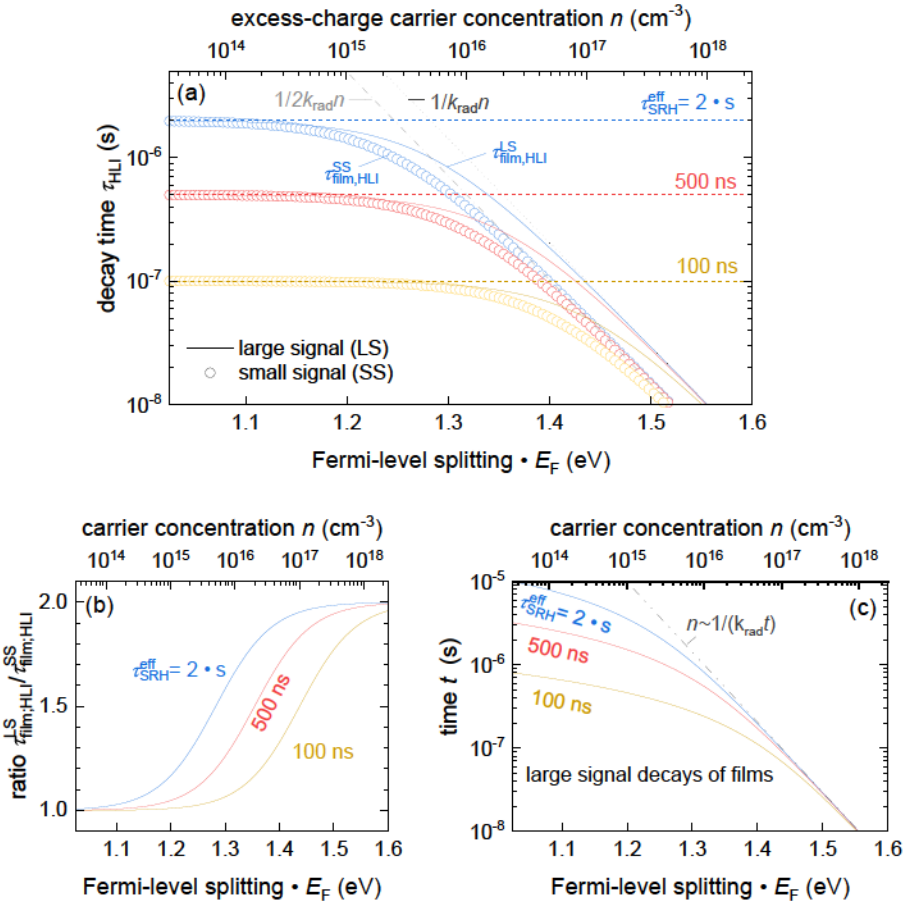

Abbildung 8.3: (*a*) Comparison of the small- (dotted symbols) and large-signal (solid lines) decay times as a function of the Fermi-level splitting ΔE_F or charge-carrier concentration n, which result from the analytical solutions of the differential equations 8.1 for high-level injection used to describe an undoped perovskite film on glass with a passivated surface. The photogeneration G is zero for the large-signal measurement mode. Furthermore, a variation of the SRH lifetime is shown, where τ_{SRH}^{eff} equals 100 ns (yellow), 500 ns (red) or 2 µs (blue). Moreover, I used a thickness of 280 nm, $k_{rad} = 10^{-10}\,cm^3s^{-1}$, $n_i = 8.05 \times 10^4\,cm^{-3}$, and an initial charge-carrier concentration of $10^{20}\,cm^{-3}$ for the calculation. Small- and large-signal decay times are similar in the SRH-dominant region at medium to low Fermi-level splittings. At high Fermi-level splitting, the decay times from the small-signal and the large-signal differential equations do not overlap and differ by a factor of 2. Thus, decay times resulting from the small-or large-signal approach differ if nonlinear recombination mechanisms are present but should give identical results for lower carrier densities, where rates $R(n)$ that are linear in n dominate recombination. Figure8.3b summarizes this observation and gives the ratio of large- to small-signal decay time. (c) Explicit solution of the large-signal differential equation, illustrating the relation between time after the laser excitation as a function of ΔE_F and n, respectively.

nation were present and dominant. Figure 8.3 summarizes these findings from the comparison of the large- and small-signal measurement mode for the scenario of a perovskite film with SRH and radiative recombination being present. Figure 8.3a illustrates the large- and small-signal decay times computed via Equations 8.2. Additionally, it shows 8.3 for three different SRH lifetimes as a function of carrier density, depicted by the top x-axis, or the associated quasi-Fermi level splitting ΔE_{F}, stated by the bottom x-axis. Here, the solid lines belong to the large signal, while the point symbols represent the small-signal decay time. It is essential to know that in order to compare large-signal and small-signal decay times, only one decay is needed for the large-signal case. However, many small-signal decays are calculated at different bias levels represented by the parameter n_{bias} in Equation 8.2. Each data point plotted over this charge-carrier density n represents such a respective calculation at a different bias level.

It is directly apparent that the small- and large-signal decay times change with charge-carrier concentration, as predicted by Equations 8.2 and 8.3. Thereby, decay times cover a wide range of values and can differ by many orders of magnitude per method and sample depending on the charge-carrier level. Thus, it is essential to compare the values of small-signal decay time from different samples at similar bias-charge carrier concentrations n_{bias}. Otherwise, the comparison loses significance. Furthermore, two regions can be identified in each decay-time curve, whereby both decay times are constant and approach the effective SRH lifetime at low carrier concentrations or low ΔE_{F} and transition to shorter values by decreasing exponentially with higher charge-carrier concentration or higher ΔE_{F}. At high charge-carrier concentrations, higher-order recombination mechanisms, in this example radiative recombination, dominate and define the shape of the large- and small-signal decay times. In this radiatively dominated region, these two decay times do not overlap. This difference is further illustrated in Figure 8.3b, which gives the ratio of the two decay times that converges towards the value two for higher quasi-Fermi level splittings. If Auger recombination is present, this ratio could increase further toward three.

These discrepancies between small- and large-signal detection modes, which occur when nonlinear recombination mechanisms dominate, are also found in the case of a complete solar cell device, as I will demonstrate in the following. Here,

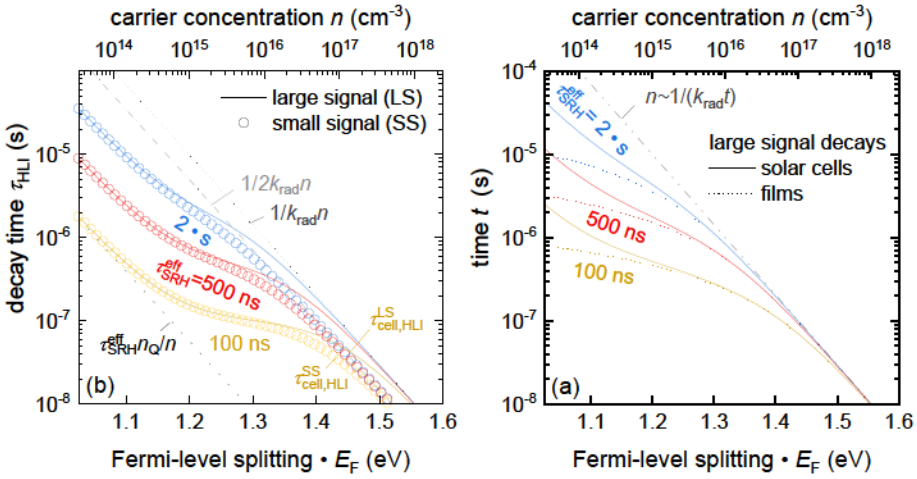

Abbildung 8.4: (*a*) Comparison of the small- (dotted symbols) and large-signal (solid lines) decay times as a function of the Fermi-level splitting ΔE_F or charge-carrier concentration n, which result from the implicit analytical solutions of the differential equations for high-level injection used to describe a perovskite solar cell. Small- and large-signal decay times are stated for three different SRH lifetimes, namely τ_{SRH}^{eff} equals 100 ns (yellow), 500 ns (red) or 2 µs (blue). The capacitance is set to $C_{area} = 50\,nF/cm^2$, whereas further input parameters are chosen to be similar as in Figure 8.3. In the capacitance-dominated, as well as in the SRH-dominated region, both decay-time definitions give comparable results. Whereas the small- and large-signal decay times at the radiatively dominated region differ by a factor of 2. (b) Explicit solution of the large-signal differential equation ($G = 0$), illustrating the relation between time t after the laser excitation as a function of ΔE_F and n, respectively. Including the junction charging (solid lines) leads to a slowing down of all three transients in the range $n < n_Q$ as compared to the transients without junction charging (dotted lines).

the differential equations for small- and large-signal condition must be extended by a term describing the capacitive charging and discharging of the electric contacts, which results in

$$\frac{dn(t)}{dt} = -k_{rad} n(t)^2 - \frac{n(t)}{\tau_{SRH}^{bulk}} - \frac{C_{area}}{q d_{pero}} \frac{dV_{ext}(t)}{dt} + G \quad . \tag{8.4}$$

C_{area} is the area-related capacitance in units of F/cm^2 and V_{ext} is the voltage between the electrodes. This capacitance controls the amount of charge that needs to be added to or subtracted from the electrodes to accommodate a change in external voltage. Thus, this contribution also changes the charge-carrier concentration in the

perovskite-absorber layer. Details and further assumptions regarding this capacitive contribution were discussed in the last chapter in section 7.4. The differential equation for the small-signal case with bias illumination must again additionally consider the continuous photogeneration rate G, whereas for a large-signal experiment, no bias light is present and $G = 0$ applies in Equation 8.4. By rewriting Equation 8.4, being executed in an analogous way as for a Equation 7.4 in the last chapter, I obtain

$$\frac{dn(t)}{dt} = f(n) = \frac{G - k_{\mathrm{rad}} n(t)^2 - n(t)/\tau_{\mathrm{SRH}}^{\mathrm{bulk}}}{1 + n_{\mathrm{Q}}/n(t)} = \frac{G - R}{1 + n_{\mathrm{Q}}/n(t)} \quad . \tag{8.5}$$

The small-signal decay time results from taking the derivative df/dn as linearization. Inserting Equation 8.5 and using mathematical transformation gives

$$\tau_{\mathrm{cell,HLI}}^{\mathrm{SS}} = \frac{dn(t)}{df(n)} = -\frac{1}{dR/dn} = \frac{n_{\mathrm{Q}}/n(t) + 1}{2k_{\mathrm{rad}} n(t) + 1/\tau_{\mathrm{SRH}}^{\mathrm{eff}}} \tag{8.6}$$

as small-signal decay time. This respective implicit solution differs from the large-signal decay time defined by

$$\tau_{\mathrm{cell,HLI}}^{\mathrm{LS}} = -\frac{n(t)}{f(n)} = -\frac{n(t)}{dn(t)/dt} = \frac{n_{\mathrm{Q}}/n(t) + 1}{k_{\mathrm{rad}} n(t) + 1/\tau_{\mathrm{SRH}}^{\mathrm{eff}}} \tag{8.7}$$

as this direct comparison demonstrates. Figure 8.4 compares these two decay-time definitions for the case of a complete solar cell. In the capacitive-dominated regime at low charge-carrier concentrations, as well as in the SRH-dominated regime, small- and large-signal decay times are similar. In contrast, both differ by a factor of 2 at high carrier densities. Here, the curves of the decay times approach $\tau_{\mathrm{cell,HLI}}^{\mathrm{SS}} \approx 1/(2k_{\mathrm{rad}}n)$ and $\tau_{\mathrm{cell,HLI}}^{\mathrm{LS}} \approx 1/(k_{\mathrm{rad}}n)$.

8.3 Influence of the Mode of Detection on the Decay Times

So far, I have discussed the general differences between small-signal and large-signal methods, as well as between samples that contain a single semiconductor layer as opposed to complete solar-cell devices that contain a non-zero capacitance due to

their electrodes. The remaining difference between TPL and TPV measurements are the mode of detection and the way how the decay times are derived from the respective observables, namely the PL photon flux $\phi_{\mathrm{TPL}}(t)$ and the external voltage decay $\Delta V_{\mathrm{oc}}(t)$. In case of TPL, this detected photon flux $\phi_{\mathrm{TPL}}(t)$ under HLI conditions will be proportional to $np = n^2$ and hence the TPL decay time is defined via

$$\tau^{\mathrm{LS}}_{\mathrm{TPL,\ HLI}} = \left(-\frac{1}{2}\frac{d\ln(\phi_{\mathrm{TPL}})}{dt}\right)^{-1} = \left(-\frac{d\ln(n)}{dt}\right)^{-1}. \tag{8.8}$$

Note that the factor 1/2 in the second term of Equation 8.8 adjusts to the large-signal decay time or $\tau^{\mathrm{LS}}_{\mathrm{film,HLI}}$ or $\tau^{\mathrm{LS}}_{\mathrm{cell,HLI}}$ of the carrier concentration under high-level injection conditions. Another typical approach in literature is based on mono- or biexponential fitting of the large-signal PL decay in order to extract the slow decay-time constant at long delay times. Sometimes people also extract a second time constant at the fast initial decay at early times after laser-pulse excitation. The respective TPL-time constants from literature, being presented in Figure 8.1, are calculated with this fitting approach. While the respective decay-time constant from a fit of the fast initial PL decay has no specific physical meaning, the slow decay-time constant might yield the effective, non-radiative SRH lifetime. However, this approach is only suited if applied to single perovskite films on glass in the SRH-dominated regime at a low excitation level. Critically, it is hard to ensure that the employed laser fluence really meets this excitation level, especially when measuring high-quality layers in which radiative recombination still dominates even at lower charge-carrier concentrations. Here the decay looks monoexponential at first sight because the decay is prolonged, although the slope from the derivative shows the opposite and keeps increasing. Therefore I recommend using Equation 8.8 when analyzing large-signal TPL data to retain all the information instead of using mono- or biexponential fitting functions.

In the case of TPV, the excess-open circuit voltage $\Delta V_{\mathrm{oc}}(t)$ is used to detect the excess-carrier density. Again, under high-level injection, we have

$$\begin{aligned}\Delta V_{\mathrm{oc}} &= \frac{k_{\mathrm{B}}T}{q}\ln\left(\frac{n^2}{n_{\mathrm{i}}^2}\right) - \frac{k_{\mathrm{B}}T}{q}\ln\left(\frac{n_{\mathrm{bias}}^2}{n_{\mathrm{i}}^2}\right) = 2\frac{k_{\mathrm{B}}T}{q}\ln\left(\frac{n}{n_{\mathrm{bias}}}\right) \\ &= 2\frac{k_{\mathrm{B}}T}{q}\ln\left(1+\frac{\Delta n_{\mathrm{laser}}}{n_{\mathrm{bias}}}\right)\end{aligned}. \tag{8.9}$$

The typically used approach in literature [139], which I explained in the method section 3.4.2 in more detail, is now to assume that $\mathrm{d}\Delta V_{\mathrm{oc}}/\mathrm{d}t \propto \mathrm{d}\Delta n_{\mathrm{laser}}/\mathrm{d}t$ holds if the excess voltage is sufficiently small. Let us briefly discuss this approach critically since generating an infinitesimally small voltage amplitude in experimental practice is impossible. Also Wood et al. [278] have previously shown that this linearization causes errors in determining the correct decay time. Thus, I want to estimate this corresponding error in the following. Assuming that $\Delta n_{\mathrm{laser}}$ decays exponentially, one might expect that also ΔV_{oc} decays exponentially with the same time constant τ. However, if I insert $\Delta n_{\mathrm{laser}}(t) = \Delta n_{\mathrm{max}} \exp(-t/\tau)$ into Equation 8.9, I obtain a decay that is not monoexponential and a decay time of the ΔV_{oc}-decay that is given by

$$\tau^{\mathrm{SS}}_{\mathrm{TPV,HLI}} = -\frac{dt}{d\ln(\Delta V_{\mathrm{oc}})} = \tau\left\{1+\frac{1}{\gamma}\exp\left(\frac{t}{\tau}\right)\right\}\ln\left\{1+\gamma\exp\left(-\frac{t}{\tau}\right)\right\} \quad . \tag{8.10}$$

Here, γ relates the additional charge carriers generated by the pulse to the charge carrier levels under bias illumination, being defined by $\gamma = \Delta n_{\mathrm{laser}}/n_{\mathrm{bias}}$. Importantly, $\tau^{\mathrm{SS}}_{\mathrm{TPV,HLI}}$ is a function of time and not a constant. Only for long times $t >> \tau$ or small values of the ratio γ, Equation 8.10 approaches $\tau^{\mathrm{SS}}_{\mathrm{TPV,HLI}} = \tau$. Therefore it also makes sense to form the inverse logarithmic derivative of the entire small-signal TPV decay via Equation 8.10, instead of using monoexponential fitting, since the

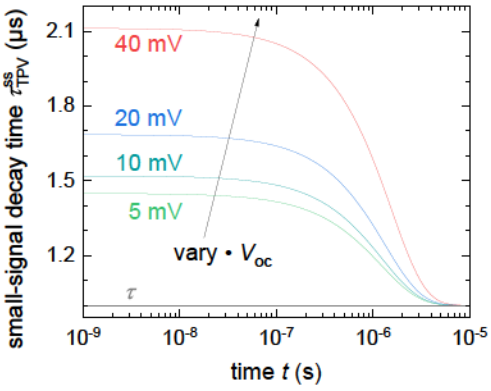

Abbildung 8.5: Calculated impact of a variation of the laser excitation strength during the small-signal TPV, which induces a change in the open-circuit voltage of ΔV_{oc}.

$\tau^{\mathrm{SS}}_{\mathrm{TPV,HLI}}$ at long times tend to approximate the actual time constant at the respective operating point. Moreover, the exact mode of fitting can lead to variations in the extracted decay time values. Figure 8.5 summarizes these findings by plotting $\tau^{\mathrm{SS}}_{\mathrm{TPV,HLI}}$ versus time for various voltage offsets ΔV_{oc}. As shown by Figure 8.5, for realistic values of γ or $\Delta V_{\mathrm{oc}} = k_{\mathrm{B}} T \ln(\gamma)$ respectively, there can be differences between the decay times $\tau^{\mathrm{SS}}_{\mathrm{TPV,HLI}} = \tau$ and τ. This deviation could, for example, affect trends and comparisons between different samples or measurements at different operating points if the voltage perturbation ΔV_{oc} is not constant. However, this error is on the order of a factor 2 or less. Therefore, it does not explain the large discrepancies between literature data from TPL and TPV introduced in Figure 8.1.

In conclusion, decay times from TPL contains deviations due to misused mono- or biexponential fitting, as well as TPV-decay times due to a discrepancy between experimental practice and ideal small-signal approximation. Additionally, the mathematical definitions of the small- and large-signal decay times differ if nonlinear recombination mechanisms are present. Therefore results from large-signal TPL and small-signal TPV analysis should differ per definition. Most importantly, the decay times from both methods are functions of the charge-carrier concentration. Typically, the trend of these decay-time curves gives shorter decay-time values the higher this carrier concentration gets. Furthermore, the decay time values measured on complete solar cell devices are getting progressively longer the lower the charge-carrier density becomes due to the capacitance discharging of the electrodes. Thus, even the extracted decay-time values measured with one method on one sample can vary by orders of magnitude depending on the injection level. Consequently, this additional information is essential for comprehensively comparing decay-time values from different methods or sample types from various publications. Hence, the corresponding information on the injection level and the sample geometry must also be stated for comparability of decay-time values.

8.4 Experimental Data

Finally, I want to apply and transfer our findings to experimental data and show that a consistent multi-method quantitative data analysis from time-resolved photo-

luminescence and transient photovoltage is possible. For this purpose, it is essential to compare data at equal charge-carrier density or quasi-Fermi level splitting and to identify whether the decay in a particular range is consistent with radiative or some type of SRH recombination or rather dominated by capacitive effects. I performed TPL and TPV measurements on the same solution-processed perovskite solar cell using the setup illustrated in Figure 3.2. Note that I have already discussed the results from TPL measurements of this particular solution-processed MAPI solar cell and its layer stacks in many details in the last chapter 7.6. Here, I focus on comparing the large-signal TPL and small-signal TPV decay times.

Figure 8.6 shows these small-signal decay times represented by the blue star symbols as a function of the external open-circuit voltage V_{oc}, which are extracted by fitting the TPV transients recorded at different bias-light intensities. Figure 3.5a and (b) have already shown the respective transient photovoltage decays. Additionally, red spheres present the large-signal decay times $\tau^{\mathrm{LS}}_{\mathrm{TPL,HLI}}$ versus the quasi-Fermi-level splitting $\Delta E_{\mathrm{F}} = qV_{\mathrm{oc}}$ derived from TPL by using Equation 8.8. The TPL data set results from stitching several measurements recorded with a gated-CCD camera, starting at different delay times after the laser pulse and using different gains and integration times as described in section 3.4.1. Note that the part of the TPL decay-time curve below 1.1 eV is part of the data that corresponds to the PL decay approaching the noise level at long delay times. Here, the decay times look particularly noisy. This poor data quality is because the procedure of taking the derivative of the raw data amplifies the already pronounced noise even further. Therefore, this part of decay-time data should not be considered to be overly trustworthy. However, this approach of merging several TPL data sets enables a very high dynamic range that is necessary to get data sets from TPL and TPV that partially overlap. Typically TPV measurements are conducted at relatively low bias-light illuminations that often do not exceed several suns. The opposite applies to the TPL condition. Here, small laser-pulse fluences in TPL experiments are more difficult to implement due to the reduced signal quality and require longer integration times. Therefore both methods are typically conducted at very different injection levels, which is one reason for the high deviations between the values illustrated in the meta-analysis from literature in Figure 8.1. Suppose only one decay time constant is reported. In that case, the result strongly depends on the laser fluence and excitation density at

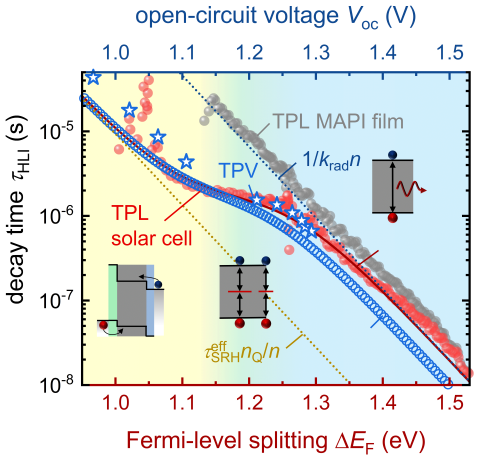

Abbildung 8.6: Experimental data of the decay time derived from large-signal TPL measurements of a perovskite solar cell and small-signal TPV measurements at different bias illumination intensities. Furthermore, solutions resulting from the analytical description of the large- $\tau^{LS}_{cell_H LI}$ and small-signal decay times $\tau^{SS}_{cell_H LI}$ are also plotted. These calculations are conducted, using $k_{rad} = 1.5 \times 10^{-10}\,cm^3 s^{-1}$ and $\tau^{eff}_{SRH} = 1.7$ s as recombination coefficients, an absorber thickness of 280 nm, an electrode capacitance of $C_{area} = 10\,nF/cm^2$ and an intrinsic charge-carrier concentration of $n_i = 8.05 \times 10^4\,cm^{-3}$.

which the solar cell is evaluated, with decay times varying from tens of nanoseconds to tens of microseconds.

If I now compare the resulting small- and large-signal decay times for the perovskite solar cell, I can see that the data sets overlap and complement each other. In addition, both experimentally determined decay-times curves show the anticipated course, consisting of three regions in accordance with the analytical solutions that were derived in the last section 8.2.1 are illustrated in Figure 8.4. Figure 8.6 also shows the respective adjusted solutions to the analytical Equations as guide-to-the eye.

8.5 Sentaurus TCAD Simulations

With Figure 8.7, I confirm that the trend of the analytical relation can also be obtained in numerical simulations of a solar cell using Sentaurus TCAD. Transient

device simulations were conducted for the TPL situation, using a laser fluence of $10\,\mu J/cm^2$ and TPV condition at different bias illumination intensities ranging from 0.01-1000 suns. In Figure 8.7a a comparison of the resulting small- and the large-signal decay times as a function of the internal (TPL) or external (TPV) Fermi-level splitting is illustrated for varying SRH-bulk lifetimes ($100\,ns - 20\,\mu s$). In this example, the interfaces between the perovskite absorber and the charge-extracting layers are nearly ideal. Accordingly, the surface-recombination velocity (S) is low and no or small band offsets are used in the simulation, just as in Figure 8.2. The fundamental difference between the small- and large-signal decay time at high Fermi-level splittings is also visible here, which leads to the small-signal decay times being smaller by a factor of two. Contrary to the analytical results presented in Figure 8.3, the small- and the large-signal decay times are also not the same at lower Fermi-level-splitting, where SRH-bulk recombination or the electrode capacitance dominate. One reason for this behavior is that the concentration of electrons and

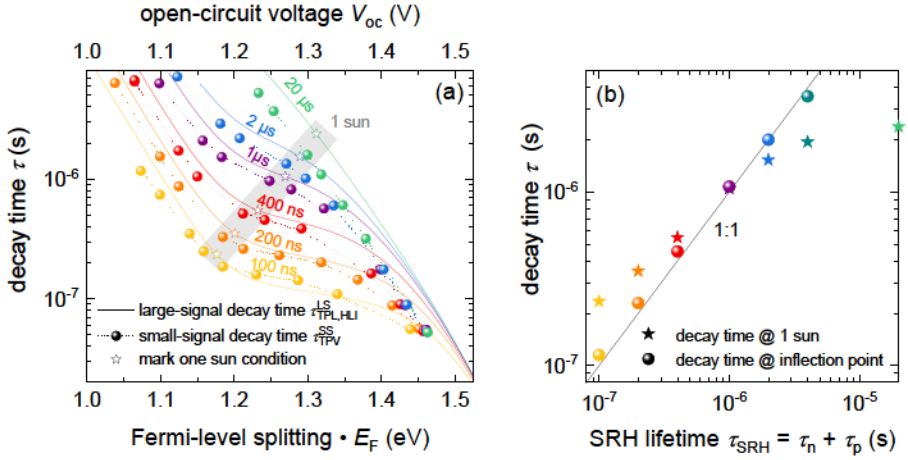

Abbildung 8.7: Decay times vs. Fermi-level splitting or open-circuit voltage resulting from numerical simulations of TPL and TPV on a solar cell stack, using Sentaurus TCAD for various SRH-bulk lifetimes. The simulated solar cell devices have slow interface-recombination velocities ($S = 0.01\,cm/s$) at both absorber-transport layer interfaces. At the same time, the SRH-bulk lifetime is varied from $\sim 100\,ns$ (yellow) to $20\,\mu s$ (green). The lines represent the large-signal decay time derived by taking the derivate of the PL at each time. The data points belong to the simulation of transient photovoltage for different bias-light intensities and result from the analysis of the small-perturbation voltage decay.

holes is not exactly the same. Besides, n and p are also spatially dependent. Therefore the solar cell is no longer exactly in high-level injection ($n = p$), which is a necessary simplification to get the analytical solutions illustrated in Figure 8.3.

8.6 Discussion and Outlook

For most state-of-the-art publications on halide-perovskite solar cells, quantifying recombination is a near-mandatory exercise. Often, transient methods are used to show how the voltage, charge-carrier density, or luminescence decay after a laser pulse. However, the measured reported decay times may vary by orders of magnitude from method to method. In particular, methods based on electrical detection, such as TPV or open-circuit voltage decay, often result in much longer time constants as compared to purely optical methods measured on thin films from the same material, as shown in Figure 8.1. This variance calls into question the physical meaning of these measured decay times. In this chapter, I demonstrated that this large method-specific variation in time constants is mainly caused by a substantial dependence of the decay time on the actual charge-carrier density in the absorber or the voltage at the terminals of the device. Thus, measured decay times without reference to the actual carrier concentration or bias voltage under which these values are obtained are essentially worthless. In a complete solar cell, essentially arbitrarily large 'lifetimes' can be measured with an electrical technique like TPV if the bias condition is sufficiently low and the cell is not shunted. It is true even if the actual SRH recombination lifetime is fairly low. Moreover, I clarified that methodological differences between both methods, e.g., due to the type of perturbation or mode of detection, exist but cause only minor deviations.

9 Impact of Charge Extraction on Small-Signal Transients

In the previous chapters 7 and 8, I studied the time-dependent behavior of charge carriers in perovskite solar cells, including radiative and non-radiative recombination, as well as charging and discharging the electrode capacitance of the device via re-injection into the absorber layer and subsequent recombination. Besides using complex, transient drift-diffusion simulations with Sentaurus TCAD, I introduced a simplified analytical model based on a flat Fermi-level approximation to describe and explain the transient characteristic of a well-behaved perovskite solar cell. This approach neglects any spatial dependences of the charge-carrier density in the solar cell and assumes that the inside of the solar cell and the electrical contacts at the outside are perfectly coupled, implying that charge extraction is infinitely fast.

In this chapter, I extend this analytical model to a two-component model considering that charge extraction happens at a finite speed. This advanced approach uses two coupled differential equations (DE). The two components of this DE system represent the chemical potential of the charge carriers inside the PV-absorber material and the electrical potential built-up by the charge carriers in the contact. This model becomes linear and analytically solvable for the small-signal situation by determining the eigenvalues of a 2×2 matrix. A comparison of these eigenvalues with the measured rise and decay times during a transient photovoltage experiment allows us to determine the rates of carrier recombination and extraction as a function of bias voltage. Furthermore, it establishes a simple link between their ratio and the efficiency losses in the perovskite solar cell.

In a nutshell, I provide a new method to analyze transient photovoltage measurements at different bias-light intensities by connecting the decay and rise times of

the photovoltage. This advanced approach combines the simplicity and comprehensibility of analytical equations with the multiplicity of physical phenomena that occur during a transient experiment on a perovskite solar cell.

9.1 Introduction

A key requirement for improving the usefulness of transient techniques is to find analysis methods that are simple enough to be used and still contain information on the different physical mechanisms contributing to the result. In the case of most transient techniques applied to perovskite solar cells, it is the combination of recombination with charge transport and extraction that complicates the analysis. The kinetics of the charge-carrier decay in response to a laser pulse in a typical time-domain measurement contains a variety of different features that would have to be numerically simulated in order to accurately extract information from the raw data, as shown in section 7.6. As these transient device simulations can only be accomplished by few and often costly simulation programs and require time-consuming fitting procedures, simplified analytical models can help to expand the basic understanding of these transient methods. In the two previous chapters, simplified analytical models helped to understand transient PL signals on different types of samples stacks and to create a coherent picture of TPL and TPV.

So far, however, these analytical descriptions do not capture the extraction behavior of charge carriers from the perovskite absorber to the electrode, which delays the increase of the external voltage V_{ext} at early times after the laser-pulse excitation. Figure 9.1 gives an overview of this effect. The panels 9.1a-c show an example of simulated band diagrams at different times during a small-signal experiment, indicating that the internal and external voltage or quasi-Fermi level splitting need some time to adjust. Figure 9.1d summarizes this displacement between the internal and external state by showing the respective response of the external voltage V_{ext} (blue) and internal voltage V_{int} (red) to the small laser excitation as a function of time. The internal voltage change occurs directly within the laser-pulse duration and decays from there on. However, in this example, the external voltage needs around 300 ns to rise and reach its peak. During this transfer time, which charge carriers

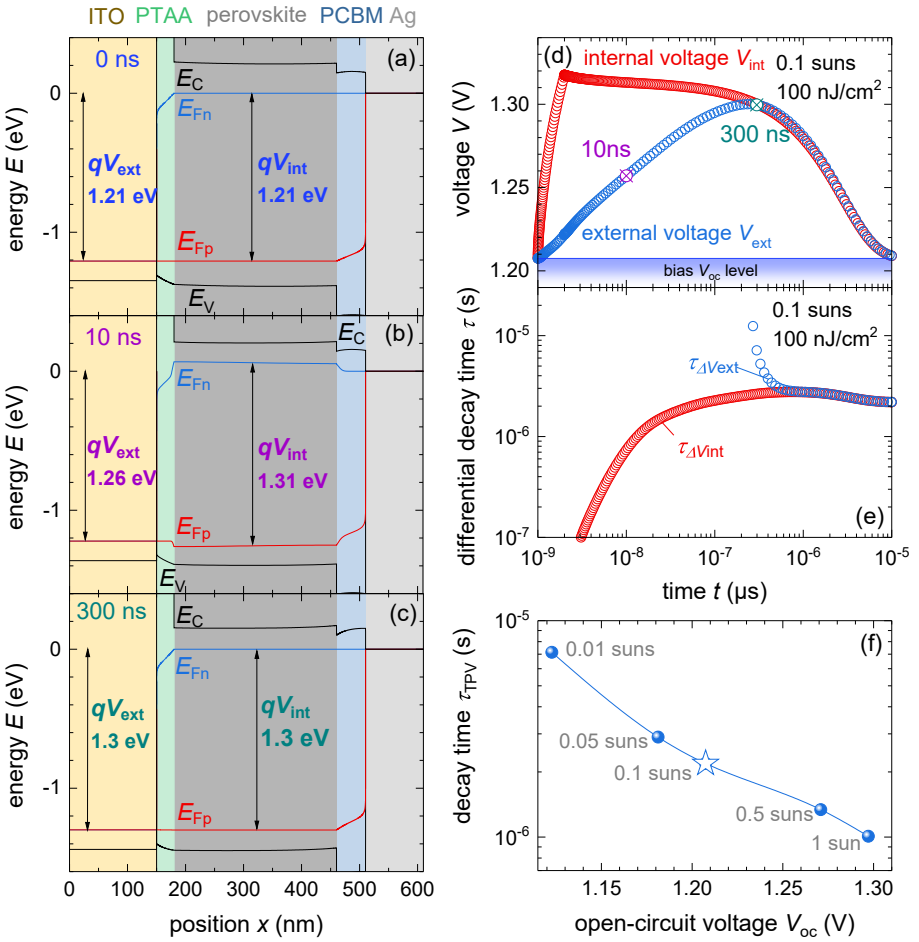

Abbildung 9.1: (a)-(c) Simulated band diagrams of a perovskite solar cell during small-perturbation measurement conditions at a bias level of 1.21 V. Figure9.1(d) illustrates the respective rise of the external voltage V_{ext} and the fall of the internal voltage V_{int} indicated in red. In addition, Figure 9.1e shows the differential decay time calculated from the slope of the internal and external decay via $\tau_{\Delta V_{ext}} = -dt/d\ln(\Delta V_{ext})$ using equation 8.10 from section 8.3.

need to go from the absorber layer to the external electrical contacts, some charge carriers have already recombined. Thus, even if the perovskite solar cell is held at open circuit during a small-signal transient experiment, the internal Fermi level can have substantial gradients. For a detailed discussion of the band diagrams, I refer to sections 7.4 and 8.2.

9.2 Experimental Data

In Figure 9.1, we noted that the external voltage takes hundreds of nanoseconds to approach the internal voltage. In the following, I will show that this observation is consistent with experimental data on MAPI solar cells. Figures 9.2 and 9.3 show exemplary experimental data from small-signal transient photoluminescence and transient photovoltage measurements, being recorded at one integrated setup illustrated in Figure 3.2. The internal voltage V_{int} results from small-signal TPL measurements and the corresponding external voltage decays V_{ext} from TPV at different bias-light intensities. For TPL, the detection is done with a gated-CCD camera, while TPV uses an oscilloscope. Figure 9.2a and (b) show the resulting transient decays of both methods. Small-signal TPL measurements conducted with a background-bias light have so far not been shown in the literature on halide perovskite solar cells. For this experiment, I used the PL intensity of the bias photoluminescence to calibrate the voltage axis of the internal voltage via $V_{\mathrm{int}}(t) = V_{\mathrm{oc,bias}} + k_{\mathrm{B}}T \ln\ \phi_{\mathrm{PL}}(t)/\phi_{\mathrm{PL,bias}}$. In addition, I assumed that the internal and external voltage are equal in the steady state. For low bias-light levels, the bias PL intensity becomes too low to be identified in the detected intensity spectrum and gets lost in the background-noise signal. In contrast, high bias levels run the risk of overexposing the gated-CCD camera. Thus, there is only a limited and small range where I can measure the internal state in the perovskite via small-signal TPL with my experimental setup. Figure 9.2c-j depicts the internal- and external-voltage curves at these four accessible bias levels. The graphs on the left-hand side show the internal and external voltage curves on a logarithmic time scale, whereas the results on the right-hand side are plotted on a linear time axis. This data set belongs to a solution-processed MAPI solar cell, similar to the devices described in section 4. In this example, the external voltage needs several hundred nanoseconds to build up and reach its maximum voltage. In addition, this rise time shifts to longer times for lower excitation. Note that also the decays of the internal and external voltage do not necessarily need to overlap, as the additional example of Figure 9.3a shows. In conclusion, these experimental results demonstrate that the exchange of the charge carriers in real-life perovskite solar cells happens with a finite speed. Thus, it is likely slow enough to interfere with the classical lifetime analysis of the TPV data.

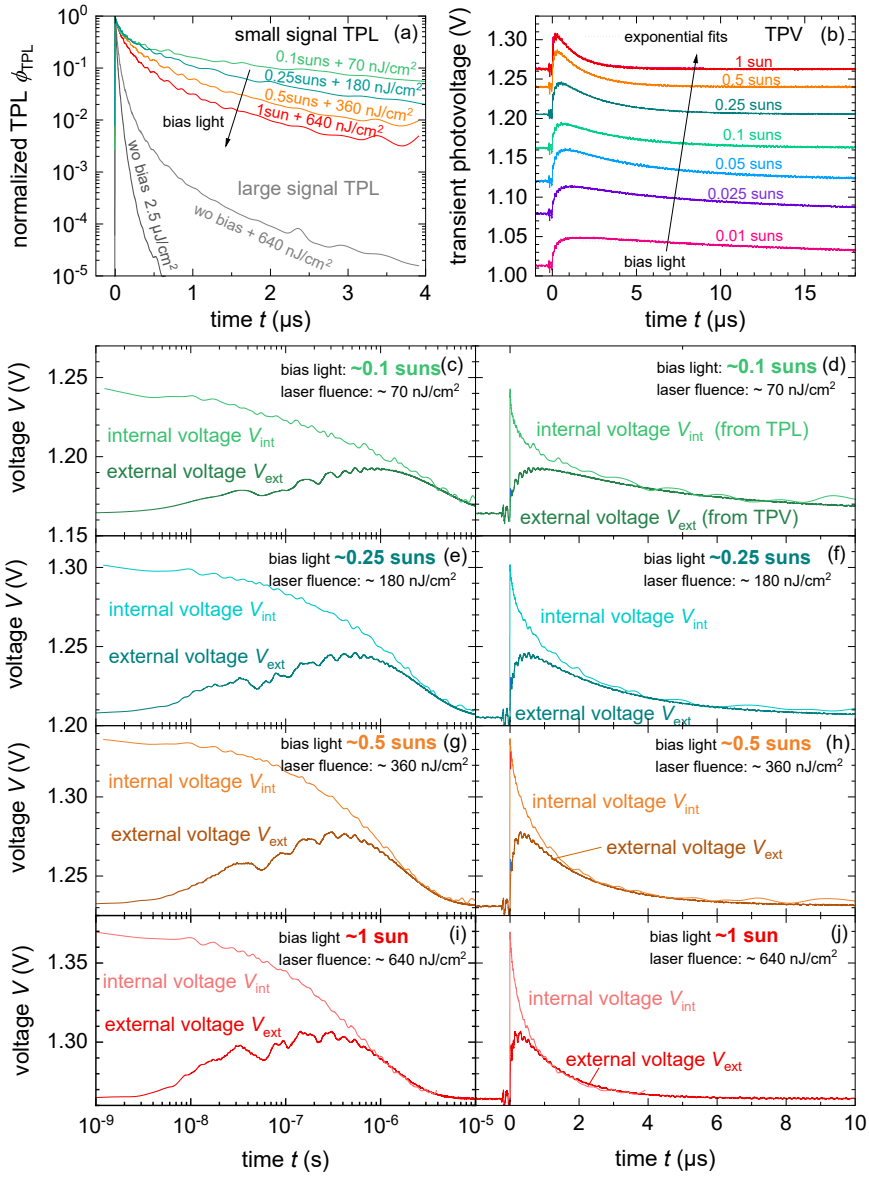

Abbildung 9.2: Experimental data of (a) large- and small-signal transient PL measurements and (b) transient photovoltage decays at different bias-light intensities, measured on a MAPI solar cell. (c)-(j) Experimental data of the internal voltage V_{int} resulting for small-signal TPL measurements and the decays of external voltage V_{ext} from TPV at different bias-light intensities, measured on a MAPI solar cell. The panels on the left show the data on a logarithmic times scale, whereas the panels on the right have a linear times scale.

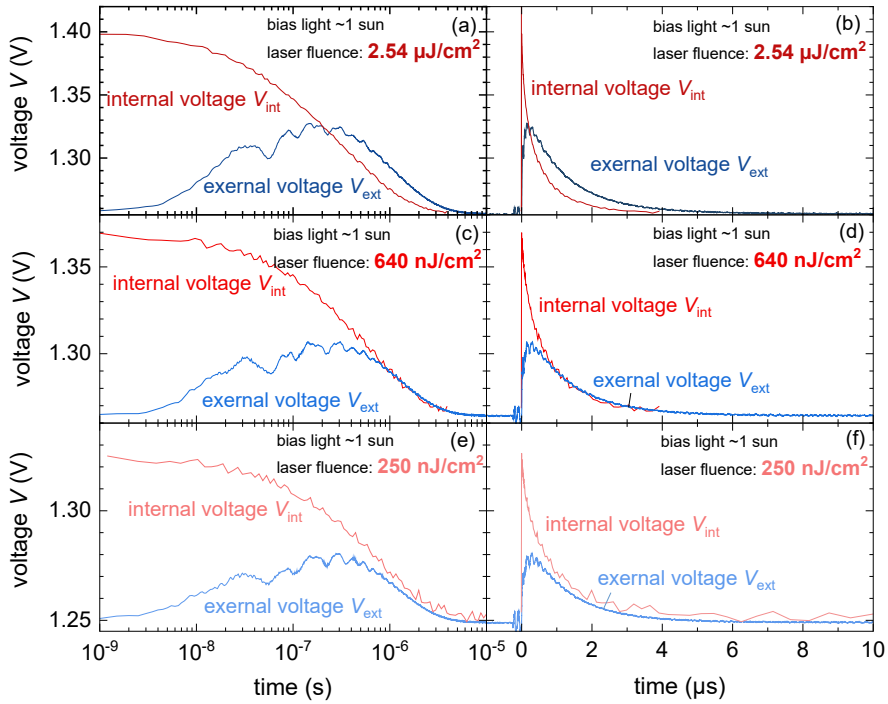

Abbildung 9.3: Experimental data of the internal voltage V_{int} resulting for small signal transient PL measurements and the external voltage decays V_{ext} from transient photovoltage at a bias-light intensity of one sun for varying laser fluences, measured on a MAPI solar cell. The panels on the left-hand side show the data on a logarithmic times scale and those on the right-hand side on a linear times scale.

Furthermore, it becomes apparent that the internal excess voltage ΔV_{int} can be several times larger than the external excess voltage ΔV_{ext}. This mismatch should be considered when choosing the laser-pulse excitation fluence in the TPV measurement.

9.3 Introduction to the Two-Component Model

Next, I introduce an extended two-component model that explicitly accounts for recombination but also for the extraction of charge carriers and, thus, for the diffe-

rences between external voltage and internal quasi-Fermi level splitting. Therefore, this model can be used to simulate and study the rise of the externally measured photovoltage following a photoexcitation pulse and not only its decay.

The simplest conceivable model that can mathematically describe the behaviour of such a system with two simultaneous relaxations of opposite signs requires at least two coupled first-order differential equations in time with time-independent coefficients. For the transient photovoltage measurement, it is plausible that the two variables in these differential equations should be (i) the concentration of photogenerated charge carriers n inside the absorber of the solar cell and (ii) the externally measured photovoltage V_{ext}. Thus, the first differential equation describes the kinetics of the charge-carrier density n inside the absorber, whereas the other one the change in the external voltage V_{ext} with time. While the concentration of charge carriers in the absorber is created almost instantaneously by the laser pulse, it takes some time for the charge carriers to be transported to the electrodes and thereby allow the external voltage to reach its maximum value. Thus, the photovoltage interacts with the charge-carrier concentration but must also be considered as an additional free variable in the DE system.

First, we take a look at the differential equation, describing the change of charge-carrier concentration n in the absorber. This DE contains the usual terms for recombination and generation G but additionally a term for the exchange current J_{exc} flowing to or from the electrodes. If this exchange current J_{exc} is positive, it will reduce the charge-carrier density in the absorber and increase the carrier density on the electrodes. Alternatively, the electrodes inject charge carriers back into the absorber layer if the current is negative. For a perfectly symmetric system in high-level injection, where n equals p and the external voltage drops to equal amounts over the electron and hole contact, the first equation reads

$$\begin{aligned}\frac{dn}{dt} &= -k_{\mathrm{rad}}n^2 - \frac{n}{\tau_{\mathrm{SRH}}^{\mathrm{eff}}} - \frac{J_{\mathrm{exc}}}{qd} + G \\ &= -k_{\mathrm{rad}}n^2 - \frac{n}{\tau_{\mathrm{SRH}}^{\mathrm{eff}}} - \frac{S_{\mathrm{exc}}}{d}\quad n - n_i \exp\quad \frac{qV_{\mathrm{ext}}}{2k_{\mathrm{B}}T}\qquad + G\ ,\end{aligned} \tag{9.1}$$

where the first two terms describe radiative and SRH recombination. G is a time-independent photogeneration rate due to bias-light excitation. Moreover, the ex-

change velocity S_{exc} is a prefactor of unit cm/s that defines how quickly electrons can be extracted or injected through the electron-transport layer, or holes through the hole-transport layer, and subsequently charge up the respective electrode. Thus, the extraction of charge carriers from the absorber is linear in concentration n. Here, the quantity S_{exc} acts as the proportionality constant, similar to a surface-recombination velocity, with the only difference that the carriers do not recombine but are extracted at the contact. The division of S_{exc} by the thickness d is necessary since the differential equation deals with carrier densities per unit volume that are assumed constant over a thickness d and are reduced or increased by an exchange current J_{exc}. To satisfy the principle of detailed balance, [28] carrier extraction from the absorber to the contact and carrier injection back into the absorber must be interlinked. The way how the exchange current is represented in equation 9.1 follows ref. [279] and is also compatible with an extended equivalent-circuit model for solar cells. [280] Moreover, the ratio d/S_{exc} between the thickness d and the exchange velocity S_{exc} defines a time constant for the increase and decrease of the carrier densities caused by the exchange current flowing to or from the electrodes. Note that equation 9.1 can also be rewritten as the change of the quasi-Fermi-level splitting ΔE_{F} or the internal voltage $V_{\mathrm{int}} = \Delta E_{\mathrm{F}}/q$. Using the relation between the internal voltage and the carrier density

$$n(t) = p(t) = n_{\mathrm{i}} \exp \quad \frac{qV_{\mathrm{int}}(t)}{2k_{\mathrm{B}}T} \tag{9.2}$$

and given that

$$\frac{dV_{\mathrm{int}}}{dn} = \frac{2k_{\mathrm{B}}T}{qn} \quad , \tag{9.3}$$

one can write

$$\frac{dV_{\mathrm{int}}}{dt} = \frac{2k_{\mathrm{B}}T}{qn(V_{\mathrm{int}})} \quad -k_{\mathrm{rad}} n(V_{\mathrm{int}})^2 - \frac{n(V_{\mathrm{int}})}{\tau_{\mathrm{SRH}}^{\mathrm{eff}}} - \frac{S_{\mathrm{exc}}}{d} \quad n(V_{\mathrm{int}}) - n_{\mathrm{i}} \exp \quad \frac{qV_{\mathrm{ext}}}{2k_{\mathrm{B}}T} \quad + G \quad . \tag{9.4}$$

This internal voltage V_{int} does not represent a voltage in the electrostatic sense but is used to relate the chemical potential of charge carriers within the device to the true, externally measurable, electrostatic potential given by V_{ext}.

The exchange of electrons between the absorber and the electric contact determines the change of the excess-charge density σ per area on the n-type electrode, according to

$$\frac{d\sigma}{dt} = qS_{\mathrm{exc}} \quad n - n_{\mathrm{i}} \exp \quad \frac{qV_{\mathrm{ext}}}{2k_{\mathrm{B}}T} \qquad . \tag{9.5}$$

Equation 9.5 implies that every electron that is extracted from the absorber contributes to the contact-charge density. Likewise, every electron that is re-injected from the contact reduces the charge density. Therefore, charge density σ per area on the electrodes will change according to the flux of electrons described by the third term on the right-hand side of equation 9.1. Note that the division by the thickness d is missing because this equation describes charge densities per unit area and not per volume as in equation 9.1.

Eventually, we want to know how the external voltage V_{ext} changes. Thereby, any change in external voltage requires a change in charge density per area. These quantities are link via the relation $V_{\mathrm{ext}} = \sigma / C_{\mathrm{area}}$, where C_{area} denotes the total electrical capacitance of the junction. In order to keep the model simple, I assume that the contacts are completely symmetric. Due to this assumption, we have not only the same S_{ext} for both types of contacts but also the same capacitance. Likewise, the voltages over the electron and the hole contact are both $V_{\mathrm{ext}}/2$. Thus, the time derivative of the external voltage follows

$$\frac{dV_{\mathrm{ext}}}{dt} = \frac{qS_{\mathrm{exc}}}{C_{\mathrm{area}}} \quad n - n_{\mathrm{i}} \exp \quad \frac{qV_{\mathrm{ext}}}{2k_{\mathrm{B}}T} \qquad . \tag{9.6}$$

Equations 9.1 and 9.6 form a system of two coupled non-linear differential equations in time using the carrier concentration and the external photovoltage as variables. Note that the term in the bracket in equation 9.6 can also be expressed as a function of the internal voltage V_{int}. Thus, we can rewrite equation 9.6

$$\frac{dV_{\mathrm{ext}}}{dt} = \frac{qS_{\mathrm{exc}}}{C_{\mathrm{area}}} n_{\mathrm{i}} \quad \exp \quad \frac{qV_{\mathrm{int}}}{2k_{\mathrm{B}}T} \quad - \exp \quad \frac{qV_{\mathrm{ext}}}{2k_{\mathrm{B}}T} \qquad . \tag{9.7}$$

Now the combination of equation 9.4 and 9.7 yields a more convenient system of two coupled differential equations describing the kinetics of two potentials.

Accordingly, the exchange-current density as a function of external and internal

voltage results in

$$J_{\mathrm{exc}} = qS_{\mathrm{exc}}n_{\mathrm{i}} \quad \exp \quad \frac{qV_{\mathrm{int}}}{2k_{\mathrm{B}}T} \quad - \exp \quad \frac{qV_{\mathrm{ext}}}{2k_{\mathrm{B}}T} \qquad . \tag{9.8}$$

Furthermore, equation 9.8 shows that the exchange between absorber and electrodes is a net flux of electrons towards the electrode if $V_{\mathrm{int}} > V_{\mathrm{ext}}$. Otherwise, we have a net flux towards the absorber once $V_{\mathrm{int}} < V_{\mathrm{ext}}$. As long as the exchange velocity S_{exc} is fairly high, which corresponds to a high mobility or conductivity of the electron and hole transport layers, the difference of V_{int} and V_{ext} will be small for a given current. In contrast, for small values of S_{exc} the difference of V_{int} and V_{ext} will be rather large. If the system is in a steady-state open-circuit situation, $V_{\mathrm{int}} = V_{\mathrm{ext}}$ holds because no current is flowing.

For a small-signal method, as is typically the case for transient photovoltage measurements, it is possible to linearize the two-component model around a specific steady-state bias voltage V_{bias}. Under this condition, the system of non-linear differential equations becomes a system of two linear differential equations. Hereby, linearization of equation 9.4 yields for the kinetics of small variations δV_{ext} and δV_{int} of the external and internal voltage after the light pulse

$$\begin{aligned} \frac{d}{dt}\delta V_{\mathrm{int}} &= \frac{2k_{\mathrm{B}}T}{qn_{\mathrm{bias}}} \quad -2k_{\mathrm{rad}}n_{\mathrm{bias}} - \frac{1}{\tau_{\mathrm{SRH}}^{\mathrm{eff}}} - \frac{S_{\mathrm{exc}}}{d} \quad \frac{dn}{dV_{\mathrm{int}}}\delta V_{\mathrm{int}} + \frac{2k_{\mathrm{B}}T}{qn_{\mathrm{bias}}}\frac{S_{\mathrm{exc}}}{d}\frac{qn_{\mathrm{bias}}}{2k_{\mathrm{B}}T}\delta V_{\mathrm{ext}} \\ &= \quad -2k_{\mathrm{rad}}n_{\mathrm{bias}} - \frac{1}{\tau_{\mathrm{SRH}}^{\mathrm{eff}}} - \frac{S_{\mathrm{exc}}}{d} \quad \delta V_{\mathrm{int}} + \frac{S_{\mathrm{exc}}}{d}\delta V_{\mathrm{ext}} \quad . \end{aligned} \tag{9.9}$$

Here, n_{bias} denotes the charge-carrier concentration at the bias condition of the small-signal measurement, i.e., the concentration just before the laser pulse. Given that TPV is measured at open circuit, this carrier density follows $n_{\mathrm{bias}} = p_{\mathrm{bias}} = n_{\mathrm{i}}\exp\left(qV_{\mathrm{int}}/2k_{\mathrm{B}}T\right) = n_{\mathrm{i}}\exp\left(qV_{\mathrm{ext}}/2k_{\mathrm{B}}T\right)$ within the logic of our model. For the linearization of equation 9.7, I obtain

$$\begin{aligned} \frac{d}{dt}\delta V_{\mathrm{ext}} &= \frac{qS_{\mathrm{exc}}}{C_{\mathrm{area}}}\frac{dn}{dV_{\mathrm{int}}}\delta V_{\mathrm{int}} - \frac{qS_{\mathrm{exc}}}{C_{\mathrm{area}}}\frac{q}{2k_{\mathrm{B}}T}n_{\mathrm{bias}}\delta V_{\mathrm{ext}} \\ &= \frac{qS_{\mathrm{exc}}}{C_{\mathrm{area}}}\frac{q}{2k_{\mathrm{B}}T}n_{\mathrm{bias}}\delta V_{\mathrm{int}} - \frac{qS_{\mathrm{exc}}}{C_{\mathrm{area}}}\frac{q}{2k_{\mathrm{B}}T}n_{\mathrm{bias}}\delta V_{\mathrm{ext}} \quad . \end{aligned} \tag{9.10}$$

In the next step, I summarize these linearized equations 9.9 and 9.10 into a matrix equation

$$\frac{d}{dt}\begin{matrix}\delta V_{\mathrm{int}}\\ \delta V_{\mathrm{ext}}\end{matrix} = \begin{matrix} -2k_{\mathrm{rad}}n_{\mathrm{bias}} + \frac{1}{\tau_{\mathrm{SRH}}^{\mathrm{eff}}} + \frac{S_{\mathrm{exc}}}{d} & \frac{S_{\mathrm{exc}}}{d} \\ \frac{S_{\mathrm{exc}}n_{\mathrm{bias}}}{n_{\mathrm{Q}}d} & -\frac{S_{\mathrm{exc}}n_{\mathrm{bias}}}{n_{\mathrm{Q}}d}\end{matrix}\begin{matrix}\delta V_{\mathrm{int}}\\ \delta V_{\mathrm{ext}}\end{matrix}, \quad (9.11)$$

with $n_{\mathrm{Q}} = 2C_{\mathrm{area}}k_{\mathrm{B}}T/\ q^2d$. With the definition of the chemical capacitance of the electrons in the perovskite absorber $C_\mu = n_{\mathrm{bias}}q^2d/(2k_{\mathrm{B}}T)$, [281] the ratio $n_{\mathrm{bias}}/n_{\mathrm{Q}} = C_\mu/C_{\mathrm{area}}$ just equals the ration between chemical and electrical capacitance. The matrix system in equation 9.11 has analytical solutions implying that it combines the simplicity of an analytical solution with the explicit consideration of a finite rate of charge extraction. The solution of equation 9.11 in terms of eigenvectors and eigenvalues is given by

$$\begin{matrix}\delta V_{\mathrm{int}}\\ \delta V_{\mathrm{ext}}\end{matrix}(t) = \delta V_0 \begin{matrix}h_1\\ 1\end{matrix} \exp\left(-\frac{t}{\tau_{\mathrm{decay}}}\right) + \delta V_0 \begin{matrix}h_2\\ -1\end{matrix} \exp\left(-\frac{t}{\tau_{\mathrm{rise}}}\right), \quad (9.12)$$

with the coefficients h_1, h_2 and $\delta V_0 = \delta V_{\mathrm{int}}^0/(h_1+h_2)$, resulting from the initial condition in the TPV experiment. At the starting point $t = 0$ of a TPV experiment, the light pulse generates a certain amount of charge carriers inside the absorber, but the external voltage is still unaffected. Thus, in the initial situation the additional external is $\delta V_{\mathrm{ext}}(t=0) = 0$ and the internal voltage equals $\delta V_{\mathrm{int}}(t=0) = \delta V_{\mathrm{int}}^0$. The coefficient δV_0 is a small prefactor with unit volts that must be small enough to ensure that the linearization used to obtain equation 9.12 is justified.

From this, the corresponding solution for the additional external voltage relative to the bias voltage V_{bias} gives

$$\delta V_{\mathrm{ext}}(t) = V_{\mathrm{ext}}(t) - V_{\mathrm{bias}} = \delta V_0 \left(\exp\left(-\frac{t}{\tau_{\mathrm{decay}}}\right) - \exp\left(-\frac{t}{\tau_{\mathrm{rise}}}\right)\right), \quad (9.13)$$

where the rise and decay times are given by

$$\tau_{\mathrm{rise}} = 2\left(k_1+k_2+k_3 + \sqrt{(k_1+k_2+k_3)^2 - 4k_1k_3}\right)^{-1} \quad (9.14)$$

and

$$\tau_{\mathrm{decay}} = 2 \quad k_1 + k_2 + k_3 - \quad \overline{(k_1 + k_2 + k_3)^2 - 4k_1k_3} \quad ^{-1} \tag{9.15}$$

with the inverse time constants

$$k_1 = \frac{1}{\tau_{\mathrm{SRH}}^{\mathrm{eff}}} + 2k_{\mathrm{rad}}n_{\mathrm{bias}} \ , \tag{9.16}$$

$$k_2 = \frac{S_{\mathrm{exc}}}{d} \tag{9.17}$$

and

$$k_3 = \frac{S_{\mathrm{exc}}n_{\mathrm{bias}}}{n_{\mathrm{Q}}d} = k_2\frac{n_{\mathrm{bias}}}{n_{\mathrm{Q}}} \ . \tag{9.18}$$

The three inverse time constants k_1, k_2 and k_3 are identified easily as the entries of the matrix in equation 9.11, where k_1 represents the actual inverse recombination lifetime combining SRH and radiative recombination at the given working condition. Furthermore, k_2 and k_3 represent the exchange rates between the absorber and the contacts. Here, the inverse time constant (k_2) is the inverse RC-constant given by the resistance of charge extraction via the charge-transfer layers multiplied by the chemical capacitance of the perovskite layer. Moreover, (k_3) is formed by the inverse RC from the resistance of charge extraction multiplied by the electrode capacitance of the solar cell.

Solving the matrix equation 9.11 also yields an expression for the additional internal voltage relative to the bias voltage V_{bias}

$$\delta V_{\mathrm{int}}(t) = V_{\mathrm{int}}(t) - V_{\mathrm{bias}} = \delta V_0 \quad h_1 \exp \quad -\frac{t}{\tau_{\mathrm{decay}}} \quad + h_2 \exp \quad -\frac{t}{\tau_{\mathrm{rise}}} \quad . \tag{9.19}$$

with the two additional prefactors

$$h_1 = -\frac{k_1 + k_2 - k_3 - \quad \overline{(k_1 + k_2 + k_3)^2 - 4k_1k_3}}{2k_3} \tag{9.20}$$

and

$$h_2 = \frac{k_1 + k_2 - k_3 + \quad \overline{(k_1 + k_2 + k_3)^2 - 4k_1k_3}}{2k_3} \ . \tag{9.21}$$

A comparison of the solution of the excess internal and external voltage in equation 9.13 and 9.19 illustrates that these equations only differ by the two prefactors h_1 and h_2 stated in equation 9.20 and 9.21. Apart from that, they are built from the same coefficients, but the solution of the additional internal voltage $\delta V_{\mathrm{int}}(t)$ is much more complicated. In the following, I will therefore mainly focus on the rise and fall of the additional external voltage $\delta V_{\mathrm{ext}}(t)$. Unfortunately, the mathematical form of equations 9.13-9.18 is too complicated to obtain direct intuitive access to the physics of the TPV transient from the equations alone. Accordingly, I will show and discuss some exemplary $\delta V_{\mathrm{ext}}(t)$ curves and illustrate the effects in some detail in the next section.

9.4 Results from the Analytical Two-Component Model

In the last section, I introduced the basic ideas and the mathematical basis of a two-component model, where the internal state in the solar cell absorber and a second external state at the outer electrodes are coupled via an exchange current. The linearization of this model allowed us to derive an analytical expression for the additional internal voltage $\delta V_{\mathrm{int}}(t)$ and external voltage $\delta V_{\mathrm{ext}}(t)$. The latter corresponds in this theory to a transient photovoltage signal. Examples of the respective analytical solutions of the normalized excess voltages $\delta V(t)/\delta V_0$ are shown in the upper two panels of Figure 9.4 and 9.5. With the help of these two Figures, I will successively discuss the influence of two important parameters on the $\delta V(t)/\delta V_0$ curves, namely the exchange velocity S_{exc} and the electrode capacitance per area C_{area}.

Figures 9.4a and (b) visualize the analytical solutions of the matrix equation for a variation of the exchange velocity S_{exc} at two different bias levels of 1.1 V and 1.25 V. The normalized external voltage $\delta V_{\mathrm{ext}}/\delta V_0$ curves are plotted as solid lines. The dotted lines belong to the corresponding normalized internal voltage decays $\delta V_{\mathrm{int}}/\delta V_0$, being calculated via equation 9.19. For the calculation of these graphs, I used three different exchange velocities S_{exc}, a high value of 10^3 cm/s (blue), a medium value of 100 cm/s (red) and a small one of $S_{\mathrm{exc}} = 10$ cm/s (grey). The exchange

velocity S_{exc} depends on the properties of the charge-transport layers, such as the mobility or electric-field distribution. Accordingly, the value of S_{exc} determines how quickly electrons or holes are extracted or injected through the two transport layers. The other additional parameters, being necessary to calculate the voltage curves, are listed in the figure caption of Figure 9.4.

The first thing to recognize is that the analytical solution of the two-component model reflects the basic trend of the internal and external voltage curves from the experiment and simulation. The normalized internal excess voltage $\delta V_{\mathrm{int}}/\delta V_0$ is highest at the very beginning and continues to decrease over time until it reaches the initial bias voltage. In contrast, the response of the normalized external excess voltage $\delta V_{\mathrm{ext}}/\delta V_0$ to the small-signal excitation is delayed. It starts at the bias-voltage level, increases slowly over time, reaches its maximum and only then begins to fall. Thus, this model is able to replicate the rise and fall of the external voltage. Furthermore, the variation of the exchange velocity S_{exc} shows that smaller exchange velocities prolong the rise of the additional external voltage and shift the maximum of the curves to longer times. This trend occurs at both shown bias levels. The associated rise times τ_{rise}, calculated via equation 9.14, are indicated next to the curves and quantify the described trend. The decay of $\delta V_{\mathrm{ext}}/\delta V_0$, on the other hand, is affected differently by the variation of exchange velocity for the two bias levels. In panel 9.4a at the lower injection level of 1.1 V, a change in S_{exc} also affects the decay of the curves, whereas at 1.25 V in panel 9.4b all three decays of the normalized external voltage $\delta V_{\mathrm{ext}}/\delta V_0$ overlap. Note that the decay time τ_{decay}, as well as the rise time τ_{rise} is injection-level dependent and therefore differs between Figure 9.4a and (b). At the higher bias voltage, the respective rise time τ_{rise} is shorter and increases by an order of magnitude when the exchange velocity decreases by an order of magnitude. Thus, it follows a power law function. However, in Figure 9.4a, the rise time is not antiproportional to the exchange velocity S_{exc}. To better understand the behaviour, Figures 9.4(c) and (d) directly depict the rise time τ_{rise} and decay time τ_{decay} as a function of the exchange velocity S_{exc} for the two different bias levels. Furthermore, additional time constants related to the eigenvalues of the matrix and the inverse coefficients $1/k_1$, $1/k_2$, and $1/k_3$ from equations 9.16-9.18 are shown as guide-to-the eye. In addition, thin vertical lines mark the parameter sets used for the three different examples in the top figures.

The rise-time curve τ_{rise}, shown as a thick, blue line, can be divided into two sections. For low exchange velocities S_{exc} the rise time is constant, which is determined by the recombination lifetime, namely $\tau_{\mathrm{R}} = \left(1/\tau_{\mathrm{SRH}}^{\mathrm{eff}} + 2k_{\mathrm{rad}}n\right)^{-1}$ (green, dashed

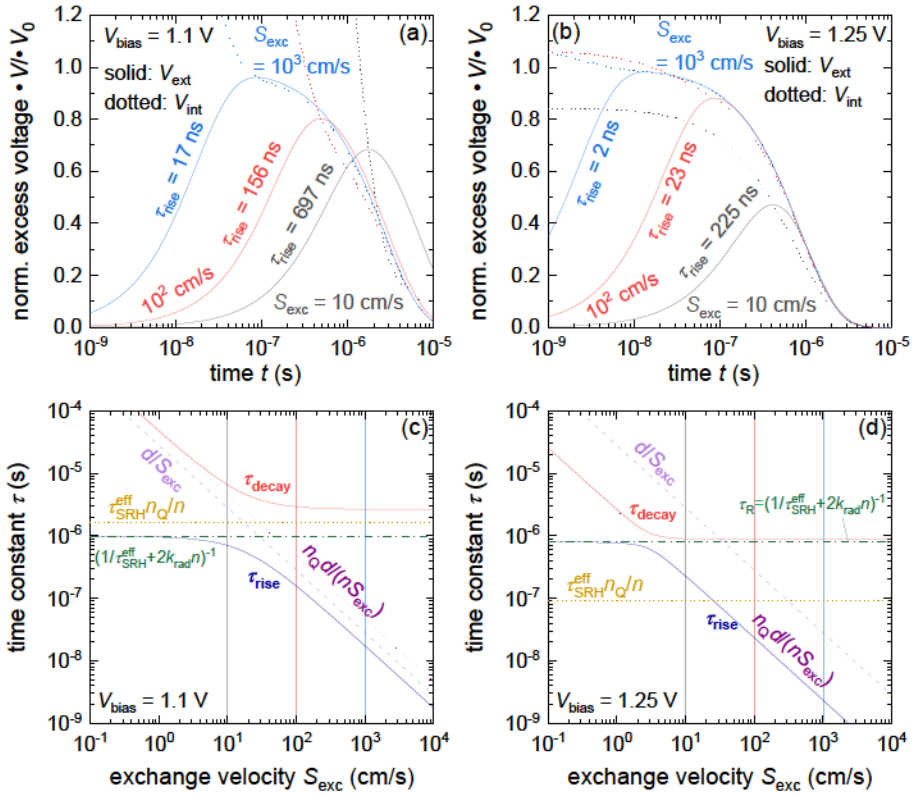

Abbildung 9.4: (a) and (b) Analytical solutions of the normalized internal excess-voltage decay $\delta V_{\mathrm{int}}/\delta V_0$ (dotted line) and the respective normalized external voltage $\delta V_{\mathrm{ext}}/\delta V_0$ curve (solid line) at two different bias voltage levels, calculated for three exemplary exchange velocities S_{exc}, namely $10^3\,\mathrm{cm/s}$ (blue), $100\,\mathrm{cm/s}$ (red) and $10\,\mathrm{cm/s}$ (grey). The rise of the normalized external voltage is prolonged for smaller exchange velocities. Additional parameters used for the calculations are a SRH lifetime $\tau_{\mathrm{SRH}}^{\mathrm{eff}} = 1\,\mu\mathrm{s}$, a radiative recombination coefficient k_{rad} of $5\times10^{-11}\,\mathrm{cm^3/s}$, an absorber-layer thickness of $280\,\mathrm{nm}$, an intrinsic carrier concentration n_{i} of $8.05\times10^4\,\mathrm{cm^{-3}}$ and a capacitance per area $C_{\mathrm{area}} = 20\,\mathrm{nF/cm^2}$. Panel (a) is conducted at a bias-voltage level of $1.1\,\mathrm{V}$, whereas plot (b) represents the analytical solution at a higher bias level of $1.25\,\mathrm{V}$. The panels on the bottom side illustrate the development of the decay time τ_{decay} and rise time τ_{rise} of the external voltage, defined by equation 9.14 as a function of the exchange velocity S_{exc}. Furthermore, additional time constants related to the eigenvalues of the matrix are depicted as a guide-to-the eye.

line). If the exchange is fast compared to recombination, the rise time gets shorter with increasing exchange velocity S_{exc}. At the lower injection level of 1.1 V and high exchange velocities, the rise time depends on the ratio of d/S_{exc} (lilac, dashed line). Thus, in this case, τ_{rise} is dominated by the resistance of charge extraction through the charge-transfer layers and the chemical capacitance of the perovskite layer, which represent a *RC*-time constant. At high bias voltages, i.e., in this example 1.25 V in Figure 9.4d, the rise time τ_{rise} follows the *RC*-time constant $n_{\mathrm{Q}}d/\left(S_{\mathrm{exc}}n_{\mathrm{bias}}\right)$, which is formed by the resistance of charge extraction multiplied with the electrode capacitance of the solar cell. The thick, red line depicts the decay time τ_{decay} calculated by using equation 9.15. This curve consists of two regions, too. In the regime where charge transfer is fast in comparison to recombination, the decay time τ_{decay} of the external voltage is constant and does not depend on S_{exc}. Depending on the bias level the corresponding saturation value of τ_{decay} is set by the times constant of electrode discharging $\tau_{\mathrm{SRH}}^{\mathrm{eff}}n_{\mathrm{Q}}/n$, or at high bias levels by recombination via τ_{R}. If the exchange velocity is small, charge transfer also affects the decay time τ_{decay} of the normalized external voltage $\delta V_{\mathrm{ext}}/\delta V_0$, which follows $n_{\mathrm{Q}}d/\left(S_{\mathrm{exc}}n_{\mathrm{bias}}\right)$ (purple, dotted line). This discussion shows that depending on the injection level and parameter set, different time constants determine both the rise and fall of the small-signal TPV curve. Thus, generalization is dangerous and leads to misinterpretation of the data.

The next Figure illustrates the influence of the electrode capacitance per area C_{area} on the analytical solutions of the two-component model. Therefore, Figure 9.5a and (b) show three exemplary curves of the normalized internal excess voltage $\delta V_{\mathrm{int}}/\delta V_0$ (dotted line) and the respective external $\delta V_{\mathrm{ext}}/\delta V_0$ (solid line) for two different bias levels. In addition, the lower two bottom panels (c) and (d) again plot the time constants of the rise and decay, but this time as a function of capacitance C_{area}.

First of all, a higher capacitance slows down both the rise and fall of the normalized internal and external voltage curves, reducing the height of the $\delta V_{\mathrm{ext}}/\delta V_0$ peak. Its value also influences the shape of the curves. Moreover, we can again identify two distinct regions in the rise- and decay-time curves for both shown examples. In one region, τ_{decay} and τ_{rise} are constant, while they are following a power law and increase for higher C_{area} in the other one. The decay time τ_{decay} does not depend on C_{area} as long as the time constant of electrode discharging is small in comparison to

the recombination lifetime $\left(1/\tau_{\mathrm{SRH}}^{\mathrm{eff}} + 2k_{\mathrm{rad}}n\right)^{-1}$. In this regime, which almost disappears in case of the lower bias voltage of 1.1 V, τ_{decay} is limited by the green dashed line. In the second regime, the decay time increases with higher electrode capaci-

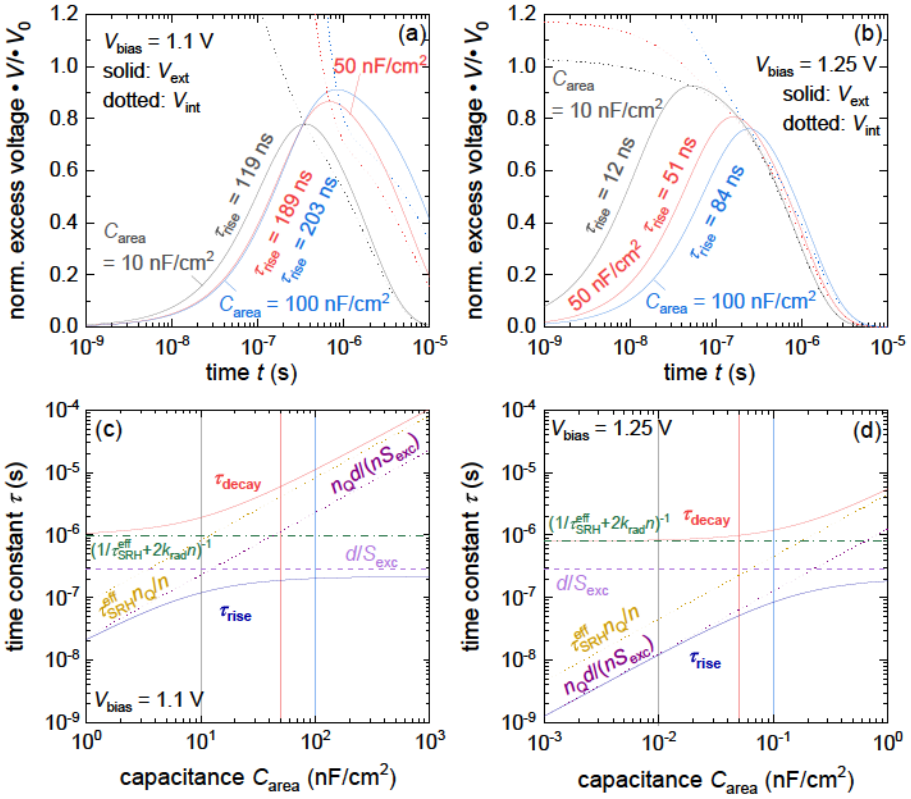

Abbildung 9.5: (a) and (b) Analytical solutions of the normalized internal excess-voltage decay $\delta V_{\mathrm{int}}/\delta V_0$ (dotted line) and the respective normalized external excess-voltage curve of $\delta V_{\mathrm{ext}}/\delta V_0$ (solid line) at two different bias-voltage levels, calculated for three different values of the electrode capacitance per area C_{area}. Similarly to Figure 9.4, the panels on the left side show the analytical results at a bias voltage level of 1.1 V, and the panels on the right side show the findings for a bias level of 1.25 V. The capacitance per area C_{area} is varied between 20 nF/cm^2 (grey), 50 nF/cm^2 (red) and 100 nF/cm^2 (blue). Besides a constant exchange velocity of $S_{\mathrm{exc}} = 100$ cm/s, other simulation parameters are similar to Figure 9.4. (c) and (d) Rise time τ_{rise} and decay time τ_{decay} from equations 9.14 and 9.15 as a function of the electrode capacitance per area C_{area} for the two different bias levels. Furthermore, additional time constants related to the eigenvalues of the matrix are shown as guide-to-the eye.

tance C_{area} and follows the yellow, dotted line of $\tau_{\mathrm{SRH}}^{\mathrm{eff}} n_{\mathrm{Q}}/n_{\mathrm{bias}}$. The rise time τ_{rise} is proportional to $n_{\mathrm{Q}} d/(S_{\mathrm{exc}} n_{\mathrm{bias}})$ and therefore increases with higher capacitance until this time constant gets larger than the RC-element formed by the resistance of charge extraction and the chemical capacitance of the absorber layer. The RC-limitation that sets the saturation value of the rise time is not universal and depends on the relations of the respective time constants to each other. Note that not only the choice of parameters, such as electrode capacitance C_{area}, exchange velocity S_{exc} or recombination coefficients k_{rad} and $\tau_{\mathrm{SRH}}^{\mathrm{eff}}$, influence the resulting values for the rise and decay time, but also the bias-voltage level.

Thus, it has been common practice, particularly in organic photovoltaics, to plot TPV-derived decay time as a function of either carrier density or open-circuit voltage. [243, 282, 283] Figure 9.6 shows the rise time τ_{rise} and decay time τ_{decay} as a function of the bias open-circuit voltage V_{oc}. The three figure panels (a)-(c) show the scenario for different values of the exchange velocity S_{exc}, namely 1000 cm/s, 100 cm/s and 10 cm/s. A comparison shows that the basic course of the decay-time and rise-time curves is the same for all three exchange velocities S_{exc}. The decay time τ_{decay}, displayed as a thick, red line, decreases by orders of magnitude for higher bias voltages and can be divided into three regions. It thereby follows the s-shaped course, reminiscent of the differential lifetime curve from the analytical model equation 7.5 in section 7.4. The rise time τ_{rise} (blue line) is always shorter than the decay time. Its curve, indicated by the thick, blue line, consists of two regions. At low bias voltages, the τ_{rise} is constant while continuously decreasing at high bias voltages. What changes significantly for the three different exchange velocities is the position and distance of the curves from τ_{rise} and τ_{decay} relative to each other. Moreover, depending on the exchange velocity, different RC-constants dominate the regimes and saturation values of the rise and decay time. For example, at low open-circuit voltages the decay time τ_{decay} is dominated by capacitive discharging following $\tau_{\mathrm{SRH}}^{\mathrm{eff}} n_{\mathrm{Q}}/n_{\mathrm{bias}}$ (yellow, dotted line) if the exchange velocity is high. In contrast, if $d/S_{\mathrm{exc}} > \tau_{\mathrm{R}}$, which applies to the example of a very slow exchange velocity of 10 cm/s in Figure 9.6c, the resistance of charge extraction slows down the decay time. Then the decay time τ_{decay} at low injection levels follows the

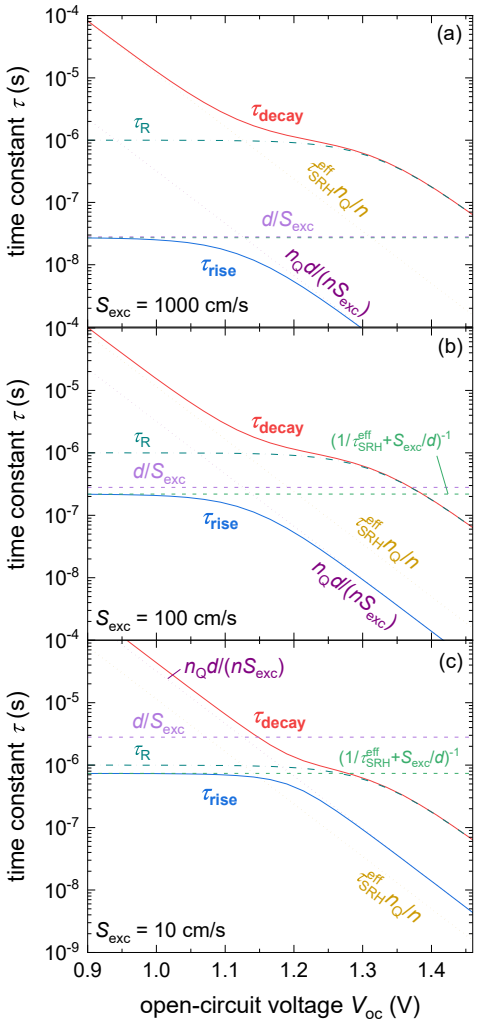

Abbildung 9.6: Analytical solutions of the decay time τ_{decay} (red) and rise time τ_{rise} (blue) as a function of the open-circuit voltage V_{oc}, resulting from the two-component model introduced in section 9.3. In addition, the inverse coefficients $1/k_2 = d/S_{\mathrm{exc}}$ and $1/k_3 = n_{\mathrm{Q}} d/(S_{\mathrm{exc}} n_{\mathrm{bias}})$ are plotted, as well as important time constant like $\tau_{\mathrm{SRH}}^{\mathrm{eff}} n_{\mathrm{Q}}/n$, being related to the RC-time constant of electrode discharging. The analytical results are calculated for three different exchange velocities, namely S_{exc} of (a) 1000 cm/s, (b) 100 cm/s and (c) 10 cm/s. Furthermore, a SRH lifetime $\tau_{\mathrm{SRH}}^{\mathrm{eff}} = 1$ s, a radiative recombination coefficient k_{rad} of $5 \times 10^{-11}\,\mathrm{cm}^3/\mathrm{s}$, an absorber-layer thickness of 280 nm, an intrinsic carrier concentration n_{i} of $8.05 \times 10^4\,\mathrm{cm}^{-3}$ and a capacitance per area $C_{\mathrm{area}} = 20\,\mathrm{nF/cm}^2$ is used for the calculations.

trend of the dark purple line, representing $n_{\mathrm{Q}}d/(S_{\mathrm{exc}}n_{\mathrm{bias}})$. In the region of high open-circuit voltages, τ_{decay} corresponds for all three examples to the recombination lifetime τ_{R}, being indicated by the dark green line. Thus, only in this regime information about the charge-carrier lifetime can be drawn from the decay times of $\delta V_{\mathrm{ext}}(t)$. A Taylor series expansion of equation 9.15 allowed me to mathematically approximate the decay time τ_{decay} and simplify it to the point where the behavior that is described above can be read directly from the formula. In this approximation, the decay time results from the sum of the three time constants mentioned above, namely

$$\tau_{\mathrm{decay}} \approx \frac{k_1+k_2+k_3}{k_1k_3} = \frac{n_{\mathrm{Q}}d}{S_{\mathrm{exc}}n_{\mathrm{bias}}} + \frac{\tau_{\mathrm{R}}n_{\mathrm{Q}}}{n_{\mathrm{bias}}} + \tau_{\mathrm{R}} \ , \tag{9.22}$$

which corresponds to a series connection of the recombination lifetime and the two RC-time constants from electrode discharging and charge transfer. As long as the exchange velocity is relatively high $\tau_{\mathrm{SRH}}^{\mathrm{eff}} > d/S_{\mathrm{exc}}$, equation 9.22 can be simplified even further, resulting in

$$\tau_{\mathrm{decay}} \approx \frac{\tau_{\mathrm{R}}n_{\mathrm{Q}}}{n_{\mathrm{bias}}} + \tau_{\mathrm{R}} = \tau_{\mathrm{R}} \quad 1 + \frac{n_{\mathrm{Q}}}{n_{\mathrm{bias}}} \quad = \frac{n_{\mathrm{Q}}/n_{\mathrm{bias}} + 1}{2k_{\mathrm{rad}}n_{\mathrm{bias}} + 1/\tau_{\mathrm{SRH}}^{\mathrm{eff}}} \tag{9.23}$$

It thereby matches the expression in equation 8.6 of the small-signal decay time $\tau_{\mathrm{cell,HLI}}^{\mathrm{SS}}$ from the single-component analytical model derived in section 8.2.1.

Using a similar mathematical approach also allows me to derive an approximation for the rise time

$$\tau_{\mathrm{rise}} \approx \frac{k_1+k_2+k_3}{(k_1+k_2+k_3)^2 - k_1k_3} \approx \frac{1}{k_1+k_2+k_3} = \quad \frac{1}{\tau_{\mathrm{R}}} + \frac{S_{\mathrm{exc}}}{d} + \frac{S_{\mathrm{exc}}n_{\mathrm{bias}}}{n_{\mathrm{Q}}d} \quad ^{-1} \ . \tag{9.24}$$

Basically, this rise-time approximation is a parallel connection of the recombination lifetime τ_{R}, the RC-time constant d/S_{exc} given by the resistance of charge transfer multiplied with the chemical capacitance of the perovskite, and finally $n_{\mathrm{Q}}d/(S_{\mathrm{exc}}n_{\mathrm{bias}})$ being the RC-time constant of charge- transfer resistance and electrode capacitance. This parallel connection means that the inverse of the rise time $1/\tau_{\mathrm{rise}}$ is formed by the sum of these three reciprocal time constants.

With the help of this mathematical simplification, also the course of τ_{rise} as a function of V_{oc}, shown in Figure 9.6a-c, is easier to understand. In the regime

of high open-circuit voltages, which is equivalent to high charge-carrier densities n_{bias}, the charge-carrier dependent time constant $n_{\mathrm{Q}}d/\left(S_{\mathrm{exc}}n_{\mathrm{bias}}\right)$ of equation 9.24 dominates. Thus, τ_{rise} vs. V_{oc} follows the dotted, dark purple line and the rise time decreases with higher open-circuit voltages. At low open-circuit voltages, the time constant d/S_{exc} and the linear, non-radiative component of the recombination lifetime τ_{R} set the saturation value of the rise time. In this regime, the rise time follows $\left(1/\tau_{\mathrm{SRH}}^{\mathrm{eff}}+S_{\mathrm{exc}}/d\right)^{-1}$, being illustrated as dashed, green line. Furthermore, looking at the rise time for the case of relatively high exchange velocities presented in Figure 9.6a and (b), indicates that the saturation value of τ_{rise} then only depends on d/S_{exc}. Thus, as long as the condition $\tau_{\mathrm{R}} > d/S_{\mathrm{exc}}$ holds, equation 9.24 can be simplified even further, resulting in

$$\tau_{\mathrm{rise}} \approx \frac{d}{S_{\mathrm{exc}}\left(1+n_{\mathrm{bias}}/n_{\mathrm{Q}}\right)} \quad . \tag{9.25}$$

So far, I discussed analytical solutions of τ_{rise} and τ_{decay} as a function of V_{oc} for the scenario of constant, voltage-independent exchange velocities S_{exc}, being presented in Figure9.6. The assumption that the quantity of S_{exc} is voltage-independent is not a very realistic scenario for my solar cell stacks. In perovskite solar cells with undoped charge-transport layers, the exchange velocity S_{exc} represents field-driven transport through the ETL and HTL that is highly voltage-dependent. To make the two-component model more applicable to the case of our MAPI solar cell, I insert a bias-voltage dependent exchange velocity to calculate the rise and decay times via equation 9.14 and 9.15. Figure9.7 shows the results of this study for the three different scenarios of a high, a medium, or a low voltage-dependent exchange velocity. While there are analytical approximations for S_{exc}, those are valid close to short circuit and inaccurate close to the open-circuit condition. Therefore these bias-depended exchange velocities S_{exc} results from numerical Sentaurus TCAD simulation of three perovskite solar cells conducted with different charge-carrier mobilities of the electron- and hole-transport layer. In this approach, the exchange velocities S_{exc} is determined using an alternative description of a current-voltage characteristic

$$J = J_{\mathrm{exc}}\left(\exp\left(\frac{qV_{\mathrm{ext}}}{2k_{\mathrm{B}}T}\right)-\exp\left(\frac{qV_{\mathrm{int}}}{2k_{\mathrm{B}}T}\right)\right) \quad , \tag{9.26}$$

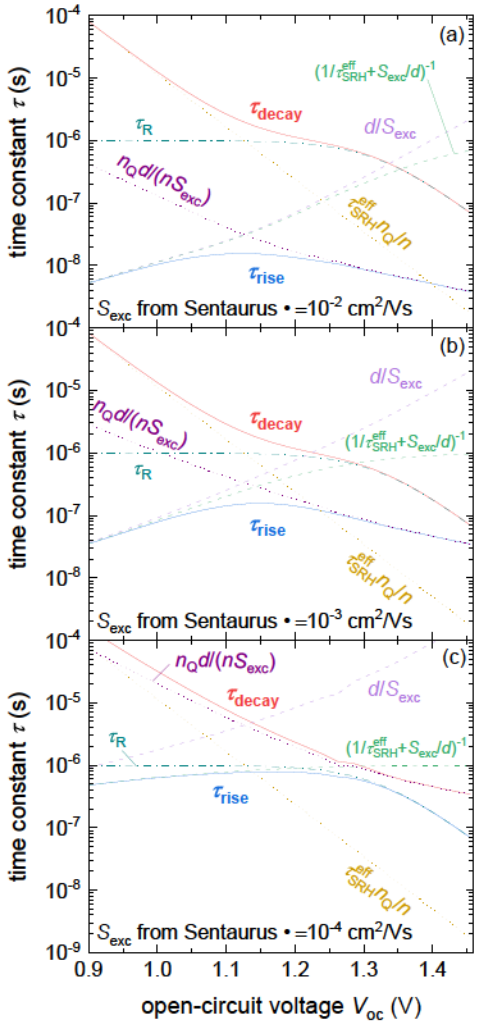

Abbildung 9.7: Decay time τ_{decay} (red) and rise time τ_{rise} (blue) as a function of the open-circuit voltage V_{oc}, resulting from the small-signal solution of the matrix equation introduced in section 9.3. Each figure panel is calculated using a different, voltage-dependent exchange velocity S_{exc} of (a) 1000 cm/s, (b) 100 cm/s and (c) 10 cm/s. These voltage-dependent exchange velocities S_{exc} account for the field-driven charge transport through the ETL or HTL, which typically appears in inverted, planar MAPI solar cells. Respective exchange velocities come from Sentaurus simulations conducted with different charge-carrier mobilities of the transport layers. The same values were used for the other parameters as in the previous calculations. Just like in Figure 9.6, the inverse coefficients $1/k_2 = d/S_{\mathrm{exc}}$ and $1/k_3 = n_{\mathrm{Q}} d/\left(S_{\mathrm{exc}} n_{\mathrm{bias}}\right)$, as well as other important time constant, are plotted as guide-to-the eye.

relating the current density J of the solar cell to the efficiency of extraction. Note that the exchange current J_{exc} depends on the exchange velocity and is defined by $J_{\mathrm{exc}} = qS_{\mathrm{exc}}n_{\mathrm{i}}$. Equation 9.26 states by how much the chemical potential of electron-hole pairs inside the solar cell has to exceed the external voltage in order to drive a current through the external circuit. Converting equation 9.26 yields a voltage-dependent expression for the exchange velocity

$$S_{\mathrm{exc}} = J/\ \ qn_{\mathrm{i}}\ \ \exp\ \ \frac{qV_{\mathrm{ext}}}{2k_{\mathrm{B}}T}\ \ -\exp\ \ \frac{qV_{\mathrm{int}}}{2k_{\mathrm{B}}T}\qquad . \tag{9.27}$$

The values for current-density J, the external voltage V_{ext} and the corresponding internal voltage V_{int} are extracted from Sentaurus simulation of the steady state current-voltage characteristic of a MAPI solar cell and their corresponding band diagrams at each bias point. Figure 9.8a shows these resulting exchange velocities S_{exc} as a function of bias open-circuit voltage V_{oc}, plotted as solid lines, for different mobilities between $10^{-4}\,\mathrm{cm}^2/(\mathrm{Vs})$ and $10^{-1}\,\mathrm{cm}^2/(\mathrm{Vs})$. Note that the exchange velocity varies strongly with voltage and increases over orders of magnitude towards small voltages.

Accordingly, this strong voltage-dependence of S_{exc} also affects the decay and rise times since the course of d/S_{exc} (lilac, dashed line) and $n_{\mathrm{Q}}d/\left(S_{\mathrm{exc}}n_{\mathrm{bias}}\right)$ (purple, dotted line) change. In comparison to Figure 9.6, d/S_{exc} in Figure 9.7 is no longer a horizontal line but increases for higher open-circuit voltages. Therefore, the rise time τ_{rise} is not constant in the regime at low open-circuit voltages, where the first two terms of

$$\tau_{\mathrm{rise}} \approx \quad \frac{1}{\tau_{\mathrm{R}}} + \frac{S_{\mathrm{exc}}\left(V_{\mathrm{oc}}\right)}{d} + \frac{S_{\mathrm{exc}}\left(V_{\mathrm{oc}}\right)n_{\mathrm{bias}}}{n_{\mathrm{Q}}d} \quad ^{-1} \tag{9.28}$$

dominate. For high exchange velocities, the last term of equation 9.28 dominates the rise time at high open-circuit voltages. It is illustrated in Figure 9.7a and (b). Since the slope of the *RC*-time constant from charge transfer $n_{\mathrm{Q}}d/\left(S_{\mathrm{exc}}n_{\mathrm{bias}}\right)$ flattens out due to the voltage dependency, the rise time decreases only slightly with higher V_{oc}'s, too. The decay time

$$\tau_{\mathrm{decay}} \approx \frac{n_{\mathrm{Q}}d}{S_{\mathrm{exc}}\left(V_{\mathrm{oc}}\right)n_{\mathrm{bias}}} + \frac{\tau_{\mathrm{R}}n_{\mathrm{Q}}}{n_{\mathrm{bias}}} + \tau_{\mathrm{R}} \tag{9.29}$$

is not affected by the exchange velocity S_{ext} and its voltage-dependency, as long as the exchange velocity is relatively high ($\tau_{\mathrm{R}} > d/S_{\mathrm{exc}}$). This situation applies in Figure 9.7a and (b), whereas in case of panel (c) a low exchange velocity causes that the decay time τ_{decay} is only dominated by $n_{\mathrm{Q}}d/(S_{\mathrm{exc}}n_{\mathrm{bias}})$ (purple, dotted line). Contrary to expectations, the decay time τ_{decay} of the external voltage does not provide then any information about the charge-carrier lifetime in the solar cell. Interestingly, in that situation, the rise time is mostly dominated by the recombination lifetime τ_{R}.

9.5 Application to Experimental TPV Data

Next, I will use the insides from this analytical two-component model to analyze and understand experimental TPV data of a MAPI solar cell. Figure 9.8b shows the rise time τ_{rise} and the decay time τ_{decay} of the experiment as blue and red spheres. These data points are extracted from the additional external voltage at nine different bias voltages by using equation 9.13 as a fitting function. The rise time changes only slightly in the evaluated voltage range between $0.9 - 1.3\,\mathrm{V}$ and is around 100 ns. The experimental decay time τ_{decay} shows three regions and decreases by orders of magnitude for higher open-circuit voltages. Considering the distance and shape of these two curves, I conclude that the recombination lifetime τ_{R} is larger than d/S_{exc}. Thus, these experimental rise and decay time curves resemble the analytical case for medium-high, voltage-dependent exchange velocities, as depicted in Figure 9.7b. Building on that, I adapted the analytical solution of the rise and decay times from the two-component model to this experimental data set in order to quantify recombination and the exchange properties of this MAPI solar cell. The additional red and blue lines in Figure 9.8b correspond to the calculated rise and decay time solution that fits best to the experiment. In addition, the related, characteristic time constants τ_{R}, d/S_{exc}, $n_{\mathrm{Q}}d/(S_{\mathrm{exc}}n_{\mathrm{bias}})$ and $\tau_{\mathrm{SRH}}^{\mathrm{eff}}n_{\mathrm{Q}}/n_{\mathrm{bias}}$ are shown as dotted or dashed lines. Here, the best-suited fitting parameters are a non-radiative recombination lifetime $\tau_{\mathrm{SRH}}^{\mathrm{eff}}$ of 2 s, a radiative recombination coefficient k_{rad} of $\times 10^{-10}\,\mathrm{cm}^3/\mathrm{s}$ and a capacitance per area $C_{\mathrm{area}} = 15\,\mathrm{nF/cm}^2$. The absorber-layer thickness is set to 280 nm and the intrinsic carrier concentration n_{i} to $8.05 \times 10^4\,\mathrm{cm}^{-3}$ for the calcu-

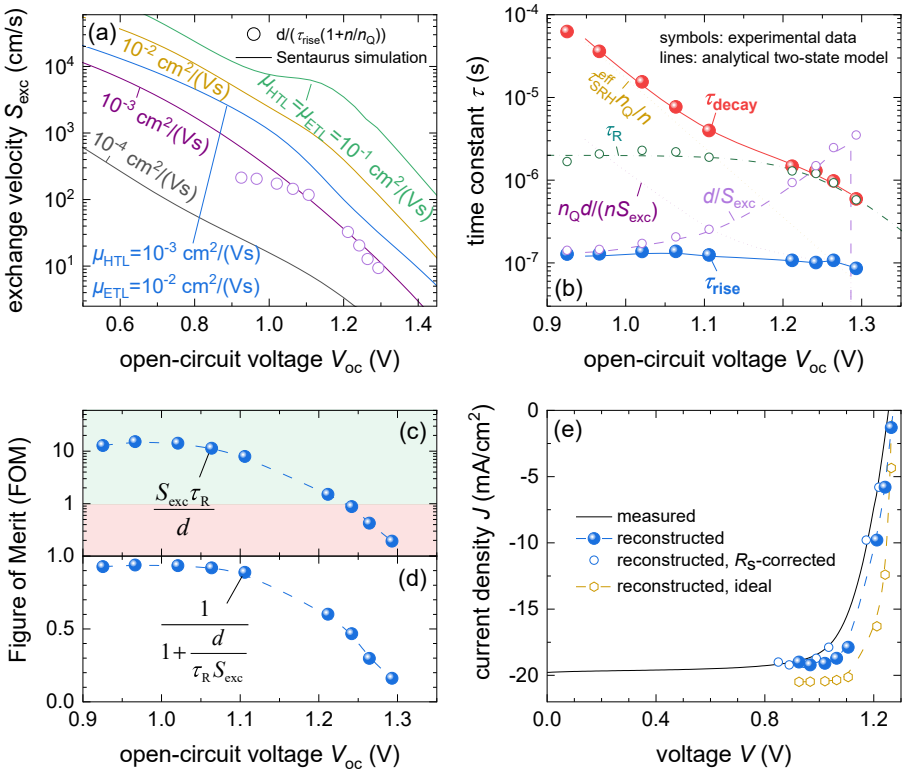

Abbildung 9.8: (a)) exchange velocity S_{exc} extracted from Sentaurus simulations conducted with various charge-carrier mobilities. Moreover, the dotted symbols show the exchange velocity S_{exc} calculated from the experimental TPV data via $S_{\mathrm{exc}} = d/\ \tau_{\mathrm{rise}}\ \ 1+n_{\mathrm{bias}}/n_{\mathrm{Q}}\ \ $. (b) Experimental data of the decay time τ_{decay} (red symbols) and rise time τ_{rise} (blue symbols) as a function of the open-circuit voltage V_{oc}. In addition, the analytical two-component model is fitted to experimental data. The lines represent these fits. (c) Figure of merit (FOM) and (e) measured and reconstructed current-voltage characteristic of the MAPI solar cell.

lation. Furthermore, I extracted the exchange velocity S_{exc} from the experimental rise time using the approximation

$$S_{\mathrm{exc}} \approx \ \ \frac{1}{\tau_{\mathrm{rise}}} - \frac{1}{\tau_{\mathrm{R}}}\ \ \ \frac{d}{1+n_{\mathrm{bias}}/n_{\mathrm{Q}}} \approx \frac{d}{\tau_{\mathrm{rise}}\ \ 1+n_{\mathrm{bias}}/n_{\mathrm{Q}}}\ \ . \tag{9.30}$$

The resulting exchange velocity as a function of bias V_{oc} takes values between $10-200\,\mathrm{cm/s}$ and is depicted in Figure 9.8a by the lilac, circular symbols. The cor-

responding values of d/S_{exc} are plotted in Figure 9.8b also as lilac, circular symbols. They dominate the rise time at low open-circuit voltages. Eliminating the capacitive component from the decay time allows us to extract an approximated recombination lifetime, resulting in

$$\tau_{\mathrm{R}} = \frac{\tau_{\mathrm{decay}}}{1+n_{\mathrm{Q}}/n_{\mathrm{bias}}} \quad . \tag{9.31}$$

Note, with τ_{R} from equation 9.31 and absorber thickness divided by the exchange velocity, namely

$$d/S_{\mathrm{exc}} \approx \tau_{\mathrm{rise}} \quad 1+n_{\mathrm{bias}}/n_{\mathrm{Q}} \quad , \tag{9.32}$$

I derived a time constant for charge-carrier recombination and another for charge extraction. These time constants quantify the two important mechanisms of recombination and charge extraction in a solar cell. As a result of this, the ratio of these time constants indicates how fast the extraction is relative to recombination. Thus, this ratio suits as a figure of merit (FOM), which is defined by

$$FOM_1 = \frac{S_{\mathrm{exc}}\tau_{\mathrm{R}}}{d} = \frac{\tau_{\mathrm{decay}}}{\tau_{\mathrm{rise}}} \frac{n_{\mathrm{Q}} n_{\mathrm{bias}}}{n_{\mathrm{Q}}+n_{\mathrm{bias}}}^{2} \quad . \tag{9.33}$$

As long as this figure of merit FOM_1 is larger than 1, charge extraction is faster than recombination. For $FOM_1 < 1$, the extraction is slower. Figure 9.8c displays this figure of merit for experimental TPV data of a perovskite solar cell.

Based on the rationale derived in ref. [284], it is possible to use the ratio of these two time constants τ_{R} and d/S_{exc} to estimate the effect of slow charge extraction on the current-voltage curve and thereby the performance of a solar cell. The steady-state equivalent of my two-component model allows us to calculate the current-voltage curve via

$$J = qd\,(R-G) = qd \quad \frac{1}{1+d/S_{\mathrm{exc}}\tau_{\mathrm{R}}} \qquad \frac{n_0}{\tau_{\mathrm{R}}} \exp \quad \frac{qV_{\mathrm{ext}}}{2k_{\mathrm{B}}T} \quad -G \quad , \tag{9.34}$$

describing how much the current density changes at a given voltage when the extraction is slow relative to recombination. [284] If $\tau_{\mathrm{R}} S_{\mathrm{exc}} \gg d$, charge extraction is efficient, and equation 9.34 predicts that the JV-curve only depends on recombination and generation but not on the efficiency of charge extraction. If, however $\tau_{\mathrm{R}} S_{\mathrm{exc}} \approx d$ the current density is reduced by about 50 %. Thus, a low value of S_{exc}

will reduce the short-circuit current density J_{sc} by the factor $(1+d/(S_{\mathrm{exc}}\tau_{\mathrm{R}}))^{-1}$. A voltage dependence of this factor can then also reduce the fill factor. In contrast, as open circuit is not affected by charge extraction, the open-circuit voltage remains independent of S_{exc}. Thus, this correction factor

$$FOM_2 = \frac{1}{1+\frac{d}{S_{\mathrm{exc}}\tau_{\mathrm{R}}}} = \frac{1}{1+\frac{\tau_{\mathrm{rise}}}{\tau_{\mathrm{decay}}}\frac{\left(n_{\mathrm{Q}}+n_{\mathrm{bias}}\right)^2}{n_{\mathrm{Q}}n_{\mathrm{bias}}}} \tag{9.35}$$

can serve as a second figure of merit. When charge extraction becomes slow compared to recombination, this factor will be less than one. Figure 9.8c for the experimental TPV data shows this second figure of merit. Both FOMs are relatively constant between 0.9 and 1.1 V, where $FOM_1 \approx 10$, implying that extraction is significantly faster than recombination. Towards higher voltages, FOM_1 significantly reduces and quickly falls below unity. As can be seen in Figure 9.8b, this drop is mostly due to d/S_{exc} getting significantly longer towards higher voltages. I assume this is because at voltages above 1.2 V, no significant electric field is likely left in the transport layers. Potentially, there are even extraction barriers implying that electrons and holes would have to diffuse against the electric field to get extracted.

Figure 9.8e illustrates the impact of the FOMs on the current-voltage curve. The solid, black line shows the experimentally measured current-voltage curve of the MAPI solar cell, whose TPV data is shown in Figure 9.8b. The yellow circles show the JV-curve according to equation 9.34, but assuming that extraction is ideal and the exchange velocity is infinitely high, i.e., $S_{\mathrm{exc}} \to \infty$. The blue spheres show the reconstruction of the current-voltage curve according to equation 9.34 combined with FOM_2 according to Figure 9.8b. Apparently, the actual JV-curve suffers from additional losses, as a comparison of the black and blue curve shows. I assume that these additional losses are ohmic series resistance losses, e.g., due to lateral transport in the transparent conductive oxide. As ohmic losses due to lateral transport would not be included in S_{exc}, it is plausible that the blue spheres do not reproduce the JV-curve. For this reason, I added an ohmic series resistance R_{s} of $4\,\Omega\mathrm{cm}^2$ to the reconstructed curve and obtain the open, blue circles, which approximate the experimental JV-curve well. Thus, we conclude that the FOMs are consistent with the JV-curve but would require additional information to predict

the JV-curve. In addition, extraction losses are mostly affecting the J_{sc} and to a lesser degree the FF, due to the rather low voltage dependence of S_{exc} up to the maximum-power point. This little dependence also implies that the fill factor FF is, in this example, most likely more affected by ohmic series resistances than by the non-ohmic charge transport through ETL and HTL. This observation is consistent with other experimental findings on charge extraction, such as the weak voltage-dependence of steady-state photoluminescence between short circuit and the maximum-power point in perovskite solar cells. [285, 286]

9.6 Conclusion and Outlook

The extraction of photogenerated charge carriers and the generation of a photovoltage belong to the fundamental functionalities of any solar cell. These processes happen not instantaneously but rather come with finite time constants, e.g., a time constant related to the rise of the externally measured open-circuit voltage following a short light pulse. In this chapter, I introduced a new method to analyze transient photovoltage measurements at different bias-light intensities. The results provide significant progress relative to previous approaches for analyzing transient photovoltage data because it explicitly includes the rise time as a source of information, too. Furthermore, I provided a comprehensible analytical solution that can be conveniently compared with experimental data. Besides, the two-component model introduced here is generic for the rise and the decay of the photovoltage in any solar cell.

10 Conclusion and Outlook

Halide perovskite materials possess remarkable properties that position them as potential candidates for commercialization in various applications, including photovoltaics, optoelectronics, X-ray detectors, and neuromorphic computing. The key distinguishing features of these materials are their solution processability, room-temperature crystal formation, and extremely high luminescence yields. Contrary to the saying by Wolfgang Pauli that "god made the bulk; the surface was invented by the devil", lead-halide perovskites exhibit excellent electronic surface quality, indicating low surface and interface recombination velocities. These peculiar properties of halide perovskites have significant consequences for their spectroscopic characterization, necessitating the development of new models and systematic approaches. The fast rise of the perovskite research community has led to a huge number of publications. However, the development in characterization techniques of films, layer stacks, and solar cell devices has not kept pace. This thesis addressed this gap by investigating the consequences of the peculiar properties of halide perovskites and proposing a series of innovations in the analysis of characterization data.

One significant consequence of the high luminescence quantum efficiency and the electronically benign surfaces and interfaces is the achievement of extremely high open-circuit voltages, approaching their respective limitations as given by the Shockley-Queisser model. [17] Consequently, it becomes necessary to develop methods to accurately quantify losses relative to these limits and establish appropriate reference points. Chapter 6 addressed this issue and proposed a standardized framework for reporting the V_{oc} limit and voltage loss in perovskite solar cells, enabling meaningful comparison and rating among various perovskite compositions. The proposed approach is an approximated version of the radiative limit that only requires a single measurement of the external quantum efficiency of the solar cell for its calculation.

The second consequence of high luminescence yield is that using luminescence as a characterization tool has become extremely popular in this specific community. However, the intrinsic nature of at least lead-halide perovskites leads to the uncommon situation that the device is often in high-level injection during these luminescence measurements, i.e., a situation where excess-carrier densities under illumination exceed dark majority-carrier densities. As a result, many transient phenomena exhibit rates that are non-linear in charge-carrier density. This non-linear dependency introduces complexities in the analysis of transient mechanisms like radiative recombination, capacitive charging and discharging, as well as recombination via defect levels that are not midgap. Thus, the analysis of transient photoluminescence decays requires approaches that go beyond the confines of single or multiexponential fitting. Chapter 7 showed how to derive differential decay times as a function of charge-carrier density and quasi-Fermi level splitting. Furthermore, I presented a comprehensive analysis of TPL data across various sample structures, starting from perovskite films and extending to multilayer systems with charge transfer between different layers, ultimately encompassing complete devices, where capacitive charging and discharging have an essential impact on the transients. Throughout the chapter, I employed numerical simulations to effectively visualize and explain the observed effects and carrier-densities dependent regimes.

Building upon the insights from Chapter 7, Chapter 8 took a step further by developing analytical equations that serve as a good approximation to the differential decay times. This analytical approach enables data analysis without relying on extensive numerical simulations. In addition, I showed how discrepancies between electrical and optical measurements of '*lifetimes*' originate from misinterpretations of decay times as lifetimes. It is important to distinguish between the model parameter within the Shockley-Read-Hall model and the characteristic decay time of any transient experiment. Thus, accurate nomenclature is highlighted as a crucial factor in distinguishing between observables and interpretations of observables that result in model parameters. To avoid confusion and provide clarity in the literature, the term '*lifetime*' should be strictly reserved for the parameters of a model. The key conceptual insights from comparing electrically and optically measured decay times are (i) that not every decay time is representative of recombination, (ii) that decay times change significantly with charge-carrier density, (iii) that decay times

without specifying carrier density or voltage are difficult or impossible to interpret, and that (iv) systematic differences between methods can be attributed to systematic variations in measurement conditions. Considering these points, a consistent interpretation of optical and electrical transients becomes possible.

In Chapter 9, I expanded the analytical approach to analyze not only recombination but also the extraction of charge carriers. This extension requires a mathematical description of the transients with a system of – at least two – differential equations. One equation represents the chemical potential of the charge carriers inside the PV-absorber material, whereas the other describes the electrical potential built-up by the charge carriers in the contact. Since these coupled differential equations are non-linear, any analytical treatment of such a scenario is limited to small-signal measurements, where linearization is possible. Therefore, a small-signal transient-photovoltage experiment serves as a starting point in the two-component model, revealing two time constants for every transient signal: A rise time and a decay time. Both associated time constants can be easily distinguished as they represent effects with opposite signs. In contrast, small-signal transient photoluminescence exhibits two time constants per transient, but both cause the signal to decay, which makes them much harder to distinguish. By expressing the linearized differential equations in the form of a 2×2 matrix, the negative inverse eigenvalues of the matrix correspond to the two observed time constants in the transient small-signal experiment. As the eigenvalues of a 2×2 matrix yield relatively simple analytical equations, an analytical description of the rise and decay time becomes attainable. Further simplification of the decay time using Taylor expansions recovers the analytical description previously derived in Chapter 8. The rise and decay time depend on the combination of three physical effects, namely recombination, extraction and capacitive charging and discharging. While the first two effects are highly relevant for steady-state device operation of the solar cell, capacitive terms are, by definition, only relevant when time-dependent changes in the external voltage occur. Therefore, it is advisable to correct for the influence of the electrode capacitance, which allows us to obtain quantitative values for a recombination- and extraction-time constant as a function of voltage.

The work presented in this thesis offers various options for future expansion of the models and methods. A recent important development is the recognition that

shallow defect levels significantly influence transient data of multi-cation perovskites, offering an intriguing opportunity for further investigation. As shallow defects are not explicitly considered in most of the work presented here, their inclusion in the model would be a very promising strategy. The presence of shallow traps could result in very different trends between steady-state and transient data, which would offer the possibility of exploiting the differences to better estimate the parameters of the defects. Furthermore, the analytical framework of the matrix model introduced in Chapter 9 could be extended to additional transient measurement methods, such as transient photocurrent measurements, or to small-signal frequency domain techniques like impedance or intensity-modulated photovoltage spectroscopy.

In summary, this Ph.D. thesis contributes to the understanding and characterizing of perovskite solar cells by developing innovative analytical approaches and models for data analysis. The work addresses the particular properties of halide perovskites, explores their implications on different characterization techniques, and offers insights into recombination, carrier extraction, and their interplay. These findings provide a solid foundation for future advancements in the field, e.g., by incorporating additional material characteristics or extending the proposed analytical framework to diverse characterization methods.

A Appendix: Additional Information

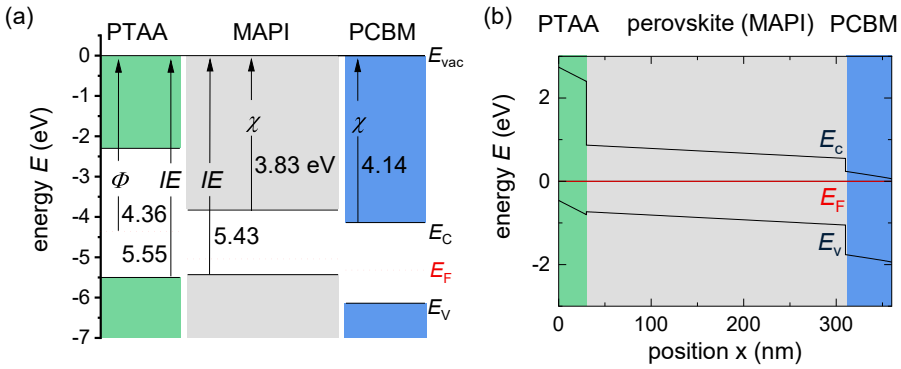

Abbildung A.1: (d) Energy-level diagram generated with UPS data. For the band gap of PTAA we assumed $\sim 3.2\,\text{eV}$ and $\sim 2\,\text{eV}$ for PCBM. (e) Band diagram generated with the respective values in SCAPS.

Tabelle A.1: Open-circuit voltages V_{oc} and the respective band gaps for various perovskite compositions published in literature. The band gap energy E_g^{ip} is calculated via the inflection point method. The data is used in Figure 4.2 in section 4.1.

Reference	year	E_g^{ip} (eV)	V_{oc} (V)
Burschka et al. [215]	2013	1.652	1.000
Jeon et al. [99]	2014	1.606	1.110
Jeon et al. [216]	2015	1.593	1.114
Yang et al. [100]	2015	1.530	1.059
Saliba et al. [142]	2016	1.624	1.240
Yang et al. [76]	2017	1.548	1.105
Jeon et al. [217]	2018	1.552	1.127
Jung et al. [201]	2019	1.559	1.144
Jiang et al. [200]	2019	1.527	1.179
Turren-Cruz et al. [202]	2018	1.528	1.108
Abdi-Jalebi et al. [143]	2018	1.590	1.170
		1.826	1.230
Yang et al. [203]	2019	1.616	1.230
Yoo et al. [213]	2019	1.576	1.186
Luo et al. [160]	2018	1.606	1.175
Gharibzadeh et al. [160]	2019	1.749	1.310
Cho et al. [287]	2018	1.592	1.140
Al-Ashouri et al. [197]	2019	1.628	1.188
Bush et al. [288]	2018	1.676	1.170
Longo et al. [180]	2018	1.687	1.119
Peña-Camargo et al. [289]	2020	1.687	1.119
Chen et al. [290]	2020	1.703	1.250
Khadka et al. [291]	2018	1.706	1.240
Wang et al. [292]	2017	1.724	1.180
Yu et al. [293]	2017	1.728	1.250
McMeekin et al. [294]	2016	1.720	1.200
Zhou et al. [295]	2017	1.736	1.240
Zhou et al. [296]	2018	1.785	1.284
Zhang et al. [297]	2020	1.845	1.340
Liu et al. [298]	2020	1.725	1.353
this work [140]	2018	1.613	1.260

Tabelle A.2: List of recipes used within the scope of this thesis to fabricate solution-processed and coevaporaed solar cells.

Layer	Device	Solution	Spin-Coating Parameters	Pretreatment
HTL	A	120 l PTAA (RT), 3.0 mg/ml in T	two-consecutive step program at 500 rpm for 4 s with a ramping rate of 500 rpm/s and 4500 rpm for 20 s with a ramping rate of 800 rpm/s	thermally annealed at 110 °C for 10 min
	B	120 l PTAA (RT), 1.5 mg/ml in T		
	C	120 l PTAA (RT), 2 mg/ml in T		
	Coevap-A, Coevap-D	120 l PTAA (RT), 3 mg/ml in DCB		
	Coevap-B	PEDOT:PSS (Ossila), cooled, 5 drops from syringe	5000 rpm for 60 s, with a ramping rate of 5000 rpm/s, statically spin coated in air	annealed at 110 °C for 10 min
	Coevap-C	120 l PolyTPD, 4 mg/ml in CB, stirred at RT, filtered with a 0.2 m PTFE filter prior to use	4000 rpm for 60 s, with a ramping rate of 800 rpm/s	20 min at RT

Table A.2 continued from previous page

Layer	Device	Solution	Spin-Coating Parameters	Pretreatment
solution-processed MAPI	A	180 l precursor solution, $Pb(CH_3COO)_2$ (0.54 M), $PbCl_2$ (0.06 M) and MAI (1.8 M) in DMF, stirred at RT for 60 min, filtered with a 0.45 m PTFE filter prior to use	two-consecutive step program at 2000 rpm for 10 s with a ramping rate of 500 rpm/s and 6000 rpm for 8 s with a ramping rate of 800 rpm/s	thermally annealed at 75 °C for 2 min
	B	135 l precursor solution, preheated to 75 °C $Pb(CH_3COO)_2$ (0.6 M), $PbCl_2$ (0.067 M), DMSO (0.667 M) and MAI (2 M) in DMF/DMSO, stirred at RT for 60 min, filtered with a 0.45 m PTFE filter prior to use	two-consecutive step program at 2000 rpm for 10 s with a ramping rate of 500 rpm/s and 6000 rpm for 30 s with a ramping rate of 800 rpm/s	

Table A.2 continued from previous page

Layer	Device	Solution	Spin-Coating Parameters	Pretreatment
	C	120 l precursor solution (RT), $Pb(CH_3COO)_2$ (0.54 M), $PbCl_2$ (0.06 M), DMSO (0.6 M) and MAI (1.791 M) in DMF/DMSO, stirred at RT for 24 hours, heated to 75 °C for 20 min, filtered with a 0.45 m PTFE filter prior to use	two-consecutive step program at 1400 rpm for 15 s with a ramping rate of 350 rpm/s and 6000 rpm for 40 s with a ramping rate of 767 rpm/s	thermally annealed at 75 °C for 2 min
PCBM	B	65 l, preheated to 75 °C, 20 mg/ml in CB and T (1 : 1), stirred at 70 °C for at least four hours, filtered with a 0.2 m PTFE filter prior to use	1200 rpm for 60 s with a ramping rate of 400 rmp/s	dried in an open petri dish for at least 20 min, at RT
	C	60 l, preheated to 75 °C 20 mg/ml in CB and T (1 : 1), stirred at 70 °C for at least four hours, filtered with a 0.2 m PTFE filter prior to use		

Table A.2 continued from previous page

Layer	Device	Solution	Spin-Coating Parameters	Pretreatment
	A, Coevap-A, Coevap-B, Coevap-C	80 l, 20 mg/ml in CB, stirred at 70 °C for at least four hours, filtered with a 0.2 m PTFE filter prior to use	1200 rpm for 60 s with a ramping rate of 400 rpm/s	dried in an open petri dish for at least 20 min, at RT
BCP	A, B, Coevap-A, Coevap-B, Coevap-C	120 l BCP (RT), 0.5 mg/ml in IPA not filtered, but ultrasonic treatment for one hour	4000 rpm for 30 s with a ramping rate of 800 rpm/s	no annealing
	C	100 l BCP (RT), 0.5 mg/ml in IPA, not filtered, but ultrasonic treatment for one hour		
Layer	**Device**	**Evaporation recipe**		
C_{60}/**BCP**	Coevap-D	20 nm C_{60} was thermally evaporated in a separate vacuum chamber ($< 5 \times 10^{-6}$ Pa) with a rate of 0.2 Å/s and 8 nm BCP with a rate of 0.2 Å/s		
Ag	all	80 nm Ag was thermally evaporated in a separate vacuum chamber ($< 5 \times 10^{-6}$ Pa) through a metal shadow mask with a rate of 2 Å/s		

Tabelle A.3: Overview of the band gap energies of lead halide perovskite solar cells calculated using common methods from literature and the value which is reported in the respective publication. This data is used in section 6.3 and 6.4.

Reference	Year	V_{oc} (V)	Stated E_g (eV)	E_g^{ip} (eV)	E_g^0 (eV)	$E_g^{EQE/2}$ (eV)	$E_g^{EQE=0.5}$ (eV)	E_g^{Tauc} (eV)	$E_g^{EQE,Tauc}$ (eV)
Gharibzadeh et al.	2019	1.310	1.72	1.749	1.700	1.749	1.754	1.716	1.723
Liu et al.	2018	1.260	1.600	1.613	1.573	1.634	1.652	1.597	1.597
Yang et al.	2019	1.230	1.570	1.616	1.575	1.615	1.619		1.587
Abdi-Jalebi et al.	2018	1.170	1.560	1.590	1.559	1.593	1.598		1.574
Luo et al.	2018	1.210	1.620	1.59	1.543	1.595	1.600	1.618	1.572
Yoo et al.	2019	1.186	1.53-1.56	1.576	1.541	1.574	1.576	1.558	1.559
Jung et al.	2019	1.152	1.500	1.559	1.524	1.562	1.562		1.542
Jiang et al.	2019	1.180	1.530	1.527	1.496	1.530	1.532		1.510
Turren-Cruz et al.	2018	1.108	1.530	1.528	1.499	1.531	1.534	1.531	1.516

Tabelle A.4: Overview of the limit of the open-circuit voltage of lead halide perovskite solar cells, being calculated using common methods from literature and the value which is reported in the respective publication and used in the meta-analysis in chapter 6.

Reference	V_{oc} (V)	Used V_{oc}^{limit} (eV)	V_{oc}^{rad} (eV)	V_{oc}^{ip} (eV)	V_{oc}^{0} (eV)	$V_{oc}^{EQE/2}$ (eV)	$V_{oc}^{EQE=0.5}$ (eV)	V_{oc}^{Tauc} (eV)	$V_{oc}^{EQE,Tauc}$ (eV)
Gharibzadeh et al.	1.310	1.438	1.443	1.465	1.419	1.465	1.470	1.433	1.440
Liu et al.	1.260	1.325	1.325	1.338	1.301	1.364	1.375	1.322	1.322
Yang et al.	1.230	1.298	1.314	1.341	1.302	1.339	1.342		1.313
Abdi-Jalebi et al.	1.170	1.288	1.305	1.316	1.287	1.318	1.323		1.300
Luo et al.	1.210	1.344	1.299	1.316	1.273	1.321	1.325	1.342	1.299
Yoo et al.	1.186		1.286	1.302	1.271	1.300	1.302	1.287	1.287
Jung et al.	1.152	1.231	1.271	1.287	1.253	1.290	1.290		1.271
Jiang et al.	1.180	1.259	1.246	1.257	1.227	1.260	1.262		1.241
Turren-Cruz et al.	1.108	1.259	1.246	1.259	1.231	1.260	1.264	1.260	1.246

Tabelle A.5: Device performance data of a range of small area lead-halide perovskite solar cells used in chapter 6 ($*$ symbol: certified values). The band gap is the one reported in the papers. The value ΔV_{oc} is defined as the difference between the radiative limit V_{oc} and the actual V_{oc}. For the limit of the short-circuit current $J_{\mathrm{sc}}^{\mathrm{SQ}}$ the value in the SQ is used calculated for the band gap $E_{\mathrm{g}}^{\mathrm{ip}}$ (inflection point method).

Reference	Eg (eV)	$\eta(\%)$	J_{sc} (mAcm^{-2})	V_{oc} (V)	$FF(\%)$	ΔV_{oc} (mV)	$J_{\mathrm{sc}}/J_{\mathrm{sc}}^{\mathrm{SQ}}$
Gharibzadeh 2019	1.72	19.80	19.30	1.310	78.00	133	0.918
Liu 2019	1.60	20.70	20.50	1.260	80.10	65	0.822
Yang 2019	1.57	21.40	22.16	1.230	77.50	84	0.889
Abdi-Jalebi 2018	1.56	21.50	23.20	1.170	79.00	135	0.862
Abdi-Jalebi 2018	1.78	17.50	17.90	1.230	79.00	263	0.89
Luo 2018	1.62	20.90	21.86	1.175	81.37	124	0.849
Luo 2018*	1.62	21.51	22.50	1.210	79.00	89	0.873
Yoo 2019	1.53	23.40	24.50	1.160	82.30	126	
Yoo 2019*	1.56	22.56	24.22	1.186	78.50	100	0.919
Jung 2019	1.50	23.30	24.33	1.152	81.40	119	0.903
Jung 2019*		22.67	24.92	1.144	79.60	127	0.925
Jiang 2019*	1.53	23.32	25.24	1.179	78.40	67	0.898
Jiang 2019		23.56	24.90	1.160	81.40	86	0.886
Turren-Cruz 2018 (masked)	1.53	20.40	25.10	1.080	75.50	166	0.893
Turren-Cruz 2018 (not masked)		20.05	24.30	1.108	74.70	138	0.864

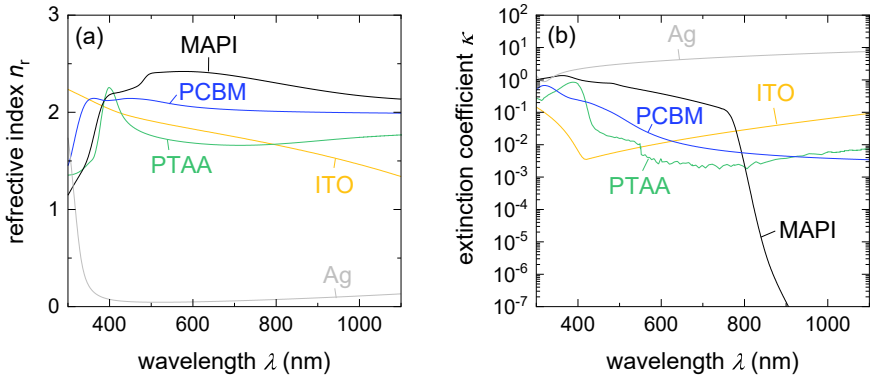

Abbildung A.2: Refractive index n_r and extinction coefficient κ used in the Sentaurus TCAD simulations in order to calculate the optical generation and the reflection at the back contact via the transfer-matrix method. The ITO data was obtained from L. Slooff. [299] The other optical data was measured in our group combining ellipsometry and UV/VIS, PDS and PL measurements. The recombination layer, which were implemented to model the interface of the absorber and the respective transport layer, the $n\kappa$-data set of the respective transport layer was used. For the thin metal tunnel layer the optical properties of ITO were used. In the ITO a quantum yield of 0 is assumed due to free carrier absorption. A quantum yield of 0 is assumed for the PTAA and PCBM layer as well due the fast geminate recombination of excitons in this layer.

Tabelle A.6: Parameters for TCAD Sentaurus Simulation.

Parameter			HTL		bulk		ETL	
	ITO	tunnel junction	PTAA	interface PTAA	MAPI	interface PCBM	PCBM	Ag
SRH lifetime $\tau_n = \tau_p$ (s)			10^{-8}		10^{-6}		10^{-8}	
rad. recombination coefficient k_{rad} (cm^3/s)			0	0	5×10^{-11}	0	0	
Auger recombination coefficient C_{Auger} (cm^6/s)			0	0	4.4×10^{-29}	0	0	
mobility $\mu_n = \mu_p$ (cm^2/Vs)	277.4		10^{-3}	20	20	20	10^{-2}	
band gap E_g (eV)	3.5		3.2	1.6	1.6	1.53	1.75	
electron affinity χ (eV)	5.471		2.23	3.83	3.83	3.83-4.19	3.9	
dielectric permittivity ϵ_r	10		3.5	30	30	30	3.5	
effective density of states								
conduction band N_C (cm^{-3})	10^{19}		2.2×10^{18}	2.2×10^{18}	2.2×10^{18}	2.2×10^{18}	2.2×10^{18}	
valence band N_V (cm^{-3})	10^{19}		2.2×10^{18}	2.2×10^{18}	2.2×10^{18}	2.2×10^{18}	2.2×10^{18}	
doping concentration (cm^{-3})	10^{20}				0	0	0	
thickness d (nm)	150	0.1	30	0.1	280	0.1	50	100
work function ϕ (eV)		5.330						4.05
resitivity (Ohm cm)		1.5×10^{-6}						1.5×10^{-6}

Tabelle A.7: Parameters of TCAD Sentaurus simulation used for fitting the experimental data of the solution-processed sample series.

Parameter	ITO	tunnel junction	HTL PTAA	interface PTAA	bulk MAPI	interface PCBM	ETL PCBM	Ag
SRH lifetime $\tau_n = \tau_p$ (s)			10^{-8}		4×10^{-5}		10^{-8}	
surface recombination velocity								
S_n (cm/s)				0.01		17		
S_p (cm/s)				0.01		17		
radiative recombination coefficient k_{rad} (cm^3/s)			0	0	7×10^{-11}	0	0	
Auger recombination coefficient C_{Auger} (cm^6/s)			0	0	4.4×10^{-29}	0	0	
mobility $\mu_n = \mu_p$ (cm^2/Vs)	277.4		10^{-3}	20	20	20	10^{-2}	
band gap E_g (eV)	3.5		3.2	1.6	1.6	1.53	1.75	
electron affinity χ (eV)	5.377		2.23	3.83	3.83	3.9		
dielectric permittivity ϵ_r	10		3.5	30	30	30	3.5	
effective density of states								
conduction band N_C (cm^{-3})	10^{19}		2.2×10^{18}	2.2×10^{18}	2.2×10^{18}	2.2×10^{18}	2.2×10^{18}	
valence band N_V (cm^{-3})	10^{19}		2.2×10^{18}	2.2×10^{18}	2.2×10^{18}	2.2×10^{18}	2.2×10^{18}	
doping concentration (cm^{-3})	10^{20}				0	0	0	
thickness d (nm)	150	0.1	16	0.1	300	0.1	55	100
work function ϕ (eV)		5.246						4.1
resitivity (Ohm cm)		1.5×10^{-6}						1.5×10^{-6}

Tabelle A.8: Parameters for TCAD Sentaurus simulation used for fitting the experimental data of the coevaporated sample series.

Parameter	ITO	tunnel junction	HTL PTAA	interface PTAA	bulk MAPI	interface PCBM	ETL PCBM	Ag
SRH lifetime $\tau_n = \tau_p$ (s)			10^{-8}		3.5×10^{-7}		10^{-8}	
surface recombination velocity								
S_n (cm/s)				100		500		
S_p (cm/s)				100		500		
radiative recombination coefficient k_{rad} (cm^3/s)			0	0	2×10^{-10}	0	0	
Auger recombination coefficient C_{Auger} (cm^6/s)			0	0	4.4×10^{-29}	0	0	
mobility $\mu_n = \mu_p$ (cm^2/Vs)	277.4		10^{-3}	20	20	20	10^{-2}	
band gap E_g (eV)	3.5		3.2	1.5	1.6	1.4	1.75	
electron affinity χ (eV)	5.377		2.13	3.83	3.83	4.03	4.03	
dielectric permittivity ϵ_r	10		3.5	30	30	30	3.5	
effective density of states								
conduction band N_C (cm^{-3})	10^{19}		2.2×10^{18}	2.2×10^{18}	2.2×10^{18}	2.2×10^{18}	2.2×10^{18}	
valence band N_V (cm^{-3})	10^{19}		2.2×10^{18}	2.2×10^{18}	2.2×10^{18}	2.2×10^{18}	2.2×10^{18}	
doping concentration (cm^{-3})	10^{20}				0	0	0	
thickness d (nm)	150	0.1	15	0.1	465	0.1	20	100
work function ϕ (eV)		5.246						4.1
resitivity (Ohm cm)		1.5×10^{-6}						1.5×10^{-6}

Tabelle A.8: Parameters for TCAD Sentaurus simulation used for fitting the experimental data of the coevaporated sample series.

Table A.8 continued from previous page

	ITO	tunnel junction	HTL PTAA	interface PTAA	bulk MAPI	interface PCBM	ETL PCBM	Ag
defect state 1 (SRH statistic)								
surface recombination velocity								
S_n (cm/s)				100		500		
S_p (cm/s)				100		500		
energetic position (eV)				-0.6		-0.69		
efect state 2 (donor like)								
defect concentration n_D (cm^{-3})						10^{16}		
energetic position (eV)						midgap		
hole capture coefficient (cm^3/s)						10^{-6}		
electron capture coefficient (cm^3/s)						10^{-6}		

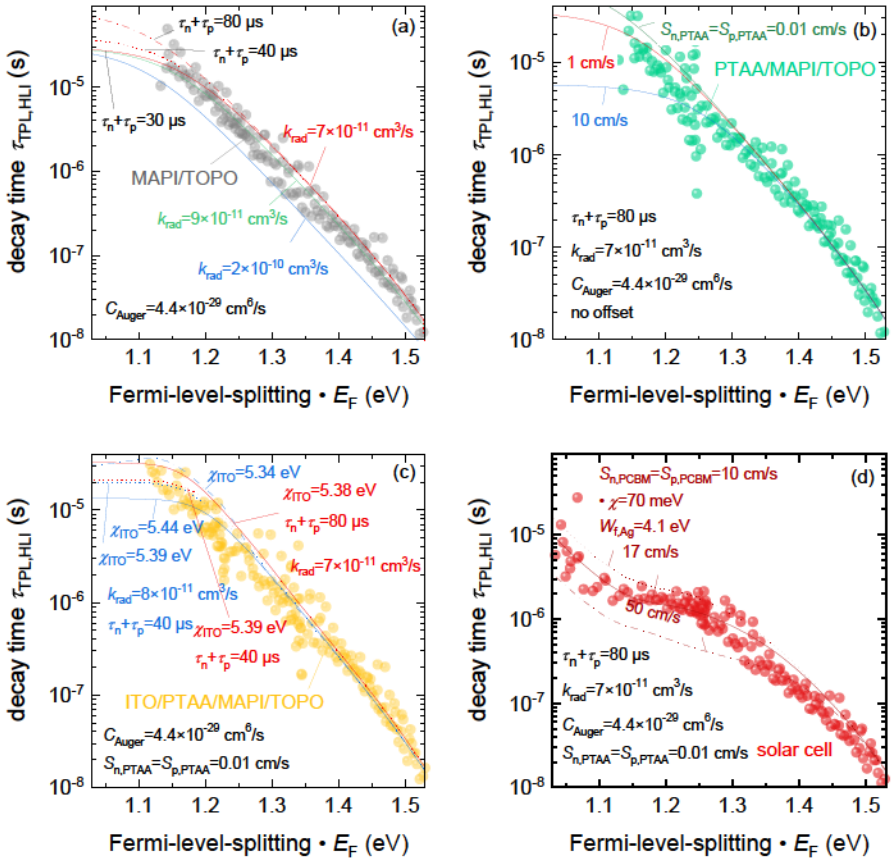

Abbildung A.3: Visualization of the impact of exemplary parameter variations in the numerical simulations with Sentaurus TCAD to the quality of the fit result, using data from solution-processed samples as a reference (symbols), being discussed in chapter 7 in section 7.6.

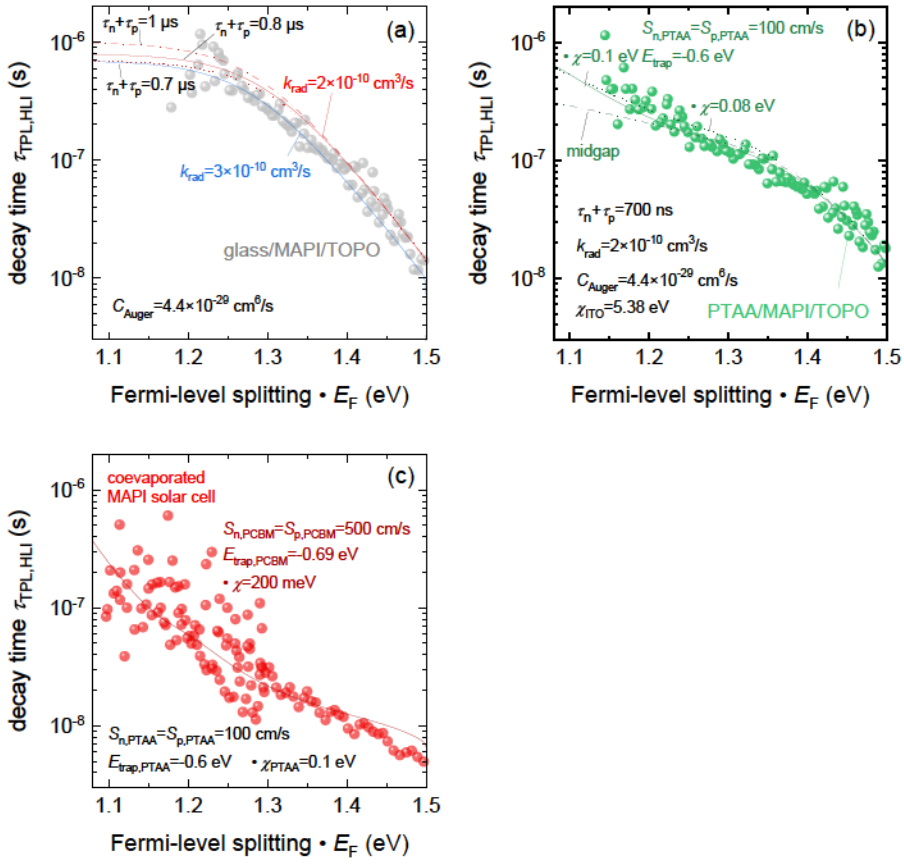

Abbildung A.4: Parameter variations in the numerical simulations with Sentaurus TCAD for fitting experimental TPL data from coevaporated samples (symbols).

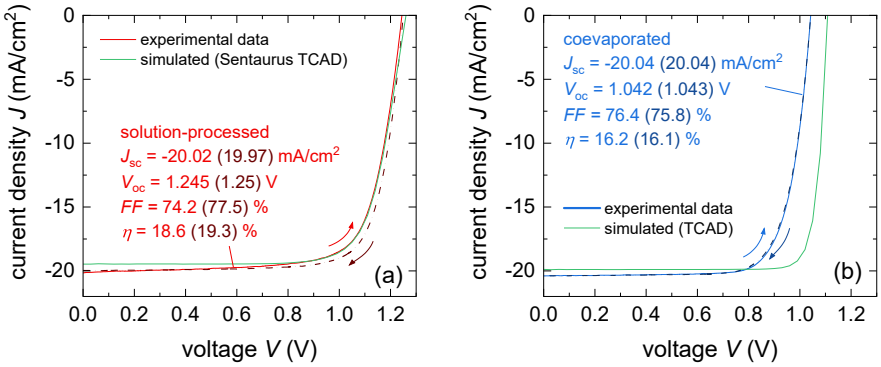

Abbildung A.5: Comparison of the simulated and measured current-voltage (JV)-characteristic for (a) the solution-processed and (b) the coevaporated MAPI solar cell. For the TCAD simulation of the current-voltage characteristic the parameters stated in Table A.8 and A.7 were used.

Tabelle A.9: Assignment of the data points from literature in Figure 8.1. This data collection from literature compares the decay time $\tau_{\mathrm{TPL}}^{\mathrm{LS}}$ of the transient PL measured on perovskite films or on pervoskite/transport layer stacks with the decay-time constant $\tau_{\mathrm{TPV}}^{\mathrm{SS}}$ resulting from transient photovoltage measurements on the respective solar cell device.

type	bias intensity (suns)	author	TPL (s)	TPV (s)
film	1	Chen et al. [254]	0.241	3.1
			0.289	1.4
film	1	Yang et al. [260]	0.27	0.27
			1.3	0.58
film	1	Zhou et al. [262]	0.382	2.5
			0.736	3
film	1	Du et al. [265]	0.45	1.374
			0.74	1.398
film	0.5	Wang et al. [258]	0.052	0.157
			0.114	0.285
film	0.5	Yao et al. [270]	8.37	3.81
			11.98	5.79
film	0.3	Xue et al. [300]	0.136	4.66
			0.136	5.84
film	not stated	Chen et al. [255]	1	2.1
			1.732	3
film	not stated	Jiang et al. [200]	0.364	8.8
			1.43	138.2
film	not stated	Tan et al. [257]	0.47	64
			0.47	145
film	not stated	Wang et al. [259]	2.5	1650
			2.5	2340
film	not stated	Zheng et al. [261]	0.903	0.56
film	not stated	Du et al. [264]	0.37	0.89
			0.735	1.04
film	not stated	Tian et al. [266]	1.24×10^{-3}	3.81
			6.80×10^{-4}	7

Tabelle A.9: Assignment of the data points from literature in Figure 8.1

film	not stated	Tan et al. [267]	1.03	6.9
film	not stated	Wang et al. [268]	0.012	3.1
			7.5×10^{-3}	4.7
film	not stated	Xiao et al. [269]	0.134	10
			0.631	43
film	not stated	Yang et al. [203]	0.267	0.5
			1.28	1.71
quencher	1	Wang et al. [186]	0.087	2.23
			0.08	2.4
			0.081	1.88
			0.096	2.48
			0.102	7.01
quencher	0.5	Li et al. [256]	0.172	3.5
			0.063	5
quencher	0.3	Xue et al. [300]	0.033	4.66
			0.02	5.84
quencher	0.01	Back et al. [263]	0.01	27.8
quencher	not stated	Tan et al. [257]	0.099	64
			0.112	145

B Abbreviations and Symbols

α	absorption coefficient
β_n	capture coefficient for electrons
β_p	capture coefficient for holes
ϵ_0	dielectric constant of vacuum
ϵ_r	relative dielectric permittivity
η	energy-conversion efficiency
κ	extinction coefficient
λ	wavelength
μ	charge-carrier mobility
μ_n	electron mobility
μ_p	hole mobility
σ	electrical conductivity
τ	charge-carrier lifetime
τ_eff	effective lifetime
$\tau_\mathrm{eff,LLI}$	effective Shockley-Read-Hall lifetime in low-level injection
τ_mono	lifetime constant of a monoexponential decay
τ_nrad	non-radiative lifetime
τ_rad	radiative lifetime
τ_SRH	Shockley-Read-Hall bulk lifetime
$\tau_\mathrm{SRH,n}$	Shockley-Read-Hall bulk lifetime of electrons
$\tau_\mathrm{SRH,p}$	Shockley-Read-Hall bulk lifetime of holes
$\tau_\mathrm{SRH}^\mathrm{eff}$	effective SRH-lifetime
τ_s	surface lifetime
τ_TPL	differential decay time from TPL
$\tau_\mathrm{TPL,HLI}$	decay time from TPL in high-level injection

$\tau_{\mathrm{TPL,LLI}}$	decay time from TPL in low-level injection
τ_{R}	recombination lifetime
ϕ_{em}	emitted photon flux
ϕ_{exc}	excitation fluence
ϕ_{bb}	black-body radiation
ϕ_{PL}	spectral photoluminescence flux
ϕ_{TPL}	transient photoluminescence flux
ϕ_{sun}	solar spectrum
φ	electrostatic potential
χ	electron affinity
ρ	net space-carrier density

a	absorptance
c	speed of light in vacuum: $2.9979 \times 10^8\,\mathrm{m\,s^{-1}}$
C_{area}	area-related capacitance
C_{Auger}	effective trap-assisted Auger recombination coefficient $C_{\mathrm{n}} + C_{\mathrm{p}}$
C_{n}	Auger-recombination coefficient for electrons
C_{p}	Auger-recombination coefficient for holes
d	thickness
$D(E)$	density of states
D	diffusion constant
D_{n}	diffusion constant of electrons
D_{p}	diffusion constant of holes
e_{n}	emission coefficient for electrons
e_{p}	emission coefficient for holes
E	energy
E_{b}	binding energy
E_{C}	energy level of conduction band
E_{g}	band gap energy
E_{F}	equilibrium-Fermi level
$E_{\mathrm{F,n}}$	quasi-Fermi level for electrons
$E_{\mathrm{F,p}}$	quasi-Fermi level for holes
ΔE_{F}	quasi-Fermi level splitting

E_t	trap depth
E_V	energy level of valence band
E_vac	vacuum energy
E_0	Urbach energy
f	electron-occupation function
F	electric field
FF	fill factor
G_ext	external generation rate
G_int	internal generation rate
h	Planck constant: $4.1357 \times 10^{-15}\,\mathrm{eV\,s}$
$I_\mathrm{PL}(t)$	photoluminescence intensity over time
$I_\mathrm{PL,norm}(t)$	normalized photoluminescence intensity over time
J	current density
J_dark	dark-current density
J_0	saturation-current density
J_0^rad	radiative saturation-current density
J_rec	recombination-current density
J_nrad	non-radiative recombination current
J_rad	radiative recombination current
J_n	electron-current density
J_p	hole-current density
J_sc	short-circuit current density
k_B	Boltzmann constant: $8.6173 \times 10^{-5}\,\mathrm{eV\,K^{-1}}$
k_rad	external radiative recombination coefficient
$k_\mathrm{rad}^\mathrm{int}$	internal radiative recombination coefficient
k_nrad	radiative bimolecular recombination coefficient
n	electron concentration
n_i	intrinsic charge-carrier concentration
n_bias	steady-state charge-carrier density
n_r	refractive index
n_0	equilibrium-electron concentration
Δn_laser	laser-induced excess-charge carrier concentration
Δn	excess-electron concentration

N_A	acceptor-doping density
N_D	donor-doping density
N_C	effective density of states in the conduction band
N_t	trap density
N_V	effective density of states in the valence band
p	hole concentration
p_a	probability of absorbing a photon parasitically
p_e	photon-outcoupling probability
p_r	reabsorption probability a photon
p_0	equilibrium-hole concentration
Δp	excess-hole concentration
P_max	maximum attainable power density of a solar cell
q	elementary charge: $1.6022 \times 10^{-19}\,\mathrm{C}$
$Q_\mathrm{e}^\mathrm{EQE}$	external-quantum efficiency
Q_e^PV	quantum efficiency
$Q_\mathrm{e}^\mathrm{lum}$	external LED quantum efficiency
$Q_\mathrm{i}^\mathrm{lum}$	internal luminescence quantum efficiency
R	total recombination rate
R_Auger	trap-assisted Auger recombination rate
R_nrad	non-radiative recombination rate
R_rad	radiative recombination rate
$R_\mathrm{rad}^\mathrm{ext}$	external radiative recombination rate
$R_\mathrm{rad}^\mathrm{int}$	internal radiative recombination rate
R_SRH	Shockley-Read-Hall recombination rate
R_s	Shockley-Read-Hall recombination rate at the surface
R_int	interface-recombination rate
S	surface-recombination velocity
S_n	surface-recombination velocity for electrons
S_p	surface-recombination velocity for holes
t	time
T	temperature
V	voltage
V_ext	external voltage

V_{int}	internal voltage
V_{oc}	open-circuit voltage
$V_{\mathrm{oc}}^{\mathrm{rad}}$	radiative limit of the open-circuit voltage
x	position

ASA	Advanced Semiconductor Analysis
APTMS	(3-aminopropyl)trimethoxysilane
BCP	bathocuproine
CB	chlorobenzene
CsBr	cesium bromide
CsI	cesium iodide
C_{60}	fullerene
CCD	charge-coupled device
CIGS	copper indium gallium selenide
1,2-DCB	1,2-dichlorobenzene
DMF	dimethylformamide
DMSO	dimethylsulfoxid
EL	electroluminescence
ETL	electron-transport layer
FAI	formamidimium iodide
FOM	figure of merit
FTO	fluorine-doped tin oxide
FTPS	Fourier transform photocurrent spectroscopy
HLI	high-level injection
HTL	hole-transport layer
IE	ionisation energy
IR	infrared
ITO	indium-tin oxide
JOSEPH	cluster tool - *Jülich online semiconductor growth experiment for photovoltaics*
JV	current-density voltage
LED	light-emitting diode
LLI	low-level injection

MAI	methylammonium iodide
MAPI	methylammonium-lead iodide $CH_3NH_3PbI_3$
MCP	microchannel plate
MeO-2PACz	([2-(3,6-dimethoxy-9H-carbazol-9-yl)ethyl]phosphonic acid)
MPP	maximum-power point
OCVD	open-circuit voltage decay
$PbCl_2$	lead chloride
PbI_2	lead iodide
$Pb(CH_3COO)_2$	dry lead acetate
PCBM	[6,6]-phenyl-C_{61}-butyric acid methyl ester
PDS	Photothermal deflection spectroscopy
PEDOT:PSS	poly(3,4-ethylenedioxythiophene)
PL	photoluminescence
PLQY	photoluminescence-quantum yield
PMT	photomultiplier tube
PolyTPD	poly(N,N'-bis-4-butylphenyl-N,N'-bisphenyl)benzidine
PTAA	poly[bis(4-phenyl)(2,4,6-trimethylphenyl)amine]
PV	photovoltaic
P3HT	poly(3-hexylthiophene-2,5-diyl)
QCM	quartz-crystal microbalances
QFLS	quasi-Fermi level splitting
SEM	scanning electron microscopy
SAM	self-assembling monolayer molecule
Spiro-OMeTAD	2,2′,7,7′-tetrakis-(N,N-di-4-methoxyphenylamino)-9,9′-spirobifluorene
SQ	Shockley-Queisser model
SRH	non-radiative Shockley-Read-Hall recombination
SSPL	steady-state photoluminescence
TCO	transparent conductive oxide
TCSPC	time-correlated single-photon counting
TMM	transfer-matrix method
TOPO	n-trioctylphosphine oxide
TPL	time-resolved photoluminescence

TPV	transient photovoltage
UHV	ultra-high vacuum
UV	ultraviolet
VBM	valence-band maximum
XPS	X-ray photoelectron spectroscopy
UPS	ultraviolet photoelectron spectroscopy

C List of Publications

Publications related to this thesis

Zhifa Liu, Lisa Krückemeier*, Benedikt Krogmeier, Benjamin Klingebiel, José A Márquez, Sergiu Levcenko, Senol Öz, Sanjay Mathur, Uwe Rau, Thomas Unold, Thomas Kirchartz. "Open-Circuit Voltages Exceeding 1.26 V in Planar Methylammonium Lead Iodide Perovskite Solar Cells.", *ACS Energy Letters*, vol. 4, no. 1, pp. 110-117, 2018.

Thomas Kirchartz, Lisa Krückemeier, Eva L Unger. "Research Update: Recombination and Open-Circuit Voltage in Lead-Halide Perovskites." *APL Materials*, vol. 6, no. 10, pp. 100702, 2018.

Lisa Krückemeier, Uwe Rau, Martin Stolterfoht, Thomas Kirchartz. "How to Report Record Open-Circuit Voltages in Lead-Halide Perovskite Solar Cells." *Advanced Energy Materials*, vol. 10, no. 1, pp. 1902573, 2020.

Lisa Krückemeier, Benedikt Krogmeier, Zhifa Liu, Uwe Rau, Thomas Kirchartz. "Understanding Transient Photoluminescence in Halide Perovskite Layer Stacks and Solar Cells.", *Advanced Energy Materials*, vol. 11, no. 19, pp. 2003489, 2021.

Lisa Krückemeier, Zhifa Liu, Benedikt Krogmeier, Uwe Rau, Thomas Kirchartz. "Consistent Interpretation of Electrical and Optical Transients in Halide Perovskite Layers and Solar Cells.", *Advanced Energy Materials*, vol. 11, no. 46, pp. 2102290, 2021.

Lisa Krückemeier, Zhifa Liu, Thomas Kirchartz, Uwe Rau. "Quantifying Charge Extraction and Recombination Using the Rise and Decay of the Transient Photovoltage of Perovskite Solar Cells.", *Advanced Materials*, vol. 35, no. 35, pp. 2300872, 2023.

*equal contribution

Further publications

Pascal Kaienburg, Lisa Krückemeier, Dana Lübke, Jenny Nelson, Uwe Rau, Thomas Kirchartz. "How Solar Cell Efficiency is Governed by the $\alpha\mu\tau$ Product.", *Physical Review Research*, vol. 2, no. 2, pp. 023109, 2020.

Jinane Haddad, Benedikt Krogmeier, Benjamin Klingebiel, Lisa Krückemeier, Stephanie Melhem, Zhifa Liu, Jürgen Hüpkes, Sanjay Mathur, Thomas Kirchartz. "Analyzing Interface Recombination in Lead-Halide Perovskite Solar Cells with Organic and Inorganic Hole-Transport Layers.", *Advanced Materials Interfaces*, vol. 7, no. 16, pp. 2000366, 2020.

Lisa Krückemeier, Pascal Kaienburg, Jan Flohre, Karsten Bittkau, Irene Zonno, Benedikt Krogmeier, Thomas Kirchartz. "Developing Design Criteria for Organic Solar Cells Using Well-Absorbing Non-Fullerene Acceptors.", *Communications Physics*, vol. 1, no. 1, pp. 1-10, 2018.

D Curriculum Vitae

Personal Details

Name	**Lisa Krückemeier**
Date of Birth	07.03.1990
Place of Birth	Essen
Citizenship	German

Education

27/9/2024	**Doctoral Examination** for Dr.-Ing Faculty of Electrical Engineering and Information Technology, RWTH Aachen University, Germany
8/2017-2/2021	**Research Assistant** and Doctoral Candidate Forschungszentrum Jülich GmbH, IMD-3 Photovoltaics, Germany
10/2009-7/2017	**Studies of NanoEngineering** University Duisburg-Essen, Germany *Interdisciplinary nanotechnology program, combining electrical, process & mechanical engineering, physics and chemistry*
7/2017	**Master of Science** (M.Sc.) in NanoEngineering *Specialization: nanoelectronics & nanooptoelectronics*
7/2014	**Bachelor of Science** (B.Sc.) in NanoEngineering
2000-2009	**General Higher Education Entrance Qualification** (Abitur) B.M.V.-Schule, Mädchengymnasium, Essen, Germany

Literaturverzeichnis

[1] H. Lee, K. Calvin, D. Dasgupta, G. Krinner, A. Mukherji, P. Thorne, C. Trisos, J. Romero, P. Aldunce, K. Barrett, G. Blanco, W. W. L. Cheung, S. L. Connors, F. Denton, A. Diongue-Niang, D. Dodman, M. Garschagen, O. Geden, B. Hayward, C. Jones, F. Jotzo, T. Krug, R. Lasco, J.-Y. Lee, V. Masson-Delmotte, M. Meinshausen, K. Mintenbeck, A. Mokssit, F. E. L. Otto, M. Pathak, A. Pirani, E. Poloczanska, H.-O. Pórtner, A. Revi, D. C. Roberts, J. Roy, A. C. Ruane, J. Skea, P. R. Shukla, R. Slade, A. Slangen, Y. Sokona, A. A. Sórensson, M. Tignor, D. van Vuuren, Y.-M. Wei, H. Winkler, P. Zhai, and Z. Zommers, "Synthesis report of the IPCC sixth assessment report (AR6)," *Intergovernmental Panel on Climate Change*, 2023.

[2] N. M. Haegel, P. Verlinden, M. Victoria, P. Altermatt, H. Atwater, T. Barnes, C. Breyer, C. Case, S. D. Wolf, C. Deline, M. Dharmrin, B. Dimmler, M. Gloeckler, J. C. Goldschmidt, B. Hallam, S. Haussener, B. Holder, U. Jaeger, A. Jaeger-Waldau, I. Kaizuka, H. Kikusato, B. Kroposki, S. Kurtz, K. Matsubara, S. Nowak, K. Ogimoto, C. Peter, I. M. Peters, S. Philipps, M. Powalla, U. Rau, T. Reindl, M. Roumpani, K. Sakurai, C. Schorn, P. Schossig, R. Schlatmann, R. Sinton, A. Slaoui, B. L. Smith, P. Schneidewind, B. Stanbery, M. Topic, W. Tumas, J. Vasi, M. Vetter, E. Weber, A. W. Weeber, A. Weidlich, D. Weiss, and A. W. Bett, "Photovoltaics at multi-terawatt scale: Waiting is not an option," *Science*, vol. 380, no. 6640, pp. 39–42, 2023.

[3] *Fraunhofer ISE: Photovoltaics Report.* Fraunhofer Institute for Solar Energy Systems, ISE with support of PSE Projects GmbH, https://www.ise.fraunhofer.de/content/dam/ise/de/documents/publications/studies/Photovoltaics-Report.pdf, updated: 21 February 2023.

[4] H. Wirth, *Aktuelle Fakten zur Photovoltaik in Deutschland.* Fraunhofer ISE,

Download von www.pv-fakten.de, Fassung vom 17.05.2023.

[5] D. M. Chapin, C. S. Fuller, and G. L. Pearson, "A new silicon p-n junction photocell for converting solar radiation into electrical power," *Journal of Applied Physics*, vol. 25, pp. 676–677, 05 2004.

[6] H. Lin, M. Yang, X. Ru, G. Wang, S. Yin, F. Peng, C. Hong, M. Qu, J. Lu, L. Fang, *et al.*, "Silicon heterojunction solar cells with up to 26.81% efficiency achieved by electrically optimized nanocrystalline-silicon hole contact layers," *Nature Energy*, pp. 1–11, 2023.

[7] M. A. Green, E. D. Dunlop, M. Yoshita, N. Kopidakis, K. Bothe, G. Siefer, and X. Hao, "Solar cell efficiency tables (version 62)," *Progress in Photovoltaics: Research and Applications*, vol. 31, no. 7, pp. 651–663, 2023.

[8] M. A. Green, A. Ho-Baillie, and H. J. Snaith, "The emergence of perovskite solar cells," *Nature Photonics*, vol. 8, no. 7, pp. 506–514, 2014.

[9] S. D. Stranks and H. J. Snaith, "Metal-halide perovskites for photovoltaic and light-emitting devices," *Nature Nanotechnology*, vol. 10, no. 5, pp. 391–402, 2015.

[10] W. Zhang, G. E. Eperon, and H. J. Snaith, "Metal halide perovskites for energy applications," *Nature Energy*, vol. 1, no. 6, pp. 1–8, 2016.

[11] A. Kojima, K. Teshima, Y. Shirai, and T. Miyasaka, "Organometal halide perovskites as visible-light sensitizers for photovoltaic cells," *Journal of the American Chemical Society*, vol. 131, no. 17, pp. 6050–6051, 2009.

[12] J. Yoo, G. Seo, M. Chua, T. G. Park, Y. Lu, F. Rotermund, Y.-K. Kim, C. Moon, N. Jeon, J.-P. Correa-Baena, V. Bulovic, S. S. Shin, M. Bawendi, and J. Seo, "Efficient perovskite solar cells via improved carrier management," *Nature*, vol. 590, no. 7847, pp. 587–593, 2021.

[13] P. Würfel and U. Würfel, *Physics of solar cells: From basic principles to advanced concepts*, pp. 93–102. Weinheim: Wiley-VCH Verlag, 1 ed., 2005.

[14] J. Nelson, *The physics of solar cells*. London: Imperial College Press, neugedruckte ed., 2013.

[15] U. Würfel, A. Cuevas, and P. Würfel, "Charge carrier separation in solar cells,"

IEEE Journal of Photovoltaics, vol. 5, no. 1, pp. 461–469, 2014.

[16] D. Abou-Ras, T. Kirchartz, and U. Rau, eds., *Advanced characterization techniques for thin film solar cells*. Weinheim: Wiley-VCH Verlag, 2nd, extended edition ed., 2016.

[17] W. Shockley and H. J. Queisser, "Detailed balance limit of efficiency of p–n junction solar cells," *Journal of Applied Physics*, vol. 32, no. 3, pp. 510–519, 1961.

[18] Y. Wang, D. Qian, Y. Cui, H. Zhang, J. Hou, K. Vandewal, T. Kirchartz, and F. Gao, "Optical gaps of organic solar cells as a reference for comparing voltage losses," *Advanced Energy Materials*, vol. 8, no. 28, p. 1801352, 2018.

[19] J.-F. Guillemoles, T. Kirchartz, D. Cahen, and U. Rau, "Guide for the perplexed to the Shockley-Queisser model for solar cells," *Nature Photonics*, vol. 13, no. 8, p. 501, 2019.

[20] "Reference air mass 1.5 spectra," *NREL.gov, https://www.nrel.gov/grid/solar-resource/spectra-am1.5.html*.

[21] A. Rao and R. H. Friend, "Harnessing singlet exciton fission to break the Shockley-Queisser limit," *Nature Reviews Materials*, vol. 2, no. 11, pp. 1–12, 2017.

[22] M. Einzinger, T. Wu, J. F. Kompalla, H. L. Smith, C. F. Perkinson, L. Nienhaus, S. Wieghold, D. N. Congreve, A. Kahn, M. G. Bawendi, *et al.*, "Sensitization of silicon by singlet exciton fission in tetracene," *Nature*, vol. 571, no. 7763, pp. 90–94, 2019.

[23] D. N. Congreve, J. Lee, N. J. Thompson, E. Hontz, S. R. Yost, P. D. Reusswig, M. E. Bahlke, S. Reineke, T. Van Voorhis, and M. A. Baldo, "External quantum efficiency above 100% in a singlet-exciton-fission–based organic photovoltaic cell," *Science*, vol. 340, no. 6130, pp. 334–337, 2013.

[24] P. Würfel, A. Brown, T. Humphrey, and M. Green, "Particle conservation in the hot-carrier solar cell," *Progress in Photovoltaics: Research and Applications*, vol. 13, no. 4, pp. 277–285, 2005.

[25] D. König, K. Casalenuovo, Y. Takeda, G. Conibeer, J. Guillemoles, R. Patterson, L. Huang, and M. Green, "Hot carrier solar cells: Principles, materials

and design," *Physica E: Low-dimensional Systems and Nanostructures*, vol. 42, no. 10, pp. 2862–2866, 2010.

[26] M. Jošt, L. Kegelmann, L. Korte, and S. Albrecht, "Monolithic perovskite tandem solar cells: A review of the present status and advanced characterization methods toward 30% efficiency," *Advanced Energy Materials*, vol. 10, no. 26, p. 1904102, 2020.

[27] H. Cotal, C. Fetzer, J. Boisvert, G. Kinsey, R. King, P. Hebert, H. Yoon, and N. Karam, "III–V multijunction solar cells for concentrating photovoltaics," *Energy & Environmental Science*, vol. 2, no. 2, pp. 174–192, 2009.

[28] P. Bridgman, "Note on the principle of detailed balancing," *Physical Review*, vol. 31, no. 1, p. 101, 1928.

[29] W. Van Roosbroeck and W. Shockley, "Photon-radiative recombination of electrons and holes in germanium," *Physical Review*, vol. 94, no. 6, p. 1558, 1954.

[30] T. Kirchartz, D. Abou-Ras, and U. Rau, "Introduction to thin-film photovoltaics," *Advanced Characterization Techniques for Thin Film Solar Cells*, pp. 1–32, 2011.

[31] G. Kirchhoff, "I. on the relation between the radiating and absorbing powers of different bodies for light and heat," *The London, Edinburgh, and Dublin Philosophical Magazine and Journal of Science*, vol. 20, no. 130, pp. 1–21, 1860.

[32] G. Kirchhoff, "Über das Verhältniss zwischen dem Emissionsvermögen und dem Absorptionsvermögen der Körper für Wärme und Licht," *Annalen der Physik*, vol. 185, no. 2, pp. 275–301, 1860.

[33] M. Planck, *The theory of heat radiation*. Courier Corporation, 2013.

[34] R. B. Wehrspohn, U. Rau, and A. Gombert, *Photon management in solar cells*, pp. 21–29. John Wiley & Sons, 2015.

[35] P. Würfel, "The chemical potential of radiation," *Journal of Physics C: Solid State Physics*, vol. 15, no. 18, pp. 3967–3985, 1982.

[36] T. Kirchartz and U. Rau, "Detailed balance and reciprocity in solar cells,"

Physica Status Solidi (a), vol. 205, no. 12, pp. 2737–2751, 2008.

[37] T. Kirchartz, "PhD thesis: Generalized detailed balance theory of solar cells," *Forschungszentrum Jülich*, vol. 38, 2009.

[38] T. Markvart, "The thermodynamics of optical étendue," *Journal of Optics A: Pure and Applied Optics*, vol. 10, p. 015008, dec 2007.

[39] M. A. Green, "Solar cell fill factors-general graph and empirical expressions," *Solid State Electronics*, vol. 24, p. 788, 1981.

[40] U. Rau, B. Blank, T. C. Müller, and T. Kirchartz, "Efficiency potential of photovoltaic materials and devices unveiled by detailed-balance analysis," *Physical Review Applied*, vol. 7, no. 4, p. 044016, 2017.

[41] T. Tiedje, E. Yablonovitch, G. D. Cody, and B. G. Brooks, "Limiting efficiency of silicon solar cells," *IEEE Transactions on Electron Devices*, vol. 31, no. 5, pp. 711–716, 1984.

[42] J. Yao, T. Kirchartz, M. S. Vezie, M. A. Faist, W. Gong, Z. He, H. Wu, J. Troughton, T. Watson, D. Bryant, and J. Nelson, "Quantifying losses in open-circuit voltage in solution-processable solar cells," *Physical Review Applied*, vol. 4, no. 1, p. 014020, 2015.

[43] T. Kirchartz, K. Taretto, and U. Rau, "Efficiency limits of organic bulk heterojunction solar cells," *The Journal of Physical Chemistry C*, vol. 113, no. 41, pp. 17958–17966, 2009.

[44] U. Rau and J. Werner, "Radiative efficiency limits of solar cells with lateral band-gap fluctuations," *Applied Physics Letters*, vol. 84, no. 19, pp. 3735–3737, 2004.

[45] U. Rau, "Reciprocity relation between photovoltaic quantum efficiency and electroluminescent emission of solar cells," *Physical Review B*, vol. 76, no. 8, p. 085303, 2007.

[46] L. Onsager, "Reciprocal relations in irreversible processes. i.," *Physical Review*, vol. 37, pp. 405–426, Feb 1931.

[47] T. Kirchartz, U. Rau, M. Kurth, J. Mattheis, and J. Werner, "Comparative study of electroluminescence from Cu(In,Ga)Se_2 and Si solar cells," *Thin Solid*

Films, vol. 515, no. 15, pp. 6238–6242, 2007.

[48] T. Kirchartz and U. Rau, "Electroluminescence analysis of high efficiency Cu(In,Ga)Se_2 solar cells," *Journal of Applied Physics*, vol. 102, no. 10, p. 104510, 2007.

[49] W. Tress, N. Marinova, O. Inganäs, M. K. Nazeeruddin, S. M. Zakeeruddin, and M. Graetzel, "Predicting the open-circuit voltage of $CH_3NH_3PbI_3$ perovskite solar cells using electroluminescence and photovoltaic quantum efficiency spectra: the role of radiative and non-radiative recombination," *Advanced Energy Materials*, vol. 5, no. 3, p. 1400812, 2015.

[50] K. Tvingstedt, O. Malinkiewicz, A. Baumann, C. Deibel, H. J. Snaith, V. Dyakonov, and H. J. Bolink, "Radiative efficiency of lead iodide based perovskite solar cells," *Scientific Reports*, vol. 4, p. 6071, 2014.

[51] K. Vandewal, S. Albrecht, E. T. Hoke, K. R. Graham, J. Widmer, J. D. Douglas, M. Schubert, W. R. Mateker, J. T. Bloking, G. F. Burkhard, A. Sellinger, J. M. J. Fréchet, A. Amassian, M. K. Riede, M. D. McGehee, D. Neher, and A. Salleo, "Efficient charge generation by relaxed charge-transfer states at organic interfaces," *Nature Materials*, vol. 13, p. 63, 2013.

[52] K. Vandewal, K. Tvingstedt, A. Gadisa, O. Inganäs, and J. V. Manca, "On the origin of the open-circuit voltage of polymer-fullerene solar cells," *Nature Materials*, vol. 8, p. 904, 2009.

[53] A. Cuevas and D. Yan, "Misconceptions and misnomers in solar cells," *IEEE Journal of Photovoltaics*, vol. 3, no. 2, pp. 916–923, 2013.

[54] U. Rau and T. Kirchartz, "Charge carrier collection and contact selectivity in solar cells," *Advanced Materials Interfaces*, vol. 6, no. 20, p. 1900252, 2019.

[55] U. Rau, G. Kron, and J. Werner, "Reply to comments on electronic transport in dye-sensitized nanoporous TiO_2 solar cells comparison of electrolyte and solid-state devices. on the photovoltaic action in pn-junction and dye-sensitized solar cells," *The Journal of Physical Chemistry B*, vol. 107, no. 48, pp. 13547–13550, 2003.

[56] O. J. Sandberg, J. Kurpiers, M. Stolterfoht, D. Neher, P. Meredith, S. Shoaee, and A. Armin, "On the question of the need for a built-in potential in perovs-

kite solar cells," *Advanced Materials Interfaces*, vol. 7, no. 10, p. 2000041, 2020.

[57] O. J. Sandberg, M. Nyman, and R. Österbacka, "Effect of contacts in organic bulk heterojunction solar cells," *Physical Review Applied*, vol. 1, p. 024003, Mar 2014.

[58] R. Brendel and R. Peibst, "Contact selectivity and efficiency in crystalline silicon photovoltaics," *IEEE Journal of photovoltaics*, vol. 6, no. 6, pp. 1413–1420, 2016.

[59] M. A. Green, "Radiative efficiency of state-of-the-art photovoltaic cells," *Progress in Photovoltaics: Research and Applications*, vol. 20, no. 4, pp. 472–476, 2012.

[60] M. A. Green and A. W. Ho-Baillie, "Pushing to the limit: Radiative efficiencies of recent mainstream and emerging solar cells," *ACS Energy Letters*, vol. 4, pp. 1639–1644, 2019.

[61] R. T. Ross, "Some thermodynamics of photochemical systems," *The Journal of Chemical Physics*, vol. 46, no. 12, pp. 4590–4593, 1967.

[62] M. A. Green, K. Emery, Y. Hishikawa, W. Warta, and E. D. Dunlop, "Solar cell efficiency tables (version 45)," *Progress in Photovoltaics: Research and Applications*, vol. 23, no. 1, pp. 1–9, 2015.

[63] M. A. Green, Y. Hishikawa, W. Warta, E. D. Dunlop, D. H. Levi, J. Hohl-Ebinger, and A. W. Ho-Baillie, "Solar cell efficiency tables (version 50)," *Progress in Photovoltaics: Research and Applications*, vol. 25, no. 7, pp. 668–676, 2017.

[64] M. A. Green, Y. Hishikawa, E. D. Dunlop, D. H. Levi, J. Hohl-Ebinger, M. Yoshita, and A. W. Ho-Baillie, "Solar cell efficiency tables (version 53)," *Progress in Photovoltaics: Research and Applications*, vol. 27, no. 1, pp. 3–12, 2019.

[65] M. A. Green, E. D. Dunlop, D. H. Levi, J. Hohl-Ebinger, M. Yoshita, and A. W. Ho-Baillie, "Solar cell efficiency tables (version 54)," *Progress in Photovoltaics: Research and Applications*, vol. 27, no. 7, pp. 565–575, 2019.

[66] M. Green, E. Dunlop, J. Hohl-Ebinger, M. Yoshita, N. Kopidakis, and X. Hao, "Solar cell efficiency tables (version 57)," *Progress in Photovoltaics: Research*

and Applications, vol. 29, no. 1, pp. 3–15, 2021.

[67] Q. Liu, Y. Jiang, K. Jin, J. Qin, J. Xu, W. Li, J. Xiong, J. Liu, Z. Xiao, K. Sun, *et al.*, "18% efficiency organic solar cells," *Science Bulletin*, vol. 65, no. 4, pp. 272–275, 2020.

[68] M. A. Green, "Accuracy of analytical expressions for solar cell fill factors," *Solar Cells*, vol. 7, no. 3, pp. 337–340, 1982.

[69] D. Weber, "$CH_3NH_3PbI_3$, ein Pb(II)-system mit kubischer Perowskitstruktur," *Zeitschrift für Naturforschung B*, vol. 33, no. 12, pp. 1443–1445, 1978.

[70] M. M. Lee, J. Teuscher, T. Miyasaka, T. N. Murakami, and H. J. Snaith, "Efficient hybrid solar cells based on meso-superstructured organometal halide perovskites," *Science*, p. 1228604, 2012.

[71] H.-S. Kim, C.-R. Lee, J.-H. Im, K.-B. Lee, T. Moehl, A. Marchioro, S.-J. Moon, R. Humphry-Baker, J.-H. Yum, J. E. Moser, *et al.*, "Lead iodide perovskite sensitized all-solid-state submicron thin film mesoscopic solar cell with efficiency exceeding 9%," *Scientific Reports*, vol. 2, no. 1, pp. 1–7, 2012.

[72] "NREL, best research-cell efficiency chart," *NREL.gov, https://www.nrel.gov/pv/cell-efficiency.html*.

[73] Y. Rong, Y. Hu, A. Mei, H. Tan, M. I. Saidaminov, S. I. Seok, M. D. McGehee, E. H. Sargent, and H. Han, "Challenges for commercializing perovskite solar cells," *Science*, vol. 361, no. 6408, 2018.

[74] N. Li, X. Niu, Q. Chen, and H. Zhou, "Towards commercialization: the operational stability of perovskite solar cells," *Chemical Society Reviews*, vol. 49, pp. 8235–8286, 2020.

[75] S. De Wolf, J. Holovsky, S.-J. Moon, P. Löper, B. Niesen, M. Ledinsky, F.-J. Haug, J.-H. Yum, and C. Ballif, "Organometallic halide perovskites: sharp optical absorption edge and its relation to photovoltaic performance," *The Journal of Physical Chemistry Letters*, vol. 5, no. 6, pp. 1035–1039, 2014.

[76] Y. Yang, M. Yang, D. T. Moore, Y. Yan, E. M. Miller, K. Zhu, and M. C. Beard, "Top and bottom surfaces limit carrier lifetime in lead iodide perovskite films," *Nature Energy*, vol. 2, no. 2, pp. 1–7, 2017.

[77] M. Sendner, P. K. Nayak, D. A. Egger, S. Beck, C. Müller, B. Epding, W. Kowalsky, L. Kronik, H. J. Snaith, A. Pucci, *et al.*, "Optical phonons in methylammonium lead halide perovskites and implications for charge transport," *Materials Horizons*, vol. 3, no. 6, pp. 613–620, 2016.

[78] D. W. deQuilettes, S. Koch, S. Burke, R. K. Paranji, A. J. Shropshire, M. E. Ziffer, and D. S. Ginger, "Photoluminescence lifetimes exceeding 8 s and quantum yields exceeding 30% in hybrid perovskite thin films by ligand passivation," *ACS Energy Letters*, vol. 1, no. 2, pp. 438–444, 2016.

[79] L. M. Herz, "Charge-carrier mobilities in metal halide perovskites: Fundamental mechanisms and limits," *ACS Energy Letters*, vol. 2, no. 7, pp. 1539–1548, 2017.

[80] Y. Chen, H. Yi, X. Wu, R. Haroldson, Y. Gartstein, Y. Rodionov, K. Tikhonov, A. Zakhidov, X.-Y. Zhu, and V. Podzorov, "Extended carrier lifetimes and diffusion in hybrid perovskites revealed by hall effect and photoconductivity measurements," *Nature Communications*, vol. 7, no. 1, pp. 1–9, 2016.

[81] I. Levine, S. Gupta, A. Bera, D. Ceratti, G. Hodes, D. Cahen, D. Guo, T. J. Savenije, J. Ávila, H. J. Bolink, *et al.*, "Can we use time-resolved measurements to get steady-state transport data for halide perovskites?," *Journal of Applied Physics*, vol. 124, no. 10, p. 103103, 2018.

[82] T. Umebayashi, K. Asai, T. Kondo, and A. Nakao, "Electronic structures of lead iodide based low-dimensional crystals," *Physical Review B*, vol. 67, no. 15, p. 155405, 2003.

[83] F. Brivio, A. B. Walker, and A. Walsh, "Structural and electronic properties of hybrid perovskites for high-efficiency thin-film photovoltaics from first-principles," *APL Materials*, vol. 1, no. 4, p. 042111, 2013.

[84] J. M. Frost, K. T. Butler, F. Brivio, C. H. Hendon, M. Van Schilfgaarde, and A. Walsh, "Atomistic origins of high-performance in hybrid halide perovskite solar cells," *Nano Letters*, vol. 14, no. 5, pp. 2584–2590, 2014.

[85] S. Tao, I. Schmidt, G. Brocks, J. Jiang, I. Tranca, K. Meerholz, and S. Olthof, "Absolute energy level positions in tin-and lead-based halide perovskites," *Nature Communications*, vol. 10, no. 1, pp. 1–10, 2019.

[86] M. H. Du, "Efficient carrier transport in halide perovskites: theoretical perspectives," *Journal of Materials Chemistry A*, vol. 2, no. 24, pp. 9091–9098, 2014.

[87] J. H. Noh, S. H. Im, J. H. Heo, T. N. Mandal, and S. I. Seok, "Chemical management for colorful, efficient, and stable inorganic-organic hybrid nanostructured solar cells," *Nano Letters*, vol. 13, no. 4, pp. 1764–1769, 2013.

[88] J.-W. Lee, S. Tan, S. I. Seok, Y. Yang, and N.-G. Park, "Rethinking the a cation in halide perovskites," *Science*, vol. 375, no. 6583, p. eabj1186, 2022.

[89] F. Ünlü, E. Jung, J. Haddad, A. Kulkarni, S. Öz, H. Choi, T. Fischer, S. Chakraborty, T. Kirchartz, and S. Mathur, "Understanding the interplay of stability and efficiency in A-site engineered lead halide perovskites," *APL Materials*, vol. 8, no. 7, p. 070901, 2020.

[90] A. Zakutayev, C. M. Caskey, A. N. Fioretti, D. S. Ginley, J. Vidal, V. Stevanovic, E. Tea, and S. Lany, "Defect tolerant semiconductors for solar energy conversion," *The Journal of Physical Chemistry Letters*, vol. 5, no. 7, pp. 1117–1125, 2014. PMID: 26274458.

[91] R. E. Brandt, V. Stevanović, D. S. Ginley, and T. Buonassisi, "Identifying defect-tolerant semiconductors with high minority-carrier lifetimes: Beyond hybrid lead halide perovskites," *Mrs Communications*, vol. 5, no. 2, pp. 265–275, 2015.

[92] M.-H. Du, "Density functional calculations of native defects in $CH_3NH_3PbI_3$: effects of spin–orbit coupling and self-interaction error," *The Journal of Physical Chemistry Letters*, vol. 6, no. 8, pp. 1461–1466, 2015.

[93] W.-J. Yin, T. Shi, and Y. Yan, "Unusual defect physics in $CH_3NH_3PbI_3$ perovskite solar cell absorber," *Applied Physics Letters*, vol. 104, no. 6, p. 063903, 2014.

[94] A. Walsh and A. Zunger, "Instilling defect tolerance in new compounds," *Nature Materials*, vol. 16, no. 10, pp. 964–967, 2017.

[95] T. Kirchartz, T. Markvart, U. Rau, and D. A. Egger, "Impact of small phonon energies on the charge-carrier lifetimes in metal-halide perovskites," *The Journal of Physical Chemistry Letters*, vol. 9, no. 5, pp. 939–946, 2018.

[96] C. Gehrmann and D. A. Egger, "Dynamic shortening of disorder potentials in anharmonic halide perovskites," *Nature Communications*, vol. 10, no. 1, p. 3141, 2019.

[97] U. Bach, D. Lupo, P. Comte, J. E. Moser, F. Weissörtel, J. Salbeck, H. Spreitzer, and M. Grätzel, "Solid-state dye-sensitized mesoporous TiO_2 solar cells with high photon-to-electron conversion efficiencies," *Nature*, vol. 395, no. 6702, pp. 583–585, 1998.

[98] G. E. Eperon, S. D. Stranks, C. Menelaou, M. B. Johnston, L. M. Herz, and H. J. Snaith, "Formamidinium lead trihalide: a broadly tunable perovskite for efficient planar heterojunction solar cells," *Energy & Environmental Science*, vol. 7, no. 3, pp. 982–988, 2014.

[99] N. J. Jeon, J. H. Noh, Y. C. Kim, W. S. Yang, S. Ryu, and S. I. Seok, "Solvent engineering for high-performance inorganic-organic hybrid perovskite solar cells," *Nature Materials*, vol. 13, no. 9, p. 897, 2014.

[100] W. S. Yang, J. H. Noh, N. J. Jeon, Y. C. Kim, S. Ryu, J. Seo, and S. I. Seok, "High-performance photovoltaic perovskite layers fabricated through intramolecular exchange," *Science*, vol. 348, no. 6240, pp. 1234–1237, 2015.

[101] M. Saliba, T. Matsui, J.-Y. Seo, K. Domanski, J.-P. Correa-Baena, M. K. Nazeeruddin, S. M. Zakeeruddin, W. Tress, A. Abate, and A. Hagfeldt, "Cesium-containing triple cation perovskite solar cells: improved stability, reproducibility and high efficiency," *Energy & Environmental Science*, vol. 9, no. 6, pp. 1989–1997, 2016.

[102] F. Peña-Camargo, J. Thiesbrummel, H. Hempel, A. Musiienko, V. M. Le Corre, J. Diekmann, J. Warby, T. Unold, F. Lang, D. Neher, *et al.*, "Revealing the doping density in perovskite solar cells and its impact on device performance," *Applied Physics Reviews*, vol. 9, no. 2, p. 021409, 2022.

[103] J. G. Fossum, "Physical operation of back-surface-field silicon solar cells," *IEEE Transactions on Electron Devices*, vol. 24, no. 4, pp. 322–325, 1977.

[104] M. Gloeckler and J. Sites, "Band-gap grading in $Cu(In,Ga)Se_2$ solar cells," *Journal of Physics and Chemistry of Solids*, vol. 66, no. 11, pp. 1891–1894, 2005.

[105] S. Selberherr, *Analytical Investigations About the Basic Semiconductor Equations*, p. 127. Vienna: Springer Vienna, 1984.

[106] R. E. I. Schropp and M. Zeman, *Electrical Device Modeling*, p. 127. Boston, MA: Springer US, 1998.

[107] A. Froitzheim, *Hetero-Solarzellen aus amorphem und kristallinem Silizium*. Philipps-Universität Marburg, 2003.

[108] J. Parrott, "Radiative recombination and photon recycling in photovoltaic solar cells," *Solar Energy Materials and Solar Cells*, vol. 30, no. 3, pp. 221–231, 1993.

[109] T. Kirchartz, F. Staub, and U. Rau, "Impact of photon recycling on the open-circuit voltage of metal halide perovskite solar cells," *ACS Energy Letters*, vol. 1, no. 4, pp. 731–739, 2016.

[110] U. Rau, U. W. Paetzold, and T. Kirchartz, "Thermodynamics of light management in photovoltaic devices," *Physical Review B*, vol. 90, no. 3, p. 035211, 2014.

[111] P. H. Berning, "Theory and calculations of optical thin films," *Physics of Thin Films*, vol. 1, p. 69, 1963.

[112] C. L. Davies, M. R. Filip, J. B. Patel, T. W. Crothers, C. Verdi, A. D. Wright, R. L. Milot, F. Giustino, M. B. Johnston, and L. M. Herz, "Bimolecular recombination in methylammonium lead triiodide perovskite is an inverse absorption process," *Nature Communications*, vol. 9, no. 1, pp. 1–9, 2018.

[113] P. Asbeck, "Self-absorption effects on the radiative lifetime in gaas-gaalas double heterostructures," *Journal of Applied Physics*, vol. 48, no. 2, pp. 820–822, 1977.

[114] R. N. Hall, "Electron-hole recombination in germanium," *Physical Review*, vol. 87, no. 2, p. 387, 1952.

[115] W. Shockley and R. W. T., "Statistics of the recombinations of holes and electrons," *Physical Review*, vol. 87, no. 5, pp. 835–842, 1952.

[116] B. K. Ridley, "On the multiphonon capture rate in semiconductors," *Solid-State Electronics*, vol. 21, no. 11-12, pp. 1319–1323, 1978.

[117] K. Huang, A. Rhys, and N. F. Mott, "Theory of light absorption and non-radiative transitions in f-centres," *Proceedings of the Royal Society of London. Series A. Mathematical and Physical Sciences*, vol. 204, no. 1078, pp. 406–423, 1950.

[118] T. Markvart, "Semiclassical theory of non-radiative transitions," *Journal of Physics C: Solid State Physics*, vol. 14, no. 29, p. L895, 1981.

[119] P. T. Landsberg, *Recombination in semiconductors*. Cambridge University Press, 2003.

[120] J. Fu, Q. Xu, G. Han, B. Wu, C. H. A. Huan, M. L. Leek, and T. C. Sum, "Hot carrier cooling mechanisms in halide perovskites," *Nature Communications*, vol. 8, no. 1, p. 1300, 2017.

[121] J. M. Richter, F. Branchi, F. Valduga de Almeida Camargo, B. Zhao, R. H. Friend, G. Cerullo, and F. Deschler, "Ultrafast carrier thermalization in lead iodide perovskite probed with two-dimensional electronic spectroscopy," *Nature Communications*, vol. 8, no. 1, p. 376, 2017.

[122] J.-X. Shen, X. Zhang, S. Das, E. Kioupakis, and C. G. Van de Walle, "Unexpectedly strong auger recombination in halide perovskites," *Advanced Energy Materials*, vol. 8, no. 30, p. 1801027, 2018.

[123] A. Richter, S. W. Glunz, F. Werner, J. Schmidt, and A. Cuevas, "Improved quantitative description of auger recombination in crystalline silicon," *Physical Review B*, vol. 86, no. 16, p. 165202, 2012.

[124] T. Kirchartz, L. Krückemeier, and E. L. Unger, "Research update: Recombination and open-circuit voltage in lead-halide perovskites," *APL Materials*, vol. 6, no. 10, p. 100702, 2018.

[125] F. Staub, H. Hempel, J. C. Hebig, J. Mock, U. W. Paetzold, U. Rau, T. Unold, and T. Kirchartz, "Beyond bulk lifetimes: Insights into lead halide perovskite films from time-resolved photoluminescence," *Physical Review Applied*, vol. 6, no. 4, p. 044017, 2016.

[126] T. Kirchartz, "High open-circuit voltages in lead-halide perovskite solar cells: experiment, theory and open questions," *Philosophical Transactions of the Royal Society A: Mathematical, Physical and Engineering Sciences*, vol. 377,

no. 2152, p. 20180286, 2019.

[127] X. Zhang, J.-X. Shen, W. Wang, and C. G. Van de Walle, "First-principles analysis of radiative recombination in lead-halide perovskites," *ACS Energy Letters*, vol. 3, no. 10, pp. 2329–2334, 2018.

[128] B. Das, I. Aguilera, U. Rau, and T. Kirchartz, "What is a deep defect? combining Shockley-Read-Hall statistics with multiphonon recombination theory," *Physical Review Materials*, vol. 4, no. 2, p. 024602, 2020.

[129] X. Zhang, M. E. Turiansky, J.-X. Shen, and C. G. Van de Walle, "Iodine interstitials as a cause of nonradiative recombination in hybrid perovskites," *Physical Review B*, vol. 101, no. 14, p. 140101, 2020.

[130] I. L. Braly, D. W. deQuilettes, L. M. Pazos-Outon, S. Burke, M. E. Ziffer, D. S. Ginger, and H. W. Hillhouse, "Hybrid perovskite films approaching the radiative limit with over 90% photoluminescence quantum efficiency," *Nature Photonics*, vol. 12, pp. 355–361, 2018.

[131] A. B. Sproul, "Dimensionless solution of the equation describing the effect of surface recombination on carrier decay in semiconductors," *Journal of Applied Physics*, vol. 76, no. 5, pp. 2851–2854, 1994.

[132] D. Kiermasch, L. Gil-Escrig, H. J. Bolink, and K. Tvingstedt, "Effects of masking on open-circuit voltage and fill factor in solar cells," *Joule*, vol. 3, no. 1, pp. 16–26, 2019.

[133] M. Saliba and L. Etgar, "Current density mismatch in perovskite solar cells," *ACS Energy Letters*, vol. 5, no. 9, pp. 2886–2888, 2020.

[134] G. El-Hajje, C. Momblona, L. Gil-Escrig, J. Ávila, T. Guillemot, J.-F. Guillemoles, M. Sessolo, H. J. Bolink, and L. Lombez, "Quantification of spatial inhomogeneity in perovskite solar cells by hyperspectral luminescence imaging," *Energy & Environmental Science*, vol. 9, no. 7, pp. 2286–2294, 2016.

[135] M. Stolterfoht, C. M. Wolff, J. A. Márquez, S. Zhang, C. J. Hages, D. Rothhardt, S. Albrecht, P. L. Burn, P. Meredith, T. Unold, and D. Neher, "Visualization and suppression of interfacial recombination for high-efficiency large-area pin perovskite solar cells," *Nature Energy*, vol. 10, no. 3, pp. 847–854, 2018.

[136] R. Ahrenkiel, "Measurement of minority-carrier lifetime by time-resolved photoluminescence," *Solid-State Electronics*, vol. 35, no. 3, pp. 239–250, 1992.

[137] M. Maiberg and R. Scheer, "Theoretical study of time-resolved luminescence in semiconductors. II. pulsed excitation," *Journal of Applied Physics*, vol. 116, no. 12, p. 123711, 2014.

[138] M. Maiberg, C. Spindler, E. Jarzembowski, and R. Scheer, "Electrical characterization of $Cu(In,Ga)Se_2$-solar cells by voltage dependent time-resolved photoluminescence," *Thin Solid Films*, vol. 582, pp. 379–382, 2015.

[139] C. Shuttle, B. O'Regan, A. Ballantyne, J. Nelson, D. D. Bradley, J. De Mello, and J. Durrant, "Experimental determination of the rate law for charge carrier decay in a polythiophene: Fullerene solar cell," *Applied Physics Letters*, vol. 92, no. 9, p. 80, 2008.

[140] Z. Liu, L. Krückemeier, B. Krogmeier, B. Klingebiel, J. A. Márquez, S. Levcenko, S. Öz, S. Mathur, U. Rau, T. Unold, and T. Kirchartz, "Open-circuit voltages exceeding 1.26 v in planar methylammonium lead iodide perovskite solar cells," *ACS Energy Letters*, vol. 4, no. 1, pp. 110–117, 2018.

[141] B. Hoex, S. Heil, E. Langereis, M. Van de Sanden, and W. Kessels, "Ultralow surface recombination of c-Si substrates passivated by plasma-assisted atomic layer deposited Al_2O_3," *Applied physics letters*, vol. 89, no. 4, p. 042112, 2006.

[142] M. Saliba, T. Matsui, K. Domanski, J.-Y. Seo, A. Ummadisingu, S. M. Zakeeruddin, J.-P. Correa-Baena, W. R. Tress, A. Abate, and A. Hagfeldt, "Incorporation of rubidium cations into perovskite solar cells improves photovoltaic performance," *Science*, vol. 354, no. 6309, pp. 206–209, 2016.

[143] M. Abdi-Jalebi, Z. Andaji-Garmaroudi, S. Cacovich, C. Stavrakas, B. Philippe, J. M. Richter, M. Alsari, E. P. Booker, E. M. Hutter, A. J. Pearson, S. Lilliu, T. J. Savenije, H. Rensmo, G. Divitini, C. Ducati, R. H. Friend, and S. D. Stranks, "Maximizing and stabilizing luminescence from halide perovskites with potassium passivation," *Nature*, vol. 555, no. 7697, p. 497, 2018.

[144] W. Albrecht, J. Moers, and B. Hermanns, "Hnf-helmholtz nano facility," *Journal of large-scale research facilities JLSRF*, vol. 3, p. 112, 2017.

[145] C.-H. Chiang, J.-W. Lin, and C.-G. Wu, "One-step fabrication of a mixed-

halide perovskite film for a high-efficiency inverted solar cell and module," *Journal of Materials Chemistry A*, vol. 4, no. 35, pp. 13525–13533, 2016.

[146] "TU Delft ASA software," *TU Delft, https://www.tudelft.nl/en/eemcs/the-faculty/departments/electrical-sustainable-energy/photovoltaic-materials-and-devices/software-platform/asa-software/.*

[147] M. Stolterfoht, P. Caprioglio, C. M. Wolff, J. A. Márquez, J. Nordmann, S. Zhang, D. Rothhart, U. Hörmann, A. Redinger, and L. Kegelmann, "The perovskite/transport layer interfaces dominate non-radiative recombination in efficient perovskite solar cells," *http://arxiv.org/abs/1810.01333*, 2018.

[148] V. Sarritzu, N. Sestu, D. Marongiu, X. Chang, S. Masi, A. Rizzo, S. Colella, F. Quochi, M. Saba, A. Mura, and G. Bongiovanni, "Optical determination of Shockley-Read-Hall and interface recombination currents in hybrid perovskites," *Scientific Reports*, vol. 7, p. 44629, 2017.

[149] M. Ban, Y. Zou, J. P. Rivett, Y. Yang, T. H. Thomas, Y. Tan, T. Song, X. Gao, D. Credington, and F. Deschler, "Solution-processed perovskite light emitting diodes with efficiency exceeding 15% through additive-controlled nanostructure tailoring," *Nature Communications*, vol. 9, no. 1, p. 3892, 2018.

[150] H. Cho, S.-H. Jeong, M.-H. Park, Y.-H. Kim, C. Wolf, C.-L. Lee, J. H. Heo, A. Sadhanala, N. Myoung, and S. Yoo, "Overcoming the electroluminescence efficiency limitations of perovskite light-emitting diodes," *Science*, vol. 350, no. 6265, pp. 1222–1225, 2015.

[151] Z. Xiao, R. A. Kerner, L. Zhao, N. L. Tran, K. M. Lee, T.-W. Koh, G. D. Scholes, and B. P. Rand, "Efficient perovskite light-emitting diodes featuring nanometre-sized crystallites," *Nature Photonics*, vol. 11, no. 2, p. 108, 2017.

[152] X. Yang, X. Zhang, J. Deng, Z. Chu, Q. Jiang, J. Meng, P. Wang, L. Zhang, Z. Yin, and J. You, "Efficient green light-emitting diodes based on quasi-two-dimensional composition and phase engineered perovskite with surface passivation," *Nature Communications*, vol. 9, no. 1, p. 570, 2018.

[153] W. Zou, R. Li, S. Zhang, Y. Liu, N. Wang, Y. Cao, Y. Miao, M. Xu, Q. Guo, and D. Di, "Minimising efficiency roll-off in high-brightness perovskite light-emitting diodes," *Nature Communications*, vol. 9, no. 1, p. 608, 2018.

[154] X.-K. Liu, W. Xu, S. Bai, Y. Jin, J. Wang, R. H. Friend, and F. Gao, "Metal halide perovskites for light-emitting diodes," *Nature Materials*, pp. 1–12, 2020.

[155] K. Lin, J. Xing, L. N. Quan, F. P. G. de Arquer, X. Gong, J. Lu, L. Xie, W. Zhao, D. Zhang, C. Yan, *et al.*, "Perovskite light-emitting diodes with external quantum efficiency exceeding 20 per cent," *Nature*, vol. 562, no. 7726, pp. 245–248, 2018.

[156] T. Fang, T. Wang, X. Li, Y. Dong, S. Bai, and J. Song, "Perovskite QLED with an external quantum efficiency of over 21% by modulating electronic transport," *Science Bulletin*, vol. 66, no. 1, pp. 36–43, 2021.

[157] B. Krogmeier, F. Staub, D. Grabowski, U. Rau, and T. Kirchartz, "Quantitative analysis of the transient photoluminescence of $CH_3NH_3PbI_3/PC_{61}BM$ heterojunctions by numerical simulations," *Sustainable Energy & Fuels*, vol. 2, no. 5, pp. 1027–1034, 2018.

[158] E. M. Hutter, J. Hofman, M. L. Petrus, M. Moes, R. D. Abellón, P. Docampo, and T. J. Savenije, "Charge transfer from methylammonium lead iodide perovskite to organic transport materials: Efficiencies, transfer rates, and interfacial recombination," *Advanced Energy Materials*, vol. 7, no. 13, p. 1602349, 2017.

[159] D. W. deQuilettes, W. Zhang, V. M. Burlakov, D. J. Graham, T. Leijtens, A. Osherov, V. Bulovic, H. J. Snaith, D. S. Ginger, and S. D. Stranks, "Photo-induced halide redistribution in organic-inorganic perovskite films," *Nature Communications*, vol. 7, p. 11683, 2016.

[160] D. Luo, W. Yang, Z. Wang, A. Sadhanala, Q. Hu, R. Su, R. Shivanna, G. F. Trindade, J. F. Watts, Z. Xu, T. Liu, K. Chen, F. Ye, P. Wu, L. Zhao, J. Wu, Y. Tu, Y. Zhang, X. Yang, W. Zhang, R. H. Friend, Q. Gong, H. J. Snaith, and R. Zhu, "Enhanced photovoltage for inverted planar heterojunction perovskite solar cells," *Science*, vol. 360, no. 6396, pp. 1442–1446, 2018.

[161] H. Tsai, R. Asadpour, J. C. Blancon, C. C. Stoumpos, O. Durand, J. W. Strzalka, B. Chen, R. Verduzco, P. M. Ajayan, S. Tretiak, J. Even, M. A. Alam, M. G. Kanatzidis, W. Nie, and A. D. Mohite, "Light-induced lattice expansion leads to high-efficiency perovskite solar cells," *Science*, vol. 360,

no. 6384, p. 67, 2018.

[162] M. De Bastiani, G. Dell'Erba, M. Gandini, V. D'Innocenzo, S. Neutzner, A. R. S. Kandada, G. Grancini, M. Binda, M. Prato, and J. M. Ball, "Ion migration and the role of preconditioning cycles in the stabilization of the J-V characteristics of inverted hybrid perovskite solar cells," *Advanced Energy Materials*, vol. 6, no. 2, p. 1501453, 2016.

[163] W. Zhang, M. Saliba, D. T. Moore, S. K. Pathak, M. T. Hörantner, T. Stergiopoulos, S. D. Stranks, G. E. Eperon, J. A. Alexander-Webber, and A. Abate, "Ultrasmooth organic-inorganic perovskite thin-film formation and crystallization for efficient planar heterojunction solar cells," *Nature Communications*, vol. 6, p. 6142, 2015.

[164] W. Qiu, T. Merckx, M. Jaysankar, C. M. de la Huerta, L. Rakocevic, W. Zhang, U. Paetzold, R. Gehlhaar, L. Froyen, and J. Poortmans, "Pinhole-free perovskite films for efficient solar modules," *Energy & Environmental Science*, vol. 9, no. 2, pp. 484–489, 2016.

[165] E. M. Hutter, G. E. Eperon, S. D. Stranks, and T. J. Savenije, "Charge carriers in planar and meso-structured organic-inorganic perovskites: Mobilities, lifetimes, and concentrations of trap states," *The Journal of Physical Chemistry Letters*, vol. 6, no. 15, pp. 3082–3090, 2015.

[166] S. D. Stranks, G. E. Eperon, G. Grancini, C. Menelaou, M. J. Alcocer, T. Leijtens, L. M. Herz, A. Petrozza, and H. J. Snaith, "Electron-hole diffusion lengths exceeding 1 micrometer in an organometal trihalide perovskite absorber," *Science*, vol. 342, no. 6156, pp. 341–344, 2013.

[167] Y. Zhao and K. Zhu, "CH_3NH_3Cl-assisted one-step solution growth of $CH_3NH_3PbI_3$: Structure, charge-carrier dynamics, and photovoltaic properties of perovskite solar cells," *The Journal of Physical Chemistry C*, vol. 118, no. 18, pp. 9412–9418, 2014.

[168] Y. Shao, Y. Yuan, and J. Huang, "Correlation of energy disorder and open-circuit voltage in hybrid perovskite solar cells," *Nature Energy*, vol. 1, p. 15001, 2016.

[169] M. G. Abebe, A. Abass, G. Gomard, L. Zschiedrich, U. Lemmer, B. S. Ri-

chards, C. Rockstuhl, and U. W. Paetzold, "Rigorous wave-optical treatment of photon recycling in thermodynamics of photovoltaics: Perovskite thin-film solar cells," *Physical Review B*, vol. 98, no. 7, p. 075141, 2018.

[170] L. M. Pazos-Outón, T. P. Xiao, and E. Yablonovitch, "Fundamental efficiency limit of lead iodide perovskite solar cells," *The Journal of Physical Chemistry Letters*, vol. 9, no. 7, pp. 1703–1711, 2018.

[171] O. D. Miller, E. Yablonovitch, and S. R. Kurtz, "Strong internal and external luminescence as solar cells approach the Shockley – Queisser limit," *IEEE Journal of Photovoltaics*, vol. 2, no. 3, pp. 303–311, 2012.

[172] R. Krimmel, "Master thesis: Process and interlayer optimization of co-evaporated $CH_3NH_3PbI_3$ solar cells," *Hochschule Düsseldorf, Fachbereich Elektrotechnik*, 2018.

[173] S. Krause, "Master thesis: Herstellung und Charakterisierung koverdampfter Blei-Halogenid-Perowskit-Solarzellen," *Hochschule Düsseldorf, Fachbereich Elektrotechnik*, 2019.

[174] J. Feider, "Bachelor thesis: Herstellung und Simulation von Perowskit-Solarzellen," *Hochschule Düsseldorf, Fachbereich Elektrotechnik*, 2020.

[175] L. Gil-Escrig, M. Roß, J. Sutter, A. Al-Ashouri, C. Becker, and S. Albrecht, "Fully vacuum-processed perovskite solar cells on pyramidal microtextures," *Solar RRL*, vol. 5, no. 1, p. 2000553, 2021.

[176] L. Cojocaru, K. Wienands, T. W. Kim, S. Uchida, A. J. Bett, S. Rafizadeh, J. C. Goldschmidt, and S. W. Glunz, "Detailed investigation of evaporated perovskite absorbers with high crystal quality on different substrates," *ACS Applied Materials & Interfaces*, vol. 10, no. 31, pp. 26293–26302, 2018.

[177] M. Liu, M. B. Johnston, and H. J. Snaith, "Efficient planar heterojunction perovskite solar cells by vapour deposition," *Nature*, vol. 501, no. 7467, pp. 395–398, 2013.

[178] J. Borchert, R. L. Milot, J. B. Patel, C. L. Davies, A. D. Wright, L. MartiÌnez Maestro, H. J. Snaith, L. M. Herz, and M. B. Johnston, "Large-area, highly uniform evaporated formamidinium lead triiodide thin films for solar cells," *ACS Energy Letters*, vol. 2, no. 12, pp. 2799–2804, 2017.

[179] T. Abzieher, J. A. Schwenzer, S. Moghadamzadeh, F. Sutterlüti, I. M. Hossain, M. Pfau, E. Lotter, M. Hetterich, B. S. Richards, U. Lemmer, *et al.*, "Efficient all-evaporated pin-perovskite solar cells: A promising approach toward industrial large-scale fabrication," *IEEE Journal of Photovoltaics*, vol. 9, no. 5, pp. 1249–1257, 2019.

[180] G. Longo, C. Momblona, M.-G. La-Placa, L. Gil-Escrig, M. Sessolo, and H. J. Bolink, "Fully vacuum-processed wide band gap mixed-halide perovskite solar cells," *ACS Energy Letters*, vol. 3, no. 1, pp. 214–219, 2018.

[181] J. Ávila, C. Momblona, P. P. Boix, M. Sessolo, and H. J. Bolink, "Vapor-deposited perovskites: the route to high-performance solar cell production?," *Joule*, vol. 1, no. 3, pp. 431–442, 2017.

[182] L. Gil-Escrig, C. Momblona, D. Forgács, S. Pla, F. Fernández-Lázaro, M. Sessolo, Á. Sastre-Santos, and H. J. Bolink, "Interface engineering in efficient vacuum deposited perovskite solar cells," *Organic Electronics*, vol. 37, pp. 396–401, 2016.

[183] O. Malinkiewicz, C. Roldán-Carmona, A. Soriano, E. Bandiello, L. Camacho, M. K. Nazeeruddin, and H. J. Bolink, "Metal-oxide-free methylammonium lead iodide perovskite-based solar cells: the influence of organic charge transport layers," *Advanced Energy Materials*, vol. 4, no. 15, p. 1400345, 2014.

[184] O. Malinkiewicz, A. Yella, Y. H. Lee, G. M. Espallargas, M. Graetzel, M. K. Nazeeruddin, and H. J. Bolink, "Perovskite solar cells employing organic charge-transport layers," *Nature Photonics*, vol. 8, no. 2, pp. 128–132, 2014.

[185] C. Momblona, L. Gil-Escrig, E. Bandiello, E. M. Hutter, M. Sessolo, K. Lederer, J. Blochwitz-Nimoth, and H. J. Bolink, "Efficient vacuum deposited pin and nip perovskite solar cells employing doped charge transport layers," *Energy & Environmental Science*, vol. 9, no. 11, pp. 3456–3463, 2016.

[186] H.-H. Wang, Q. Chen, H. Zhou, L. Song, Z. St Louis, N. De Marco, Y. Fang, P. Sun, T.-B. Song, and H. Chen, "Improving the TiO_2 electron transport layer in perovskite solar cells using acetylacetonate-based additives," *Journal of Materials Chemistry A*, vol. 3, no. 17, pp. 9108–9115, 2015.

[187] M. Roß, L. Gil-Escrig, A. Al-Ashouri, P. Tockhorn, M. Jošt, B. Rech, and

S. Albrecht, "Co-evaporated pin perovskite solar cells beyond 20% efficiency: Impact of substrate temperature and hole-transport layer," *ACS Applied Materials & Interfaces*, vol. 12, no. 35, pp. 39261–39272, 2020.

[188] L. A. Frolova, D. V. Anokhin, A. A. Piryazev, S. Y. Luchkin, N. N. Dremova, K. J. Stevenson, and P. A. Troshin, "Highly efficient all-inorganic planar heterojunction perovskite solar cells produced by thermal coevaporation of CsI and PbI_2," *The Journal of Physical Chemistry Letters*, vol. 8, no. 1, pp. 67–72, 2017.

[189] W. Chen, J. Zhang, G. Xu, R. Xue, Y. Li, Y. Zhou, J. Hou, and Y. Li, "A semitransparent inorganic perovskite film for overcoming ultraviolet light instability of organic solar cells and achieving 14.03% efficiency," *Advanced Materials*, vol. 30, no. 21, p. 1800855, 2018.

[190] Y. Hu, Q. Wang, Y.-L. Shi, M. Li, L. Zhang, Z.-K. Wang, and L.-S. Liao, "Vacuum-evaporated all-inorganic cesium lead bromine perovskites for high-performance light-emitting diodes," *Journal of Materials Chemistry C*, vol. 5, no. 32, pp. 8144–8149, 2017.

[191] L. Gil-Escrig, C. Momblona, M.-G. La-Placa, P. P. Boix, M. Sessolo, and H. J. Bolink, "Vacuum deposited triple-cation mixed-halide perovskite solar cells," *Advanced Energy Materials*, vol. 8, no. 14, p. 1703506, 2018.

[192] H. A. Dewi, J. Li, H. Wang, B. Chaudhary, N. Mathews, S. Mhaisalkar, and A. Bruno, "Excellent intrinsic long-term thermal stability of co-evaporated $MAPbI_3$ solar cells at 85°C," *Advanced Functional Materials*, vol. 31, no. 22, p. 2100557, 2021.

[193] S. Wang, L. K. Ono, M. R. Leyden, Y. Kato, S. R. Raga, M. V. Lee, and Y. Qi, "Smooth perovskite thin films and efficient perovskite solar cells prepared by the hybrid deposition method," *Journal of Materials Chemistry A*, vol. 3, no. 28, pp. 14631–14641, 2015.

[194] O. Malinkiewicz, "PhD thesis: Low cost, efficient, hybrid solar cells," *University of Valencia*, 2017.

[195] D. Pérez-del Rey, P. P. Boix, M. Sessolo, A. Hadipour, and H. J. Bolink, "Interfacial modification for high-efficiency vapor-phase-deposited perovskite solar

cells based on a metal oxide buffer layer," *The Journal of Physical Chemistry Letters*, vol. 9, no. 5, pp. 1041–1046, 2018.

[196] M. Stolterfoht, P. Caprioglio, C. M. Wolff, J. A. Márquez, J. Nordmann, S. Zhang, D. Rothhardt, U. Hörmann, Y. Amir, A. Redinger, L. Kegelmann, F. Zu, S. Albrecht, N. Koch, T. Kirchartz, M. Saliba, T. Unold, and D. Neher, "The impact of energy alignment and interfacial recombination on the internal and external open-circuit voltage of perovskite solar cells," *Energy & Environmental Science*, vol. 12, no. 9, pp. 2778–2788, 2019.

[197] A. Al-Ashouri, A. Magomedov, M. Roß, M. Jošt, M. Talaikis, G. Chistiakova, T. Bertram, J. A. Márquez, E. Köhnen, E. Kasparavičius, *et al.*, "Conformal monolayer contacts with lossless interfaces for perovskite single junction and monolithic tandem solar cells," *Energy & Environmental Science*, vol. 12, no. 11, pp. 3356–3369, 2019.

[198] F. Staub, "PhD thesis: Time-resolved photoluminescence on perovskite absorber materials for photovoltaic applications," vol. 513, 2020.

[199] S. Gharibzadeh, B. Abdollahi Nejand, M. Jakoby, T. Abzieher, D. Hauschild, S. Moghadamzadeh, J. A. Schwenzer, P. Brenner, R. Schmager, A. A. Haghighirad, L. Weinhardt, U. Lemmer, B. S. Richards, I. A. Howard, and U. W. Paetzold, "Record open-circuit voltage wide-bandgap perovskite solar cells utilizing 2D/3D perovskite heterostructure," *Advanced Energy Materials*, p. 1803699, 2019.

[200] Q. Jiang, Y. Zhao, X. Zhang, X. Yang, Y. Chen, Z. Chu, Q. Ye, X. Li, Z. Yin, and J. You, "Surface passivation of perovskite film for efficient solar cells," *Nature Photonics*, vol. 13, no. 7, pp. 460–466, 2019.

[201] E. H. Jung, N. J. Jeon, E. Y. Park, C. S. Moon, T. J. Shin, T.-Y. Yang, J. H. Noh, and J. Seo, "Efficient, stable and scalable perovskite solar cells using poly (3-hexylthiophene)," *Nature*, vol. 567, no. 7749, p. 511, 2019.

[202] S.-H. Turren-Cruz, A. Hagfeldt, and M. Saliba, "Methylammonium-free, high-performance, and stable perovskite solar cells on a planar architecture," *Science*, vol. 362, no. 6413, pp. 449–453, 2018.

[203] S. Yang, J. Dai, Z. Yu, Y. Shao, Y. Zhou, X. Xiao, X. C. Zeng, and J. Huang,

"Tailoring passivation molecular structures for extremely small open circuit voltage loss in perovskite solar cells," *Journal of the American Chemical Society*, vol. 141, no. 14, pp. 5781–5787, 2019.

[204] J. Tauc, *Optical Properties of Amorphous Semiconductors*, pp. 159–220. Springer, 1974.

[205] J. Tauc, "Optical properties and electronic structure of amorphous Ge and Si," *Materials Research Bulletin*, vol. 3, no. 1, pp. 37–46, 1968.

[206] B. K. Ridley, *Quantum Processes in Semiconductors*. Oxford University Press, 2013.

[207] X. Chen, H. Lu, Y. Yang, and M. C. Beard, "Excitonic effects in methylammonium lead halide perovskites," *The Journal of Physical Chemistry Letters*, vol. 9, no. 10, pp. 2595–2603, 2018.

[208] T. Kirchartz and U. Rau, "Decreasing radiative recombination coefficients via an indirect band gap in lead halide perovskites," *The Journal of Physical Chemistry Letters*, vol. 8, no. 6, pp. 1265–1271, 2017.

[209] T. Wang, B. Daiber, J. M. Frost, S. A. Mann, E. C. Garnett, A. Walsh, and B. Ehrler, "Indirect to direct bandgap transition in methylammonium lead halide perovskite," *Energy & Environmental Science*, vol. 10, no. 2, pp. 509–515, 2017.

[210] M. Ledinsky, T. Schönfeldová, J. Holovsky, E. Aydin, Z. Hájková, L. Landová, N. Neyková, A. Fejfar, and S. De Wolf, "Temperature dependence of the urbach energy in lead iodide perovskites," *The Journal of Physical Chemistry Letters*, vol. 10, no. 6, pp. 1368–1373, 2019.

[211] F. Urbach, "The long-wavelength edge of photographic sensitivity and of the electronic absorption of solids," *Physical Review*, vol. 92, no. 5, pp. 1324–1324, 1953.

[212] S. John, C. Soukoulis, M. H. Cohen, and E. Economou, "Theory of electron band tails and the urbach optical-absorption edge," *Physical Review Letters*, vol. 57, no. 14, p. 1777, 1986.

[213] J. J. Yoo, S. Wieghold, M. Sponseller, M. Chua, S. N. Bertram, N. T. P. Hartono, J. Tresback, E. Hansen, J.-P. Correa-Baena, and V. Bulovic, "An

interface stabilized perovskite solar cell with high stabilized efficiency and low voltage loss," *Energy & Environmental Science*, vol. 12, no. 7, pp. 2192–2199, 2019.

[214] P. K. Nayak, S. Mahesh, H. J. Snaith, and D. Cahen, "Photovoltaic solar cell technologies: analysing the state of the art," *Nature Reviews Materials*, vol. 4, no. 4, pp. 269–285, 2019.

[215] J. Burschka, N. Pellet, S.-J. Moon, R. Humphry-Baker, P. Gao, M. K. Nazeeruddin, and M. Grätzel, "Sequential deposition as a route to high-performance perovskite-sensitized solar cells," *Nature*, vol. 499, no. 7458, p. 316, 2013.

[216] N. J. Jeon, J. H. Noh, W. S. Yang, Y. C. Kim, S. Ryu, J. Seo, and S. I. Seok, "Compositional engineering of perovskite materials for high-performance solar cells," *Nature*, vol. 517, no. 7535, p. 476, 2015.

[217] N. J. Jeon, H. Na, E. H. Jung, T.-Y. Yang, Y. G. Lee, G. Kim, H.-W. Shin, S. I. Seok, J. Lee, and J. Seo, "A fluorene-terminated hole-transporting material for highly efficient and stable perovskite solar cells," *Nature Energy*, vol. 3, no. 8, p. 682, 2018.

[218] W. S. Yang, B.-W. Park, E. H. Jung, N. J. Jeon, Y. C. Kim, D. U. Lee, S. S. Shin, J. Seo, E. K. Kim, and J. H. Noh, "Iodide management in formamidinium-lead-halide-based perovskite layers for efficient solar cells," *Science*, vol. 356, no. 6345, pp. 1376–1379, 2017.

[219] M. A. Green, E. D. Dunlop, D. H. Levi, J. Hohl-Ebinger, M. Yoshita, and A. W. Ho-Baillie, "Solar cell efficiency tables (version 54)," *Progress in Photovoltaics: Research and Applications*, vol. 27, no. 7, pp. 565–575, 2019.

[220] J. Tong, Z. Song, D. H. Kim, X. Chen, C. Chen, A. F. Palmstrom, P. F. Ndione, M. O. Reese, S. P. Dunfield, and O. G. Reid, "Carrier lifetimes of > 1 s in Sn-Pb perovskites enable efficient all-perovskite tandem solar cells," *Science*, vol. 364, no. 6439, pp. 475–479, 2019.

[221] G. E. Eperon, M. T. Hörantner, and H. J. Snaith, "Metal halide perovskite tandem and multiple-junction photovoltaics," *Nature Reviews Chemistry*, vol. 1, no. 12, p. 0095, 2017.

[222] T. Kirchartz, S. Korgitzsch, J. Hüpkes, C. O. R. Quiroz, and C. J. Brabec,

"Performance evaluation of semitransparent perovskite solar cells for application in four-terminal tandem cells," *ACS Energy Letters*, vol. 3, no. 8, pp. 1861–1867, 2018.

[223] N. Mundhaas, Z. J. Yu, K. A. Bush, H. Wang, J. Häusele, S. Kavadiya, M. D. McGehee, and Z. C. Holman, "Series resistance measurements of perovskite solar cells using $j_{sc} - v_{oc}$ measurements," *Solar RRL*, vol. 3, no. 4, p. 1800378, 2019.

[224] K. P. Goetz, A. D. Taylor, F. Paulus, and Y. Vaynzof, "Shining light on the photoluminescence properties of metal halide perovskites," *Advanced Functional Materials*, vol. 30, no. 23, p. 1910004, 2020.

[225] T. Kirchartz, J. A. Márquez, M. Stolterfoht, and T. Unold, "Photoluminescence-based characterization of halide perovskites for photovoltaics," *Advanced Energy Materials*, vol. 10, no. 26, p. 1904134, 2020.

[226] S. D. Stranks, V. M. Burlakov, T. Leijtens, J. M. Ball, A. Goriely, and H. J. Snaith, "Recombination kinetics in organic-inorganic perovskites: Excitons, free charge, and subgap states," *Physical Review Applied*, vol. 2, no. 3, p. 034007, 2014.

[227] S. Draguta, J. A. Christians, Y. V. Morozov, A. Mucunzi, J. S. Manser, P. V. Kamat, J. M. Luther, and M. Kuno, "A quantitative and spatially resolved analysis of the performance-bottleneck in high efficiency, planar hybrid perovskite solar cells," *Energy & Environmental Science*, vol. 11, no. 4, pp. 960–969, 2018.

[228] W. E. I. Sha, H. Zhang, Z. S. Wang, H. L. Zhu, X. Ren, F. Lin, A. K.-Y. Jen, and W. C. H. Choy, "Quantifying efficiency loss of perovskite solar cells by a modified detailed balance model," *Advanced Energy Materials*, vol. 8, no. 8, p. 1701586, 2018.

[229] D. Luo, R. Su, W. Zhang, Q. Gong, and R. Zhu, "Minimizing non-radiative recombination losses in perovskite solar cells," *Nature Reviews Materials*, vol. 5, no. 1, pp. 44–60, 2020.

[230] G.-J. A. H. Wetzelaer, M. Scheepers, A. M. Sempere, C. Momblona, J. Ãvila, and H. J. Bolink, "Trap-assisted non-radiative recombination in organic-

inorganic perovskite solar cells," *Advanced Materials*, vol. 27, no. 11, pp. 1837–1841, 2015.

[231] J. M. Richter, M. Abdi-Jalebi, A. Sadhanala, M. Tabachnyk, J. P. Rivett, L. M. Pazos-Outon, K. C. Gödel, M. Price, F. Deschler, and R. H. Friend, "Enhancing photoluminescence yields in lead halide perovskites by photon recycling and light out-coupling," *Nature Communications*, vol. 7, p. 13941, 2016.

[232] J. Chen and N.-G. Park, "Causes and solutions of recombination in perovskite solar cells," *Advanced Materials*, vol. 31, no. 47, p. 1803019, 2019.

[233] J. Haddad, B. Krogmeier, B. Klingebiel, L. Krückemeier, S. Melhem, Z. Liu, J. Hüpkes, S. Mathur, and T. Kirchartz, "Analyzing interface recombination in lead-halide perovskite solar cells with organic and inorganic hole-transport layers," *Advanced Materials Interfaces*, vol. 7, no. 16, p. 2000366, 2020.

[234] P. Schulz, D. Cahen, and A. Kahn, "Halide perovskites: Is it all about the interfaces?," *Chemical Reviews*, vol. 119, no. 5, pp. 3349–3417, 2019.

[235] M. Stolterfoht, M. Grischek, P. Caprioglio, C. M. Wolff, E. Gutierrez-Partida, F. Peña-Camargo, D. Rothhardt, S. Zhang, M. Raoufi, J. Wolansky, M. Abdi-Jalebi, S. D. Stranks, S. Albrecht, T. Kirchartz, and D. Neher, "How to quantify the efficiency potential of neat perovskite films: Perovskite semiconductors with an implied efficiency exceeding 28%," *Advanced Materials*, vol. 32, no. 17, p. 2000080, 2020.

[236] C. M. Wolff, P. Caprioglio, M. Stolterfoht, and D. Neher, "Nonradiative recombination in perovskite solar cells: The role of interfaces," *Advanced Materials*, vol. 31, no. 52, p. 1902762, 2019.

[237] E. M. Hutter, T. Kirchartz, B. Ehrler, D. Cahen, and E. v. Hauff, "Pitfalls and prospects of optical spectroscopy to characterize perovskite-transport layer interfaces," *Applied Physics Letters*, vol. 116, no. 10, p. 100501, 2020.

[238] R. Ahrenkiel, "Influence of junctions on photoluminescence decay in thin-film devices," *Journal of Applied Physics*, vol. 62, no. 7, pp. 2937–2941, 1987.

[239] D. Kuciauskas, J. V. Li, A. Kanevce, H. Guthrey, M. Contreras, J. Pankow, P. Dippo, and K. Ramanathan, "Charge-carrier dynamics in polycrystalline

thin-film $CuIn_{1-x}GaxSe_2$ photovoltaic devices after pulsed laser excitation: Interface and space-charge region analysis," *Journal of Applied Physics*, vol. 117, no. 18, p. 185102, 2015.

[240] W. Metzger, D. Albin, D. Levi, P. Sheldon, X. Li, B. Keyes, and R. Ahrenkiel, "Time-resolved photoluminescence studies of CdTe solar cells," *Journal of Applied Physics*, vol. 94, no. 5, pp. 3549–3555, 2003.

[241] F. Steiner, S. Foster, A. Losquin, J. Labram, T. D. Anthopoulos, J. M. Frost, and J. Nelson, "Distinguishing the influence of structural and energetic disorder on electron transport in fullerene multi-adducts," *Materials Horizons*, vol. 2, no. 1, pp. 113–119, 2015.

[242] L. Castaner, E. Vilamajo, J. Llaberia, and J. Garrido, "Investigations of the ocvd transients in solar cells," *Journal of Physics D: Applied Physics*, vol. 14, no. 10, p. 1867, 1981.

[243] D. Kiermasch, A. Baumann, M. Fischer, V. Dyakonov, and K. Tvingstedt, "Revisiting lifetimes from transient electrical characterization of thin film solar cells; a capacitive concern evaluated for silicon, organic and perovskite devices," *Energy & Environmental Science*, vol. 11, no. 3, pp. 629–640, 2018.

[244] O. J. Sandberg, K. Tvingstedt, P. Meredith, and A. Armin, "Theoretical perspective on transient photovoltage and charge extraction techniques," *The Journal of Physical Chemistry C*, vol. 123, no. 23, pp. 14261–14271, 2019.

[245] Z. S. Wang, F. Ebadi, B. Carlsen, W. C. H. Choy, and W. Tress, "Transient photovoltage measurements on perovskite solar cells with varied defect concentrations and inhomogeneous recombination rates," *Small Methods*, vol. 4, no. 9, p. 2000290, 2020.

[246] M. J. Trimpl, A. D. Wright, K. Schutt, L. R. V. Buizza, Z. Wang, M. B. Johnston, H. J. Snaith, P. Müller-Buschbaum, and L. M. Herz, "Charge-carrier trapping and radiative recombination in metal halide perovskite semiconductors," *Advanced Functional Materials*, vol. 30, no. 42, p. 2004312, 2020.

[247] S. Wheeler, D. Bryant, J. Troughton, T. Kirchartz, T. Watson, J. Nelson, and J. R. Durrant, "Transient optoelectronic analysis of the impact of material energetics and recombination kinetics on the open-circuit voltage of hybrid

perovskite solar cells," *The Journal of Physical Chemistry C*, vol. 121, no. 25, pp. 13496–13506, 2017.

[248] I. Levine, A. Al-Ashouri, A. Musiienko, H. Hempel, A. Magomedov, A. Drevilkauskaite, V. Getautis, D. Menzel, K. Hinrichs, T. Unold, *et al.*, "Charge transfer rates and electron trapping at buried interfaces of perovskite solar cells," *Joule*, vol. 5, no. 11, pp. 2915–2933, 2021.

[249] E. M. Hutter, R. J. Sutton, S. Chandrashekar, M. Abdi-Jalebi, S. D. Stranks, H. J. Snaith, and T. J. Savenije, "Vapour-deposited cesium lead iodide perovskites: microsecond charge carrier lifetimes and enhanced photovoltaic performance," *ACS Energy Letters*, vol. 2, no. 8, pp. 1901–1908, 2017.

[250] Y. Yamada, T. Nakamura, M. Endo, A. Wakamiya, and Y. Kanemitsu, "Photocarrier recombination dynamics in perovskite $CH_3NH_3PbI_3$ for solar cell applications," *Journal of the American Chemical Society*, vol. 136, no. 33, pp. 11610–11613, 2014.

[251] J. Bisquert and M. Janssen, "From frequency domain to time transient methods for halide perovskite solar cells: The connections of IMPS, IMVS, TPC, and TPV," *The Journal of Physical Chemistry Letters*, vol. 12, no. 33, pp. 7964–7971, 2021.

[252] S. Ravishankar, A. Riquelme, S. K. Sarkar, M. Garcia-Batlle, G. Garcia-Belmonte, and J. Bisquert, "Intensity-modulated photocurrent spectroscopy and its application to perovskite solar cells," *The Journal of Physical Chemistry C*, vol. 123, no. 41, pp. 24995–25014, 2019.

[253] A. O. Alvarez, S. Ravishankar, and F. Fabregat-Santiago, "Combining modulated techniques for the analysis of photosensitive devices," *Small Methods*, vol. 5, no. 10, p. 2100661, 2021.

[254] Q. Chen, H. Zhou, Y. Fang, A. Z. Stieg, T.-B. Song, H.-H. Wang, X. Xu, Y. Liu, S. Lu, and J. You, "The optoelectronic role of chlorine in $CH_3NH_3PbI_3$(Cl)-based perovskite solar cells," *Nature Communications*, vol. 6, p. 7269, 2015.

[255] B. Chen, S.-W. Baek, Y. Hou, E. Aydin, M. De Bastiani, B. Scheffel, A. Proppe, Z. Huang, M. Wei, and Y.-K. Wang, "Enhanced optical path and electron diffusion length enable high-efficiency perovskite tandems," *Nature Commu-*

nications, vol. 11, no. 1, pp. 1–9, 2020.

[256] Y. Li, Y. Zhao, Q. Chen, Y. Yang, Y. Liu, Z. Hong, Z. Liu, Y.-T. Hsieh, L. Meng, and Y. Li, "Multifunctional fullerene derivative for interface engineering in perovskite solar cells," *Journal of the American Chemical Society*, vol. 137, no. 49, pp. 15540–15547, 2015.

[257] H. Tan, A. Jain, O. Voznyy, X. Lan, F. P. G. de Arquer, J. Z. Fan, R. Quintero-Bermudez, M. Yuan, B. Zhang, and Y. Zhao, "Efficient and stable solution-processed planar perovskite solar cells via contact passivation," *Science*, vol. 355, no. 6326, pp. 722–726, 2017.

[258] R. Wang, J. Xue, L. Meng, J.-W. Lee, Z. Zhao, P. Sun, L. Cai, T. Huang, Z. Wang, and Z.-K. Wang, "Caffeine improves the performance and thermal stability of perovskite solar cells," *Joule*, vol. 3, no. 6, pp. 1464–1477, 2019.

[259] R. Wang, J. Xue, K.-L. Wang, Z.-K. Wang, Y. Luo, D. Fenning, G. Xu, S. Nuryyeva, T. Huang, Y. Zhao, J. L. Yang, J. Zhu, M. Wang, S. Tan, I. Yavuz, K. N. Houk, and Y. Yang, "Constructive molecular configurations for surface-defect passivation of perovskite photovoltaics," *Science*, vol. 366, no. 6472, pp. 1509–1513, 2019.

[260] S. Yang, S. Chen, E. Mosconi, Y. Fang, X. Xiao, C. Wang, Y. Zhou, Z. Yu, J. Zhao, and Y. Gao, "Stabilizing halide perovskite surfaces for solar cell operation with wide-bandgap lead oxysalts," *Science*, vol. 365, no. 6452, pp. 473–478, 2019.

[261] X. Zheng, B. Chen, J. Dai, Y. Fang, Y. Bai, Y. Lin, H. Wei, X. C. Zeng, and J. Huang, "Defect passivation in hybrid perovskite solar cells using quaternary ammonium halide anions and cations," *Nature Energy*, vol. 2, no. 7, pp. 1–9, 2017.

[262] H. Zhou, Q. Chen, G. Li, S. Luo, T.-b. Song, H.-S. Duan, Z. Hong, J. You, Y. Liu, and Y. Yang, "Interface engineering of highly efficient perovskite solar cells," *Science*, vol. 345, no. 6196, pp. 542–546, 2014.

[263] H. Back, G. Kim, H. Kim, C.-Y. Nam, J. Kim, Y. R. Kim, T. Kim, B. Park, J. R. Durrant, and K. Lee, "Highly stable inverted methylammonium lead triiodide perovskite solar cells achieved by surface re-crystallization," *Energy &*

Environmental Science, vol. 13, no. 3, pp. 840–847, 2020.

[264] T. Du, J. Kim, J. Ngiam, S. Xu, P. R. F. Barnes, J. R. Durrant, and M. A. McLachlan, "Elucidating the origins of subgap tail states and open-circuit voltage in methylammonium lead triiodide perovskite solar cells," *Advanced Functional Materials*, vol. 28, no. 32, p. 1801808, 2018.

[265] T. Du, W. Xu, S. Xu, S. R. Ratnasingham, C.-T. Lin, J. Kim, J. Briscoe, M. A. McLachlan, and J. R. Durrant, "Light-intensity and thickness dependent efficiency of planar perovskite solar cells: charge recombination versus extraction," *Journal of Materials Chemistry C*, vol. 8, no. 36, pp. 12648–12655, 2020.

[266] J. Tian, J. Wang, Q. Xue, T. Niu, L. Yan, Z. Zhu, N. Li, C. J. Brabec, H. Yip, and Y. Cao, "Composition engineering of all-inorganic perovskite film for efficient and operationally stable solar cells," *Advanced Functional Materials*, p. 2001764, 2020.

[267] F. Tan, H. Tan, M. I. Saidaminov, M. Wei, M. Liu, A. Mei, P. Li, B. Zhang, C.-S. Tan, X. Gong, Y. Zhao, A. R. Kirmani, Z. Huang, J. Z. Fan, R. Quintero-Bermudez, J. Kim, Y. Zhao, O. Voznyy, Y. Gao, F. Zhang, L. J. Richter, Z.-H. Lu, W. Zhang, and E. H. Sargent, "In situ back-contact passivation improves photovoltage and fill factor in perovskite solar cells," *Advanced Materials*, vol. 31, no. 14, p. 1807435, 2019.

[268] J. Wang, J. Zhang, Y. Zhou, H. Liu, Q. Xue, X. Li, C.-C. Chueh, H.-L. Yip, Z. Zhu, and A. K. Jen, "Highly efficient all-inorganic perovskite solar cells with suppressed non-radiative recombination by a lewis base," *Nature Communications*, vol. 11, 2020.

[269] K. Xiao, R. Lin, Q. Han, Y. Hou, Z. Qin, H. T. Nguyen, J. Wen, M. Wei, V. Yeddu, M. I. Saidaminov, Y. Gao, X. Luo, Y. Wang, H. Gao, C. Zhang, J. Xu, J. Zhu, E. H. Sargent, and H. Tan, "All-perovskite tandem solar cells with 24.2% certified efficiency and area over 1cm^2 using surface-anchoring zwitterionic antioxidant," *Nature Energy*, 2020.

[270] Q. Yao, Q. Xue, Z. Li, K. Zhang, T. Zhang, N. Li, S. Yang, C. J. Brabec, H.-L. Yip, and Y. Cao, "Graded 2D/3D perovskite heterostructure for efficient and operationally stable MA-free perovskite solar cells," *Advanced Materials*,

vol. 32, no. 26, p. 2000571, 2020.

[271] S. Jariwala, S. Burke, S. Dunfield, R. C. Shallcross, M. Taddei, J. Wang, G. E. Eperon, N. R. Armstrong, J. J. Berry, and D. S. Ginger, "Reducing surface recombination velocity of methylammonium-free mixed-cation mixed-halide perovskites via surface passivation," *Chemistry of Materials*, vol. 33, no. 13, pp. 5035–5044, 2021.

[272] D. Kiermasch, L. Gil-Escrig, A. Baumann, H. J. Bolink, V. Dyakonov, and K. Tvingstedt, "Unravelling steady-state bulk recombination dynamics in thick efficient vacuum-deposited perovskite solar cells by transient methods," *Journal of Materials Chemistry A*, vol. 7, no. 24, pp. 14712–14722, 2019.

[273] K. Tvingstedt, L. Gil-Escrig, C. Momblona, P. Rieder, D. Kiermasch, M. Sessolo, A. Baumann, H. J. Bolink, and V. Dyakonov, "Removing leakage and surface recombination in planar perovskite solar cells," *ACS Energy Letters*, vol. 2, no. 2, pp. 424–430, 2017.

[274] P. R. Barnes, K. Miettunen, X. Li, A. Y. Anderson, T. Bessho, M. Gratzel, and B. C. O'Regan, "Interpretation of optoelectronic transient and charge extraction measurements in dye-sensitized solar cells," *Advanced Materials*, vol. 25, no. 13, pp. 1881–1922, 2013.

[275] B. C. O'Regan, J. R. Durrant, P. M. Sommeling, and N. J. Bakker, "Influence of the $TiCl_4$ treatment on nanocrystalline TiO_2 films in dye-sensitized solar cells. 2. charge density, band edge shifts, and quantification of recombination losses at short circuit," *The Journal of Physical Chemistry C*, vol. 111, no. 37, pp. 14001–14010, 2007.

[276] R. Hamilton, C. G. Shuttle, B. O'Regan, T. C. Hammant, J. Nelson, and J. R. Durrant, "Recombination in annealed and nonannealed polythiophene/fullerene solar cells: transient photovoltage studies versus numerical modeling," *The Journal of Physical Chemistry Letters*, vol. 1, no. 9, pp. 1432–1436, 2010.

[277] A. Foertig, J. Rauh, V. Dyakonov, and C. Deibel, "Shockley equation parameters of P3HT: PCBM solar cells determined by transient techniques," *Physical Review B*, vol. 86, no. 11, p. 115302, 2012.

[278] S. Wood, J. C. Blakesley, and F. A. Castro, "Assessing the validity of transient photovoltage measurements and analysis for organic solar cells," *Physical Review Applied*, vol. 10, p. 024038, Aug 2018.

[279] U. Rau, "Superposition and reciprocity in the electroluminescence and photoluminescence of solar cells," *IEEE Journal of Photovoltaics*, vol. 2, no. 2, pp. 169–172, 2012.

[280] O. Breitenstein, "An alternative one-diode model for illuminated solar cells," *IEEE Journal of Photovoltaics*, vol. 4, no. 3, pp. 899–905, 2014.

[281] J. Bisquert, "Chemical capacitance of nanostructured semiconductors: its origin and significance for nanocomposite solar cells," *Physical Chemistry Chemical Physics*, vol. 5, no. 24, pp. 5360–5364, 2003.

[282] D. Credgington and J. R. Durrant, "Insights from transient optoelectronic analyses on the open-circuit voltage of organic solar cells," *The Journal of Physical Chemistry Letters*, vol. 3, no. 11, pp. 1465–1478, 2012.

[283] J. Wu, H. Cha, T. Du, Y. Dong, W. Xu, C.-T. Lin, and J. R. Durrant, "A comparison of charge carrier dynamics in organic and perovskite solar cells," *Advanced Materials*, vol. 34, no. 2, p. 2101833, 2022.

[284] U. Rau, V. Huhn, and B. E. Pieters, "Luminescence analysis of charge-carrier separation and internal series-resistance losses in $Cu(In,Ga)Se_2$ solar cells," *Physical Review Applied*, vol. 14, no. 1, p. 014046, 2020.

[285] M. Stolterfoht, V. M. Le Corre, M. Feuerstein, P. Caprioglio, L. J. A. Koster, and D. Neher, "Voltage-dependent photoluminescence and how it correlates with the fill factor and open-circuit voltage in perovskite solar cells," *ACS Energy Letters*, vol. 4, no. 12, pp. 2887–2892, 2019.

[286] D. Grabowski, Z. Liu, G. Schöpe, U. Rau, and T. Kirchartz, "Fill factor losses and deviations from the superposition principle in lead halide perovskite solar cells," *Solar RRL*, vol. 6, no. 11, p. 2200507, 2022.

[287] K. T. Cho, G. Grancini, Y. Lee, E. Oveisi, J. Ryu, O. Almora, M. Tschumi, P. A. Schouwink, G. Seo, S. Heo, *et al.*, "Selective growth of layered perovskites for stable and efficient photovoltaics," *Energy & Environmental Science*, vol. 11, no. 4, pp. 952–959, 2018.

[288] K. A. Bush, K. Frohna, R. Prasanna, R. E. Beal, T. Leijtens, S. A. Swifter, and M. D. McGehee, "Compositional engineering for efficient wide band gap perovskites with improved stability to photoinduced phase segregation," *ACS Energy Letters*, vol. 3, no. 2, pp. 428–435, 2018.

[289] F. Peña-Camargo, P. Caprioglio, F. Zu, E. Gutierrez-Partida, C. M. Wolff, K. Brinkmann, S. Albrecht, T. Riedl, N. Koch, D. Neher, *et al.*, "Halide segregation versus interfacial recombination in bromide-rich wide-gap perovskite solar cells," *ACS Energy Letters*, vol. 5, no. 8, pp. 2728–2736, 2020.

[290] C. Chen, Z. Song, C. Xiao, R. A. Awni, C. Yao, N. Shrestha, C. Li, S. S. Bista, Y. Zhang, L. Chen, *et al.*, "Arylammonium-assisted reduction of the open-circuit voltage deficit in wide-bandgap perovskite solar cells: the role of suppressed ion migration," *ACS Energy Letters*, vol. 5, no. 8, pp. 2560–2568, 2020.

[291] D. B. Khadka, Y. Shirai, M. Yanagida, T. Noda, and K. Miyano, "Tailoring the open-circuit voltage deficit of wide-band-gap perovskite solar cells using alkyl chain-substituted fullerene derivatives," *ACS Applied Materials & Interfaces*, vol. 10, no. 26, pp. 22074–22082, 2018.

[292] Z. Wang, Q. Lin, F. P. Chmiel, N. Sakai, L. M. Herz, and H. J. Snaith, "Efficient ambient-air-stable solar cells with $2D-3D$ heterostructured butylammonium-caesium-formamidinium lead halide perovskites," *Nature Energy*, vol. 2, no. 9, pp. 1–10, 2017.

[293] Y. Yu, C. Wang, C. R. Grice, N. Shrestha, D. Zhao, W. Liao, L. Guan, R. A. Awni, W. Meng, and A. J. Cimaroli, "Synergistic effects of lead thiocyanate additive and solvent annealing on the performance of wide-bandgap perovskite solar cells," *ACS Energy Letters*, vol. 2, no. 5, pp. 1177–1182, 2017.

[294] D. P. McMeekin, G. Sadoughi, W. Rehman, G. E. Eperon, M. Saliba, M. T. Hörantner, A. Haghighirad, N. Sakai, L. Korte, and B. Rech, "A mixed-cation lead mixed-halide perovskite absorber for tandem solar cells," *Science*, vol. 351, no. 6269, pp. 151–155, 2016.

[295] Y. Zhou, F. Wang, Y. Cao, J. Wang, H. Fang, M. A. Loi, N. Zhao, and C. Wong, "Benzylamine-treated wide-bandgap perovskite with high thermal-

photostability and photovoltaic performance," *Advanced Energy Materials*, vol. 7, no. 22, p. 1701048, 2017.

[296] Y. Zhou, Y.-H. Jia, H.-H. Fang, M. A. Loi, F.-Y. Xie, L. Gong, M.-C. Qin, X.-H. Lu, C.-P. Wong, and N. Zhao, "Composition-tuned wide bandgap perovskites: From grain engineering to stability and performance improvement," *Advanced Functional Materials*, vol. 28, no. 35, p. 1803130, 2018.

[297] J. Zhang, Z. Wang, A. Mishra, M. Yu, M. Shasti, W. Tress, D. J. Kubicki, C. E. Avalos, H. Lu, Y. Liu, *et al.*, "Intermediate phase enhances inorganic perovskite and metal oxide interface for efficient photovoltaics," *Joule*, vol. 4, no. 1, pp. 222–234, 2020.

[298] Z. Liu, J. Siekmann, B. Klingebiel, U. Rau, and T. Kirchartz, "Interface optimization via fullerene blends enables open-circuit voltages of 1.35V in $CH_3NH_3Pb(I_{0.8}Br_{0.2})_3$ solar cells," *Advanced Energy Materials*, vol. 11, no. 16, p. 2003386, 2021.

[299] L. Slooff, S. Veenstra, J. Kroon, D. Moet, J. Sweelssen, and M. Koetse, "Determining the internal quantum efficiency of highly efficient polymer solar cells through optical modeling," *Applied Physics Letters*, vol. 90, no. 14, p. 143506, 2007.

[300] Q. Xue, Y. Bai, M. Liu, R. Xia, Z. Hu, Z. Chen, X.-F. Jiang, F. Huang, S. Yang, Y. Matsuo, H.-L. Yip, and Y. Cao, "Dual interfacial modifications enable high performance semitransparent perovskite solar cells with large open circuit voltage and fill factor," *Advanced Energy Materials*, vol. 7, no. 9, p. 1602333, 2017.

Acknowledgments

I want to express my sincere gratitude to all the incredible individuals and organizations who have supported me throughout this thesis. This journey would not have been possible without their guidance, assistance, and belief in me.

First, I want to express my appreciation to the Forschungszentrum Jülich, IEK-5 Photovoltaics, for providing the necessary resources and facilities that have been instrumental in carrying out my research.

My deepest thanks go to Prof. Dr. Uwe Rau, the head of the institute and my Doktorvater, for his genuine interest in my studies and his excellent ideas. His guidance and keen involvement have been invaluable. I am truly grateful to him for being an excellent supervisor and conducting the examination of this thesis.

I am thankful to Prof. Dr. Bruno Ehrler for taking on the responsibility as the second assessor.

I want to express my deep appreciation to Prof. Dr. Thomas Kirchartz, who has not only provided valuable scientific input but also encouraged me to think outside the box. His immense knowledge and expertise have provided me with abundant scientific insights and brilliant ideas. I am grateful for his trust in my abilities, especially when I have questioned them, and for granting me the freedom to explore during my research. He is an excellent group leader and I immensely appreciate his guidance.

Dr. Benjamin Klingebiel deserves a special mention for his versatile help and support in the chemistry lab. Many thanks for always being a reliable contact person, especially for everything closely related to chemistry and all topics related to Joseph. His support was crucial for developing coevaporation solar cells in our group.

I would also like to thank Markus Hülsbeck for his support with EL, PL and TPL setups and for providing expertise in the optical lab. His experience and wil-

lingness to teach and help whenever needed have been invaluable to my research.

A big thanks goes to Dr. Zhifa Liu for his invaluable collaboration, assistance with perovskite fabrication and provision of solar cells for characterization. His expertise in fabricating perovskite solar cells with exceptionally high open-circuit voltages has significantly contributed to advancing my research.

Dr. Karsten Bittkau and Benedikt Krogmeier deserve recognition for their help in simulations and models, which have significantly enriched the depth of my thesis.

I thank Oliver Thimm for his contributions to PDS measurements and analysis, providing me with optical data for numerical simulations.

I extend my appreciation to the entire IEK-5 team, particularly our group members, for their countless contributions and wonderful community. The support and collaboration within the institute have been vital to my research and have shaped this thesis. The positive working atmosphere has genuinely made this journey enjoyable. Additionally, I want to thank my officemate Kathy for the nice companionship.

I want to acknowledge Dr. Maurice Nuys and the HITEC team for providing diverse training opportunities that have enhanced my skills and knowledge.

A special thanks goes to Dr. Thomas Unold and his group from Helmholtz-Zentrum Berlin for the collaboration, especially to Dr. José A. Márquez Prieto and Dr. Sergiu Levcenko for their spontaneous and immediate help with hyperspectral imaging and TPL.

Lastly, I would like to express my deepest gratitude to my family and friends. To my parents, thank you for your perpetual support throughout my entire life and scientific career. I am grateful for your unwavering belief in me. To my sister Charly and my friends Patty, Claudi, Sevi, and anyone else I may have unintentionally omitted but who truly deserves recognition, I am grateful for your constant encouragement and presence in my life.

Many thanks to all of you!

Band / Volume 655
Entwicklung alternativer Brenngaselektroden für die Hochtemperatur-Elektrolyse
F. E. Winterhalder (2025), vii, 161 pp
ISBN: 978-3-95806-805-6

Band / Volume 656
Oxide-based All-Solid-State Batteries for and from Recycling Processes
V. M. Kiyek (2025), viii, 128 pp, xix
ISBN: 978-3-95806-806-3

Band / Volume 657
Investigation of current and future anthropogenic chemical regimes in simulation chamber experiments
M. Färber (2025), 213 pp
ISBN: 978-3-95806-809-4

Band / Volume 658
Dynamischer Betrieb von Polymer-Elektrolyt-Membran Wasserelektrolyseuren
E. Rauls (2025), XIV, 239 pp
ISBN: 978-3-95806-811-7

Band / Volume 659
Pore-scale reactive transport modeling in cementitious materials: Development and application of a high-performance computing code based on the Lattice-Boltzmann method
S. Rohmen (2025), X, 295 pp
ISBN: 978-3-95806-812-4

Band / Volume 660
Recyclingmöglichkeiten für die Keramikkomponenten einer Festoxidzelle
S. Sarner (2025), VIII, 122 pp
ISBN: 978-3-95806-816-2

Band / Volume 661
Methodological Approach Enabling the Two-phase Flow Investigation in Alkaline Electrolysis under Demanding Conditions
S. Renz (2025), IX, 252 pp
ISBN: 978-3-95806-821-6

Band / Volume 662
Variable renewable energy potential estimates based on high-resolution regional atmospheric modelling over southern Africa
S. Chen (2025), XIII, 141 pp
ISBN: 978-3-95806-822-3

Band / Volume 663
Advances in Understanding Nitrate Aerosol Formation and the Implications for Atmospheric Radiative Balance
A. Milousis (2025), 195 pp
ISBN: 978-3-95806-823-0

Band / Volume 664
Optimization of NaSICON-type lithium-ion conductors for solid-state batteries
A. Loutati (2025), viii, 104 pp
ISBN: 978-3-95806-824-7

Band / Volume 665
Innovative Plasma Sprayed Thermal Barrier Coatings for Enhanced Flexibility in Gas Turbine Operation
J. Igel (2025), V, 153, XXXVI pp
ISBN: 978-3-95806-827-8

Band / Volume 666
Techno-ökonomisches Potenzial dezentraler und autarker Energiesysteme
S. K. A. Risch (2025), xxiii, 210 pp
ISBN: 978-3-95806-829-2

Band / Volume 667
Reactive Field Assisted Sintering of Novel Rare Earth Garnets for Plasma Etching Applications
C. Stern (2025), VII, 101, XXVIII pp
ISBN: 978-3-95806-833-9

Band / Volume 668
Effects of mucilage and extracellular polymeric substances on soil gas diffusion
A. Haupenthal (2025), v, 99 pp
ISBN: 978-3-95806-834-6

Band / Volume 669
Quantifying Recombination Losses and Charge Extraction in Halide Perovskite Solar Cells
L. Krückemeier (2025), vi, 286 pp
ISBN: 978-3-95806-835-3

Weitere ***Schriften des Verlags im Forschungszentrum Jülich*** unter
http://wwwzb1.fz-juelich.de/verlagextern1/index.asp

Energie & Umwelt / Energy & Environment
Band / Volume 669
ISBN 978-3-95806-835-3

Mitglied der Helmholtz-Gemeinschaft

JÜLICH
Forschungszentrum